Lídia Sofia Leitão Santos

Licenciada em Química Tecnológica

Engineering of Metal Oxide Nanoparticles for Application in Electrochemical Devices

Dissertação para obtenção do Grau de Doutor em

Nanotecnologias e Nanociências

Orientador:	Doutora Elvira Maria Correia Fortunato, Professora Catedrática, Faculdade de Ciências e Tecnologias da Universidade Nova de Lisboa
Co-orientador:	Doutor Luís Miguel Nunes Pereira, Professor Auxiliar, Faculdade de Ciências e Tecnologias da Universidade Nova de Lisboa

	Júri:
Presidente:	Professor Doutor Fernando José Pires Santana
Arguentes:	Prof. Doutora Verónica Cortés de Zea Bermudez
	Prof. Doutora Maria Goreti Ferreira Sales
Vogais:	Professor Doutor Rodrigo Ferrão de Paiva Martins
	Prof. Doutora Florinda Mendes da Costa
	Prof. Doutora Maria Manuela Silva Pires Silva
	Prof. Doutor Pedro Miguel Cândido Barquinha

FACULDADE DE CIÊNCIAS E TECNOLOGIA
UNIVERSIDADE NOVA DE LISBOA

Julho de 2015

Lídia Sofia Leitão Santos

Licenciada em Química Tecnológica

Engineering of Metal Oxide Nanoparticles for Application in Electrochemical Devices

Dissertação para obtenção do Grau de Doutor em

Nanotecnologias e Nanociências

Orientador:	Doutora Elvira Maria Correia Fortunato, Professora Catedrática, Faculdade de Ciências e Tecnologias da Universidade Nova de Lisboa
Co-orientador:	Doutor Luís Miguel Nunes Pereira, Professor Auxiliar, Faculdade de Ciências e Tecnologias da Universidade Nova de Lisboa

	Júri:
Presidente:	Professor Doutor Fernando José Pires Santana
Arguentes:	Prof. Doutora Verónica Cortés de Zea Bermudez
	Prof. Doutora Maria Goreti Ferreira Sales
Vogais:	Professor Doutor Rodrigo Ferrão de Paiva Martins
	Prof. Doutora Florinda Mendes da Costa
	Prof. Doutora Maria Manuela Silva Pires Silva
	Prof. Doutor Pedro Miguel Cândido Barquinha

FACULDADE DE CIÊNCIAS E TECNOLOGIA
UNIVERSIDADE NOVA DE LISBOA

Julho de 2015

Engineering of Metal Oxide Nanoparticles for Application in Electrochemical Devices

Acknowlegments

Even if my PhD took four years to complete, I will take this opportunity to appreciate all the people that, by one way or another, helped me to get here and finish this work.

First I would like to thank my supervisors, Professor Elvira Fortunato and Professor Luis Pereira for helping me planning this work, giving new ideas and discussing the results. Thank you for all your support and enthusiasm throughout this years. You are both responsible for me getting here!

To Professor Rodrigo Martins, together with Professor Elvira Fortunato, for being an example in achieving and retrieving, always, for better results, as well as, giving me all the tools to get there and, allowing to develop this work in DCM and CENIMAT facilities.

To Fundação para a Ciência e Tecnologia for the fellowship (SFRH/BD/73810/2010) that assured me these four years of work experience.

To the actual and former colleagues in CENIMAT and DCM that share the work, lab, lunch and breaks with me: Pedro Barquinha, for your expertise and fruitful discussions; Sonia Pereira e Alexandra Gonçalves, for helping in all what it is needed in the lab; Ana Ramos e Sofia Cruz, main accompaniers in the beginning of this work; Pawel Wojcik, Joana Pinto, Joana Neto, Daniela Gomes, Tomás Calmeiro, for our enthusiastic debates around science in general; Daniela Salgueiro, Diana Gaspar and Ana Baptista, also for sharing the room with me; Andreia Cardoso, Mafalda Costa, Antonio Vincente, Tiago Mateus, Ricardo Ferreira, Ana Catarina, Raquel Barros, Paulo Duarte, Jonas Deuermeier, Asal Kiazadeh, Ana Rovisco, Jorge Martins, Cristina Fernandes and the rest of the group, I really enjoy working, and sharing the daily life with all of you!

To Paulo Manteigas, Susana Mendes, Patricia Carrão, Valeria Gomes, Carla Saldanha, Sara Oliveira and Sónia Seixas for all the help and support in all the bureaucratic issues.

To Professor Gabriela Almeida and Dr. Célia Silveira for all your help and patience in introducing me in the field of electrochemistry and biosensors, as well as, sharing the lab facilities in REQUIMTE, FCT/UNL.

To Dr. Smilja Todorovic for your support with the Raman measurements in ITQB and with the writing of the article.

To Prof. Jaime Viegas and Dr. Elamurugu Elangovan for your time and help doing the TEM images in i-Micro, Masdar Institute of Science and Technology.

To all my friends that I got on the way, Alberto Batista and Diana Marcelino, Rafael Vidigal and Andreia Silva, Diogo Duarte and Filipa Alcaide, Carla and Ricardo Pinheiro, it was a real pleasure to meet you!

To my other friends that known me long time ago, during my chemistry degree, Hugo Teixeira, Vanessa Leite, Bruno Amaral, Pedro Costa, Sofia Miguel, Filipa Siopa, you are very special to me!

A special thanks to Rita Branquinho since you are, in fact, the person responsible for me being here in CENIMAT, so thank you for that and for putting up with me for all these years!

To all my very “old” friends from Peniche (the real “amigos de Peniche”), Hélia Janardo, Ricardo Rodrigues, Carla Franco, Agnelo Rodrigues, Teresa Marreiros, David Vieira, Nuno Franco, Elina Costa, Ana Ferreira, Lena Simões, Hélder Blayer and Ivone Ribeiro (you are also a little bit from Peniche!) for sharing so many good times with me, I appreciate all of it!

To my family… No words to explain how important you are to me! To my mom, you are the main responsible for me being who I am, thank you for everything, my brothers, Paulo e Cajó, you were my role model, thank you for taking care of me, my sister, Susana, my best friend ever, thank you for being who you are, my sisters-in-law, Paula and Paula, my brother-in-law, João, my nephews, Filipe (almost a daddy), João, António, Diogo and Xavier, and my nieces, Frederica and Sofia, you mean the world to me!

To Nuno’s family, that also became mine, Maria da Fé, Herculano Trovão e Cristina Monteiro, Francisco Trovão and Maria (almost Trovão), Filipe Otero, Cinda Ferreira, Filipa and Henrique Marconi, Ricardo Trovão and Isabel Nunes, thank you for taking me into your family and life.

To Margarida, thank you for your love!

And most especially, to Nuno, I want to thank you for all the patience and love that you show me every day, all the jokes, all the talks,… you make me a better person!

Abstract

The growing demand for materials and devices with new functionalities led to the increased interest in the field of nanomaterials and nanotechnologies. Nanoparticles, not only present a reduced size as well as high reactivity, which allows the development of electronic and electrochemical devices with exclusive properties, when compared with thin films.

This dissertation aims to explore the development of several nanostructured metal oxides by solvothermal synthesis and its application in different electrochemical devices. Within this broad theme, this study has a specific number of objectives: a) research of the influence of the synthesis parameters to the structure and morphology of the nanoparticles; b) improvement of the performance of the electrochromic devices with the application of the nanoparticles as electrode; c) application of the nanoparticles as probes to sensing devices; and d) production of solution-processed transistors with a nanostructured metal oxide semiconductor.

Regarding the results, several conclusions can be exposed. Solvothermal synthesis shows to be a very versatile method to control the growth and morphology of the nanoparticles.

The electrochromic device performance is influenced by the different structures and morphologies of WO_3 nanoparticles, mainly due to the surface area and conductivity of the materials. The deposition of the electrochromic layer by inkjet printing allows the patterning of the electrodes without wasting material and without any additional steps.

Nanostructured WO_3 probes were produced by electrodeposition and drop casting and applied as pH sensor and biosensor, respectively. The good performance and sensitivity of the devices is explained by the high number of electrochemical reactions occurring at the surface of the nanoparticles.

GIZO nanoparticles were deposited by spin coating and used in electrolyte-gated transistors, which promotes a good interface between the semiconductor and the dielectric. The produced transistors work at low potential and with improved ON-OFF current ratio, up to 6 orders of magnitude.

To summarize, the low temperatures used in the production of the devices are compatible with flexible substrates and additionally, the low cost of the techniques involved can be adapted for disposable devices.

Keywords: Nanoparticles; Metal oxides; Solvothermal synthesis; Electrochemical devices; Electrochromic; Sensors; Transistors.

Resumo

A crescente demanda por materiais e dispositivos com novas funcionalidades impulsionou o interesse na área dos nanomateriais e nanotecnologias. As nanopartículas não só apresentam dimensões reduzidas como elevada reactividade, que possibilitam a fabricação de dispositivos electrónicos e electroquímicos com propriedades únicas, quando comparadas com a utilização do mesmo material na forma de filme fino.

Nesta dissertação pretende-se desenvolver diferentes óxidos metálicos nanoestruturados por síntese solvotermal, bem como a sua aplicação em diferentes dispositivos electroquímicos. Dentro deste vasto tema, o presente trabalho apresenta os seguintes objectivos: a) estudo da influência dos parâmetros de síntese na estrutura e morfologia das nanopartículas; b) melhorar a performance dos dispositivos electrocrómicos com a aplicação das nanopartículas como eléctrodos; c) aplicar as nanopartículas em sondas para diferentes tipos de sensores; d) produção de transístores compatíveis com processos de solução utilizando semiconductores de óxidos metálicos nanoestruturados.

De acordo com os resultados obtidos podem ser retiradas diversas conclusões. A síntese solvotermal é um método bastante versátil para controlar o crescimento e morfologia das nanopartículas.

A performance dos dispositivos electrocrómicos foi influenciada pelas diferentes estruturas e morfologias das nanopartículas de WO_3 devido, principalmente, à área superficial e conductividade dos materiais. A deposição da camada electrocrómica efectuada por impressão de jacto de tinta possibilita definir diferentes padrões sem desperdício de materiais ou quaisquer passos adicionais.

As sondas de WO_3 nanoestruturadas foram produzidas por electrodeposição e “drop casting” para aplicação em sensores de pH e em biossensores, respectivamente. A elevada performance e sensibilidade destes sensores deve-se ao número elevado de reacção electroquímicas que ocorrem à superfície das nanopartículas.

Nanopartículas de GIZO foram depositadas por “spin coating” e aplicadas em transístores onde o dieléctrico foi substituído por electrólito. Esta estrutura permite uma melhor interface entre o semiconductor e o electrólito, e os transístores operam com um potencial eléctrico reduzido e uma elevada diferença de corrente entre os estados ON e OFF (até 6 ordens de grandeza).

Por último, a reduzida temperatura utilizada na produção destes dispositivos é compatível com substractos flexíveis e adicionalmente, devido ao baixo custo das técnicas utilizadas estes processos podem ser potencialmente adaptados para a produção de dispositivos descartáveis.

Palavras-chave: Nanopartículas; Óxidos metálicos; Síntese solvotermal; Dispositivos electroquímicos; Electrocrómicos; Sensores; Transístores.

Contents

LIST OF FIGURES ..... **XIV**

LIST OF TABLES ..... **XX**

ABBREVIATIONS ..... **XXI**

SYMBOLS ..... **XXIII**

CHAPTER 1. INTRODUCTION **1**

1.1. NANOSCIENCE AND NANOTECHNOLOGY 2

1.2. NANOMATERIALS 4

1.3. NANOPARTICLES ENGINEERING 8

1.3.1. Dispersions Stability *9*

1.3.2. Synthesis Techniques *14*

1.3.3. Particle Nucleation and Growth Theory *21*

1.4. METAL OXIDES NANOPARTICLES 24

1.4.1. Tungsten trioxide (WO_3) *25*

1.4.2. Multi-Element Oxides *31*

1.5. MOTIVATION AND THESIS OUTLINE 33

1.6. REFERENCES 35

CHAPTER 2. SOLVOTHERMAL SYNTHESIS OF METAL OXIDE NANOPARTICLES 45

2.1. TUNGSTEN OXIDE (WO_x) 46

2.1.1. Peroxopolytungstic Acid (PTA) Precursor *46*

2.1.2. Sodium Tungstate Precursor ($Na_2WO_4 \cdot 2H_2O$) *48*

2.2. VANADIUM PENTOXIDE (V_2O_5) 50

2.3. NICKEL OXIDE (NiO_x) 51

2.4. HAFNIUM OXIDE (HfO_2) 52

2.5. MANGANESE OXIDE (MnO_2) 53

2.6. GALLIUM-INDIUM-ZINC OXIDE (GIZO) 54

2.7. ZINC-TIN OXIDE (ZTO) 54

2.8. REFERENCES 55

CHAPTER 3. WO_3 AS ELECTROCHROMIC MATERIAL **57**

3.1. ABSTRACT 58

3.2. INTRODUCTION 58

3.3. RESULTS AND DISCUSSION 59

3.3.1. Nanoparticles Characterization ... *59*
3.3.2. Thin Film Production ... *65*
3.3.3. Electrochromic Characterization ... *66*
3.3.4. Stability Studies ... *68*
3.4. CONCLUSION ... 70
3.5. EXPERIMENTAL SECTION ... 71
3.6. ACKNOWLEDGEMENTS ... 72
3.7. REFERENCES ... 73
3.8. SUPPORTING INFORMATION ... 74

CHAPTER 4. WO_3 AS PH SENSOR ... 77
4.1. ABSTRACT ... 78
4.2. INTRODUCTION ... 78
4.3. EXPERIMENTAL SECTION ... 79
4.4. RESULTS AND DISCUSSION ... 82
4.4.1. WO_3 Nanoparticles Characterization ... *82*
4.4.2. Sensor Assembly ... *84*
4.4.3. Wax Cytocompatibility ... *85*
4.4.4. Sensing Layer ... *85*
4.4.5. WO_3 Sensing Layer Electrochemical Characterization ... *87*
4.4.6. pH Sensitivity and Reproducibility ... *88*
4.4.7. Reversibility ... *90*
4.4.8. Response Time ... *91*
4.4.9. Proof of Concept: Flexible pH Sensor ... *92*
4.5. CONCLUSIONS ... 93
4.6. ACKNOWLEDGMENTS ... 94
4.7. REFERENCES ... 94
4.8. SUPPORTING INFORMATION ... 96

CHAPTER 5. WO_3 FOR BIOSENSOR APPLICATIONS ... 99
5.1. ABSTRACT ... 100
5.2. INTRODUCTION ... 100
5.3. EXPERIMENTAL SECTION ... 102
5.4. RESULTS AND DISCUSSION ... 103
5.4.1. WO_3 Nanoparticles Characterization ... *103*
5.4.2. Electrochemical Properties of WO_3 Films ... *106*
5.4.3. Proof of concept: nitrite biosensor ... *110*
5.5. CONCLUSIONS ... 113
5.6. ACKNOWLEDGEMENTS ... 113
5.7. REFERENCES ... 114
5.8. SUPPORTING INFORMATION ... 118

CHAPTER 6. GIZO AS ACTIVE LAYER IN ELECTROLYTE-GATED TRANSISTORS (EGTS) 125

6.1. ABSTRACT 126
6.2. INTRODUCTION 126
6.3. EXPERIMENTAL SECTION 129
6.4. RESULTS AND DISCUSSION 131
6.4.1. Nanoparticles Characterization 131
6.4.2. GIZO Inks and Film Characterization 132
6.4.3. Electrolyte Characterization 134
6.4.4. EGTs Characterization 135
6.5. CONCLUSION 139
6.6. ACKNOWLEDGMENT 139
6.7. REFERENCES 139
6.8. SUPPORTING INFORMATION 142

CHAPTER 7. CONCLUSIONS AND FUTURE WORK 147
7.1. FUTURE PERSPECTIVES 148

CHAPTER 8. APPENDIX 1 151

List of Figures

Figure 1.1. Major historic events for the development of nanoscience and nanotechnology. 3
Figure 1.2. Number of manuscripts published in 2000, 2005, 2010 and 2013 under the topics: Nano, Nanoparticle, Nanotechnology and Nanotoxicology. Based on topic search performed in ISI web of knowledge, at Dec. 2014. 4
Figure 1.3. Nanomaterials classification according to its dimensionality. 5
Figure 1.4. Electronic density of states for a bulk 3D, 2D, 1D nanocrystalline material and 0D quantum dot. The arrows represent the spatial confinement occurring in each system. 6
Figure 1.5. a) Nanotechnology consumers' products evolution; b) Most common materials used in the products; and c) Products categories. The inventory was performed in October 2013.[21] 7
Figure 1.6. SEM images of: a) Diatom Frustule (image copyright © Dennis Kunkel Microscopy, Inc.), b) Diatom Coscinodiscus wailesii algaes (adapted from [28]), c) Swallowtail butterfly (image copyright © Dennis Kunkel Microscopy, Inc.), and d) Lycaenid butterfly wing scales (adapted from [29]). 9
Figure 1.7. Electrostatic double layer (EDL), van der Waals and Derjaguin-Landau-Verwey-Overbeak (DLVO) forces represented as total potential energy as a function of nanoparticles separation distance. 10
Figure 1.8. Representation of the surface charge dependence with the pH. 11
Figure 1.9. Schematic representation of the electrical double layer (EDL) structure. 12
Figure 1.10. Representation of electrostatic and steric stabilization between two nanoparticles. 13
Figure 1.11. Extended Derjaguin-Landau-Verwey-Overbeak (xDLVO) forces represented as the total potential energy as a function of the nanoparticles separation distance. 13
Figure 1.12. a) Example of a ball mill from RETSCH[44], b) Typical containers and balls used in the equipment and c) Schematic representation of the ball milling process. 14
Figure 1.13. Representation of the most common physical processes used in nanostructures production. 15
Figure 1.14. Sol-gel synthesis process representation. 16
Figure 1.15. Number of articles published in 2000, 2005, 2010 and 2013 under the topics of hydrothermal and solvothermal synthesis. Based on topic search performed in ISI web of knowledge. 18
Figure 1.16. Dielectric constant of water as a function of the temperature.[60] 19
Figure 1.17. Autoclave (acid digestion vessel) image from Parr Instrument Company.[62] 20
Figure 1.18. Continuous hydrothermal synthesis apparatus from Promethean Particles.[64] 20
Figure 1.19. a) Plot of LaMer model for the generation of atoms, nucleation, and subsequent growth of colloidal synthesis;[67] b) Representation of Gibbs free energy variation for nucleation as function of the radius of the solid cluster;[70] c) Schematic representation of the influence of the nucleation' kinetics to the final nanoparticles size, in the absence of Ostwald ripening.[71] 23
Figure 1.20. Scheme of nanocrystal growth controlled by Ostwald ripening mechanism[73] 24
Figure 1.21. Transition and post-transition metals groups highlighted in the periodic table.[80] 25

Figure 1.22. Schematic band structure of WO_3 (filled states are colored). The energy band gap (E_g) vary from 2.6 to 3.2 eV for amorphous and crystalline states, respectively.[85] 26
Figure 1.23. Schematic representation of the energy versus the momentum for the valence (VB) and conduction bands (CB) of semiconductors and the difference between direct and indirect transitions (or band gaps). 27
Figure 1.24. WO_3 crystal structures, designed in CrystalMaker software for: a) Monoclinic (*m*-WO_3) and b) Hexagonal (*h*-WO_3) configurations. 27
Figure 1.25. Crystal structure, designed in CrystalMaker software, for orthorhombic hydrated WO_3 (*ortho*-$WO_3 \cdot 0.33H_2O$). 28
Figure 1.26. a) Pourbaix diagram for W-H_2O system at 25 ºC and tungsten molar concentration of 10^{-4} M (dashed lines represent the limits of stability of water), and b) Solubility diagram for a fixed potential of E_h = 0.2 V, 25 ºC and 3 M ionic strength.[100]–[102] 29
Figure 1.27. Schematic representation of an electrochromic device, a) before and b) after charge appliance (with the cation insertion and color modification of the electrochromic material). 30
Figure 1.28. Examples of electrochromic applications developed in CENIMAT: a) Electrochromic passive matrix in paper, under the project SMART-EC (FP7-ICT-2009.3.9/258203), b) Transparent electrochromic window, and c) Gas sensor prototype with EC display on paper, under the project A3PLE (FP7-NMP-2010-SME/262782-2). 30
Figure 1.29. Schematic band structure of Ga_2O_3-In_2O_3-ZnO (filled states are colored). The energy band gaps (E_g) are reported for crystalline structures.[127] 32
Figure 1.30. Evolution of the transistors' size used in Intel® processors during the last decades. 35
Figure 2.1. Schematic representation of the hydrothermal synthesis process. 46
Figure 2.2. a) SEM images and b) XRD diffractograms of the hydrothermal synthesized WO_x nanopowders, using PTA as precursor with three different synthesis acidities and times. Adapted from [3]. 47
Figure 2.3. a) SEM images and b) XRD diffractograms of the hydrothermal synthesized WO_x nanopowders using Na_2WO_4 as precursor with three different synthesis acidities and times. 49
Figure 2.4. SEM images of the microwave assisted hydrothermal synthesized WO_3 nanopowders using Na_2WO_4 as precursor, Na_2SO_4 as structure directing agent, for 1 hour, with constant power of 100 W and at a) pH 1.8 and b) pH 0. 49
Figure 2.5. XRD diffractograms of the hydrothermal synthesized V_2O_5 xerogels with three different synthesis times and using: a) 0.1 g, b) 0.05 g and c) 0.01 g of V_2O_5 powder as precursor. 50
Figure 2.6. a) SEM image of the hydrothermal synthesized V_2O_5 xerogel with 0.05 g of precursor and for 24 h and b) simulation of the *m*-V_2O_5 layered structure, performed in CrystalMaker software. 51
Figure 2.7. SEM image and XRD diffractogram of the hydrothermal synthesized hexagonal $Ni(OH)_2$ powder from: a) and b) $NiSO_4$, and c) and d) $Ni(CH_3COO)_2$ precursors. 52
Figure 2.8. a) SEM image and b) XRD diffractogram of the hydrothermal synthesized monoclinic HfO_2 nanopowder. 53
Figure 2.9. a) SEM image and b) XRD diffractogram of the hydrothermal synthesized tetragonal α-MnO_2 nanowires. 53
Figure 2.10. a) SEM image and b) XRD diffractograms of the hydrothermal synthesized GIZO nanopowder and after annealing at 900 °C for 1 h. 54

Figure 2.11. a) SEM image and b) XRD diffractogram of the hydrothermal synthesized ZTO nanopowder. 55
Figure 3.1. a) XRD diffractograms of the nanopowders synthesized n: (a) H_2O; (b) 0.3 M HCl and (c) 3 M HCl. Reference diffractograms for *ortho*-$WO_3 \cdot 0.33H_2O$ (ICDD: 01-072-0199) and *m*-WO_3 (ICDD: 43-1035) have been placed above; b) Graphic representation of the crystallographic structure of the synthesized polymorphs (*m*-WO_3 and *ortho*-$WO_3.0.33H_2O$) obtained using Crystal Maker® software. 60
Figure 3.2. SEM images, EDS element distribution and TEM analysis of nanopowders obtained via hydrothermal synthesis performed in: a) H_2O; b) 0.3 M HCl and c) 3 M HCl. SEM images are false colored for a better visualization of the nanostructures. 61
Figure 3.3. TG of nanopowders obtained via hydrothermal synthesis performed from in: a) H_2O; b) 0.3 M HCl and c) 3 M HCl 62
Figure 3.4. a) Impedance plot for the full frequency range. Nyquist plot of WO_x nanopowders performed at room temperature and their theoretical fit (red line) to a CPE circuit (inset) for: b) m-WO_3 + *ortho*-$WO_3.0.33H_2O$; c) *ortho*-$WO_3.0.33H_2O$; d) *m*-WO_3 64
Figure 3.5. a) UV/Vis absorbance spectra and the correspondent Tauc's plots corresponding to: b) indirect and c) direct transitions of WO_3 nanoparticles dispersed in water. 65
Figure 3.6. *In situ* transmittance measurements at 800 nm applying a potential of ± 2 V for 30 s of inkjet dual-phase thin films: a) *a*-WO_3/(*m*-WO_3+*ortho*-$WO_3.0.33H_2O$); b) *a*-WO_3/*ortho*-$WO_3.0.33H_2O$; c) *a*-WO_3/*m*-WO_3 and d) single *a*-WO_3 thin film. 66
Figure 3.7. Cyclic voltammograms of inkjet printed dual-phase thin films performed in an electrochemical cell with platinum wire as counter electrode, Ag/AgCl as reference electrode in lithium based gel electrolyte at a scan rate of 50 mV/s. 67
Figure 3.8. Stability of CV measurements of inkjet printed thin films for 1000 cycles for a potential range from 0.5 to -1V. Capacity loss represents the charge difference between first and following cycles obtained by the integration of the cyclic voltammogram. 69
Figure 3.9. Ex-situ lithiation study of a) *ortho*-$WO_3.033H_2O$ and b) *m*-WO_3 nanoparticles deposited on ITO/glass substrates with 0.5 M $LiClO_4$ in PC electrolyte. 70
Figure 4.1. Simplified schematics of the first pH device using a WO_3 sensing layer. The device turns ON ($I_D > 0$) and OFF ($I_D = 0$) depending on the oxidized (insulating) or reduced (conductive) states of WO_3, respectively. Similar effect is observed by varying the pH (adapted from the work published by Wrighton et al.[22]). 79
Figure 4.2. Scheme of the: a) sensor production procedure, b) sensor design and structure and c) photograph of the final fabricated sensor. 81
Figure 4.3. SEM image of WO_3 nanoparticles. The inset shows a higher magnification of the nanoparticles exhibiting nanoslabs-type shape agglomerates. 83
Figure 4.4. a) XRD diffractograms of WO_3 synthesized powder and orthorhombic $WO_3 \cdot 0.33H_2O$ reference pattern (the * peaks correspond to unidentified structure); b) Crystal structure simulation of orthorhombic $WO_3 \cdot 0.33H_2O$ (produced in crystal maker© software); c) FTIR spectrum and d) Nitrogen adsorption-desorption isotherms of WO_3 nanoparticles performed at standard temperature and pressure (STP). 84

Figure 4.5. SEM images of: a) Sensing area after $WO_3 \cdot 0.33H_2O$ nanoparticles electrodeposition; b) Cross-section overview of Ti/Au, electrodeposited WO_3 nanoparticles and carbon sacrificial layers after FIB milling (The image was colored for better understanding of the layered structure). 86
Figure 4.6. a) Calibration curve of transmittance values at 280 nm wavelength for WO_3 dispersions of different concentrations and b) Transmittance of the PBS solution after dipping the WO_3 sensor at 37 ºC for 8 days. 87
Figure 4.7. Impedance modulus (solid lines) and phase angle (dashed lines) plots of the electrode before and after $WO_3.0.33H_2O$ nanoparticles electrodeposition. 88
Figure 4.8. pH sensitivity measured from pH 9 to 5 of: a) Au/WO_3 nanoparticles electrodes; b) Au electrode. The sensitivity is indicated inside the graphic. 89
Figure 4.9. Electrochemical potential behavior of the pH sensor during three completes cycles for pH range of 9 to 5 and 5 to 9. 90
Figure 4.10. Electrochemical potential behavior of the electrode after dipping in buffer solution of pH 9, 7 and 5. The response time was calculated as the time necessary to reach 90% of the maximum potential value. 92
Figure 4.11. a) pH sensitivity of WO_3 sensor using a flexible Ag/AgCl reference electrode in a non-planar surface made of gelatin-based electrolyte; b) photograph of the prototype. 93
Figure 5.1. Representation of the 3D structure of cytochrome c nitrite reductase, with the heme groups coordinating a central iron atom (deep red spheres). 101
Figure 5.2. *Left side:* a) XRD patterns of hydrothermally synthesized WO_3 powders; W1) 2.7 M, W2) 1.5 M and W3) 0.3 M of HCl (reference diffractograms for *m*-WO_3, ICDD: 43-1035 and *ortho*-$WO_3 \cdot 0.33H_2O$, ICDD: 01-072-0199 has been placed at bottom), b) Representation of (002) crystallographic plane projection (performed in crystal maker© software) for *m*-WO3 and c) *ortho*-$WO_3 \cdot 0.33H_2O$. *Right side:* SEM microstructures and TEM lattice-images of hydrothermal synthesized WO_3 nanoparticles: d), g) W1; e), h) W2; and f), i) W3. SEM images were false colored for better visualization of the nanoparticles structure while the darker background corresponds to the ITO electrode. The inset on TEM lattice-images shows the corresponding FFT images. The size scales of SEM and TEM images are the same in the three samples. 104
Figure 5.3. Electrochemical characterization of ITO and WO_3/ITO electrodes. a) Nyquist plots measured with an alternative voltage of 10 mV and frequency range 1-10^6 Hz; b) cyclic voltammograms performed at a scan rate 50 mV/s. The supporting electrolyte was 0.1 M KCl in 0.05 M tris-HCl pH 7.6 buffer. 107
Figure 5.4. Cyclic voltammograms of cyt *c* at ITO and WO_3/ITO electrodes measured at variable scan rates, from 35 to 750 mV s^{-1}. Protein concentration was 0.2 mM in 0.1 M KNO_3, 0.05 M phosphate buffer pH 7.6., Inset: Variation of anodic and cathodic peak current as a function of the square root of the scan rate. 109
Figure 5.5. Typical electrochemical response of *cc*NiR/WO_3/ITO electrodes in response to variable nitrite concentration (0-0.8 mM). a) Cyclic voltammograms performed at a scan rate of 50 mV s^{-1} in 0.05 M tris-HCl pH 7.6 buffer with 0.1 M KCl; b) Catalytic current (measured at -0.8 V) as a function of nitrite concentration and fitting (solid line) of the experimental data to the Michaelis-Menten equation. 111

Figure 6.1. a) Comparison of the cross section of an inorganic GIZO based nanoparticles transistor using a conventional dielectric film and an electrolyte; b) Schematics of the voltage (V) and electric field (E) distributions in a conventional dielectric and in electrolyte gate insulator when a positive gate voltage is applied; c) Schematics of the transistors architecture for a conventional structure incorporating thick gate dielectric (~100 nm) and for an EGT in which the gate dielectric is replaced by a polymer electrolyte, with indication of both EDLs at the gate/electrolyte and semiconductor/electrolyte interfaces. 127
Figure 6.2. a) XRD diffractograms before and after annealing at 900 ºC and reference ICDD diffractograms of *c*-In_2O_3, *m*-Ga_2O_3 and *h*-ZnO (file numbers 06-0416, 41-1103 and 05-0664, respectively); b) TEM image of GIZO nanoparticles before annealing (inset shows the diffraction pattern of the nanoparticles). 131
Figure 6.3. SEM images: a) before and b) after FIB milling; c) –f) EDS mapping of the elements; g) EDS spectrum and h) average of the atomic weights performed in 10 samples of GIZO (colored) and their percentages before synthesis (blank). 132
Figure 6.4. AFM topographic and phase images of GIZO20 films annealed at: a) 250 ºC and b) 350 ºC. The inset corresponds to the nanoparticles radius size distribution measured with the Gwyddion software. 134
Figure 6.5. a) Impedance modulus (□), phase angle (○) and capacitance (Δ) plot from EIS measurement (the inset represents the equivalent electric circuit, where *R* is the resistance, *W* the Warburg and CPE the constant phase elements) and b) Cyclic voltammogram of ITO/electrolyte/ITO capacitor structure at a scan rate of 50 mV/s. EIS conditions: alternative voltage 10 mV and frequency range 1-10^6 Hz. 135
Figure 6.6. Transfer characteristics, gate current with different gate voltage ranges (the red dashed line corresponds to V_G from -2 to 1 V and the solid black line from -2 to 2 V) and high resolution SEM image, after FIB milling, of the cross-section of EGT built with: a) GIZO30 and b) GIZO20 after 1 h annealing at 350 °C. Transfer characteristics and gate current were measured with 0.5 s delay time and the arrows represent the sweep direction. 138
Figure 7.1. Bitalino plugged kit, available at www.bitalino.com, as an example of a commercial wearable sensor. 150

Figure S 3.1. a) SEM image of inkjet printed *a*-WO_3/*ortho*-$WO_3.0.33H_2O$ (detail of the pattern formed by the *a*-WO_3 layer), b) Transmittance plots and c) Tauc's plots for all inkjet printed thin films. 75
Figure S 3.2 Transmittance plots for all inkjet printed thin films in colored (2 V) and bleached (-2 V) states, after applying a fixed potential for 60 s. 75
Figure S 4.1. Schematic and real image of the electrodeposition set-up composed by WO_3 nanoparticles dispersion in water, flexible gold working electrode, platinum wire as counter electrode and Ag/AgCl as reference electrode. 97
Figure S 4.2. Impedance modulus and phase angle of the flexible reference electrode after anodization of the Ag layer and saturation in KCl solution. 97
Figure S 5.1. Schematic representation of the set-up used in electrochemical characterization; composed by a WO_3/ITO working electrode, buffer electrolyte, platinum wire as counter electrode and Ag/AgCl as reference electrode. 119

Figure S 5.2. Raman spectra obtained from the samples W1, W2 and W3 at RT with 413 nm laser excitation, 6.5 mW laser power and 30 s accumulation. 120
Figure S 5.3. Nyquist plots of: a) WO_3 pellets performed at RT between two gold flat electrodes and b) WO_3/ITO electrodes performed in 0.05 M tris-HCl pH 7.6 buffer with 0.1 M KCl as electrolyte. The alternative voltage was of 10 mV and the frequency range between 1-10^6 Hz. The theoretical fitting is represented by the solid lines. 120
Figure S 5.4. Representation of the drop casting method for the preparation of the WO_3/ITO electrodes. 121
Figure S 5.5. Cyclic voltammograms of ITO and WO_3/ITO electrodes in 1 mM $[Fe(CN)_6]^{4-/3-}$ solution at variable scan rate, from 10 to 250 mV/s (insets correspond to the plots of peak current vs. square root of scan rate). 121
Figure S 5.6. Resonance Raman spectra of *cc*NiR immobilized in WO_3/ITO electrodes, measured with 413 nm excitation, 1.2 mW laser power and 5 s accumulation time, at RT. Each spectrum represents a sum of 5 individual spectra. 122
Figure S 6.1. Schematic representation of the semiconductor (green)/electrolyte (blue) interface when a positive gate voltage is applied, considering: a) electric double layer and b) electrochemical operation modes. 142
Figure S 6.2. Final transistor structure with top gate, electrolyte and GIZO nanoparticles as semiconductor 143
Figure S 6.3. Tauc's plot for GIZO nanoparticles dispersion. 144
Figure S 6.4. a) DLS size distributions and b) DSC-TG curves performed in air up to 600 ºC, for the two GIZO inks after filtration. 145

Figure A 1.. Front cover of the first issue of Advanced Electronic Materials. 152

List of Tables

Table 1.1. Resume of the latest research on nanostructured EC oxides, deposition methods, optical modulation (ΔT_{max}), applied potential, coloration (τ_{col}) and bleaching (τ_{bl}) times, and coloration efficiency (*CE*). 34
Table 3.1. Comparison of nanoparticles sizes from SEM images and DLS hydrodynamic diameter, BET surface areas and fitted bulk conductivity calculated from Nyquist plots of WO_3 pellets. 63
Table 3.2. Optical densities (ΔOD), charge ratio (Q_{ratio}) and coloration efficiency (*CE*) of inkjet printed thin films. 68
Table 4.1. Relative cell viabilities after 24, 48 and 72 hours of incubation of the cells with conditioned media. 85
Table 4.2. Electrochemical potential values of three WO_3 sensors measured from pH 9 to 5 and corresponding sensitivity. 90
Table 4.3. Electrochemical potential values for the same WO_3 sensor measured from pH 9 to 5 and 5 to 9, during three complete cycles and the resulting sensitivity. 91
Table 5.1. Comparison of nanoparticle sizes measured by SEM and DLS techniques along with BET surface areas and fitted bulk conductivity calculated from Nyquist plots of the 3 samples. 105
Table 5.2 Electrochemical parameters of cytochrome *c* on different WO_3/ITO electrodes (anodic and cathodic peak current ratio (*I*c/*I*a), peak separation (ΔEp), formal redox potential (E^0), diffusion coefficient (D_0) and heterogeneous exchange rate constant (k^0)), as obtained by cyclic voltammetry, in 0.05 M phosphate buffer, pH 7.6, 0.1 M KNO_3, at variable scan rates (from 35 to 750 mV s^{-1}). 109
Table 5.3. Comparison of the kinetic and analytical parameters of the bioelectrode configurations tested in this work with previously reported amperometric or voltammetric biosensors also based on *cc*NiR from *D. desulfuricans*. Michaelis-Menten constant (K_M); limit of detection (LOD); linear range and sensitivity. PG: pyrolytic graphite; SWCNT: single-walled carbon nanotubes; MWCNT: multi-walled carbon nanotubes; CPSPE: carbon paste screen-printed electrode; ND: not determined; R^2: correlation coefficient. 112
Table 6.1. Key factors of the reported work for EGTs with metal oxide nanoparticles: deposition technique, post-treatment, electrolyte, channel width to length ratio (*W*/*L*), on-off current ratio (I_{ON}/I_{OFF}), threshold voltage (V_{Th}), drain voltage (V_D), mobility (μ) and sub-threshold swing (*SS*). . 128
Table 6.2. Resume of the electric characterization of the produced EGTs: channel weight and length ratio (*W*/*L*), drain voltage (V_D), gate current range (V_G), on-off current ratio (I_{ON}/I_{OFF}), threshold voltage (V_{Th}), mobility (μ) and subthreshold swing (*SS*). 136

Abbreviations

0D	Zero dimensions
1D	One dimension
2D	Two dimensions
3D	Tree dimensions
aq.	Aqueous
a-	Amorphous
AC	Alternating Current
AFM	Atomic Force Microscope
BET	Brunauer-Emmet-Teller
c-	Cubic
CB	Conduction Band
*cc*NiR	Cytochrome c nitrite reductase
CE	Coloration Efficiency
CENIMAT	Materials Research Center
CSPE	Composite Solid Polymer Electrolyte
CV	Cyclic Voltammetry
Cyt *c*	Cytochrome *c*
DL	Diffusion Layer
DLS	Dynamic Light Scattering
DLVO	Derjaguin-Landau-Verwey-Overbeak
DMSO	Dimethyl Sulphoxide
EC	Electrochromic
ECT	Electrochemical Transistor
EDL	Electric Double Layer
EDLT	Electric Double Layer Transistor
EDS	X-Ray Spectroscopy
EGT	Electrolyte-gated Transistor
EIS	Electrochemical Impedance Spectroscopy
FIB	Focused Ion Beam
FTIR	Fourier Transform Infrared Spectroscopy
GIZO	Gallium-Indium-Zinc-Oxide
h-	Hexagonal
i3N	Institute of Nanostructures, Nanomodelling and Nanofabrication
IBM	International Business Machines
ICDD	International Center for Difraction Data
IHP	Inner Helmholtz Plane

ISFET	Ion Sensitive Field Effect Transistor
ISO	Internation Standard Organization
ITO	Indium-Tin Oxide
IZO	Indium-Zinc Oxide
LSW	Lifshitz-Slyozov-Wagner
m-	Monoclinic
M	Metal
MRI	Magnetic Ressonance Imaging
MWCNTs	Multi-wall Carbon Nanotubes
ortho-	Orthorhombic
O	Oxygen
OHP	Outer Helmholtz Plane
PBS	Phosphate Buffer Solution
PC	Propylene carbonate
PET	Polyethylene Terephthalate
PTA	Peroxopolytungstic Acid
PTFE	Polytetrafluoroethylene (Teflon)
PZC	Point of Zero Charge
QD	Quantum Dot
R	Organic group
rpm	Rotation per minute
RR	Ressonance Raman
RT	Room Temperature
S:V	Surface to volume ratio
SEM	Scanning Electron Microscopy
STM	Scanning Tunneling Microscopy
STP	Standard Temperature and Pressure
t-	Tetragonal
TEM	Tunneling Electron Microscopy
TFT	Thin-film Transistor
TG	Thermogravimetry
UV	Ultraviolet
UV/vis	Ultraviolet-visible
VB	Valence Band
WO_x	Tungsten Oxide
xDLVO	Extended Derjaguin-Landau-Verwey-Overbeak
XRD	X-Ray Diffraction
ZTO	Zinc-Tin Oxide

Symbols

a	Absorption Coefficient
τ_{bl}	Bleaching Time
τ_{col}	Coloration Time
ε_F	Fermi Level
ΔE_p	Peak Potential Separation
ΔG	Free Gibbs Energy
ΔG^*	Energy barrier for the formation of the nuclei of the nanoparticle
ΔG_S	Surface Free Energy
ΔG_v	Volume Free Energy
ΔOD	Optical Density
ΔT	Optical Modulation
γ	Surface Energy per unit area
μ	Mobility
μ_{FE}	Field-effect Mobility
μ_{LIN}	Linear Mobility
μ_{SAT}	Saturation Mobility
σ	Conductivity
A	Hamaker constant
C_{DL}	Double Layer Capacity
C_S	Equilibrium Solubility
$C^{nucleation}{}_{min}$	Minimum Solubility for Nucleation
$C^{nucleation}{}_{max}$	Maximum Solubility for Nucleation
D_0	Diffusion Coeficient
E^0	Formal Redox Potential
E_g	Band Gap Energy
eV	Electron Volt
G	Gibbs Energy
$h\upsilon$	Photon energy
I	Current
I_c/I_a	Anodic and Cathodic Peak Current Ratio
I_{cat}	Catalytic Current
I_{max}	Catalytic Current observed at the maximum turnover rate
I_{ON}/I_{OFF}	On-off Current Ratio
I_p	Current Peak

k^0	Exchange Rate Constant
K_M	Michaelis-Menten Constant
l	Thickness
Q_{ratio}	Charge Ratio
Q_i	Charge Intercalated
Q_{di}	Charge Deintercalated
r	Nanoparticle Nuclei Radius
r^*	Minimum Nuclei Size for a Stable Nanoparticle
R	Reflectance
R^2	Correlation coefficient
R_e	Electrical Resistance
R_s	Solution Resistance
SS	Subtreshold Swing
T	Transmittance
T_{bl}	Transmittance in the Bleached State
T_{col}	Transmittance in the Colored State
V_A	Attractive Forces
V_D	Drain Voltage
V_G	Gate Voltage
V_R	Repulsive Forces
V_T	Total Potential Energy
V_{Th}	Threshold Voltage
W/L	Width to Length Ratio
Y_0	Bulk Resistance
Z	Impedance
Z_{imag}	Imaginary part of the Impedance (Z'')
Z_{real}	Real part of the Impedance (Z')
Z_{phase}	Impedance Phase
$Z_{modulus}$	Impedance Modulus (|Z|)

Chapter 1. INTRODUCTION

This chapter aims to frame this thesis in the field of nanoscience and nanotechnology. It starts with a brief history of the nanotechnology, and then explores the definitions and properties of nanomaterials that are relevant for this work. It gives also some insights about nanoparticles engineering focusing in the metal oxides that were applied in the electrochemical devices. Finally, it ends with the motivation and thesis outline.

1.1. Nanoscience and Nanotechnology

Nanoscience and nanotechnology became a distinguishable and multidisciplinary field of research with emerging applications. It is one of the most visible and growing research areas in science and technology and, all over the world research funding agencies have been supporting the exploitation of the potentialities of this field in the areas of chemistry, materials, engineering and medicine. Nanoscience and nanotechnology are fueling a new industrial revolution supported by the scientific ability to fabricate, model and manipulate objects with a small numbers of atoms, and the almost daily discovery of new phenomena at the nanoscale.[1], [2]

The term “nanotechnology” has first appeared in a conference in 1974 by Norio Taniguchi,[3] but the idea of building “small” things is usually attributed to Richard Feynman based on the talk he gave in 1959, where he predicted that machines would build even smaller machines and other products with atom by atom control, a process which was later called molecular manufacturing.[4] Truthfully, interfaces and colloids science existed for nearly a century before they became associated with nanotechnology. The first observations and size measurements of nanoparticles have been performed in the beginning of 20th century by Richard Zsigmondy, winner of the 1925 Nobel Prize in Chemistry for his demonstration of the heterogeneous nature of colloid solutions and for the methods he used, which have since become fundamental in modern colloid chemistry.[5], [6] Zsigmondy was also the first to use the term “nanometer” explicitly for characterizing particle sizes. At the same time, Irving Langmuir, winner of the 1932 Nobel Prize in Chemistry introduced the concept of a monolayer, a layer of material with one molecule thick.[7]

Later on, the major boost to further develop the nanotechnology was achieved in 1981 by Gerd Binnig and Heinrich Rohrer at IBM Zurich Research Laboratory with the invention of the scanning tunneling microscope (STM), for which they were awarded with the Nobel Prize in Physics in 1986,[8] and in 1985 Binnig, Calvin Quate and Christoph Gerber invented the atomic force microscope (AFM).[9] At this time (1985), the first fullerene was discovered by Harry Kroto, Richard Smalley and Robert Curl, who together won the 1996 Nobel Prize in Chemistry.[10] The discovery of carbon nanotubes even if generally attributed to Sumio Iijima due to the impact of his “Nature” paper in 1991,[11] was first published in 1952 by L. V. Radushkevich and V. M. Lukyanovich, but in Russian language.[12] Still in 1986, Eric Dexter published the book “Engines of Creation” and he is described as the founding father of nanotechnology. He established main fundamentals of molecular engineering and described the implementation and applications of advanced nanotechnologies.[13] Drexler was also one of the co-founders of the Foresight Institute that is: “the primary force pushing for the kind of nanotechnology that will truly transform our future, from medicine to the environment to space settlement”.[14]

In Europe, the research and interest for nanotechnology started some years later. In 2004 the European Commission promoted the communication “Towards a European Strategy for Nanotechnology” and in 2008 releases the “Code of conduct for responsible nanosciences and nanotechnologies research”. In 2006 is established the first institute in Portugal in the field of nanoscience and nanotechnology, i3N – Institute of Nanostructures, Nanomodelling and Nanofabrication, which is a partnership between three research units, IPC (Institute for Polymers and Composites, hosted by University of Minho), CENIMAT (Materials Research Center, hosted by the

New University of Lisbon) and FSCOSD (Physics of Semiconductors, Optoelectronics and disordered Systems, hosted by the University of Aveiro).

In 2013**,** IBM launches “A Boy and His Atom: The World’s Smallest Movie” in which the atoms are moved by using their STM and recorded in a movie to further promote IBM’s research in the field of atomic-scale memory and to reveal the latest developments and new possibilities in nanotechnology. [15]

Figure 1.1 depicts the major events related with nanoscience and nanotechnology.

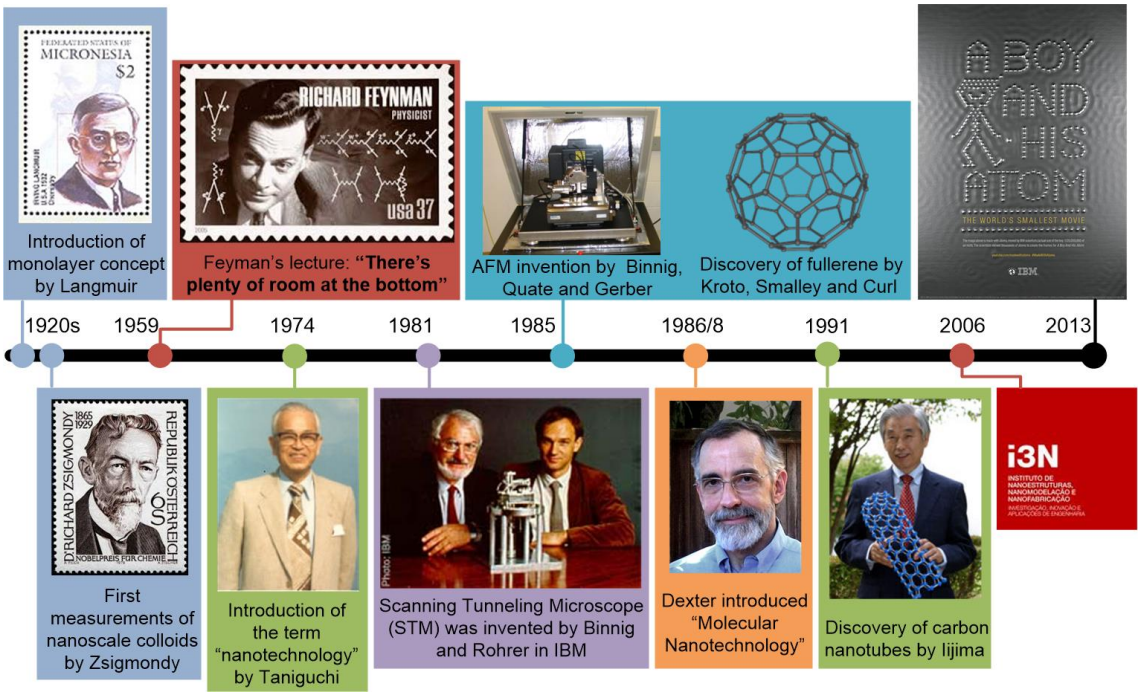

Figure 1.1. Major historic events for the development of nanoscience and nanotechnology.

Nanotechnology has, and will continue to have, considerable impact on our lives as well as on the global economy, but questions are being raised about potential health risks and the possible environmental impact. **Figure 1.2** demonstrates the number of manuscripts published in scientific journals concerning the broad topics: “Nano”, “Nanoparticle”, “Nanotechnology” and the more specific case of the “Nanotoxicology”. We are still far from the full understanding of the impact that nanotechnology can bring to the planet. Even so, in the last decade, the number of manuscripts has increased more than 20 times in all the topics related with the “nano-world”.

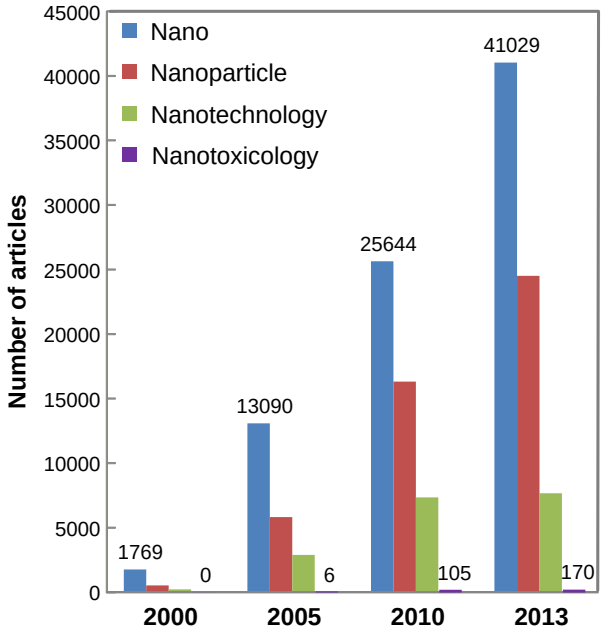

Figure 1.2. Number of manuscripts published in 2000, 2005, 2010 and 2013 under the topics: Nano, Nanoparticle, Nanotechnology and Nanotoxicology. Based on topic search performed in ISI web of knowledge, at Dec. 2014.

The main reason for the fascination in nanostructures is their interesting properties, which are not found in the bulk materials. Surface and quantum effects arise in nanostructures due to the large surface-to-volume (S:V) ratio and to the dimensions that are comparable to the electron wavelength, respectively.[16]

1.2. Nanomaterials

Nanostructured materials (nanomaterials) include atomic clusters, layered or lamellar films, filamentary structures, and bulk nanostructured materials. The common thread to these various material forms is the nanoscale dimensionality, i.e. at least one dimension less than 100 nm.[1] This systems can be classified as 0D if the system exhibits a nanometric size in the three spatial dimensions, 1D if the nanometric size is in two dimensions or 2D systems if one spatial dimension is nanometric. Bulk nanostructured materials are classified as 3D systems. In solid-state physics and optoelectronics 0D, 1D and 2D structures are usually named quantum dots, quantum wires and quantum wells, respectively (**Figure 1.3**). However, the interest for this kind of systems is not restricted only to these scientific fields since confined structures are also widely employed in catalysis, energy storage applications, thermoelectric materials, photocatalysis, mechanical metamaterials and biotechnology.[17] Structural geometry of nanostructures becomes more complicated in the case of composite and multi-component materials. Categories of nanocomposites consisting of a minimum of two phases (with at least one phase having sizes less than 100 nm), are specified by the size scales and geometry of the constituent phases.

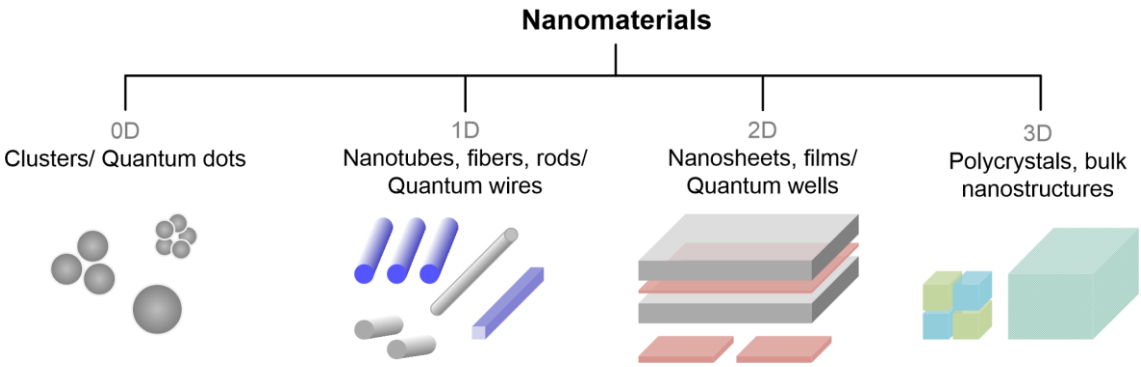

Figure 1.3. Nanomaterials classification according to its dimensionality.

Surfaces and interfaces are also important in explaining nanomaterial behavior. In bulk materials, only a relatively small percentage of atoms will be at, or near, a surface or interface. In nanomaterials, the small feature size ensures that many atoms, perhaps half or more in some cases, will be near interfaces. Surface properties such as energy levels, electronic structure, and reactivity can be quite different from interior states, and give rise to different material properties.[1]

In fact, as highlighted above, their peculiar dimensionality gives rise to quantum confinement phenomena, which modify the structural, optical, chemical and electronic properties with respect to the corresponding bulk materials. For instance, systems with different dimensionalities show significantly different optical properties, which arise from their peculiar density of states (**Figure 1.4**). A bulk material exhibits a square root energy ($E^{1/2}$) dependence of the density of states, while in 2D system is described by a step function, the 1D systems show a $E^{-1/2}$ dependence for each quantized state, and in 0D, all available states exist only at discrete energy values since the electron is confined in all three spatial dimensions.[17], [18]

Structural nanomaterials can exist in various forms, such as, metals, oxides and composites. Furthermore, the internal structure of nanoparticles, often meaning the way in which their atoms are distributed, may also vary. Some are amorphous (randomly distributed atoms) while others are crystalline (regularly distributed atoms). Crystalline materials may be polycrystalline, which means that the structure contains different areas with different single crystalline orientations, or monocrystalline with only one orientation. Each type exhibits different properties, thus having an immense potential for many applications in every field of science and engineering.

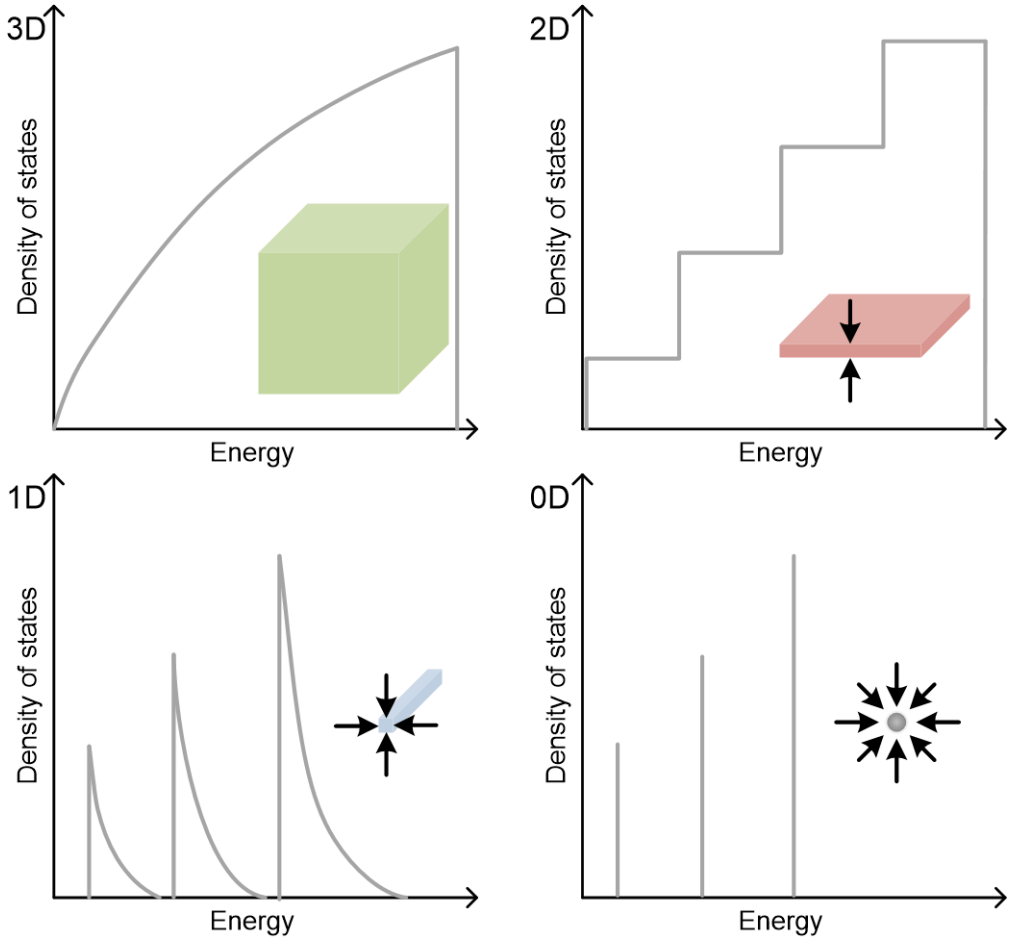

Figure 1.4. Electronic density of states for a bulk 3D, 2D, 1D nanocrystalline material and 0D quantum dot. The arrows represent the spatial confinement occurring in each system.

The diversity of applications is reflected in the amount of consumer products that increases every year (**Figure 1.5**). In October of 2013 the number had reached a maximum of 1628 products, with the main constituents based on silver, titanium and carbon. Silver is typically used for its antibacterial properties,[19] titanium oxide is a common pigment but is also used in sunscreens, and carbon (including fullerenes and nanotubes) is used in household appliances, automobiles, biomedical devices, space vehicles, among others.[20] The larger category of products (health and fitness) includes personal care, clothing, cosmetics and sunscreens with a total of 788 available products. This inventory was based in products manufactured in 30 different countries.[21]

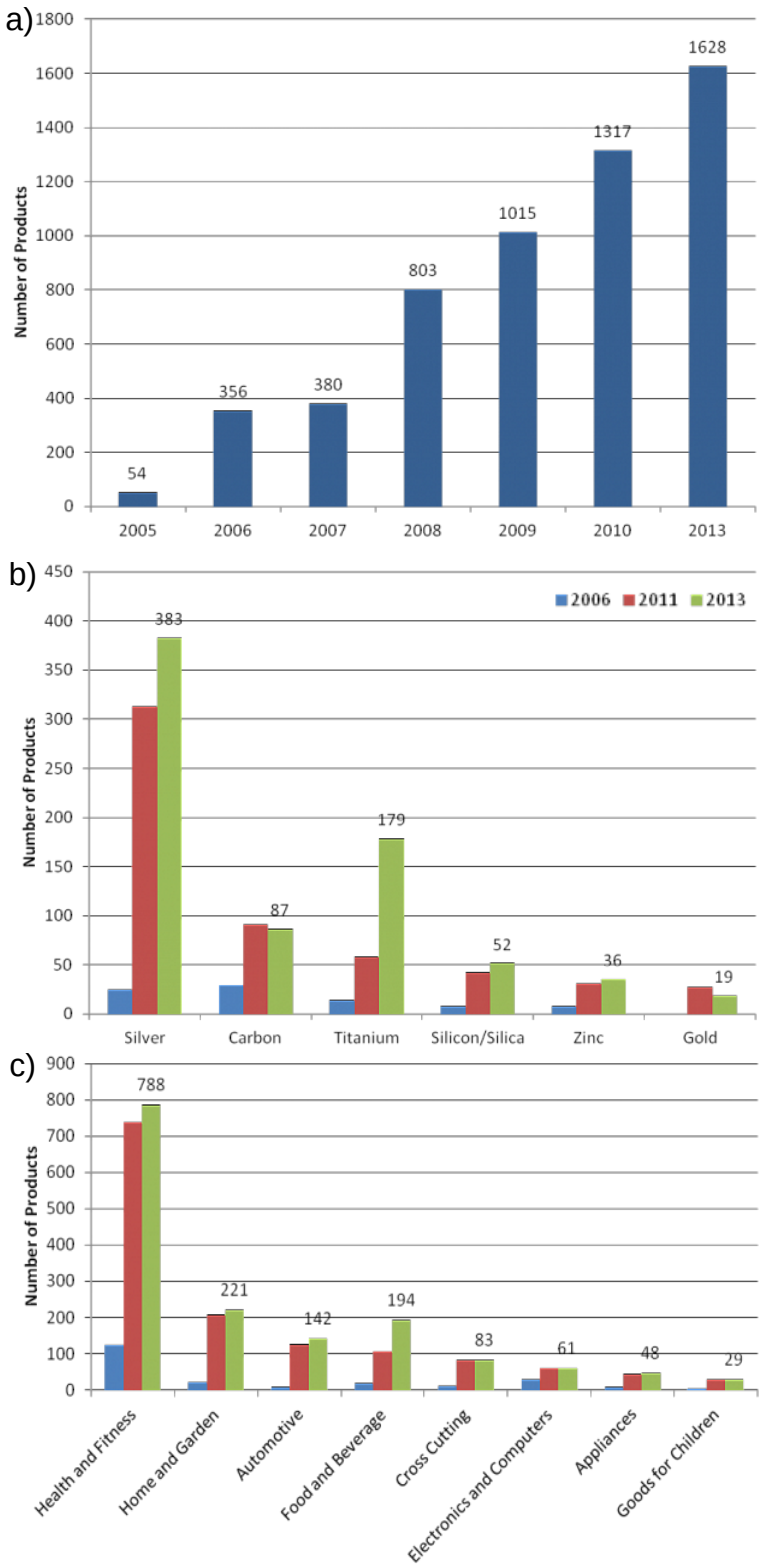

Figure 1.5. a) Nanotechnology consumers' products evolution; b) Most common materials used in the products; and c) Products categories. The inventory was performed in October 2013.[21]

In the field of medicine and biology, several nanoparticle applications have already been approved for clinical use, and many others are at different stages of development. Nanoparticle-based biomedical applications include drug delivery, tissue engineering, fluorescent biological labeling, and magnetic ressonance imaging (MRI) contrast enhancement.[22]

As discussed before, the extraordinary optical, mechanical, electrical, and chemical properties of the nanomaterials are highlighted in some of the major breakthroughs of this field:[23]

1) Magnetic nanoparticle assemblies that present novel magnetic properties with respect to their bulk constituent components due to surface effects produced by the modified atomic symmetry, in such, low dimensional systems and magnetic coupling between the particles.
2) The combination of low toxicity, high surface area, biocompatibility, and colloidal stability of gold nanoparticles allowed the its integration into biosensors. The use of nanomaterials and their composite results not only on a stable immobilization matrix (in the electrode surface) but also act as catalyst for many reactions, thus resulting in enhanced signal response.
3) The luminescence emission and absorption edge that were tuned by changing the particle size and by controlling the defect chemistry of ZnO nanostructures (photocatalyst).
4) Nanohybrid materials formed between conducting polymers, and inorganic oxides with carbon nanotube that demonstrate an excellent solar energy conversion capacity. This resulted in a dramatic increase in the surface area and increase in electronic conductivity, and electrolyte accessibility of the nanoporous structure, which improved the performance of the nanohybrid photoanode and cathode as a solar energy extraction material. These results on nanocomposites also suggested that nanoporous composites of multi wall carbon nanotubes (MWCNTs) with conducting polymers are promising for energy conversion devices such as biosolar cells and QD sensitized solar cells.

1.3. Nanoparticles Engineering

The nanoparticles can be generated both unintentionally, e.g. from internal combustion engines [24] or intentionally, specially engineered for a specific application. But material engineers are not the only ones interested in designing functional materials to solve problems encountered in science and technology.[25] Organisms have spent millions of years optimizing structural materials for performance, durability and appearance, which scientists can be inspired in two ways: by directly using those with different applications[26] or by miming the natural features in the engineered materials.[27] Some examples of the features found in nature are exposed in **Figure 1.6**.

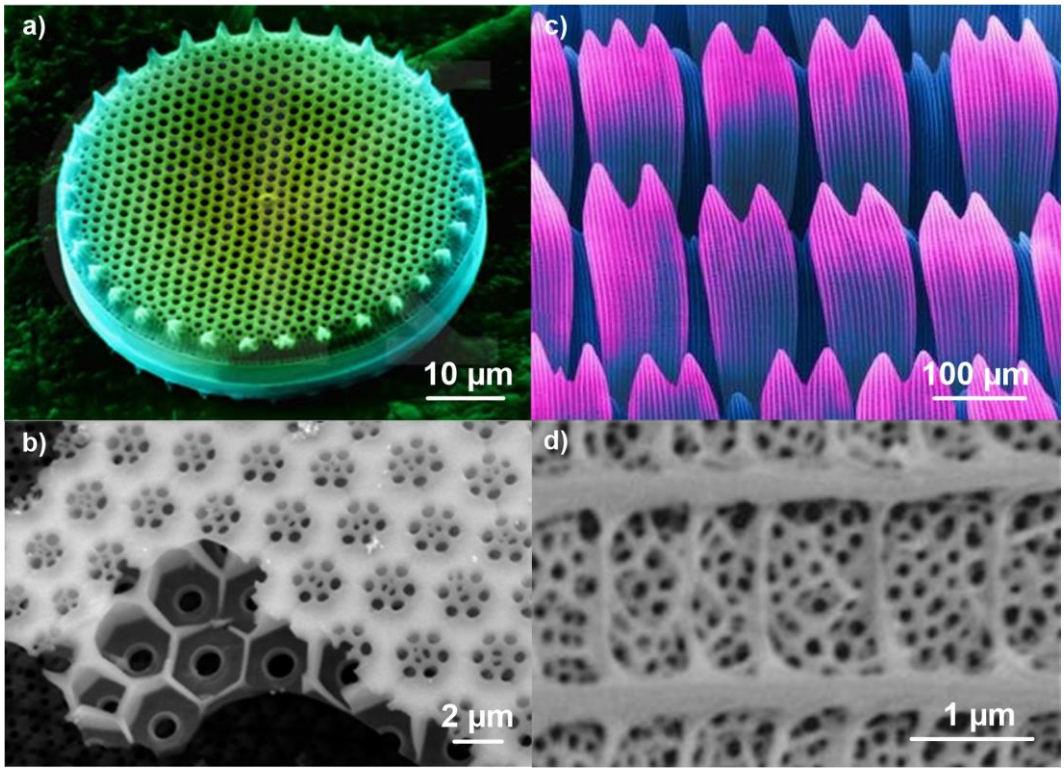

Figure 1.6. SEM images of: a) Diatom Frustule (image copyright © Dennis Kunkel Microscopy, Inc.), b) Diatom Coscinodiscus wailesii algaes (adapted from [28]), c) Swallowtail butterfly (image copyright © Dennis Kunkel Microscopy, Inc.), and d) Lycaenid butterfly wing scales (adapted from [29]).

Depending on the application, the most important features of the engineered nanomaterials are the chemical composition and the structural properties (size, morphology, crystallinity and crystallography). Therefore, the synthesis method should selectively yield the desired particle' properties, and in large quantities. Following to the production of the nanoparticles, generally there is the need to produce a dispersion that preserves the material' properties with a good quality and homogeneity. Stable dispersions are ideally achieved without the addition of a dispersant, however, it is extremely difficult to attain it as the nanoparticles tend to agglomerate fairly quickly.[30] Hence, it is of great importance to fully understand the mechanism of the stability of the dispersion.[1]

1.3.1. Dispersions Stability

Nanoparticles aggregation and stability is mostly explained using the colloid science principles, based around Derjaguin-Landau-Verwey-Overbeak (DLVO) theory.

According to classical DLVO theory, the aggregation of nanoparticles is determined by the sum of the van der Waals attractive and electrostatic double layer repulsive forces.[31]

Since the potential energy due to the van der Waals attraction forces (V_A) and to the electrostatic repulsive forces (V_R) are given by the following **equations 1.1** and **1.2**:[32]

$$V_A = -\frac{A}{12}\left[\frac{4r^2}{c^2-4r^2} + \frac{4r^2}{c^2} + 2ln\left(\frac{c^2-4r^2}{c^2}\right)\right] \quad \textbf{(1.1)}$$

$$V_R = \frac{\varepsilon_p r}{8}\left[2Z_1Z_2 ln\left(\frac{1+e^{-Kc}}{1-e^{-Kc}}\right) + \left(Z_1^2 + Z_2^2\right) ln(1 - e^{-2Kc})\right] \quad \textbf{(1.2)}$$

where *A* is the Hamaker constant and is a material property,[33] *r* is the particle radius, *c* the center-to-center distance between two interactive particles, ε_p is the electrical permittivity, $\mathcal{Z}$ the zeta potential of the two particles and *K* is the Debye-Huckel function,[34] then, the total potential energy, given by DLVO theory, can be described as:

$$V_T = V_A + V_R \quad \textbf{(1.3)}$$

and is represented in **Figure 1.7**.

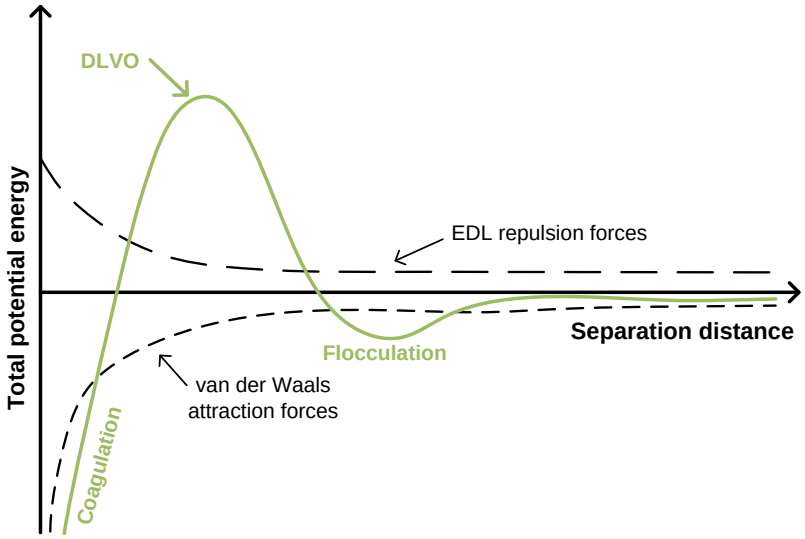

Figure 1.7. Electrostatic double layer (EDL), van der Waals and Derjaguin-Landau-Verwey-Overbeak (DLVO) forces represented as total potential energy as a function of nanoparticles separation distance.

The total potential energy presents two minima values depending on the separation distance between the nanoparticles. These regions are characterized by flocculation (aggregated material that can be re-dispersed by agitation and sonication) and coagulation (irreversible aggregation of the material) that occur at larger and smaller particle separations, respectively (**Figure 1.7**).

Depending on the assumptions taken by the authors, the **equations 1.1** and **1.2** can be derived in simpler equations. For example, when the separation distance between two particles is much lower than its radius (c<<r), then V_A can be simplified to:[35]

$$V_A = -\frac{A \cdot r}{12h} \quad \textbf{(1.4)}$$

for spherical particles, where *h* is the separation distance between two interactive particle surfaces, or to:[1],[36]

$$V_A = -\frac{A}{12\pi h^2} \quad \textbf{(1.5)}$$

for plate-shaped particles. With this assumption, it is clear the dependence of the attractive potential energy with the shape of the particle, and for spherical particles the decays of the energy with the separation distance is slower than for plate-shaped particles. This slower decay can be explained by the fact that at short distances, only part of the spheres are close together. A small change of the distance between the spheres has a substantial effect on the points of closest approach, whereas the bulk of the spherical nanoparticle maintains its properties constant.[36]

The electrostatic repulsive forces are dependent of the charge on the particle surface (**equation 1.2**). In the case of hydrous oxides in aqueous solutions, the OH^- groups at the surface of the particles can protonate (and deprotonate) depending on the pH of the solution. This process result in the creation of a charge on the particle surface according with the following equations:

$$\mathbf{M–OH + H^+ \rightarrow M–OH_2^+} \qquad \mathbf{(1.6)}$$

$$\mathbf{M–OH + OH^- \rightarrow M–O^- + H_2O} \qquad \mathbf{(1.7)}$$

The pH at which the charge on the particle is zero is called the “point of zero charge” (PZC), and is a property of the material. At pH < PZC, the particle is positively charged while for pH > PZC, the charge of the particle is negative (**Figure 1.8**).[37]

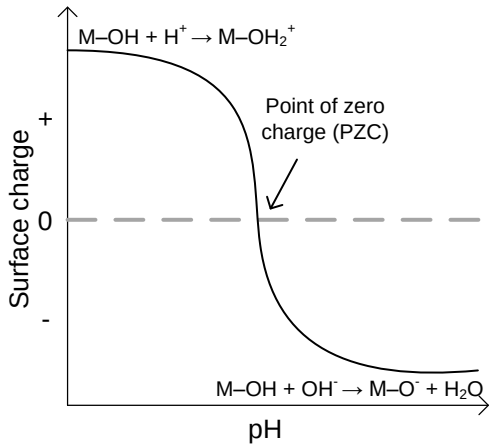

Figure 1.8. Representation of the surface charge dependence with the pH.

The surface charge of the particle attracts ions (known as counterions) of opposite charge in the solution. These counterions bind to the particles via van der Waals and electrostatic forces. The water molecules are also attracted towards the surface charge and are held by van der Waals forces as well as by hydrogen bonds. Hence, the particle surface charge is screened by the counterions and create an electrical double layer (EDL). This EDL, associated with every colloidal particle, is responsible for generating a repulsive force between two neighboring particles, thus avoiding flocculation of particles (electrostatic stabilization).

The EDL (**Figure 1.9**) is formed by three distinct regions: inner Helmholtz plane, outer Helmholtz plane and diffuse layer. The first region consists in the adsorbed ions on the surface, the second the solvated ions in contact with the surface and the diffuse layer is composed of ions attracted to the surface of the particle via electrostatic forces and is dependent of the ions concentration in the bulk of the electrolyte. For high ion concentration, the contribution of the diffuse layer and adsorbed ions to the EDL can be neglected. In this case, the EDL is determined by the

solvated ions, which are usually considered as being confined in a region with a thickness of 1 nm.[38], [39] This model was later symplified by Stern, to only two layers: Stern and diffuse layers. His theory states that ions have a finite size, so cannot approach the surface closer than a few nanometers. The first ions of the EDL are not at the surface, but at a distance *d* away from the surface that is usually taken as the radius of the ion. Stern also assumed that some of the ions are specifically adsorbed by the surface of the particle, and this layer has became known as the Stern layer.[32]

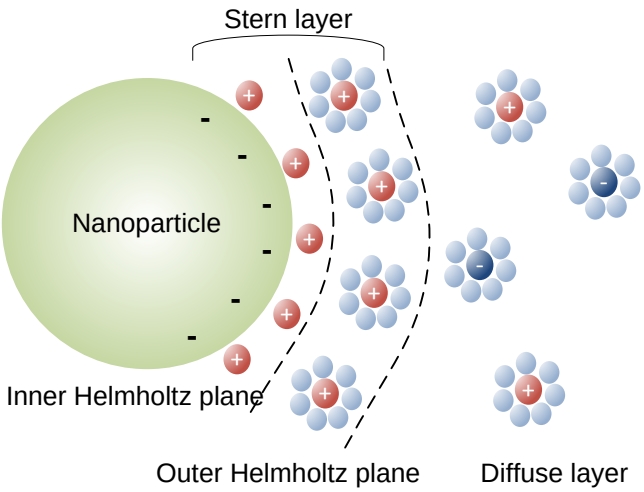

Figure 1.9. Schematic representation of the electrical double layer (EDL) structure.

Small variations in the electrolyte concentration are known to change the characteristics of the EDL of the nanoparticles and hence affect the repulsive forces. This change in the stability of the dispersions can occur with only minor external changes and should be controlled during nanoparticles suspension.[40], [41]

Though, engineered nanoparticles challenge the limits of colloid science due to its variable shape, size, structure, composition, and presence of adsorbed or grafted organic molecules.[41] Consequently, researchers all over the world are continuously discovering new evidences and theories to further understand this mechanism, mainly using computer modeling.[42],[43]

Although nanoparticles dispersions are most commonly stabilized by the EDL of the particles, it is also possible to prevent coagulation by using a thick adsorbed layer, which constitutes a steric barrier (**Figure 1.10**). The most common strategy to create an effective barrier is by adsorbing a polymeric layer on the nanoparticle surface where the following requirements should be fulfilled:

- the surface of the nanoparticle should be completely covered with the polymer (to prevent polymer chains from attaching to two particles simultaneously);
- the polymer should be firmly anchored to the surface of the nanoparticle so that it is not displaced during Brownian collisions;
- the layer must be thick enough (typically >3 nm) to keep the point of closest approach outside the range of the attractive van der Waals forces;

- the non-anchored portion of the polymer must be well solvated by the liquid.

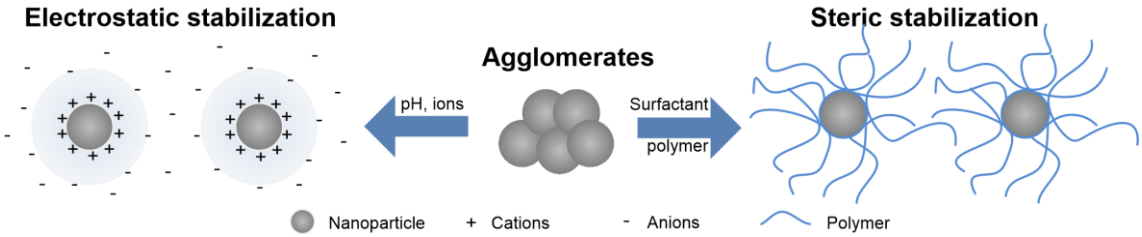

Figure 1.10. Representation of electrostatic and steric stabilization between two nanoparticles.

The adsorbed layer of the polymer prevents coagulation of the particles in two ways: entropicly and enthalpicly. When the two particles approach each other, the adsorbed layers overlap, resulting in a decrease in the degree of motion of the polymer chains. This is the entropic contribution of the adsorbed polymer against the particle coagulation. As the particles approach each other, the solvent molecules, which surround the particles, are squeezed out. However, an osmotic pressure is created that tends to suck the liquid back into the space between the particles. This increases the energy required for the particles' approach and it is the enthalpic contribution. The block polymers are particularly effective steric barriers in this respect, because one end can be made to be strongly adsorbed at the particle surface, while the rest of the chain can be tailored to have a high affinity for the solvent. The higher the affinity of the solvent for the polymer, the greater the enthalpic contribution to the stabilization.[1],[37]

Steric repulsion forces resulting from adsorbed polymer, polyelectrolyte coatings or natural organic matter makes the total potential energy to have only one minimum. Coated nanoparticles may therefore aggregate reversibly, which has significant consequences regarding the fate, transport, bioavailability, and effects of nanoparticles in the environment. In addition to steric repulsion forces, also bridging, osmotic, hydrophobic Lewis acid-base, and magnetic forces have been applied to match experimental data of various types of aggregating particles. These additional forces are collectively known as the extended DLVO (xDLVO) theory and is represented in **Figure 1.11**.[41]

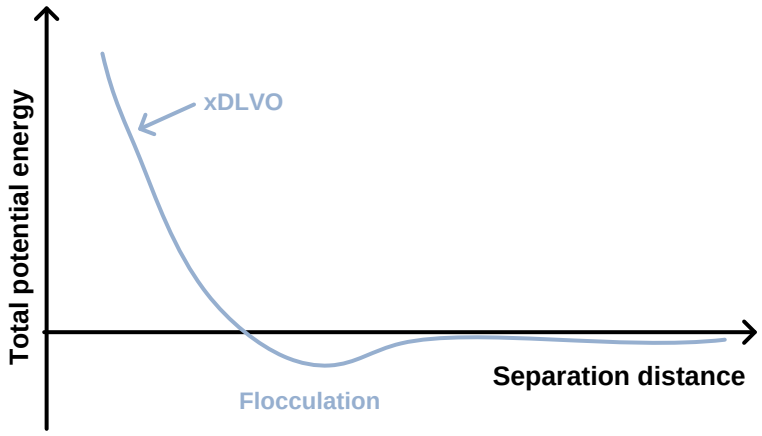

Figure 1.11. Extended Derjaguin-Landau-Verwey-Overbeak (xDLVO) forces represented as the total potential energy as a function of the nanoparticles separation distance.

The relevant force type depends on the system tested, and frequently more than one xDLVO force is important. Moreover, forces are not completely independent of one another. In the case of nanomaterials, understanding aggregation using a DLVO- or xDLVO-based theory presents many challenges.

1.3.2. Synthesis Techniques

The techniques used to engineer nanoparticles are usually divided into mechanical milling, physical processing, biological processing and chemical processing. Nevertheless, the development of new fabrication and processing technologies, along with a fundamental understanding of the relationship between the structure and properties of the feedstock powders created, and continues to create, a variety of possibilities to produce nanostructured materials not only as powders but also in films, composites and coatings.[1]

Mechanical milling (or mechanical attrition) involves grinding a large piece of material into small particles (**Figure 1.12**). A very high energy input is required to produce small nanoparticles with this method, and it is difficult to manufacture particles with uniform size and shape. The significant advantage of this method is that it can be readily implemented commercially.[1] This "top down" approach is dependent of the gridding ball size and the dispersion medium used in the milling, with no possibility to control the crystallographic structure.

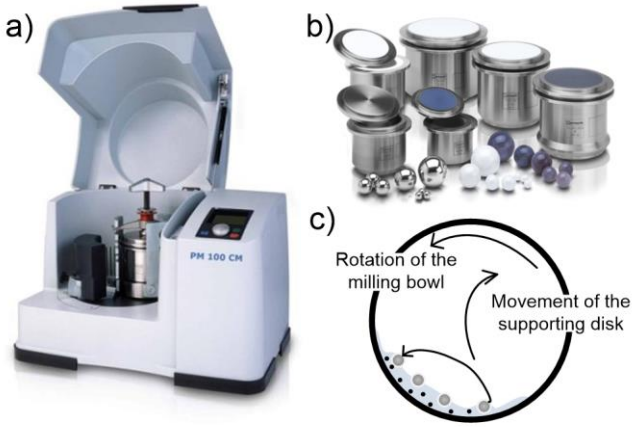

Figure 1.12. a) Example of a ball mill from RETSCH[44], b) Typical containers and balls used in the equipment and c) Schematic representation of the ball milling process.

Nanoparticle production by physical processes comprises sputtering[45] or evaporation [46], [47] in an inert gas. Nanoparticle generation by physical processes may be complex and a fairly high energy input is sometimes required. Lithography,[48] laser ablation (pulsed laser deposition)[49] and injections systems[50] are other physical processes that can be used as single or combined methods to produce nanostructured films or particles (**Figure 1.13**). These methods are out of the scope of this thesis and therefore will not be discussed in further detail.

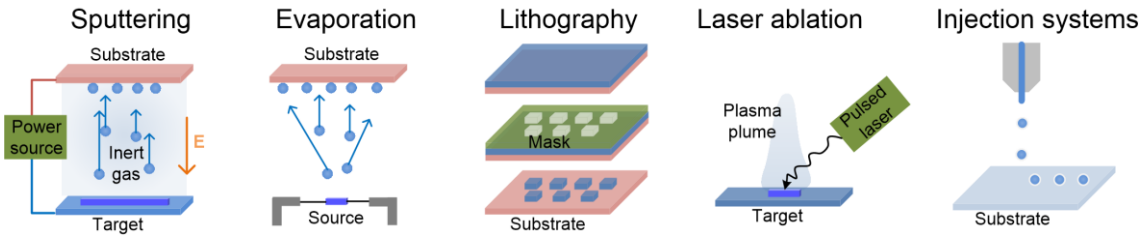

Figure 1.13. Representation of the most common physical processes used in nanostructures production.

In biological systems, shape controlled synthesis of nanomaterials is achieved either by growth in constrained environments such as membrane vesicles or through functional molecules such as poly-peptides that bind specifically to crystallographic planes of inorganic surfaces.[51][52] By adapting biological specificity to materials synthesis and functionality, generation of structures of controlled composition, size, and shape can be achieved for technologically important applications ranging from plasmonics and biomedical devices to energy technologies.[53] Nevertheless, the specificity of this systems require special equipment and usually results in an expensive procedure.

In chemical processing, precursors and solvents in liquid or gas form are used to produce nanoparticles. These methods can require expensive chemicals, result in partly contaminated particles, and create significant amounts of chemical waste. Nevertheless, the strength of chemistry in materials science is its versatility in designing and synthesizing new materials, which can be processed and fabricated into final products. Chemical synthesis permits the manipulation of matter at the molecular level which allows good chemical homogeneity. Also, by understanding the relationship between how matter is assembled on an atomic and molecular level and the material macroscopic properties, molecular synthetic chemistry can be tailor designed to prepare novel starting components. Better control of the particle size, shape, and size distribution can be achieved in particle synthesis. To benefit from the advantages of chemical processing, an understanding of the principles of crystal chemistry, thermodynamics, phase equilibrium, and reaction kinetics is required.[30], [54] Chemical preparation of nanoscale particles with desired material properties is a “bottom-up” manufacturing approach and the most common chemical processes are exposed below.

1.3.2.1. Sol-gel

The synthesis of oxide nanoparticles by this procedure is based upon the hydrolysis and condensation/dehydration of metal alkoxide $M(OR)_n$, where M is the metal, O is the oxygen and R is the organic group. Since the metal alkoxide is not soluble in water, they are required to be dissolved in a common alcoholic solvent in order to carry out their reaction. According to this model, the alkoxide group, being highly electronegative, creates a positive charge on the central metal atom. Since, in the water molecule, exists a partial negative charge on the oxygen atom, the water molecule attacks the metal atom from the alkoxide, which results in the hydrolysis of the alkoxide (**Equation 1.8**).

Hydrolysis: $M(OR)_4 + H_2O \rightarrow HO\text{-}M(OR)_3 + R\text{-}OH$ **(1.8)**

Condensation/ Dehydration: $2HO\text{-}M(OR)_3 \rightarrow (OR)_3M\text{–}O\text{–}M(OR)_3 + H_2O$ **(1.9)**

Two partially hydrolyzed molecules can link together in a condensation reaction that results in the M–O–M bond with the release of a water or alcohol molecule (**Equation 1.9**). The kinetics of hydrolysis and condensation reactions are mainly governed by the water to alkoxide (R) ratio. In general, low R values (<3) are suitable for fiber and thin-film formation while large R values (>3) generate powder particles. The oxide nanoparticle size and its distribution and particle surface morphology are hence affected by this R value (**Figure 1.14**).[37]

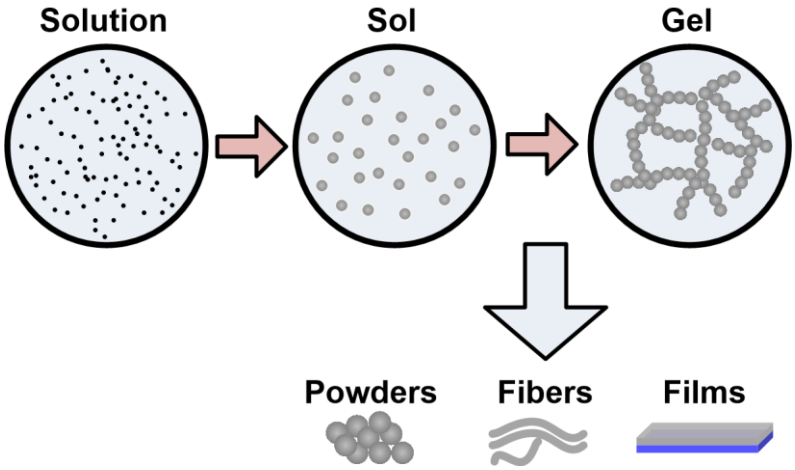

Figure 1.14. Sol-gel synthesis process representation.

The most common processes used to generate nanoparticles from sol-gel approach are the gelation, precipitation and solvothermal treatments.[55] This last procedure will be described in detail in section 1.3.2.5.

1.3.2.2. Aerosol Spray Pyrolysis

In this technique, aqueous metal salts are sprayed as a fine mist, dried, and then passed into a hot flow tube where pyrolysis converts the salts to the final products. This technique has two main advantages in synthesizing fine particles. First, materials are mixed in solution, hence they are homogeneously mixed on the atomic level at the start. Second, only sub-sintering temperatures are necessary to form crystallized particles. This method of synthesis creates particle sizes typically in the range of 5 to 500 nm.[30]

1.3.2.3. Self-assemble

In the last two decades, as the understanding of nanoscience has advanced, the field of self-assembly has grown tremendously. Using techniques such as solid- or liquid-state peptide synthesis, chemical ligation, recombinant processes, or enzymatic synthesis it is now possible to design peptides and proteins with the right codes to produce a large variety of structures including

self-assembled monolayers, tapes, belts, fibrils, tubes, vesicles, or bilayer membranes. In general, self-assembling systems can be divided into five key parts: the subunits, a driving force, a repulsive force, a binding force and the environment.[48], [56]

1.3.2.4. Electrodeposition

Electrodeposition is another “one-step” processing method in that the coatings or free-standing foils are nanocrystalline and the consolidation of particles is not required. This eliminates one category of artifact, which is porosity or incomplete particle bonding that is common in “two-step” processes. Electrodeposition occurs by the nucleation of crystallites on the substrate surface and their subsequent growth along with nucleation of new crystallites. In order to have a nanocrystalline grain size, nucleation events should be favored over growth. The variables in electrodeposition include bath composition, pH, temperature, overpotential, additives, and direct current vs. pulse electrodeposition. It has been stated that the two most important mechanisms that are rate-determining steps for formation of nanoscale grains in electrodeposition are charge transfer at the electrode surface and surface diffusion of the adsorbed ions on the crystal surface.[1]

1.3.2.5. Solvothermal Synthesis

Solvothermal synthesis is generally defined as a chemical reaction taking place in a solvent at temperatures above the boiling point and pressures above 1 bar. The medium used in a solvothermal synthesis can be anything from water (hydrothermal) to alcohol or any other organic or inorganic solvent.[57] Nevertheless, the term “hydrothermal” is generally used, in many reports, describing all types of synthesis that occur in a closed vessel with controlled temperature and pressure. In fact, the number of articles associated to hydrothermal synthesis are almost 9 times higher than to solvothermal synthesis (**Figure 1.15)**.

The method is not a new invention, the term hydrothermal has its origins in geological science and was first used in the beginning of the 19th century, to describe the action of water at elevated temperature and pressure in bringing changes in the earth’s crust, and leading to the formation of various rocks and minerals. However, materials scientists popularized the technique, particularly during 1940s and today is still being adopted and optimized.[58]

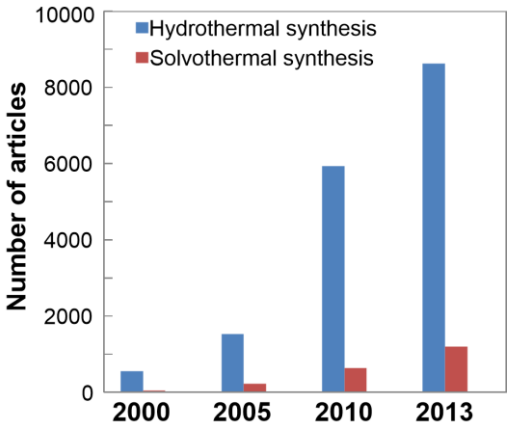

Figure 1.15. Number of articles published in 2000, 2005, 2010 and 2013 under the topics of hydrothermal and solvothermal synthesis. Based on topic search performed in ISI web of knowledge.

The temperature and pressure conditions facilitate the dissolution of the chemical reagents and the production of the products by crystallization. This technique provides a one-step reaction route to complex materials. The use of solvents also offers high diffusivity which increases the mobility of the dissolved ions and allows a better mixing of the reagents.[59]

The precursors used in the synthesis of inorganic compounds are often aqueous solutions of simple salts such as metal chlorides, nitrates or acetates. Depending on the specific synthesis, these can be precipitated to the corresponding metal hydroxides prior to the synthesis using a base (e.g., NaOH, KOH or NH_4OH) and other additives for pH control, reduction or oxidation, coating, among others, can equally be added prior to the solvothermal treatment. The reaction mechanisms are naturally highly system dependent. The solvothermal method exploits that by increasing temperature and pressure, the fundamental properties of water, or other solvent used, changes. Important characteristics such as the ionic product, density, thermal conductivity, viscosity, heat capacity and the dielectric constant are all highly dependent of both pressure and temperature, and by tuning the synthesis parameters, specific solvent properties can be obtained. As an example, **Figure 1.16** shows the dielectric constant of water as function of temperature. With temperature, the dielectric constant drops rapidly. This drop has large implications in the solubility of polar and ionic species which are often used in the synthesis of inorganic materials. As the dielectric constant decreases, the ionic species can precipitate to a solid phase.

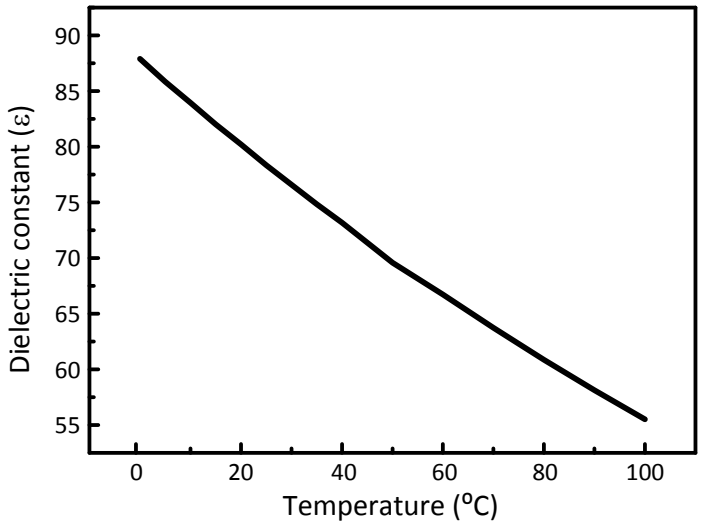

Figure 1.16. Dielectric constant of water as a function of the temperature.[60]

The synthesis of metal oxide particles is described by the two steps mechanism described in sol-gel synthesis (**Equation 1.8** and **1.9**) and as the temperature is increased, the equilibria shift to the right, leading to the formation of metal oxide particles. However, even in this simple example, several aspects of the reactions are not known. The intermediate phase is hard to characterize as the second reaction often happens quickly after the formation of the hydrated phase. Furthermore, as the intermediate phase is often amorphous and nanosized, it is difficult to obtain structural information from traditional characterization methods. The mechanisms controlling the reactions are thus not well understood.

The further development of the solvothermal method, led to the establishment of the supercritical synthesis for general nanoparticle production, and the method is already used commercially.[61] Here, an aqueous solution of a metal salt is very rapidly brought to temperatures above the critical point, and instantaneously, the low dielectric constant will force nanoparticles to precipitate. Because all the metal ions present in the precursor will precipitate in numerous particle nuclei simultaneously, very small homogenous particles with a narrow size distribution can be obtained. In subcritical synthesis, the nucleation does not happen instantaneously, the fraction of the precursor that does not immediately precipitate will slowly crystallize around the particle nuclei and thus result in particle growth, giving much larger particles with wide size distributions.

Solvothermal synthesis is usually performed in a reaction vessel called an autoclave, as represented in **Figure 1.17**. The autoclaves are made up of a strong alloy such as steel to withstand the pressure developed during the reaction. Generally, highly acidic or basic conditions are used so the autoclave contains a Teflon (PTFE, polytetrafluoroethylene) liner, which protects it from corrosion and provides a chemically inert vessel for reaction. Solvothermal reactions are usually performed in conventional ovens up to a maximum temperature of 250 °C, while the pressure is most often autogenously generated. Depending on the degree of autoclave filling, pressures of several hundred bar can be obtained, even at low temperatures. The volume of the

autoclave varies from few milliliters for laboratory scale synthesis to thousands of liters for industrial scale material production.

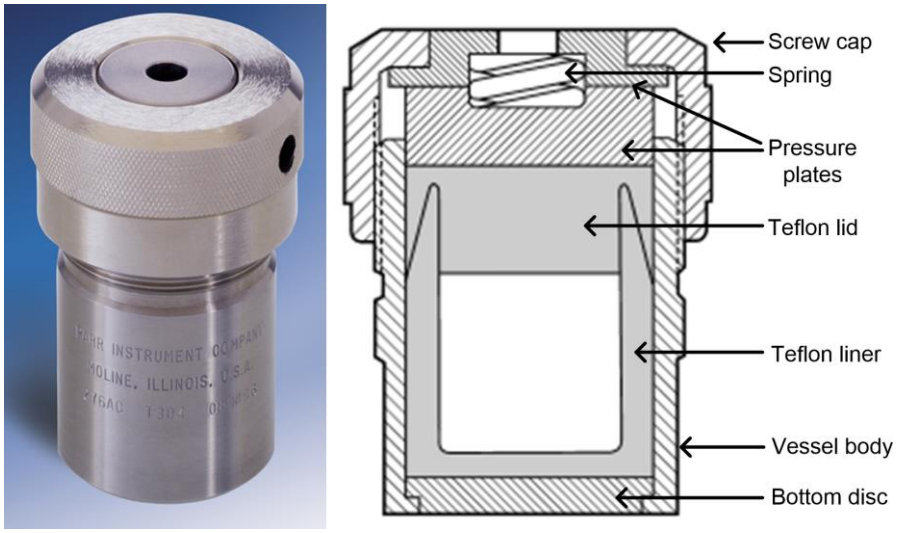

Figure 1.17. Autoclave (acid digestion vessel) image from Parr Instrument Company.[62]

Although batch reactors have proved to be very powerful for material production, there is a general interest in developing flow reactors, where material can be continuously synthesized, especially for scaling proposes.[63] Flow reactors are especially well suited for supercritical synthesis, where rapid heating rates are required. **Figure 1.18** demonstrates the apparatus developed by Promethean Particles with a flow reactor that allows the continuous synthesis of nanoparticles.

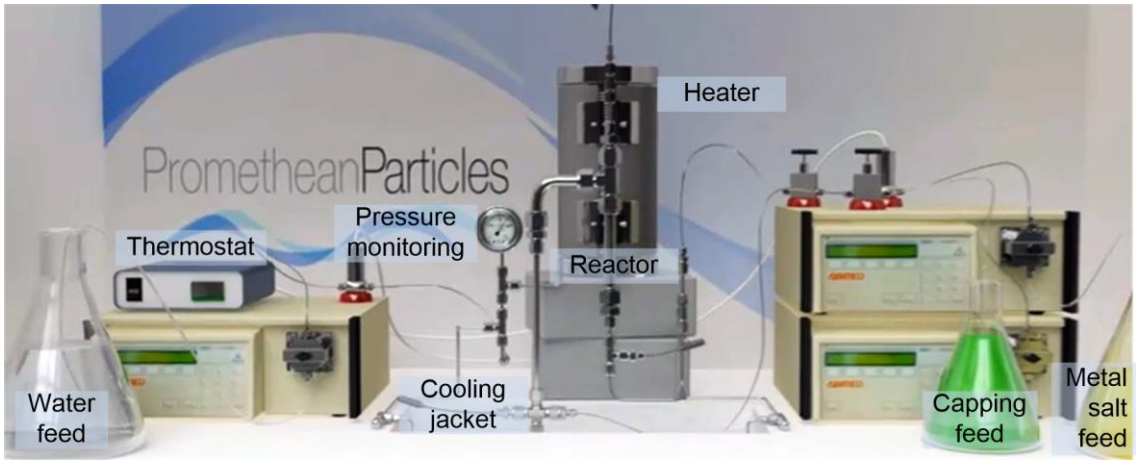

Figure 1.18. Continuous hydrothermal synthesis apparatus from Promethean Particles.[64]

In recent years, much attention has also been given to the improvement of the method with new mixing technologies, setups for core-shell nanoparticle synthesis and microwave solvothermal synthesis method are also being used in different systems.[65]

Solvothermal synthesis also have certain disadvantages. Since the reactions are carried out in a closed vessel, it is not possible to observe the growth of the crystals, which limits the amount of useful information available for understanding the synthesis process. In the recent years, remarkable progress has been made in this area through the entry of physical chemists, and the modeling as well as the study of kinetics of the solvothermal processes have contributed greatly to the understanding of this technique. However, the closed solvothermal system can be affected by many factors such as pH, temperature, reagent concentrations, pressure and solvent filling levels, meaning that as yet, a full exploration of all the reaction conditions has not been made. Exploratory solvothermal synthesis often involves a trial and error approach.

The solvothermal technique exhibits a great degree of flexibility, which is being rightly exploited by a large scientific community with diversified interests and has become a most powerful tool, in the last decade, for transforming various inorganic compounds and treating raw materials for technological applications.[58] The advantages over other growth processes, such as, the use of simple equipment, catalyst-free growth, low cost, large area uniform production, environmental friendliness, low hazardous and low temperature makes this method attractive for microelectronics and flexible electronics.[23]

1.3.3. Particle Nucleation and Growth Theory

In a typical synthesis of inorganic nanocrystals, the precursor compound in bulk solution is decomposed to generate atoms followed by the precipitation step to form the nanocrystals. An understanding of the process and parameters controlling the precipitation helps to improve the engineering of the growth of nanocrystals to the desired size and shape. The precipitation process consists of a nucleation step followed by a crystal growth stage. The nucleation can be classified as homogeneous, heterogeneous or secondary nucleation, depending on the nanoparticle sizes discrepancy.[66] In the chemical synthesis, homogeneous nucleation occurs in the absence of a solid interface by combining solute molecules to produce nuclei, since the supersaturated solution is not energetically stable.

Seed formation proceeds according to the LaMer model, [67] as shown in **Figure 1.19a**. While the concentration of atoms steadily increases with time, as the precursor is decomposed by heating, no nucleation occurs, even above the equilibrium solubility (C_s). Only when the supersaturation reaches a certain value above the equilibrium solubility ($C_{min}^{nucleation}$), than the nucleation stage will start, which corresponds to the energy barrier for the formation of nuclei (ΔG^*). After the initial nucleation, the concentration or supersaturation of the growth species decreases until no more nuclei would be formed, whereas the growth will proceed until the concentration of growth species reach the equilibrium solubility. Although, growth process cannot occur when there is no nucleus. Once nuclei are formed, growth occurs simultaneously. Above the minimum concentration, nucleation and growth are inseparable processes; however, these two processes proceed at different speeds.[68]

In the classical nucleation theory, the driving force for spontaneous phase transition is the exothermicity of lattice formation (**Figure 1.19b**).[69] The free Gibbs energy change for the formation of a nucleus (ΔG) is determined by the sum of the volume free energy (ΔG_v) and surface free energy (ΔG_s). Assuming spherical nuclei with a radius r, then ΔG can be described as:

$$\Delta G = 4/3\pi r^3 \Delta G_v + 4\pi r^2 \gamma \quad (1.10)$$

where γ is the surface energy per unit area.

As the nanocrystals are more stable than the solvated precursors, ΔG_v is negative while, the introduction of solid-liquid interfaces generally increases the free energy with the increase of the surface area of the nuclei. As a result, the evolution of nuclei depends on the competition between a decrease in ΔG_v, which favors condensation of solvated precursors into nuclei, and an increase in ΔG_s, which destabilizes the nuclei toward solvation in proportion to the crystals' surface area. From the figure, one can easily see that the newly formed nucleus is stable only when its radius exceeds a critical size, *r**. A nucleus smaller than *r** will dissolve into the solution to reduce the overall free energy, whereas a nucleus larger than *r* * is stable and will continue to grow. The critical size and energy are defined by:

$$r^* = -2(\gamma / \Delta G_v) \quad (1.11)$$

$$\Delta G^* = 16\pi\gamma / (3\Delta G_v^2) \quad (1.12)$$

ΔG* is the energy barrier that a nucleation process must overcome and *r** represents the minimum size of a stable spherical nucleus.[68]

Thermodynamically, the nucleation step can be controlled by modulating ΔG_S and ΔG_v as, by varying surfactants and temperature (that can change the ΔG_s), by chemical transformation of the nuclei material or by changing the reaction environment, such as etching and dissolution of the nuclei. Nevertheless, the size and uniformity of the nanoparticles can also be controlled kinetically during the nucleation step. If the nucleation occurs at a fast rate, all the nuclei are likely to have the same or similar size, since they are formed under the same conditions. In addition, all the nuclei will have the same subsequent growth (**Figure 1.19c**). If the nucleation occurs at a slower rate, the nanoparticles will usually became bigger and with variable sizes.[68]

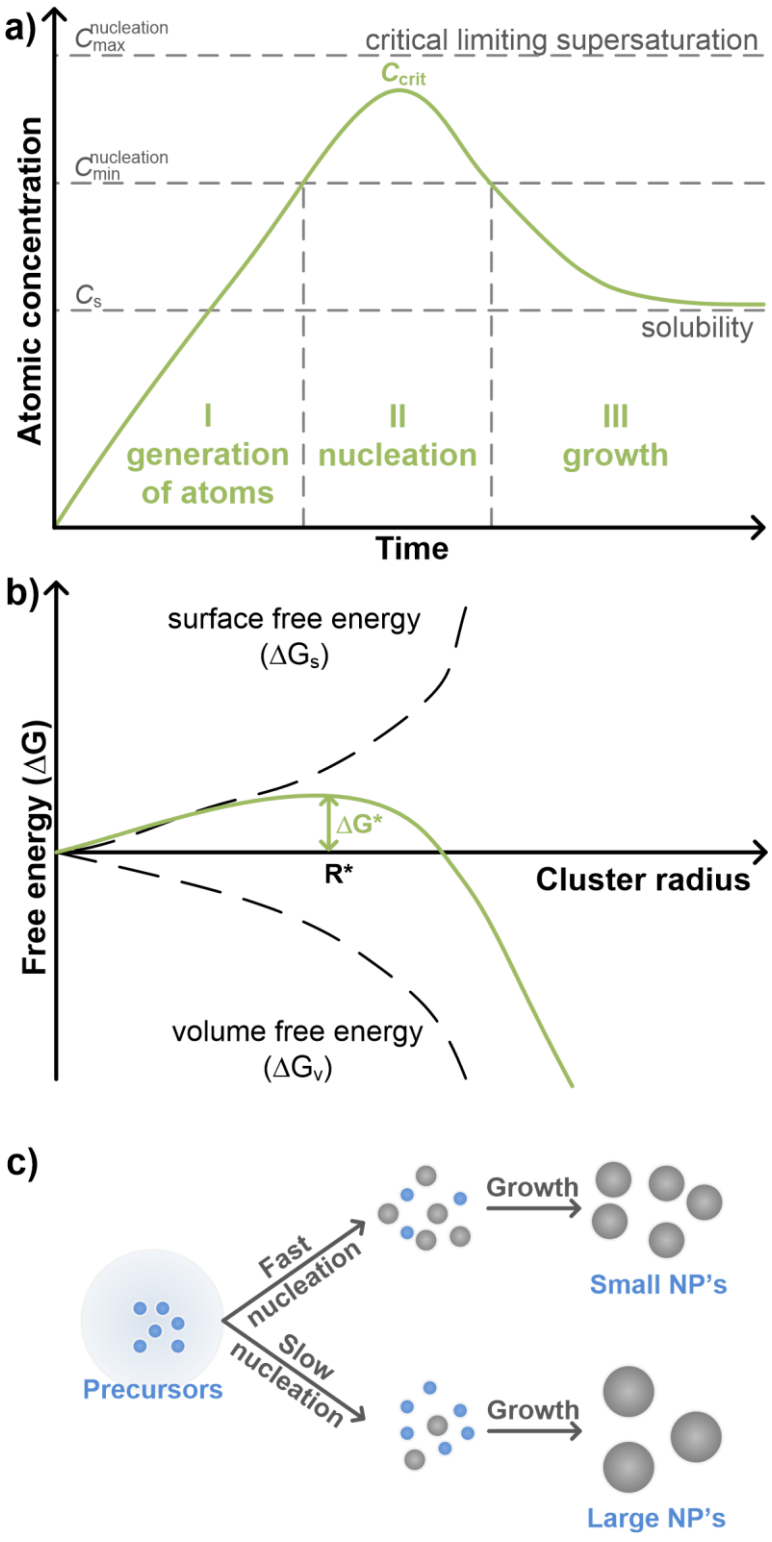

Figure 1.19. a) Plot of LaMer model for the generation of atoms, nucleation, and subsequent growth of colloidal synthesis;[67] b) Representation of Gibbs free energy variation for nucleation as function of the radius of the solid cluster;[70] c) Schematic representation of the influence of the nucleation' kinetics to the final nanoparticles size, in the absence of Ostwald ripening.[71]

Classically, particle growth is described based on differences in surface energy of small and large particles. For solid species with a solid-liquid interface, the chemical potential increases with decreasing particle size, following the thermodynamic theory presented above. This leads to re-dissolution of the smallest, newly formed particles, creating a concentration gradient in the solution. Uniformity of the concentration is reestablished by material diffusion towards the larger particles, thus leading to particle growth (**Figure 1.20**). This was first described by Ostwald in 1901 and the mechanism is therefore known as Ostwald ripening.[72] Since the growth rate is dictated by material diffusion between particles, the process is often termed diffusion limited growth.

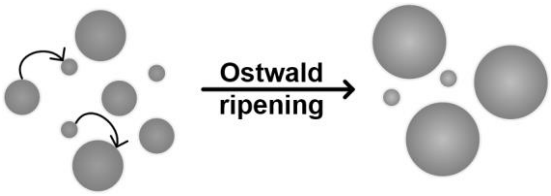

Figure 1.20. Scheme of nanocrystal growth controlled by Ostwald ripening mechanism[73]

The full mathematical treatment of the process was done in 1961 by Lifshitz and Slyozov, followed by the work of Wagner and is known as LSW theory. If the diffusion of material to the growing particles is faster than the actual reaction of the material with the particle surface, the growth is reaction limited.[72] New theories, such as the two-step model, where the first step is the formation of a sufficient size cluster of solute molecules and the second step is the reorganization of such a cluster into an ordered structure, have also been proposed.[70] However, the nucleation happening in a solvothermal synthesis is much more complex and the reaction energies related to hydrolysis and condensation need to be taken into account. The attempts to describe nucleation in solvothermal synthesis was based on both experiments and theory but it is now widely accepted that the nucleation process is highly system dependent and cannot easily be generalized. It is expected that with the developments in characterization methods, further advanced models regarding nucleation and growth of nanoparticles will appear in the coming years.

1.4. Metal Oxides Nanoparticles

In the field of metal oxides, the discovery of superconductive oxides [74] and oxides with large magnetoresistance [75] has raised special attention especially to oxides with transition metals (**Figure 1.21**).[76] Transition metal oxides are also commonly used as catalysts, and in electronics with applications varying from semiconductors, dielectrics and conductive electrodes, which suggests the importance of these materials.[77] Metal oxides benefit from the large electronegativity of the oxygen to induce strong electron connections with the nearby atoms, which affects the chemical properties and surface energy of the materials.[78] At the same time, nanostructured metal oxides compared with the bulk materials benefit from the spatial confinement along with

the large fraction of surface atoms, high surface energy, strong surface adsorption and increased surface-to-volume ratio that greatly improves the performance of these materials.[30]

The range of electronic structures in oxides is quite wide, where transition and post-transition metal oxides show very interesting properties. Transition metal oxides are characterized by a small energy difference between a cation d^n and either a d^{n+1} or d^{n-1} configurations, which allows to quick transformation between the different forms. However, the structure instability and non-optimality of other parameters can limit the fields of application. Only metal oxides with d^0 and d^{10} electronic configurations show stable properties. The d^0 configuration is found in transition-metal oxides, such as, TiO_2, V_2O_5 and WO_3, whereas d^{10} configuration is found in post-transition-metal oxides, as In_2O_3 or SnO_2.[79]

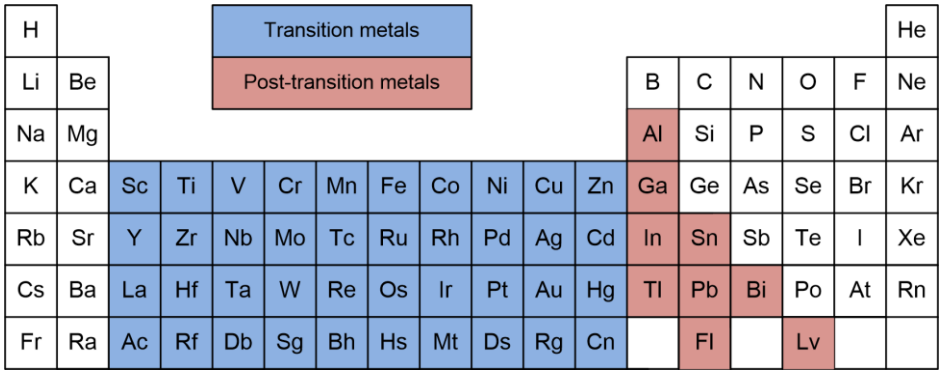

Figure 1.21. Transition and post-transition metals groups highlighted in the periodic table.[80]

The deposition of nanostructured metal oxides has been already described by both physical and chemical methods,[77], [81] and it is believed that all the understanding regarding the synthesis, properties and applications of nanoparticles, described previously, can also be extended to oxide nanoparticles.

1.4.1. Tungsten trioxide (WO_3)

Tungsten oxide (WO_x) is a well-studied semiconductor used for several applications as chromogenic material, sensor and catalyst.[82] The major important features is its low cost and availability, improved stability, reversible change of conductivity and optical properties, high sensitivity, selectivity and biocompatibility.[83]

The structure of the crystalline material is based on corner-sharing WO_6 octahedra, as in the amorphous structure, although with more ordered bond lengths and angles. The bonds are mainly of ionic character with a significant covalent part, and stoichiometric WO_3 can be pictured as being composed of W^{6+} and O^{2-} ions. The valence band is largely composed of O 2p orbitals, while the conduction band derives mainly from W 5d orbitals and the Fermi level is positioned in the middle of the band gap, as shown in **Figure 1.22**.[84]

Amorphous WO_3, with the most distorted structure, normally possesses a relatively large E_g on the order of ~3.25 eV, whereas monoclinic WO_3, in bulk form, has been reported to show a

typical E_g of ~2.62 eV at room temperature. In nanostructured WO_3, the bandgap generally increases with the reduction of the grain size. Experimentally, this is often observed as a blue shift of the optical absorption band edge as the nanostructure dimensions are reduced, and it is widely accepted that this observed blue shift can be attributed to the quantum confinement effect.[85]

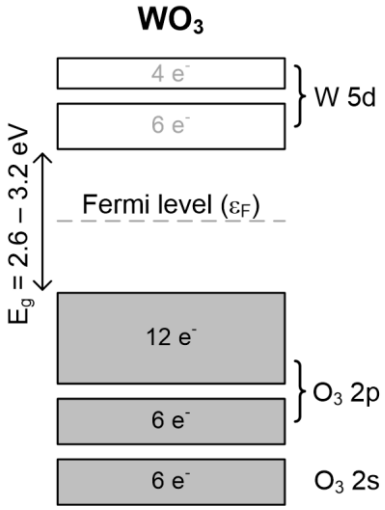

Figure 1.22. Schematic band structure of WO_3 (filled states are colored). The energy band gap (E_g) vary from 2.6 to 3.2 eV for amorphous and crystalline states, respectively.[85]

The optical properties of WO_3 in the visible region are dominated by the absorption threshold, which is defined by the bandgap energy of the material. Therefore, WO_3 is essentially transparent to most visible wavelengths with a slightly yellow tint for smaller bandgap samples, which absorb part of the blue spectrum. The optical band gap energy (E_g) can be calculated using the Tauc's plot and by applying the equation (**1.13**):

$$\alpha h\upsilon = A(h\upsilon - E_g)^n \qquad \textbf{(1.13)}$$

where A is a constant, $h\upsilon$ is the corresponding photon energy, α is the absorption coefficient and n depends on the type of the optical transition. For crystalline semiconductors n is ½ or 2 for direct or indirect allowed transitions (**Figure 1.23**), respectively.[86]

The electrical conductivity of single crystal WO_3 ranges from 10 to 10^{-4} S cm^{-1} depending on the stoichiometry.[87] Additionally, structural factors such as grain size, grain boundary, film thickness and phase also have a great influence on the material's conductivity. For example, it has been reported a high carrier concentration (5×10^{19} cm^{-3}) and electron mobility (6.5 cm^2 V^{-1} s^{-1}) for WO_3 films synthesized using an elevated substrate temperature during thermal evaporation deposition.[88] High substrate temperature tends to detach some oxygen ions under vacuum conditions, allowing more free electrons for conduction. It has also been suggested that by confining the free carriers' movement in well oriented 1D or 2D crystal structures, with smooth boundaries, the carrier mobility increases as the scattering effects are reduced.

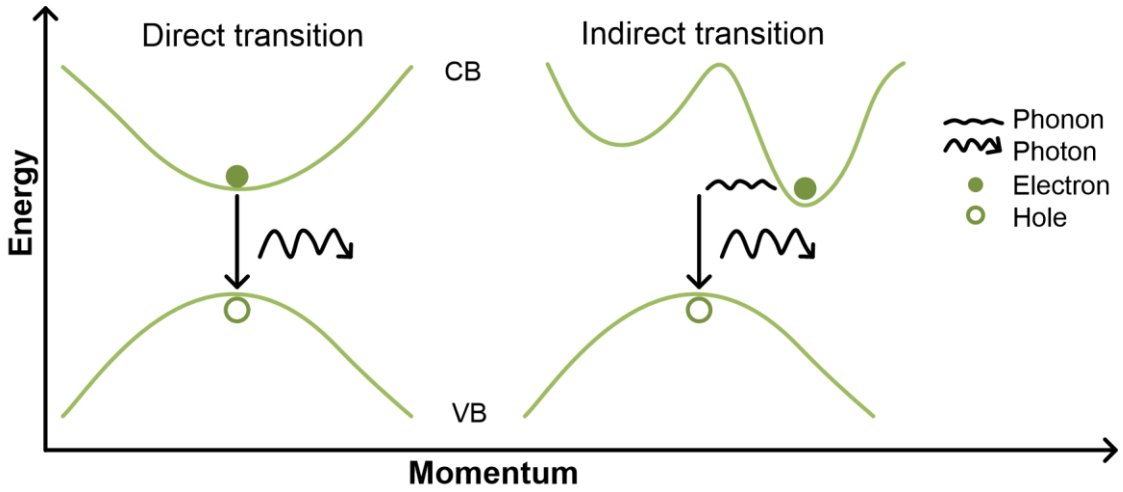

Figure 1.23. Schematic representation of the energy versus the momentum for the valence (VB) and conduction bands (CB) of semiconductors and the difference between direct and indirect transitions (or band gaps).

Like other metal oxides, WO_3 crystal phase transitions can take place during annealing and cooling. At room temperature, monoclinic has been reported as the most stable phase (**Figure 1.24a**), with a phase transformation to orthorhombic at 330 °C, followed of tetragonal phase above 740 °C. [85] The phase transitions have been reported to be partially reversible. In addition to the above-mentioned crystal phases, another possible stable phase for WO_3 is the hexagonal (*h*-WO_3) which was originally obtained from the slow dehydration of tungstic acids (**Figure 1.24b**). [89] The phase transition behavior in nanostructured WO_3 can be more complex, as it depends on the material morphology, which is greatly affected by the nanostructure synthesis process and initial precursors. The reduction of size of WO_3 crystallites enhances the surface energy of the system which decreases melting and sublimation temperatures. Therefore, generally the phase transitions occur at lower annealing temperatures when compared to the bulk counterparts.[85]

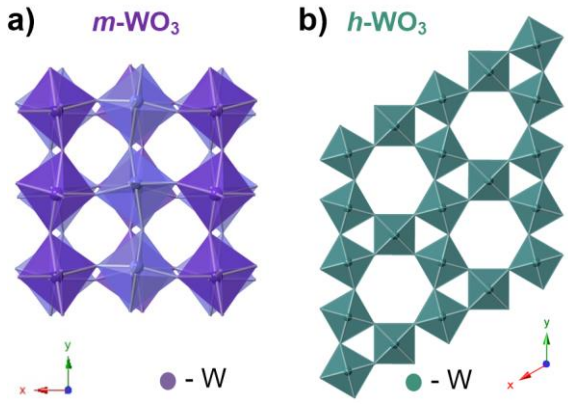

Figure 1.24. WO_3 crystal structures, designed in CrystalMaker software for: a) Monoclinic (*m*-WO_3) and b) Hexagonal (*h*-WO_3) configurations.

In addition to the transparent oxide WO_3, there exists a number of sub-stoichiometric phases of the forms W_mO_{3m-1} and W_mO_{3m-2} (m = 1, 2…), all the way down to WO_2. Only a partial loss of the WO_3 oxygen content is needed to affect its electronic band structure and increase its conductivity by a large amount. However, the reduction of WO_3 is usually accompanied by structural changes. The sub-stoichiometric phases exhibit different colors, ranging from blue in the case of a slight sub-stoichiometry to brownish for WO_2. In these cases, the Fermi level is situated in the W 5d band.[84]

The WO_3 hydrates ($WO_3 \cdot nH_2O$) or "tungstic acids" are also an important category as they are closely related to WO_3. The four most studied structures are the $WO_3 \cdot 2H_2O$ (dihydrate); $WO_3 \cdot H_2O$ (monohydrate); $WO_3 \cdot 0.5H_2O$ (hemihydrate); and $WO_3 \cdot 0.33H_2O$ (**Figure 1.25**) and the crystal structures are highly dependent on the water content. In the orthorhombic hydrated polymorph ($WO_3 \cdot 0.33H_2O$) some of the octahedra are composed of two terminals, one W=O double bond and one W-H_2O long bond ($WO_5(OH_2)$) which, by one hand, weaken the stacking of the layers in the c (or z) direction and by other hand, results in a less compact structure.[90]

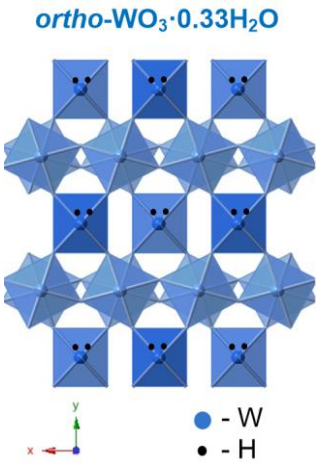

Figure 1.25. Crystal structure, designed in CrystalMaker software, for orthorhombic hydrated WO_3 (*ortho*-$WO_3 \cdot 0.33H_2O$).

Many different approaches for the synthesis of nanostructured WO_3 have been implemented using both vapor and liquid phase based methods,[85] like temperature annealing,[50] hot wire chemical vapor deposition,[91] sol-gel,[92] sputtering,[93] precipitation,[94] electrodeposition[95], [96] or hydrothermal methods.[97]–[99] Concerning solution processed synthesis, as it is the method used in this thesis, both Pourbaix and solubility diagrams, presented in **Figure 1.26**, are of great importance due to the variability of tungsten oxides structures that are originated depending on the experimental conditions. Pourbaix diagram shows that WO_2 (s) and W_2O_5 (s) are stable up to pH 7 and pH 5, respectively, in a narrow potential range (approximately -250 to 100 mV at pH 0 and -450 to -250 mV at pH 5). In contrast, WO_3 (s) is stable below pH 2 throughout all the oxidizing conditions. The solubility diagram shows that H_2WO_4 (aq) is stable at relatively low metal concentrations in acidic solutions, while WO_3 is predominant at higher metal concentrations. High metal concentrations favor the formation of polytungtates ($[W_6O_{20}(OH)]^{5-}$, $[W_{12}O_{39}]^{6-}$, $[W_{12}O_{41}]^{10-}$) above pH 2; with increase in the metal concentration, the high pH boundary of the polytungstate stability region expands from pH 4 to 8. The solubility diagram also demonstrate

that under basic conditions the $[WO_4]^{2-}$ is the predominant species in solution. Therefore, $[WO_4]^{2-}$ can be expected as a product of WO_3 dissolution as well as active W metal dissolution at high pH.[100]

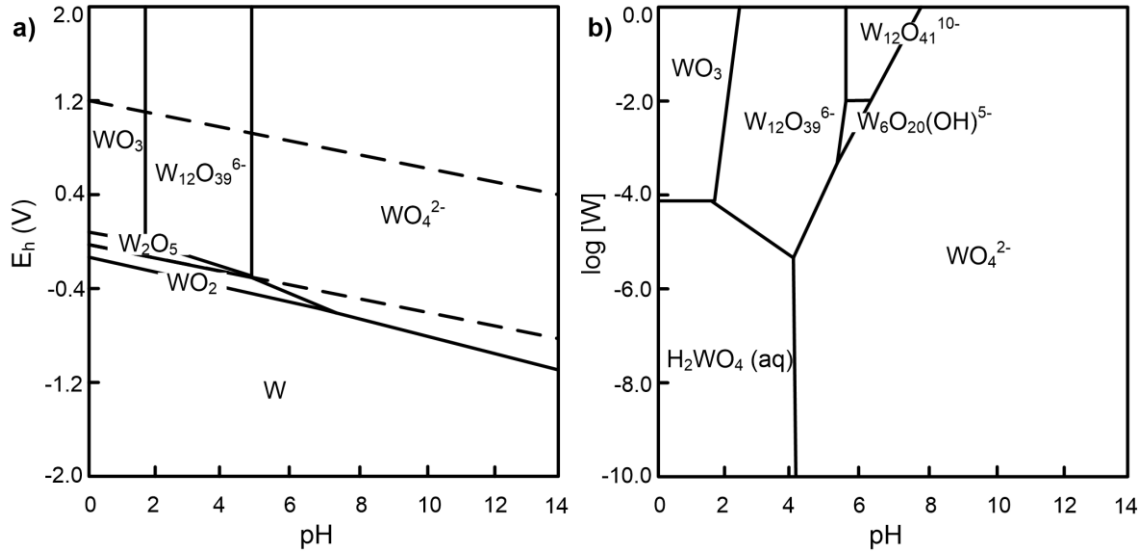

Figure 1.26. a) Pourbaix diagram for W-H_2O system at 25 ºC and tungsten molar concentration of 10^{-4} M (dashed lines represent the limits of stability of water), and b) Solubility diagram for a fixed potential of E_h = 0.2 V, 25 ºC and 3 M ionic strength.[100]–[102]

The electrochromism is the most studied application of WO_3 nanostructures. In fact, in 1815 Berzelius already reported that WO_3 changed color when warmed and in contact with hydrogen gas. The stoichiometric material is yellowish to greenish in bulk form and it can be chemically reduced to produce a blue compound. Color changes obtained by reacting tungsten oxide with sodium were reported in 1824 by Wohler and it is known that Wohler had produced a material similar to the one obtainable by ion intercalation in electrochromic crystalline tungsten oxide films (sodium tungsten bronze). Electrochemical, rather than purely chemical, reduction of tungsten oxide has also been studied extensively for many years. In particular, in 1930 the work by Kobosew and Nekrassow, found that tungsten oxide powders could be colored blue by electrochemical reduction in acidic solution.[86] The coloration reaction occurs upon electrochemical insertion of small cations (M) such as H^+, Li^+, and Na^+ and the simultaneous insertion of charge balancing electrons (**equation 1.14**).

$$\mathbf{WO_x + \mathit{y}M^+ + \mathit{y}e^- \leftrightarrow M_\mathit{y}WO_x} \qquad \mathbf{(1.14)}$$

In the typical electrochromic devices (**Figure 1.27**), when an electron is injected into the material, a cation from the electrolyte will compensate the charge insertion, generating in this way a tungsten bronze (M_yWO_x) which corresponds to the colored state. In the opposite way, when a reversible voltage is applied, the inverse process takes place and the film gets to the former state in the bleached condition. The fully mechanism is still under discussion and several theories have been presented for both amorphous and crystalline phases.[103] The most accepted theory is explained by small polaron transitions (formation of W^{5+} sites) for amorphous films and Drude-

like free electron scattering for crystalline films. The major difference between these two mechanisms, for amorphous and crystalline WO_x, is the electron localization or delocalization, respectively.[104]–[106] **Figure 1.28** shows some of the applications developed in CENIMAT with WO_3 as electrochromic material.

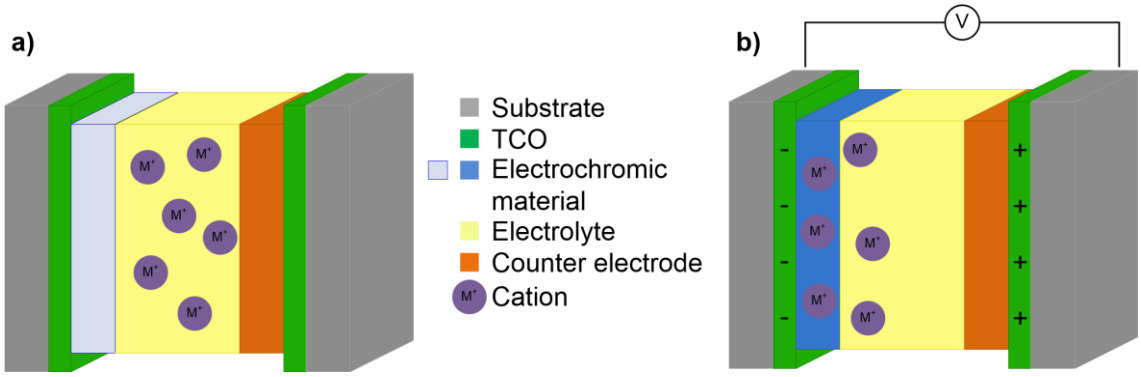

Figure 1.27. Schematic representation of an electrochromic device, a) before and b) after charge appliance (with the cation insertion and color modification of the electrochromic material).

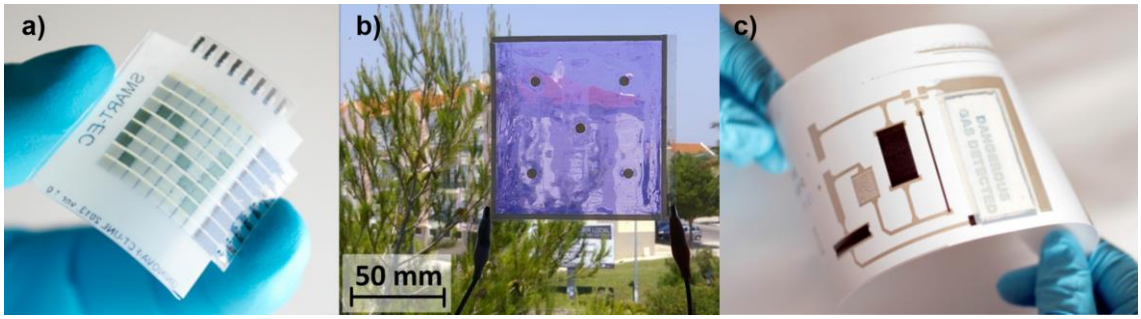

Figure 1.28. Examples of electrochromic applications developed in CENIMAT: a) Electrochromic passive matrix in paper, under the project SMART-EC (FP7-ICT-2009.3.9/258203), b) Transparent electrochromic window, and c) Gas sensor prototype with EC display on paper, under the project A3PLE (FP7-NMP-2010-SME/262782-2).

Other common application of WO_3 is as photocatalyst. In this field the main goal is to find suitable materials for efficient solar hydrogen production and organic pollutant degradation. In 1969, Fujishima and Honda reported the first photoelectrolysis of water using single-crystal rutile-structured TiO_2 under UV irradiation. Since then, TiO_2 and other semiconductor materials, including WO_3, were intensively explored for their photocatalytic abilities. For passive photocatalytic systems (without applying an external potential), which are preferable given today's energy issues, WO_3 nanoparticles are usually mixed with other metal oxides to form an overall complementary band structure, or doped with materials that can shift the WO_3 conduction band to a more negative position.[85], [107]

Precise and affordable monitoring of chemical gases is a critical issue for human health, industrial processes and environmental protection. For that, nanostructured WO_3, when compared with the bulk material, has been intensively studied as it enhances sensor capabilities,

reduces power consumption, and produces excellent reproducibility. Many of the enhanced features of the nanostructured WO_3 sensors are mainly ascribed to the increased surface area and complete depletion of carriers within the nanostructure when exposed to the target gas.[85], [108]

The application of WO_3 to other sensing platforms, as in biosensors, are mainly due to the electrical and optical properties mentioned above.[109] In fact, it was already demonstrated that nanoparticles of metal oxides applied to suitable electrode surfaces allow proteins immobilization and biocatalytic processes to be driven electrochemically.[110]

The pH value can be used as an indicator for disease diagnostics, medical treatment optimization, and monitoring of biochemical and biological processes.[111] Nevertheless, the integration of pH sensing systems into the next generation of wearable devices requires a different architecture than currently used in typical glass-type electrodes with a minimal electrode size.[112] Among all oxides being studied (IrO_x, RuO_2, SnO_2, Ta_2O_5, TiO_2, ZnO) WO_3 is a very promising material.[113]–[118] In fact, the first report of a WO_3 based pH sensor was reported in 1987 by Wrighton et al.,[119] where a microelectrochemical transistor was operating either electrically or chemically by changing the gate voltage or the solution pH, respectively. Nevertheless, the use of WO_3 with high surface area has mainly been reported as gas sensor and has not been fully exploited as pH sensor.[96], [120], [121] The pH sensing mechanism for this material even if not fully understood is believed to be dependent of the redox reaction involving the production of the tungsten bronze with a higher conductivity than the tungsten oxide (**equation 1.14**).

1.4.2. Multi-Element Oxides

Mixed-metal oxides (and multi-element oxides) are important materials in the world today. However, the study of these materials at a nanoscale, its influence on the structural and electronic parameters and its chemical reactivity has only been addressed systematically for a small number of oxides.[122]

The distinction between mixed-metal and multi-element oxides is that the first are materials in which the nanostructure stabilizes a specific polymorph which is not stable as bulk material, and the second are oxides that have the same phase as nanostructures and bulk. The first group is typical, but not exclusive, of oxide systems in which the stable bulk polymorph phase has an oxygen close-packed structure.[123] In both types, the electronic, magnetic or catalyt properties, can be tuned by partial replacement of one element (or oxide) by another, where the crystal structure remains unchanged over the whole composition range, or by the addition of dopants which can introduce favorable properties.[124] So, it is expected that the oxides can be tailored to have higher mobility, controlled carrier concentration and, at the same time, a stable chemical and physical composition depending on the application envisaged. Mobility is affected by the type of overlap that occurs between orbitals and therefore different cation percentages are considered to potentially modify it. In this scenario, a promising material for the realization of a mixed-metal oxide semiconductor with interesting variability of its electronic properties is the Ga_2O_3–In_2O_3–ZnO (GIZO) ternary oxide.

1.4.2.1. Gallium-Indium-Zinc-Oxide (GIZO)

Amorphous GIZO based thin-film transistors (TFTs) have been intensively studied since it allows good performances at low processing, and post processing, temperatures, making possible the production of flexible and transparent TFTs.[124], [125] The high performance in the amorphous phase is derived from the formation of a conduction band minimum in the spherical s orbitals of the post transition metal cations. These spherical s orbitals are significantly larger than O 2p orbitals, which form the valence band maximum (**Figure 1.29**). Even if a distortion of the metal–oxygen–metal bonds occurs, the large direct overlap between the neighboring metallic s orbitals ensures carrier transport. Therefore, crystalline GIZO thin films show quite similar performance than the amorphous ones.[124], [126]

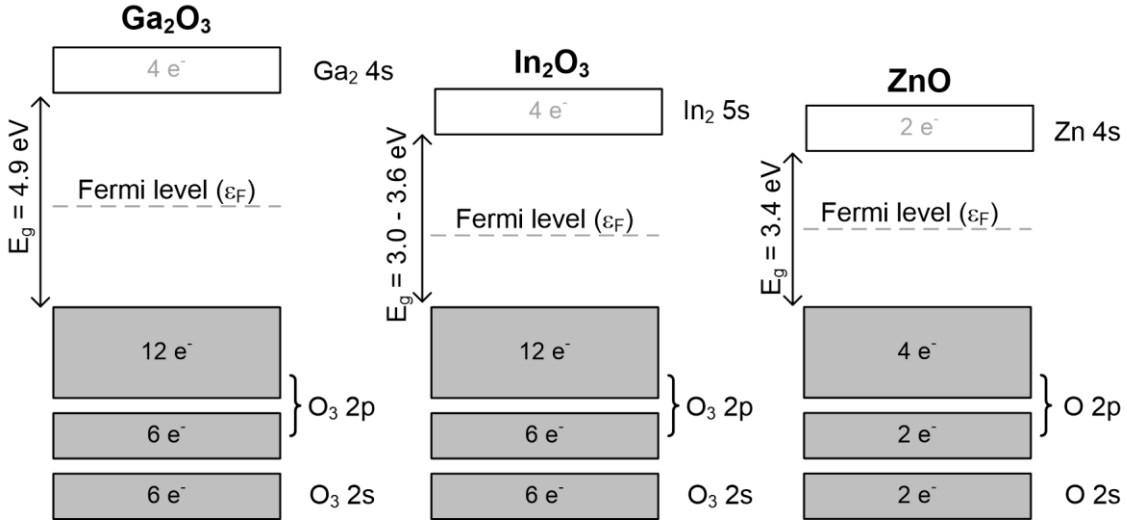

Figure 1.29. Schematic band structure of Ga_2O_3-In_2O_3-ZnO (filled states are colored). The energy band gaps (E_g) are reported for crystalline structures.[127]

The atomic concentration ratio between the composing cations have its own impact on the electronic properties of the material, and hence on the final performance of the devices. The idea behind this multicomponent concept is the role that each metal oxide has to play within the film. In a simplified initial approach, it should be plausible to describe that indium allows for high mobility that is driven by the overlap of its large and spherical 5s orbitals that enhance the cation band conduction; gallium has stronger bonds with oxygen than In or Zn, so it can restrain free carrier generation; and zinc stabilizes the structure of the film. Therefore, GIZO constitutes one of the most promising candidates for having n-type active layers, useful to contribute to the so-called post silicon electronic era, by playing an important role in transparent electronics processed on low-temperature substrates, as required for the emerging field of flexible electronics. Moreover, these multicomponent oxide films can be deposited by various techniques such as magnetron sputtering, pulsed laser deposition, or spin coating.[124]

Based on previous studies with this material system, indium richer compositions deliver the best electrical performance and stability, but the incorporation of gallium in the structure is always

required in order to properly control the carrier concentration. The 2.9:6:1 and 3.2:5.9:2 film compositions presented the most promising electrical properties with high field effect mobility (μ_{FE}), above 50 $cm^2\ V^{-1}\ s^{-1}$, low threshold voltage (V_{Th}) and low subthreshold swing (*SS*), while the overall stability of the devices is optimized.[77], [124]

1.5. Motivation and Thesis Outline

The main motivation of this thesis arrives from the need to better explore all the potentialities of metal oxide nanoparticles. In fact, we are now facing with the real development of the “nano” world but not all the phenomenon are well explained, or even understood, by the researchers. There are a background on the application of these materials in the bulk form but when the size is reduced to the nanoscale all the properties are changed and the potentialities are elevated to another level.

So, the first step of this thesis (**Chapter 2**) is the nanoparticles engineering. For that, we chose the solvothermal synthesis as it can be upscale to the industry and it allows a good control of the morphology and structure of the nanoparticles by adjusting the different synthesis parameters. This chapter reports all the experimental details and the main characterization (X-ray diffraction and scanning electron microscopy images) of the resulting metal oxide nanopowders as a contribution for further developments of these materials by other researchers.

The second part of the thesis, is the application of some of the nanoparticles synthesized (WO_3 and GIZO) to different electrochemical devices. The deposition techniques were adapted in each work to better control the films morphologies depending on the substrate material and on the final device apparatus.

Chapter 3 describes the influence of the morphology and structure of the WO_3 nanoparticles for electrochromic (EC) application. In fact, in the last years several researchers are improving the EC performances (**Table 1.1**) with metal oxide nanoparticles as the working electrodes. The power consumption is reduced and the optical modulation can go up to 92%. Nevertheless, future developments of these devices are needed to improve both the stability and life time, without compromising the optical performances. For that, the understanding of the EC mechanism of the different types of nanoparticles is a crucial parameter that will help to further design (or engineer) the best possible EC nanoparticles. Furthermore, the WO_3 nanoparticles were deposited by inkjet printing which is a technique compatible with flexible substrates.

Chapter 4 and **5** describe the work with WO_3 nanoparticles functionalized electrodes for sensing applications. The quantum confinement effect in nanoparticles is an important feature that allows the application of metal oxides in electrochemical devices that were typically built by metals. The great surface atom density associated with the reversible electrochemical reaction and high capacitance of WO_3, makes these nanoparticles as good candidates for sensing devices. In **Chapter 4** the pH sensor was built by electrodeposition of WO_3 in flexible substrates and the sensing performance was tested in a curve surface with gelatin based electrolyte. In **Chapter 5**, the WO_3 probes were built by drop casting and the biosensor combines the WO_3 nanoparticles

with cytochrome *c* nitrite reductase, as the sensitive biological element, to detect nitrite in solution, due to the redox reaction to ammonia.

Table 1.1. Resume of the latest research on nanostructured EC oxides, deposition methods, optical modulation (ΔT_{max}), applied potential, coloration (τ_{col}) and bleaching (τ_{bl}) times, and coloration efficiency (*CE*).

EC nanomaterial	Deposition method	ΔT_{max} (%)	Applied potential (V)	τ_{col} (90%)	τ_{bl} (90%)	*CE* (cm^2/C)	Ref.
WO_3	Inkjet printing	60	(±1.2 V)			65.5	[128]
WO_3	Hydrothermal synthesis	66.5	(-0.7, +1 V)	3.6	4.6	126	[99]
WO_3	Hydrothermal synthesis	57	(±2 V)	21	7	120	[129]
WO_3/PANI	Hydrothermal synthesis	42	(-0.2, +0.8 V)	0.5	0.8	76	[130]
WO_3	Ultrasonic spray deposition	75	(+2, +4 V vs Li/Li^+)	7	6	50	[131]
WO_3	Doctor blade/ UV	21*	(-0.1, +0.5 V)				[132]
WO_3-TiO_2	Anodic oxidation	77.7	(±1 V)	10	64	46.8	[133]
WO_3	Electrophoretic deposition	70	(-0.8, +1.2 V)	4.1	2.9	70	[134]
WO_3	Electrodeposition	92	(-1.2, +0.4 V)	9	15	51	[95]
WO_3/PEDOT	Electroplating	41.3	(±2 V)				[135]
WO_3	Electroplating	62	(±1 V)	7.5	3.9		[136]
NiO/PANI	Hydrothermal synthesis	62	(-0.6, +1.2 V)	0.09	0.12	121.6	[130]
α-$Ni(OH)_2$	Chemical bath deposition	58	(-0.4, +0.8 V)				[137]

* Due to the paper substrate used in this work, the optical characterization was measured as the difference of reflectance between colored and bleached states (ΔR_{max}).

In **Chapter 6**, GIZO nanoparticles are applied as the semiconductor layer in electrolyte-gated transistors (EGTs). The use of metal oxides in electronics is dated back in 1960's but the evolution is considered to follow Moore's law.[138] At the present time, microprocessors are built with 14 nm (**Figure 1.30**) and with more than 6 billion transistors therefore, the need for smaller and more powerful integrated circuits makes nanomaterials highly significant for the electronics field.[1] Moreover, EGT shows great potential in the field of biosensors by adapting the electrolyte to a specific application. In this work, the benefits and operation mechanism of EGTs with GIZO nanoparticles are discussed.

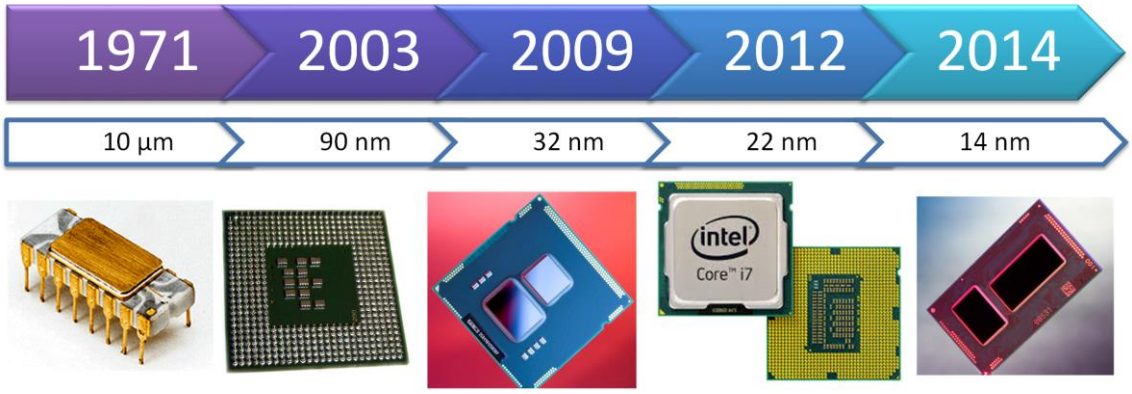

Figure 1.30. Evolution of the transistors' size used in Intel® processors during the last decades.

Finally, **Chapter 7** describes the main conclusions of all the produced devices and presents a list of actions for future work.

1.6. References

[1] C. C. Koch, I. A. Ovid'ko, S. Seal, and S. Veprek, *Structural Nanocrystalline Materials: Fundamentals and Applications*. Cambridge, UK: Cambridge University Press, 2007.

[2] M. C. Roco, "Broader societal issues of nanotechnology," *J. Nanoparticle Res.*, vol. 5, pp. 181–189, 2003.

[3] N. Taniguchi, "On the Basic Concept of 'Nano-Technology,'" in *Proc. Intl. Conf. Prod. Eng. Tokyo. Part II.*, Tokyo, Japan: Japan Society of Precision Engineering, 1974, pp. 5–10.

[4] R. P. Feynman, "There's plenty of room at the bottom," *J. Microelectromechanical Syst.*, vol. 1, no. 1, p. 60, 1992.

[5] T. Mappes, N. Jahr, A. Csaki, N. Vogler, J. Popp, and W. Fritzsche, "The invention of immersion ultramicroscopy in 1912-the birth of nanotechnology?," *Angew. Chem. Int. Ed. Engl.*, vol. 51, no. 45, pp. 11208–12, Nov. 2012.

[6] R. A. Zsigmondy, "Properties of colloids," in *Nobel Lectures, Chemistry 1922-1941*, vol. 1, Amsterdam, Netherlands: Elsevier Publishing Company, 1966.

[7] I. Langmuir, "Surface chemistry," in *Nobel Lectures, Chemistry 1922-1941*, Amsterdam, Netherlands: Elsevier Publishing Company, 1966.

[8] G. Binnig, "Scanning tunneling microscopy - From Birth to Adolescence," in *Nobel Lectures, Physics 1981-1990*, vol. 152–153, Singapore: World Scientific Publishing Co., 1993.

[9] G. Binnig, C. F. Quate, and C. Gerber, "Atomic Force Microscope," *Phys. Rev. Lett.*, vol. 56, no. 9, p. 930, 1986.

[10] R. E. Smalley, “Discovering the fullerenes,” in *Nobel Lectures, Chemistry 1996-2000*, Singapore: World Scientific Publications Co., 2003, p. 89.

[11] S. Iijima, “Helical microtubes of graphitic carbon,” *Nature*, vol. 354, p. 56, 1991.

[12] Л. В. Радушкевич, “О Структуре Углерода, Образующегося При Термическом Разложении Окиси Углерода На Железном Контакте,” *Журнал Физической Химии*, vol. 26, p. 88, 1952.

[13] K. E. Drexler, *Engines of Creation 2.0 - The Coming Era of Nanotechnology*. Wowio, 2006.

[14] “Foresight Institute.” [Online]. Available: http://www.foresight.org/.

[15] IBM, “A Boy And His Atom: The World’s Smallest Movie,” 2013. [Online]. Available: http://www.youtube.com/watch?v=oSCX78-8-q0&feature=player_detailpage.

[16] R. Society, *Nanoscience and Nanotechnologies: Opportunities and Uncertainties*. London, UK: The Royal Society & The Royal Academy of Engineering, 2004.

[17] L. Mino, G. Agostini, E. Borfecchia, D. Gianolio, A. Piovano, E. Gallo, and C. Lamberti, “Low-dimensional systems investigated by x-ray absorption spectroscopy: a selection of 2D, 1D and 0D cases,” *J. Phys. D. Appl. Phys.*, vol. 46, no. 42, p. 423001, Oct. 2013.

[18] A. I. Gusev and A. A. Rempel, Eds., *Nanocrystalline Materials*. Cambridge, UK: Cambridge International Science Publishing Ltd, 2004.

[19] P. R. Khaydarov, “Silver nanoparticles,” in *Nanomaterials: Risks and Benefits*, I. Linkov and J. Steevens, Eds. Amsterdam, Netherlands: Springer Science + Business Media B.V., 2009, pp. 287–297.

[20] L. Dai, Ed., *Carbon Nanotechnology - Recent developments in chemistry, physics, materials science and device applications*. Amsterdam, Netherlands: Elsevier B.V., 2006.

[21] “The project on Emerging Nanotechnologies - Consumer Products Inventory,” 2014. [Online]. Available: http://www.nanotechproject.org/cpi/about/analysis/.

[22] O. V Salata, “Applications of nanoparticles in biology and medicine,” *J. Nanobiotechnology*, vol. 2, p. 3, 2004.

[23] S. Thomas, N. Kalarikkal, A. M. Stephan, B. Raneesh, and A. K. Haghi, Eds., *ADVANCED NANOMATERIALS - Synthesis, Properties, and Applications*. Toronto: Apple Academic Press, 2014.

[24] C. L. Myung and S. Park, “Exhaust nanoparticle emissions from internal combustion engines: A review,” *Int. J. Automot. Technol.*, vol. 13, no. 1, pp. 9–22, Oct. 2012.

[25] G. A. Ozin, A. C. Arsenault, and L. Cademartiri, *Nanochemistry: A Chemical Approach to Nanomaterials*. Cambridge, UK: Royal Society of Chemistry, 2009.

[26] D. W. Green, W.-F. Lai, and H.-S. Jung, “Evolving marine biomimetics for regenerative dentistry.,” *Mar. Drugs*, vol. 12, no. 5, pp. 2877–912, May 2014.

[27] A. Lakhtakia, R. J. Martín-Palma, M. a Motyka, and C. G. Pantano, “Fabrication of free-standing replicas of fragile, laminar, chitinous biotemplates.,” *Bioinspir. Biomim.*, vol. 4, no. 3, p. 034001, Sep. 2009.

[28] I. A. Ødegård, J. Romann, A. Fossdal, A. Røyset, and G. Tranell, “Synthesis and properties of silicon/magnesium silicon nitride diatom frustule replicas,” *J. Mater. Chem. A*, vol. 2, no. 39, pp. 16410–16415, 2014.

[29] Z. Vértesy, Z. Bálint, K. Kertész, D. Méhn, I. Kiricsi, V. Lousse, J. Vigneron, and L. P. Biró, “Modifications to Wing Scale Microstructures in Lycaenid Butterflies,” *Microsc. Anal.*, vol. 18, no. 4, pp. 25–27, 2004.

[30] A. S. Edelstien and R. C. Cammarata, Eds., *Nanomaterials - Synthesis, Properties and Applications*. London, UK: IOP Publishing Ltd, 1996.

[31] B. V Derjaguin, Y. I. Rabinovich, and N. V Churaev, “Direct measurement of molecular forces,” *Nature*, vol. 272, pp. 313–318, 1978.

[32] R. Holdich, “Colloids and agglomeration,” in *Fundamentals of Particle Technology*, Loughborough, UK: Midland Information Technology and Publishing, 2002, pp. 131–140.

[33] H. C. Hamaker, “THE LONDON--VAN DER WAALS ATTRACTION BETWEEN SPHERICAL PARTICLES,” *Phys. IV*, vol. 10, pp. 1058–1072, 1937.

[34] M. R. Wright, *An Introduction to Aqueous Electrolyte Solutions*. Chichester, UK: John Wiley & Sons, 2007.

[35] E. J. W. Verwey and J. T. G. Overbeek, *Theory of the stability of lyophobic colloids - The interaction of sol particles having an electric double layer*. Leiden, Netherlands: Elsevier, 1948.

[36] J. Mahanty and B. W. Ninham, *Dispersion Forces*. London, UK: Academic Press, Inc., 1976.

[37] C. F. Brinker and G. W. Scherer, *Sol-Gel Science - The Physics and Chemistry of Sol-Gel Processing*. San Diego, USA: Academic Press, Inc., 1990.

[38] K. Ueno, H. Shimotani, Y. Iwasa, and M. Kawasaki, “Electrostatic charge accumulation versus electrochemical doping in $SrTiO_3$ electric double layer transistors,” *Appl. Phys. Lett.*, vol. 96, no. 25, p. 252107, 2010.

[39] H. Shimotani, H. Asanuma, A. Tsukazaki, A. Ohtomo, M. Kawasaki, and Y. Iwasa, “Insulator-to-metal transition in ZnO by electric double layer gating,” *Appl. Phys. Lett.*, vol. 91, no. 8, p. 082106, 2007.

[40] B. L. V Prasad, C. M. Sorensen, and K. J. Klabunde, “Gold nanoparticle superlattices.,” *Chem. Soc. Rev.*, vol. 37, no. 9, pp. 1871–83, Sep. 2008.

[41] E. Hotze, T. Phenrat, and G. Lowry, “Nanoparticle Aggregation: Challenges to Understanding Transport and Reactivity in the Environment,” *J. Environ. Qual.*, vol. 39, no. 6, pp. 1909–1924, 2010.

[42] V. Dahirel and M. Jardat, “Effective interactions between charged nanoparticles in water: What is left from the DLVO theory?,” *Curr. Opin. Colloid Interface Sci.*, vol. 15, no. 1–2, pp. 2–7, Apr. 2010.

[43] S. M. Gatica, M. W. Cole, and D. Velegol, “Designing van der Waals Forces between Nanocolloids.,” *Nano Lett.*, vol. 5, no. 1, pp. 169–73, Jan. 2005.

[44] “Ball Mill from RETSCH.” [Online]. Available: http://www.azom.com/article.aspx?ArticleID=8402.

[45] P. Thangadurai, I. Zergioti, S. Saranu, C. Chandrinou, Z. Yang, D. Tsoukalas, a. Kean, and N. Boukos, “ZnO nanoparticles produced by novel reactive physical deposition process,” *Appl. Surf. Sci.*, vol. 257, no. 12, pp. 5366–5369, Apr. 2011.

[46] D. Gaspar, a C. Pimentel, T. Mateus, J. P. Leitão, J. Soares, B. P. Falcão, a Araújo, a Vicente, S. a Filonovich, H. Aguas, R. Martins, and I. Ferreira, “Influence of the layer thickness in plasmonic gold nanoparticles produced by thermal evaporation.,” *Sci. Rep.*, vol. 3, p. 1469, Jan. 2013.

[47] A. Araújo, C. Caro, M. J. Mendes, D. Nunes, E. Fortunato, R. Franco, H. Aguas, and R. Martins, “Highly efficient nanoplasmonic SERS on cardboard packaging substrates.,” *Nanotechnology*, vol. 25, no. 41, p. 415202, Sep. 2014.

[48] K. H. Smith, E. Tejeda-Montes, M. Poch, and A. Mata, “Integrating top-down and self-assembly in the fabrication of peptide and protein-based biomedical materials.,” *Chem. Soc. Rev.*, vol. 40, no. 9, pp. 4563–77, Sep. 2011.

[49] V. Resta, J. Gonzalo, C. N. Afonso, E. Piscopiello, and J. García López, “Coverage induced regulation of Au nanoparticles during pulsed laser deposition,” *J. Appl. Phys.*, vol. 109, no. 9, p. 094302, 2011.

[50] P. J. Wojcik, A. S. Cruz, L. Santos, L. Pereira, R. Martins, and E. Fortunato, “Microstructure Control of Dual-phase Inkjet Printed a-WO_3/TiO_2/WO_X Films for High Performance Electrochromic Applications,” *J. Mater. Chem.*, vol. 22, pp. 13268–13278, 2012.

[51] P. R. Sajanlal, T. S. Sreeprasad, A. K. Samal, and T. Pradeep, “Anisotropic nanomaterials: structure, growth, assembly, and functions.,” *Nano Rev.*, vol. 2, pp. 1–62, Jan. 2011.

[52] K. E. Sapsford, W. R. Algar, L. Berti, K. B. Gemmill, B. J. Casey, E. Oh, M. H. Stewart, and I. L. Medintz, “Functionalizing nanoparticles with biological molecules: developing chemistries that facilitate nanotechnology.,” *Chem. Rev.*, vol. 113, no. 3, pp. 1904–2074, Mar. 2013.

[53] B. D. Briggs and M. R. Knecht, “Nanotechnology Meets Biology: Peptide-based Methods for the Fabrication of Functional Materials,” *J. Phys. Chem. Lett.*, vol. 3, no. 3, pp. 405–418, Feb. 2012.

[54] G. M. Whitesides, J. P. Mathias, and C. T. Seto, “Molecular Self-Assembly and Nanochemistry : A Chemical Strategy for the Synthesis Nanostructures,” *Science (80)*, vol. 254, p. 1312, 1991.

[55] P. Saravanan, R. Gopalan, and V. Chandrasekaran, “Synthesis and Characterisation of Nanomaterials,” *Def. Sci. J.*, vol. 58, no. 4, pp. 504–516, 2008.

[56] K. J. Si, D. Sikdar, Y. Chen, Z. Xu, Y. Tang, W. Xiong, P. Guo, S. Zhang, Y. Lu, Q. Bao, W. Zhu, M. Premaratne, and W. Cheng, “Giant Plasmene Nanosheets, Nanoribbons, and Origami,” *ACS Nano*, p. DOI: 10.1021/nn504615a, 2014.

[57] R. I. Walton, “Subcritical solvothermal synthesis of condensed inorganic materials,” *Chem. Soc. Rev.*, vol. 31, no. 4, pp. 230–238, Jun. 2002.

[58] K. Byrappa and M. Yoshimura, *HANDBOOK OF HYDROTHERMAL TECHNOLOGY - A Technology for Crystal Growth and Materials Processing*. Norwich, NY, USA: Noyes Publication, 2001.

[59] M. Yoshimura and K. Byrappa, “Hydrothermal processing of materials: past, present and future,” *J. Mater. Sci.*, vol. 43, no. 7, pp. 2085–2103, Nov. 2007.

[60] J. A. Dean, *LANGE’S HANDBOOK OF CHEMISTRY*, Fifteenth . New York, USA: McGraw-Hill, Inc., 1999.

[61] A. Nugroho and J. Kim, “Effect of KOH on the continuous synthesis of cobalt oxide and manganese oxide nanoparticles in supercritical water,” *J. Ind. Eng. Chem.*, vol. 20, no. 6, pp. 4443–4446, Nov. 2014.

[62] “Parr Instrument Company.” [Online]. Available: http://www.parrinst.com/products/sample-preparation/acid-digestion/.

[63] F. Moro, S. V. Yu Tang, F. Tuna, and E. Lester, “Magnetic properties of cobalt oxide nanoparticles synthesised by a continuous hydrothermal method,” *J. Magn. Magn. Mater.*, vol. 348, pp. 1–7, Dec. 2013.

[64] “Promethean Particles.” [Online]. Available: http://www.prometheanparticles.co.uk/our_technology.

[65] A. Pimentel, D. Nunes, P. Duarte, J. Rodrigues, F. M. Costa, T. Monteiro, R. Martins, and E. Fortunato, “Synthesis of Long ZnO Nanorods under Microwave Irradiation or Conventional Heating,” *J. Phys. Chem. C*, vol. 118, no. 26, pp. 14629–14639, Jul. 2014.

[66] T. Nguyen and T. Do, “Size- and Shape-Controlled Synthesis of Monodisperse Metal Oxide and Mixed Oxide Nanocrystals,” in *Nanocrystal*, Y. Masuda, Ed. InTech, 2011.

[67] V. K. LaMer and R. H. Dinegar, “Theory, Production and Mechanism of Formation of Moodispersed Hydrosols,” *J. Am. Chem. Soc.*, vol. 72, no. 11, pp. 4847–4854, 1950.

[68] G. Cao, “Nanostructures and Nanomaterials - Synthesis, Properties & Applications.” Imperial College Press, London, UK, 2004.

[69] Y. Sun, “Controlled synthesis of colloidal silver nanoparticles in organic solutions: empirical rules for nucleation engineering.,” *Chem. Soc. Rev.*, vol. 42, no. 7, pp. 2497–511, Apr. 2013.

[70] D. Erdemir, A. Y. Lee, and A. S. Myerson, “Nucleation of crystals from solution: classical and two-step models.,” *Acc. Chem. Res.*, vol. 42, no. 5, pp. 621–9, May 2009.

[71] N. Soltani, E. Saion, M. Erfani, K. Rezaee, G. Bahmanrokh, G. P. C. Drummen, A. Bahrami, and M. Z. Hussein, “Influence of the polyvinyl pyrrolidone concentration on particle size and dispersion of ZnS nanoparticles sythesized by mcrowave iradiation.,” *Int. J. Mol. Sci.*, vol. 13, no. 10, pp. 12412–27, Jan. 2012.

[72] C. N. R. Rao, A. Muller, and A. K. Cheetham, Eds., *Nanomaterials Chemistry - Recent developments and New Directions*. Weinheim, Germany: WILEY-VCH Verlag GmbH & Co. KGaA, 2007.

[73] J. H. Yao, K. R. Elder, H. Guo, and M. Grant, “Theory and simulation of Ostwald ripening,” *Phys. Rev. B*, vol. 47, no. 21, pp. 14110–14125, 1993.

[74] R. J. Cava, “Oxide Superconductores,” *J. Am. Ceram. Soc.*, vol. 83, no. 1, pp. 5–28, 2000.

[75] J. Z. Sun and A. Gupta, “Spin-Dependent Transport and Low-Field Magnetoresistance in Doped Manganites,” *Annu. Rev. Mater. Sci.*, vol. 28, pp. 45–78, 1998.

[76] C. N. R. Rao, A. Muller, and A. K. Cheetham, Eds., *The chemistry of nanomaterials: Synthesis, Properties and Applications*, vol. 1. Weinheim, Germany: WILEY-VCH Verlag GmbH & Co. KGaA, 2004.

[77] P. Barquinha, R. Martins, L. Pereira, and E. Fortunato, *Transparent Oxide Electronics*. Chichester, UK: John Wiley & Sons, Ltd, 2012.

[78] S. Djoki, Ed., *Electrodeposition and Surface Finishing*. New York, USA: Springer, 2014.

[79] C. Wang, L. Yin, L. Zhang, D. Xiang, and R. Gao, “Metal oxide gas sensors: Sensitivity and influencing factors,” *Sensors*, vol. 10, pp. 2088–2106, 2010.

[80] “IUPAC Periodic Table of the Elements,” 2013. [Online]. Available: http://www.iupac.org/fileadmin/user_upload/news/IUPAC_Periodic_Table-1May13.pdf. [Accessed: 12-Feb-2015].

[81] C. C. Koch, Ed., *Nanostructured Materials: Processing, Properties, and Applications*. Norwich, NY, USA: William Andrew Publishing, 2007.

[82] D. Vernardou, H. Drosos, E. Spanakis, E. Koudoumas, C. Savvakis, and N. Katsarakis, “Electrochemical and photocatalytic properties of WO_3 coatings grown at low temperatures,” *J. Mater. Chem.*, vol. 21, no. 2, p. 513, 2011.

[83] S.-J. Yuan, H. He, G.-P. Sheng, J.-J. Chen, Z.-H. Tong, Y.-Y. Cheng, W.-W. Li, Z.-Q. Lin, F. Zhang, and H.-Q. Yu, “A photometric high-throughput method for identification of electrochemically active bacteria using a WO_3 nanocluster probe,” *Sci. Rep.*, vol. 3, p. 1315, Jan. 2013.

[84] G. A. Niklasson and C. G. Granqvist, “Electrochromics for smart windows: thin films of tungsten oxide and nickel oxide, and devices based on these,” *J. Mater. Chem.*, vol. 17, no. 2, p. 127, 2007.

[85] H. Zheng, J. Z. Ou, M. S. Strano, R. B. Kaner, A. Mitchell, and K. Kalantar-Zadeh, “Nanostructured Tungsten Oxide - Properties, Synthesis, and Applications,” *Adv. Funct. Mater.*, vol. 21, pp. 2175–2196, May 2011.

[86] C. G. Granqvist, *Handbook of inorganic Electrochromic Materials*. Amsterdam, Netherlands: Elsevier, 2002.

[87] V. O. Makarov and M. Trontelj, “Sintering and Electrical Conductivity of Doped WO_3,” *J. Eur. Ceram. Soc.*, vol. 16, no. 95, pp. 791–794, 1996.

[88] K. J. Patel, C. J. Panchal, V. a. Kheraj, and M. S. Desai, “Growth, structural, electrical and optical properties of the thermally evaporated tungsten trioxide (WO_3) thin films,” *Mater. Chem. Phys.*, vol. 114, pp. 475–478, 2009.

[89] S. S. Kalanur, Y. J. Hwang, S. Y. Chae, and O. S. Joo, “Facile growth of aligned WO_3 nanorods on FTO substrate for enhanced photoanodic water oxidation activity,” *J. Mater. Chem. A*, vol. 1, p. 3479, 2013.

[90] L. Zhou, J. Zou, M. Yu, P. Lu, J. Wei, Y. Qian, Y. Wang, and C. Yu, “Green Synthesis of Hexagonal-Shaped $WO_3.0.33H_2O$ Nanodiscs Composed of Nanosheets,” *Cryst. Growth Des.*, vol. 8, no. 11, pp. 3993–3998, 2008.

[91] C. M. White, D. T. Gillaspie, E. Whitney, S.-H. Lee, and A. C. Dillon, “Flexible electrochromic devices based on crystalline WO_3 nanostructures produced with hot-wire chemical vapor deposition,” *Thin Solid Films*, vol. 517, no. 12, pp. 3596–3599, Apr. 2009.

[92] Z. Xie, L. Gao, B. Liang, X. Wang, G. Chen, Z. Liu, J. Chao, D. Chen, and G. Shen, “Fast fabrication of a $WO_3 \cdot 2H_2O$ thin film with improved electrochromic properties,” *J. Mater. Chem.*, vol. 22, no. 37, p. 19904, 2012.

[93] C.-K. Wang, C.-K. Lin, C.-L. Wu, S. Brahma, S.-C. Wang, and J.-L. Huang, “Characterization of electrochromic tungsten oxide film from electrochemical anodized RF-sputtered tungsten films,” *Ceram. Int.*, vol. 39, no. 4, pp. 4293–4298, May 2013.

[94] S. Songara, V. Gupta, M. Kumar Patra, J. Singh, L. Saini, G. Siddaramana Gowd, S. Raj Vadera, and N. Kumar, “Tuning of crystal phase structure in hydrated WO_3 nanoparticles under wet chemical conditions and studies on their photochromic properties,” *J. Phys. Chem. Solids*, vol. 73, no. 7, pp. 851–857, Jul. 2012.

[95] L. Liu, M. Layani, S. Yellinek, A. Kamyshny, H. Ling, P. S. Lee, S. Magdassi, and D. Mandler, “‘Nano to nano’ electrodeposition of WO_3 crystalline nanoparticles for electrochromic coatings,” *J. Mater. Chem. A*, vol. 2, no. 38, pp. 16224–16229, Jul. 2014.

[96] L. Santos, J. P. Neto, A. Crespo, D. Nunes, N. Costa, I. M. Fonseca, P. Barquinha, L. Pereira, J. Silva, R. Martins, and E. Fortunato, “WO_3 Nanoparticle-Based Conformable pH Sensor.,” *ACS Appl. Mater. Interfaces*, vol. 6, no. 15, pp. 12226–12234, Jul. 2014.

[97] J. Yang, L. Jiao, Q. Zhao, Q. Wang, H. Gao, Q. Huan, W. Zheng, Y. Wang, and H. Yuan, “Facile preparation and electrochemical properties of hierarchical chrysanthemum-like $WO_3 \cdot 0.33H_2O$,” *J. Mater. Chem.*, vol. 22, no. 9, p. 3699, 2012.

[98] D. Zhang, S. Wang, J. Zhu, H. Li, and Y. Lu, “WO_3 nanocrystals with tunable percentage of (001)-facet exposure,” *Appl. Catal. B Environ.*, vol. 123–124, pp. 398–404, Jul. 2012.

[99] G. F. Cai, J. P. Tu, D. Zhou, X. L. Wang, and C. D. Gu, “Growth of vertically aligned hierarchical WO_3 nano-architecture arrays on transparent conducting substrates with outstanding electrochromic performance,” *Sol. Energy Mater. Sol. Cells*, vol. 124, pp. 103–110, May 2014.

[100] M. Anik, “Effect of concentration gradient on the anodic behavior of tungsten,” *Corros. Sci.*, vol. 48, pp. 4158–4173, 2006.

[101] K. Osseo-Asare, “Solution chemistry of tungsten leaching systems,” *J. Electron. Mater.*, vol. 13B, no. 4, pp. 555–564, 1982.

[102] C. F. Baes Jr. and R. E. Mesmer, *The Hydrolysis of Cations*. New York, USA: John Wiley & Sons, Inc., 1976.

[103] C. G. Granqvist, “Oxide electrochromics: An introduction to devices and materials,” *Sol. Energy Mater. Sol. Cells*, vol. 99, pp. 1–13, Apr. 2012.

[104] S.-H. Lee, M. Je, H. M. Cheong, E. Ozkan, E. C. Tracy, and S. K. Deb, “Effect of crystallinity on electrochromic mechanism of Li_xWO_3 thin films,” *Solid State Ionics*, vol. 156, pp. 447–452, 2003.

[105] C. M. Lampert, “Electrochromic materials and devices for energy efficient windows,” *Sol. Energy Mater.*, vol. 11, no. 1, pp. 1–27, 1984.

[106] S. Hotchandani, I. Bedja, R. Fessenden, and P. Kamat, “Electrochromic and Photoelectrochromic Behavior of Thin WO_3 Films Prepared from Quantum Size Colloidal Particles,” *Langmuir*, vol. 10, no. 1, pp. 17–22, Jan. 1994.

[107] M. Rodríguez-Pérez, C. Chacón, E. Palacios-González, G. Rodríguez-Gattorno, and G. Oskam, “Photoelectrochemical water oxidation at electrophoretically deposited WO_3 films as a function of crystal structure and morphology,” *Electrochim. Acta*, vol. 140, pp. 320–331, 2014.

[108] S. Bai, K. Zhang, L. Wang, J. Sun, R. Luo, D. Li, and A. Chen, “Synthesis mechanism and gas-sensing application of nanosheet-assembled tungsten oxide microspheres,” *J. Mater. Chem. A*, vol. 2, no. 21, p. 7927, 2014.

[109] L. Santos, C. M. Silveira, E. Elangovan, J. P. Neto, D. Nunes, L. Pereira, R. Martins, J. Viegas, J. J. G. Moura, S. Todorovic, M. G. Almeida, and E. Fortunato, “Synthesis of WO_3 Nanoparticles for biosensing applications,” *Under revision*, 2015.

[110] Y. Wu and S. Hu, “Biosensors based on direct electron transfer in redox proteins,” *Microchim. Acta*, vol. 159, no. 1–2, pp. 1–17, Apr. 2007.

[111] D. D. Zhou, “Microelectrodes for in-vivo determination of pH,” in *Electrochemical sensors, biosensors and their biomedical applications*, Academic Press, Inc., 2008, pp. 261–305.

[112] A. J. Bandodkar, V. W. S. Hung, W. Jia, G. Valdés-Ramírez, J. R. Windmiller, A. G. Martinez, J. Ramírez, G. Chan, K. Kerman, and J. Wang, “Tattoo-based potentiometric ion-selective sensors for epidermal pH monitoring.,” *Analyst*, vol. 138, no. 1, pp. 123–8, Jan. 2013.

[113] L.-M. Kuo, K.-N. Chen, Y.-L. Chuang, and S. Chao, “A Flexible pH-Sensing Structure Using WO_3/IrO_2 Junction with Al_2O_3 Encapsulation Layer,” *ECS Solid State Lett.*, vol. 2, no. 3, pp. P28–P30, Dec. 2013.

[114] W.-D. Huang, H. Cao, S. Deb, M. Chiao, and J. C. Chiao, “A flexible pH sensor based on the iridium oxide sensing film,” *Sensors Actuators A Phys.*, vol. 169, no. 1, pp. 1–11, Sep. 2011.

[115] A. Fulati, S. M. U. Ali, M. Riaz, G. Amin, O. Nur, and M. Willander, “Miniaturized pH Sensors Based on Zinc Oxide Nanotubes/Nanorods,” *Sensors*, vol. 9, no. 11, pp. 8911–8923, 2009.

[116] R. Branquinho, J. V Pinto, T. Busani, P. Barquinha, L. Pereira, P. V. Baptista, R. Martins, and E. Fortunato, “Plastic Compatible Sputtered Ta_2O_5 Sensitive Layer for Oxide Semiconductor TFT Sensors,” *J. Disp. Technol.*, vol. 9, no. 9, pp. 723–728, 2013.

[117] N. C. S. Vieira, A. Figueiredo, A. D. Faceto, A. A. A. de Queiroz, V. Zucolotto, and F. E. G. Guimarães, "Dendrimers/TiO_2 nanoparticles layer-by-layer films as extended gate FET for pH detection," *Sensors Actuators B Chem.*, vol. 169, pp. 397–400, Jul. 2012.

[118] P. Kurzweil, "Metal Oxides and Ion-Exchanging Surfaces as pH Sensors in Liquids: State-of-the-Art and Outlook," *Sensors*, vol. 9, pp. 4955–4985, 2009.

[119] M. J. Natan, T. E. Mallouk, and M. S. Wrighton, "pH-Sensitive WO_3-Based Microelectrochemical Transistors," *J. Phys. Chem.*, vol. 91, no. 1, pp. 648–654, 1987.

[120] Y.-G. Choi, G. Sakai, K. Shimanoe, and N. Yamazoe, "Wet process-based fabrication of WO_3 thin film for NO_2 detection," *Sensors Actuators B Chem.*, vol. 101, no. 1–2, pp. 107–111, Jun. 2004.

[121] E. K. Heidari, C. Zamani, E. Marzbanrad, B. Raissi, and S. Nazarpour, "WO_3-based NO_2 sensors fabricated through low frequency AC electrophoretic deposition," *Sensors Actuators B Chem.*, vol. 146, no. 1, pp. 165–170, Apr. 2010.

[122] N. Izyumskaya, Y. Alivov, and H. Morkoç, "Oxides, Oxides, and More Oxides: High-κ Oxides, Ferroelectrics, Ferromagnetics, and Multiferroics," *Crit. Rev. Solid State Mater. Sci.*, vol. 34, no. February 2015, pp. 89–179, 2009.

[123] M. Fernandez-Garcia, a Martinez-Arias, J. C. Hanson, and J. a Rodriguez, "Nanostructured Oxides in Chemistry: Characterization and Properties," *Chem. Rev.*, vol. 104, pp. 4063–4104, 2004.

[124] A. Olziersky, P. Barquinha, A. Vilà, C. Magaña, E. Fortunato, J. R. Morante, and R. Martins, "Role of Ga_2O_3–In_2O_3–ZnO channel composition on the electrical performance of thin-film transistors," *Mater. Chem. Phys.*, vol. 131, no. 1–2, pp. 512–518, Dec. 2011.

[125] P. Barquinha, L. Pereira, G. Gonçalves, R. Martins, and E. Fortunato, "Toward High-Performance Amorphous GIZO TFTs," *J. Electrochem. Soc.*, vol. 156, no. 3, p. H161, 2009.

[126] N. Fukuda, Y. Watanabe, S. Uemura, Y. Yoshida, T. Nakamura, and H. Ushijima, "In–Ga–Zn oxide nanoparticles acting as an oxide semiconductor material synthesized via a coprecipitation-based method," *J. Mater. Chem. C*, vol. 2, no. 13, p. 2448, 2014.

[127] D. Kang, I. Song, C. Kim, Y. Park, T. D. Kang, H. S. Lee, J.-W. Park, S. H. Baek, S.-H. Choi, and H. Lee, "Effect of Ga/In ratio on the optical and electrical properties of GaInZnO thin films grown on SiO_2/Si substrates," *Appl. Phys. Lett.*, vol. 91, no. 9, p. 091910, 2007.

[128] M. Layani, P. Darmawan, W. L. Foo, L. Liu, A. Kamyshny, D. Mandler, S. Magdassi, and P. S. Lee, "Nanostructured electrochromic films by inkjet printing on large area and flexible transparent silver electrodes.," *Nanoscale*, vol. 6, no. 9, pp. 4572–6, May 2014.

[129] C. J. Hung, Y. H. Huang, C. H. Chen, P. Lin, and T. Y. Tseng, "Hydrothermal Formation of Tungsten Trioxide Nanowire Networks on Seed-Free Substrates and Their Properties in Electrochromic Device," *IEEE Trans. Components, Packag. Manuf. Technol.*, pp. 1–1, 2014.

[130] D. Ma, G. Shi, H. Wang, Q. Zhang, and Y. Li, "Controllable growth of high-quality metal oxide/conducting polymer hierarchical nanoarrays with outstanding electrochromic properties and solar-heat shielding ability," *J. Mater. Chem. A*, vol. 2, p. 13541, 2014.

[131] C.-P. Li, F. Lin, R. M. Richards, C. Engtrakul, R. C. Tenent, and C. a. Wolden, “The influence of sol–gel processing on the electrochromic properties of mesoporous WO_3 films produced by ultrasonic spray deposition,” *Sol. Energy Mater. Sol. Cells*, vol. 121, pp. 163–170, Feb. 2014.

[132] A. Danine, L. Cojocaru, C. Faure, C. Olivier, T. Toupance, G. Campet, and A. Rougier, “Room Temperature UV treated WO_3 thin films for electrochromic devices on paper substrate,” *Electrochim. Acta*, vol. 129, pp. 113–119, May 2014.

[133] Y. Gui and D. J. Blackwood, “Electrochromic Enhancement of WO_3-TiO_2 Composite Films Produced by Electrochemical Anodization,” *J. Electrochem. Soc.*, vol. 161, no. 14, pp. 191–201, 2014.

[134] B. Moshofsky and T. Mokari, “Electrochromic active layers from ultrathin nanowires of tungsten oxide,” *J. Mater. Chem. C*, vol. 2, p. 3556, 2014.

[135] C. Dulgerbaki and A. Uygun, “Efficient Electrochromic Materials Based on PEDOT/WO_3 Composites Synthesized in Ionic Liquid Media,” *Electroanalysis*, vol. 26, pp. 2501–2512, 2014.

[136] A. J. More, R. S. Patil, D. S. Dalavi, S. S. Mali, C. K. Hong, M. G. Gang, J. H. Kim, and P. S. Patil, “Electrodeposition of nano-granular tungsten oxide thin films for smart window application,” *Mater. Lett.*, vol. 134, pp. 298–301, Nov. 2014.

[137] M. A. Vidales-Hurtado and A. Mendoza-Galván, “Electrochromic Properties of Nanoporous α and β Nickel Hydroxide Thin Films Obtained by Chemical Bath Deposition,” *J. Nano Res.*, vol. 28, pp. 63–72, 2014.

[138] G. E. Moore, “Cramming More Components onto Integrated Circuits,” *Proc. IEEE*, vol. 86, no. 1, pp. 82–85, 1998.

[139] P. J. Wojcik, L. L. Santos, L. Pereira, R. Martins, and E. Fortunato, “Tailoring Nanoscale Properties of Tungsten Oxide for Inkjet Printed Electrochromic Devices,” *Nanoscale*, p. DOI: 10.1039/C4NR05765A, Nov. 2014.

Chapter 2. SOLVOTHERMAL SYNTHESIS OF METAL OXIDE NANOPARTICLES

This chapter aims to summarize the final results related with the solvothermal synthesis of several metal oxide nanoparticles developed during the thesis. Some of the nanostructures were not fully optimized or tested in a specific device, nevertheless, these materials are of great importance for several electrochemical device applications, due to the properties related to the nanostructures, and that can be adapted in the future. As a resume, WO_x is commonly used as electrochromic, sensor and catalyst, V_2O_5 and NiO as electrochromic and capacitor, HfO_2 and MnO_2 as dielectrics, and GIZO and ZTO as semiconductors in thin-film transistors.

The solvothermal synthesis fundaments were previously exposed in section 1.3.3 and all the synthesis were produced using a 23 or 45 mL general purpose acid digestion vessel from Parr (**Figure 1.17**). The X-ray diffraction (XRD) measurements were performed using a PANalytical's X'Pert PRO MRD diffractometer with CuKα radiation and the scanning electron microscopy (SEM) images were taken using a Carl Zeiss AURIGA CrossBeam workstation.

2.1. Tungsten Oxide (WO_x)

As explained before, the synthesis parameters have a great influence on the structure and morphology of the nanoparticles. In the hydrothermal synthesis of tungsten oxide nanoparticles, the parameters studied were the tungsten precursor (peroxopolytungstic acid – PTA and sodium tungstate dehydrate – $Na_2WO_4 \cdot 2H_2O$), the duration of the synthesis and the pH of the precursor solution. According to Pourbaix and solubility diagrams (**Figure 1.26**), the formation of WO_3 is only favorable below pH 2 therefore, the synthesis condition were always kept in this condition by adjusting the amount of HCl in solution. The other parameters, as the precursor concentration, temperature and additives, were kept constant.

2.1.1. Peroxopolytungstic Acid (PTA) Precursor

Peroxopolytungstic acid (PTA) was synthesized based on the procedure previously reported.[1] Tungsten metal monocrystalline powder (W, Aldrich, 0.6–1 mm, 99.9%) was carefully added to a 50 ml mixture (1:1) of distilled water (Millipore) and hydrogen peroxide (H_2O_2, Sigma-Aldrich, 30% by weight). Cooling was employed and the solution was kept slowly stirring for 24 h in a refrigerator to prevent thermal changes due to the strong exothermic nature of dissolution. The excess tungsten powder was then removed by filtration (Roth, 0.45 µm syringe filter) leading to a transparent solution. In order to remove the excess hydrogen peroxide, the solution was dried at 65 °C and washed several times with distilled water. After drying, a water-soluble ($WO_3.xH_2O_2.yH_2O$) orange crystal powder (PTA)[2] was obtained as the final product (**equation 2.1**).

For the hydrothermal synthesis of WO_x, 0.4 g of PTA was dissolved in an acidic aqueous solution. The hydrochloric acid (HCl, 37%, Merck) concentration was modified in each experiment (0, 0.3 and 3 M). The final solution was transferred to a PTFE chamber, set inside a stainless steel autoclave and installed in the oven (L3/11/B170, Nabertherm) at 180 °C for 2, 4 and 6 h (**equation 2.2**). The product of synthesis was collected by centrifugation at 3000 rpm for 2 min (F140, Focus instruments) and washed three times with distilled water (**Figure 2.1**).

$$\mathbf{W + nH_2O_2 \rightarrow WO_3 \cdot xH_2O_2 \cdot yH_2O + 1/2O_2} \qquad \mathbf{(2.1)}$$

$$\mathbf{WO_3 \cdot xH_2O_2 \cdot yH_2O \rightarrow WO_3 \cdot nH_2O + 1/2O_2 \rightarrow WO_3 + nH_2O} \qquad \mathbf{(2.2)}$$

Figure 2.1. Schematic representation of the hydrothermal synthesis process.

These results were published in "**Nanoscale**" journal [3] and it is evident, by analyzing the SEM and XRD results (**Figure 2.2**) that the pH plays a great importance on the morphology and structure of the nanocrystals, respectively. At the same time, the variation from 2 to 6 hours of synthesis has a small influence on the size of the nanoparticles, where the major difference occurs in the synthesis in water (0 M HCl). In this conditions, there are the formation of two polymorphs, *m*-WO_3 nanosheets and *ortho*-$WO_3 \cdot 0.33H_2O$ nanorods. For longer synthesis times, the nanorods tend to "disappear" and after 24 h of synthesis only the monoclinic phase is detected (results not shown). These results substantiates the formation of the hydrate structure as intermediate, as described in **equation 2.2**.

The addition of HCl in the WO_3 hydrothermal synthesis, resulted in 2 different structures, at lower concentration (0.3 M) the *ortho*-$WO_3 \cdot 0.33H_2O$ nanorods and *m*-WO_3 nanoslabs at higher concentration (3 M).

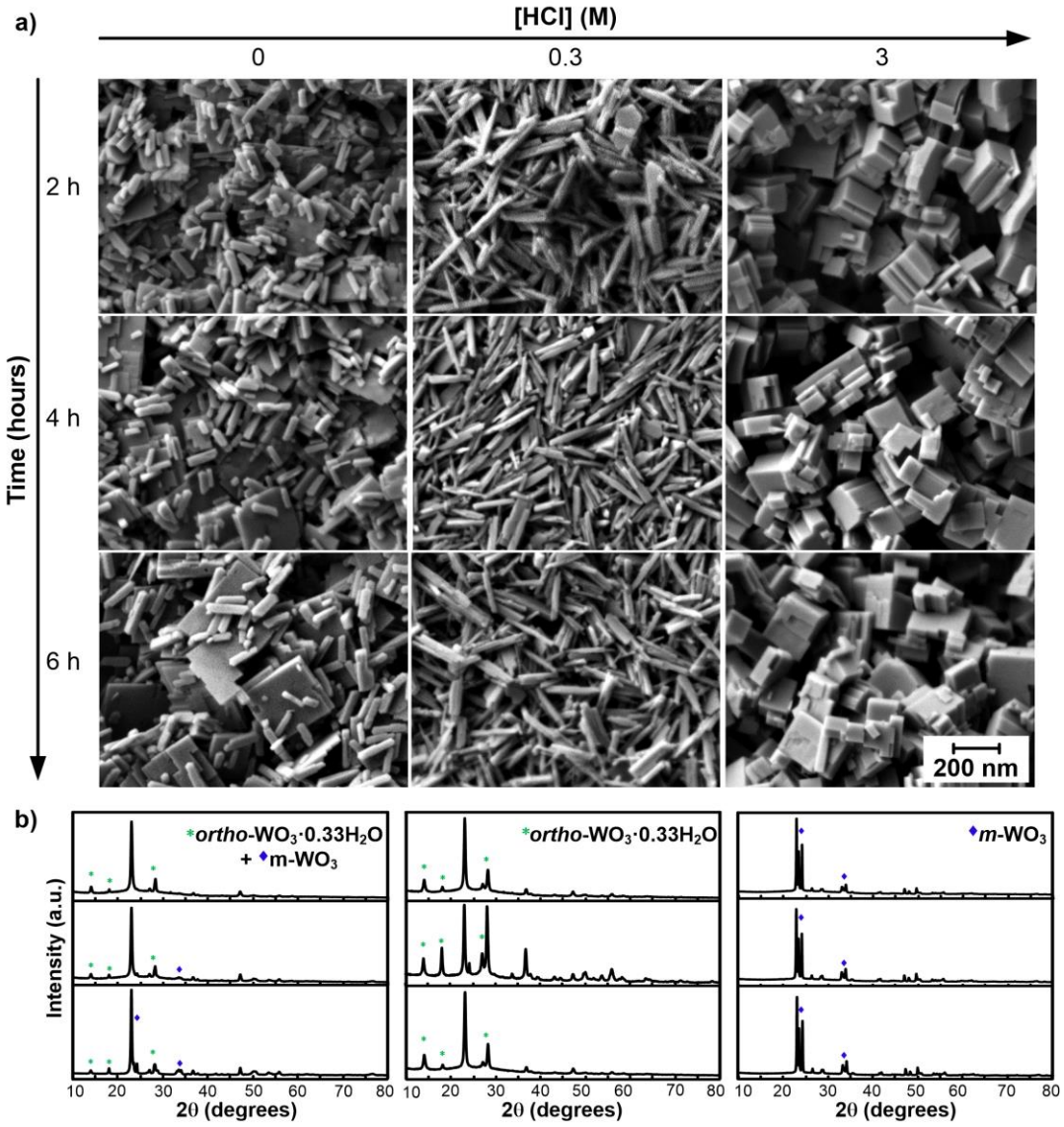

Figure 2.2. a) SEM images and b) XRD diffractograms of the hydrothermal synthesized WO_x nanopowders, using PTA as precursor with three different synthesis acidities and times. Adapted from [3].

2.1.2. Sodium Tungstate Precursor ($Na_2WO_4 \cdot 2H_2O$)

The use of the commercial precursor ($Na_2WO_4 \cdot 2H_2O$) reduced the number of variables during the chemical synthesis of WO_3 but as a comparison the same type of experiments were performed as with PTA as precursor. For that, 0.4 g of sodium tungstate dehydrate ($Na_2WO_4 \cdot 2H_2O$, Fluka, 99%) was dissolved in 8 g of distilled water with 0.15 g of structure-directing agent, sodium chloride (NaCl, Panreac, 99.5%) (**equation 2.3**).[4] The HCl (37%, Merck) concentration was modified in each experiment (0.3, 1.5 and 2.7 M). The final solution was transferred to a PTFE chamber, set inside a stainless steel autoclave and installed in the oven at 180 °C for 2, 4 and 6 h (**equation 2.4**). The product of synthesis was collected by centrifugation at 3000 rpm for 2 min and washed three times with distilled water.

$$\mathbf{Na_2WO_4 \cdot 2H_2O + 2HCl + NaCl \rightarrow H_2WO_4 \cdot 2H_2O + 3NaCl} \quad \textbf{(2.3)}$$

$$\mathbf{H_2WO_4 \cdot nH_2O \rightarrow WO_3 \cdot nH_2O + H_2O \rightarrow WO_3 + nH_2O} \quad \textbf{(2.4)}$$

SEM and XRD results, summarized in **Figure 2.3**, show the influence of pH and time of synthesis and, when comparing with **Figure 2.2**, the effect of the W precursor can also be observed. At higher pH, the grain boundaries of the nanoparticles produced from PTA precursor are better defined and, generally, the sizes are bigger. The fact that PTA is already acid can accelerate the formation of the intermediate ($WO_3 \cdot nH_2O$) and therefore explain the difference in the nanoparticles' morphologies for both synthesis approaches. Nevertheless, the two WO_3 structures (monoclinic and orthorhombic) are produced in both cases. The structure transformation, with the increase of protons in solution (lower pH), from orthorhombic hydrated WO_3 to monoclinic WO_3 occurs with both precursors, and can be verified in the solubility diagram (**Figure 1.26b**) exposed before. This reaction also supports the establishment of the hydrated structure as an intermediate of WO_3 synthesis.

The effect of NaCl as structure-directing agent was not evident, as the structures were not uniform or well-defined, especially at higher pH. Similar conclusions were observed for the microwave assisted hydrothermal synthesis of WO_3, also produced in our group. [5] Only with a different structure-directing agent (sodium sulfate, Na_2SO_4) and at pH 1.8, it was possible to produce the hexagonal structure of WO_3 (**Figure 2.4a**) nanorods. When the solution was kept at pH 0, the monoclinic WO_3 nanosheets were again formed (**Figure 2.4b**). It is believed that the sulfate act as capping agents covering some facets of WO_3 crystal nuclei during particle growth. At pH 1.8 a faster growth rate along c axis is observed, yielding to one dimensional rod-like structures. In the meantime, a certain amount of sodium cations is required as stabilization ions for the hexagonal and triangular tunnels in the formation of *h*-WO_3.

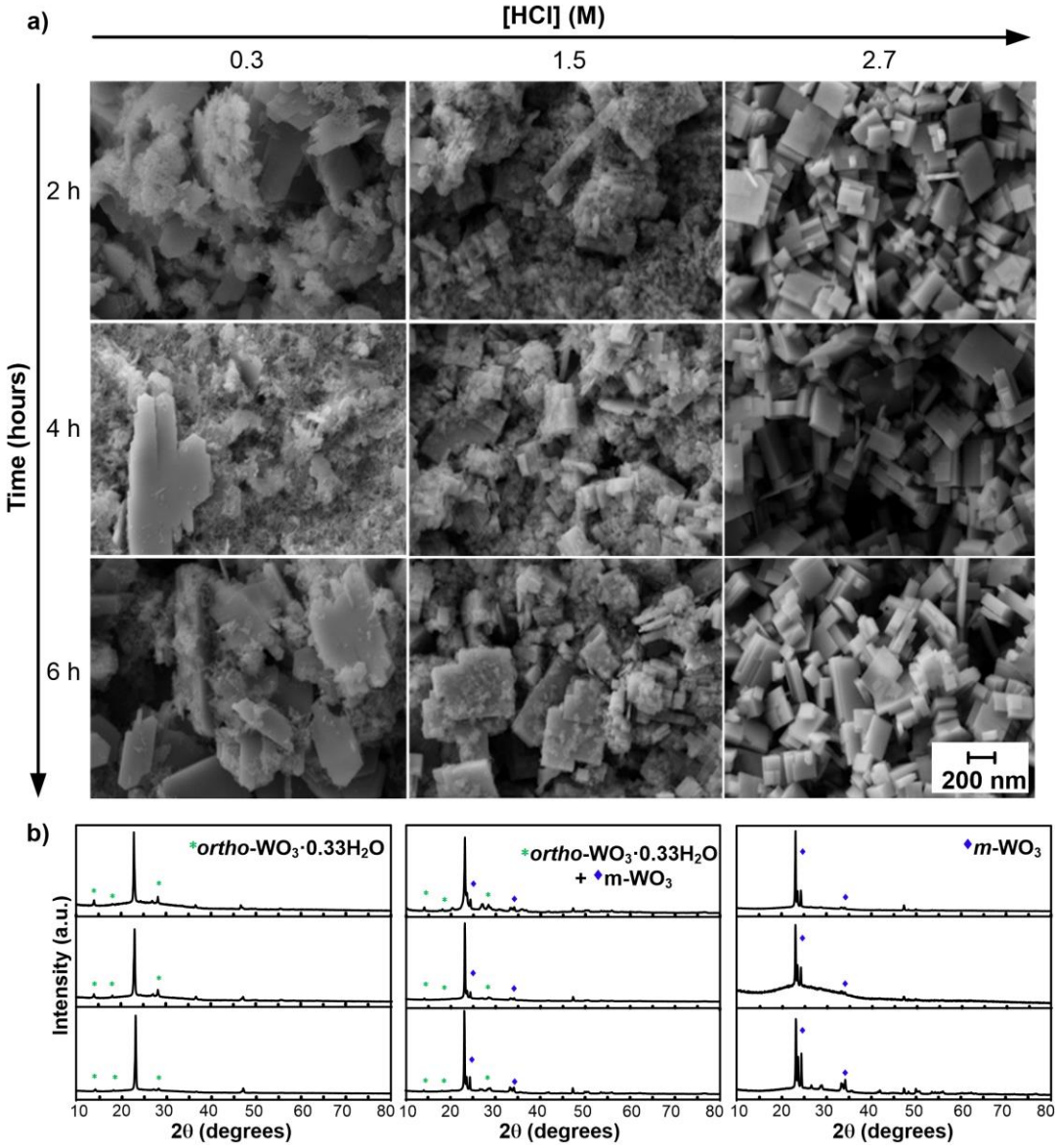

Figure 2.3. a) SEM images and b) XRD diffractograms of the hydrothermal synthesized WO_x nanopowders using Na_2WO_4 as precursor with three different synthesis acidities and times.

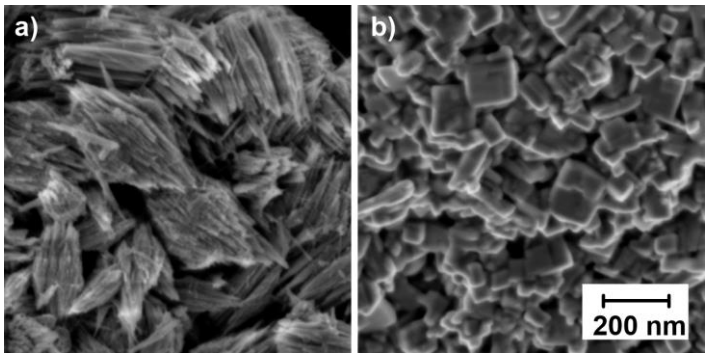

Figure 2.4. SEM images of the microwave assisted hydrothermal synthesized WO_3 nanopowders using Na_2WO_4 as precursor, Na_2SO_4 as structure directing agent, for 1 hour, with constant power of 100 W and at a) pH 1.8 and b) pH 0.

2.2. Vanadium Pentoxide (V_2O_5)

The nanostructured V_2O_5 was synthesized from peroxovanadate, by dissolving 0.1, 0.05 and 0.01 g of V_2O_5 powder (Super Conductor Materials, Inc., 99.995%) in 20 g of a mixture of water with H_2O_2 (1:1). The formation of a clear yellow solution after 10 min indicates the presence of vanadium peroxide in the solution. The **equations 2.5, 2.6** and **2.7** are an attempt to describe the phase transformations during V_2O_5 synthesis, based on the work previously reported by Alonso et al. [6] The solution was transferred to the PTFE chamber, set inside the autoclave and installed in the oven at 180 °C for 3, 24 and 72 h.

$$V_2O_5 + 5H_2O_2 \rightarrow [VO(O_2)_2]^- + [VO(O_2)]^+ + O_2 + 5H_2O \quad (2.5)$$

$$7[VO(O_2)_2]^- + 7[VO(O_2)]^+ + H_2O \rightarrow [H_2V_{10}O_{28}]^{4-} + 4[VO_2]^+ + 10.5O_2 \quad (2.6)$$

$$[H_2V_{10}O_{28}]^{4-} + 4[VO_2]^+ \rightarrow 7V_2O_5{\cdot}nH_2O \quad (2.7)$$

The X-ray diffraction pattern of the xerogels with different precursor concentrations and after submitted to the hydrothermal treatment for different times, (**Figure 2.5**) exhibits in most cases a series of (001) peaks typical of some preferred orientation of a layered structure of monoclinic $V_2O_5{\cdot}nH_2O$, as represented in **Figure 2.6b**.[6] This structure was also confirmed by SEM, as in **Figure 2.6a**. The slight variation of the peaks' angle is associated with the amount of intercalated water in the structure and therefore on the distance between the V_2O_5 layers.

However, in specific experimental conditions (0.05 g of precursor and 72 h of hydrothermal treatment), the orthorhombic structure was also characterized, which corresponds to the phase transformation that occurs due to the removal of the interlayer water of the monoclinic structure. Only increasing the time and/or temperature of the synthesis a pure phase would probably be obtained.

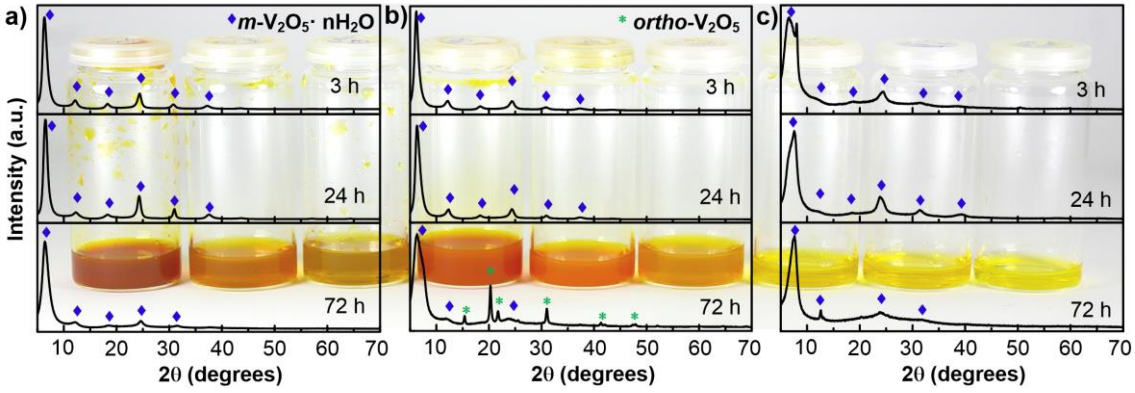

Figure 2.5. XRD diffractograms of the hydrothermal synthesized V_2O_5 xerogels with three different synthesis times and using: a) 0.1 g, b) 0.05 g and c) 0.01 g of V_2O_5 powder as precursor.

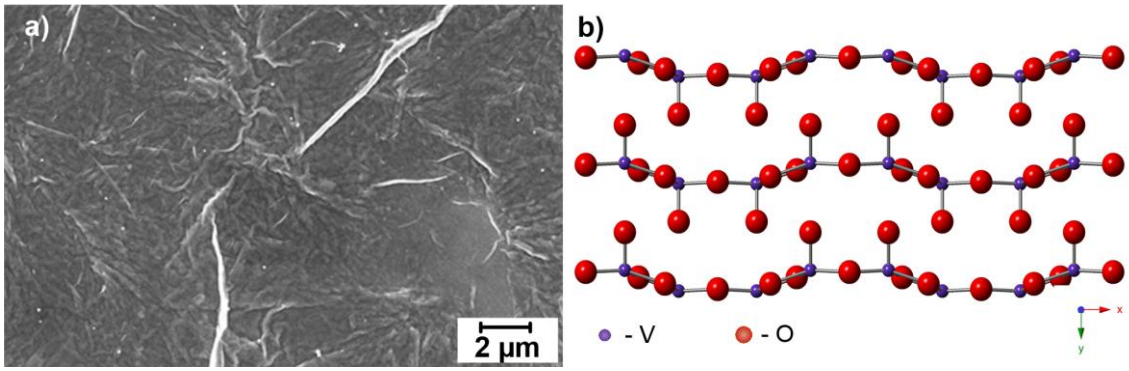

Figure 2.6. a) SEM image of the hydrothermal synthesized V_2O_5 xerogel with 0.05 g of precursor and for 24 h and b) simulation of the *m*-V_2O_5 layered structure, performed in CrystalMaker software.

2.3. Nickel Oxide (NiO_x)

The strategy for the hydrothermal synthesis of NiO was based on two approaches: 1) the sol-gel synthesis of $Ni(OH)_2$ precursor and further dehydration to form the oxide structure (**equations 2.8** and **2.9**); and 2) the decomposition of nickel acetate in hydrochloric acid (**equation 2.10**).[7]

$$NiSO_4 \cdot 6H_2O + 2NaOH \rightarrow Ni(OH)_2 + Na_2SO_4 + 6H_2O \quad (2.8)$$

$$Ni(OH)_2 \rightarrow NiO + H_2O \quad (2.9)$$

$$Ni(CH_3COO)_2 + HCl + H_2O \rightarrow NiO + 2CH_3COOH + HCl \quad (2.10)$$

In the first synthesis, 0.37 g of nickel sulfate hexahydrate ($NiSO_4 \cdot 6H_2O$, Panreac, p.a.) was dissolved in 10 mL of distilled water with 4 g of NaOH (Pronalab, 98.6%). The solution was kept stirring for 1 h and transferred to a PTFE chamber, set inside a stainless steel autoclave and installed in an oven at 200 °C for 24 h.

For the second approach, 0.37 g of nickel acetate tetrahydrate ($Ni(CH_3COO)_2 \cdot 4H_2O$, Sigma-Aldrich, 99%) was dissolved in 10 mL of distilled water and acidified with 4 drops of 3 M HCl (Sigma-Aldrich, 37%). The solution was kept stirring for 1 h at 60 °C, aged for 24 h at room temperature, transferred to the autoclave and installed in an oven at 200 °C for 6 h.

In both methods the powders were characterized as nickel hydroxide ($Ni(OH)_2$) with hexagonal structure and with a vast size dispersion (**Figure 2.7**). For a better control of the morphology of the particles further adjustments on the time and temperature of the hydrothermal synthesis are required.

Since nickel hydroxide has several well-known applications, as electrochromic and capacitor, this material should be further characterized before further attempts to convert the powder to the oxide phase by annealing at high temperatures.[7]

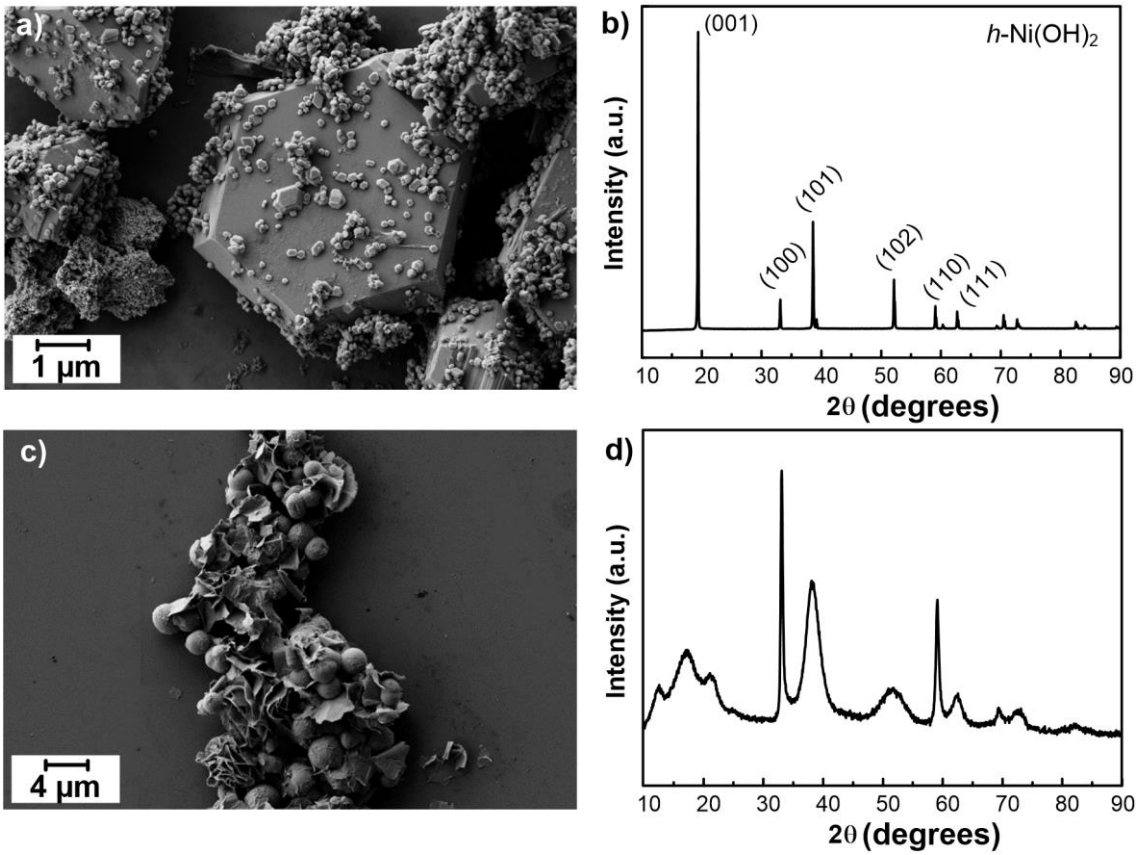

Figure 2.7. SEM image and XRD diffractogram of the hydrothermal synthesized hexagonal $Ni(OH)_2$ powder from: a) and b) $NiSO_4$, and c) and d) $Ni(CH_3COO)_2$ precursors.

2.4. Hafnium Oxide (HfO_2)

The HfO_2 nanoparticles were synthesized using 0.32 g of hafnium tetrachloride ($HfCl_4$, Alfa Aesar, 98%) in 10 mL of distilled water. After, a 0.4 M aqueous solution of NaOH (Pronalab, 98.6%) was added dropwise into the aqueous solution of hafnium tetrachloride and allowed to vigorous stirring, which yielded a white color precipitate of hafnium hydroxide (**equation 2.11**).[8] The dispersion was then transferred to a PTFE chamber, set inside a stainless steel autoclave and installed in an oven at 180 °C for 6 hours. The product of synthesis was collected by centrifugation at 4000 rpm for 5 min and washed two times with water (**equation 2.12**).

$$\mathbf{HfCl_4 + 4NaOH \rightarrow Hf(OH)_4 + 4NaCl} \qquad \mathbf{(2.11)}$$

$$\mathbf{Hf(OH)_4 \rightarrow HfO_2 + 2H_2O} \qquad \mathbf{(2.12)}$$

The nanopowder characterization (**Figure 2.8**) was in conformity with the reported results of HfO_2 nanoparticles,[8] and the nanoparticles shows a very uniform size distribution, important for deposition purposes.

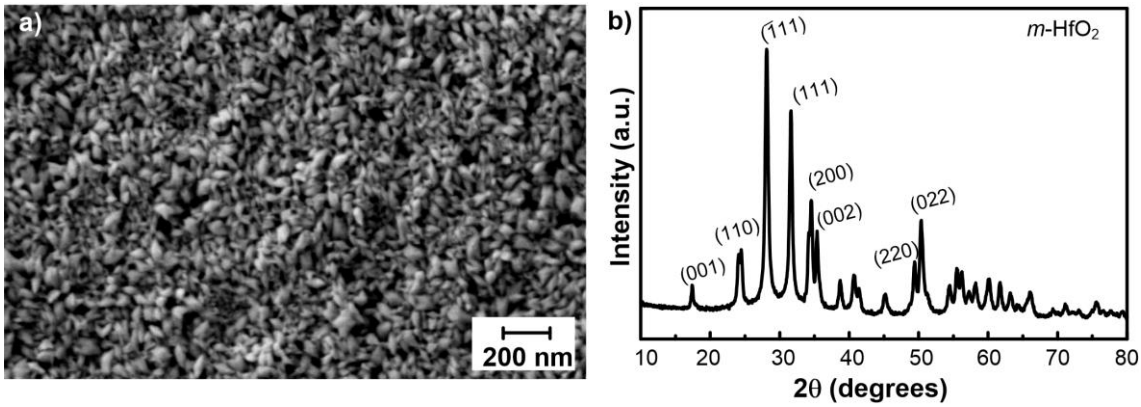

Figure 2.8. a) SEM image and b) XRD diffractogram of the hydrothermal synthesized monoclinic HfO_2 nanopowder.

2.5. Manganese Oxide (MnO_2)

In a typical process, 0.19 g of potassium permanganate ($KMnO_4$, Scharlau, 99%) and 0.32 g of manganese sulfate hydrate ($MnSO_4 \cdot H_2O$, Sigma-Aldrich, 99%) were dissolved in 10 ml of distilled water and magnetically stirred to form a homogeneous solution. Then the solution was transferred into a PTFE chamber, set in the stainless steel autoclave and maintained at 180 °C for 24 h (**Equation 2.13**). The resulting solid products were centrifuged and rinsed several times with de-ionized water and absolute ethanol, and finally dried at 100 °C for 8 h. The final black powder was collected for characterization.[9]

$$\mathbf{2KMnO_4 + MnSO_4 \cdot H_2O \rightarrow 3MnO_2 + K_2SO_4 + H_2O + O_2} \qquad \mathbf{(2.13)}$$

The nanopowder consisted in tetragonal α-MnO_2 nanowires (**Figure 2.9**) with approximately 50 nm of diameter and 2 µm long. The high surface to volume ratio (S:V) of these structures make this material as a promising candidate for electrochemical applications.

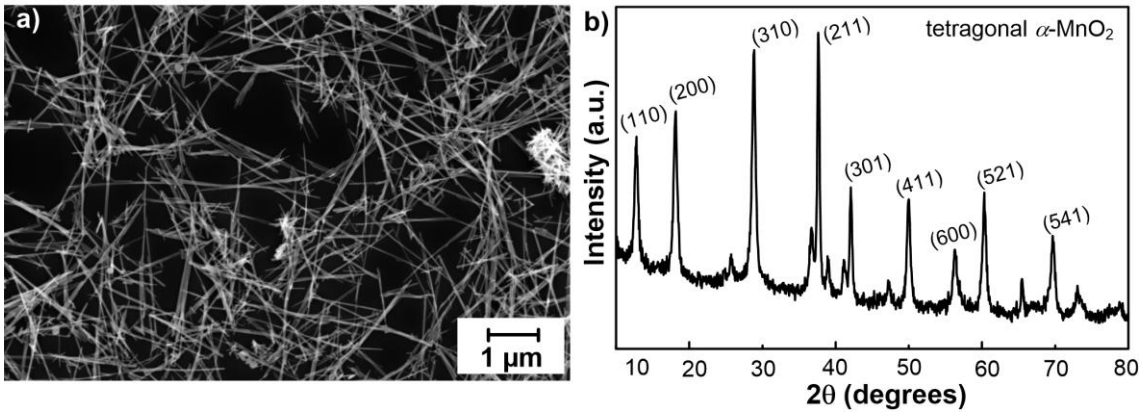

Figure 2.9. a) SEM image and b) XRD diffractogram of the hydrothermal synthesized tetragonal α-MnO_2 nanowires.

2.6. Gallium-Indium-Zinc Oxide (GIZO)

Gallium nitrate hydrate ($Ga(NO_3)_3 \cdot xH_2O$, Sigma-Aldrich, 99.9 %), indium acetate ($In(CH_3COO)_3$, Sigma-Aldrich, 99.99%) and zinc acetate ($Zn(CH_3COO)_2 \cdot 2H_2O$, Sigma-Aldrich, 99.5 %) were dissolved in 2-methoxythanol (6 mL, Fluka, 99 %) with a molar ratio of 3:6:2, respectively, and left stirring at 50 ºC for 1 h with ethanolamine (0.2 mL, Fluka, 98 %).[10] The final solution was transferred to a PTFE chamber, set inside a stainless steel autoclave and installed in an oven at 180 °C for 24 hours. The product of synthesis was collected by centrifugation at 4000 rpm for 5 min and washed with water.

$$\mathbf{2Ga(NO_3)_3 \cdot xH_2O + 3H_2O \rightarrow Ga_2O_3 + 6HNO_3 + xH_2O} \quad \textbf{(2.14)}$$

$$\mathbf{2In(CH_3COO)_3 + 3H_2O \rightarrow In_2O_3 + 6CH_3COOH} \quad \textbf{(2.15)}$$

$$\mathbf{Zn(CH_3COO)_2 + H_2O \rightarrow ZnO + 2CH_3COOH} \quad \textbf{(2.16)}$$

The X-ray diffraction (XRD) measurements of the as-synthesized GIZO nanopowder, shown in **Figure 2.10b**, is consistent with the reduced-size nanoparticles observed in the magnified SEM image (**Figure 2.10a**), due to the broad peak at 31.88 °. Nevertheless, the phase determination turned to be inconclusive since the peak could be attributed to the presence of a nanocrystalline phase of *c*-In_2O_3 or *h*-$InGaZn_2O_5$. So, further annealing at 900 ºC was required to distinguish the ternary mixture of oxides (Ga_2O_3-In_2O_3-ZnO).

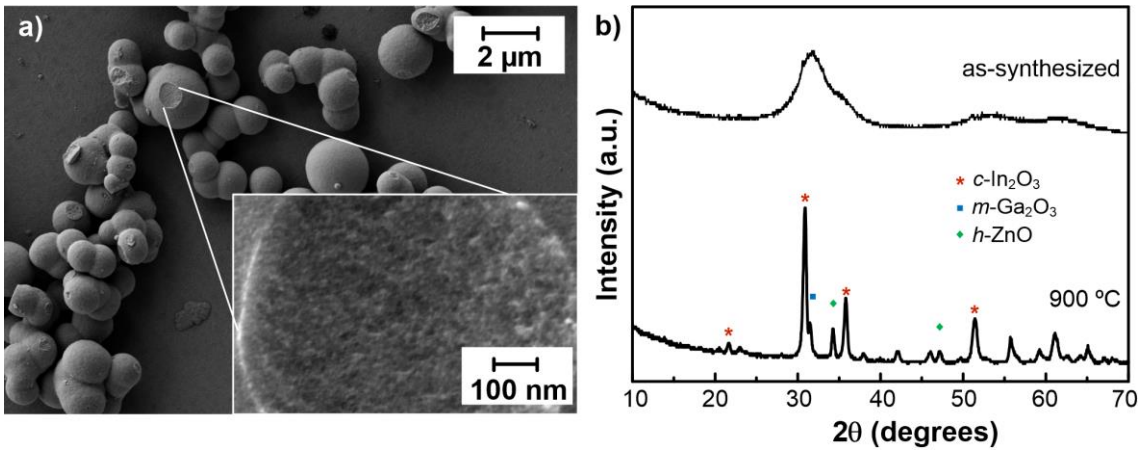

Figure 2.10. a) SEM image and b) XRD diffractograms of the hydrothermal synthesized GIZO nanopowder and after annealing at 900 °C for 1 h.

2.7. Zinc-Tin Oxide (ZTO)

The synthesis of ZTO was performed with 0.34 g of zinc chloride ($ZnCl_2$, Merck, 98%) and 0.44 g of tin tetrachloride ($SnCl_4 \cdot 5H_2O$, Riedel-deHean 98%) as precursors, dissolved in 10 mL of distilled water. After, sodium carbonate (Na_2CO_3, Merck, 99.9%) solution (0.33 g in 5 mL of water) was added dropwise to the mixture under magnetic stirring for 15 min and transferred to a PTFE

chamber, set inside a stainless steel autoclave and installed in the oven at 180 °C for 48 h (**equation 2.17**). The product of synthesis was collected by centrifugation at 4000 rpm for 2 min and washed three times with water.[11]

$$2ZnCl_2 + SnCl_4 + 4Na_2CO_3 + H_2O \rightarrow Zn_2SnO_4 + 8NaCl + 4CO_2 \quad (2.17)$$

The powder resulted in a pure phase of cubic Zn_2SnO_4 nanoparticles (**Figure 2.11**). The influence of precursors and time of synthesis was also analyzed but generally the synthesis led to the formation of $ZnSn(OH)_6$ (an intermediate of the reaction) and/or $ZnSnO_3$. These experimental conditions allowed the formation of a pure Zn_2SnO_4 phase, but with a large size distribution.

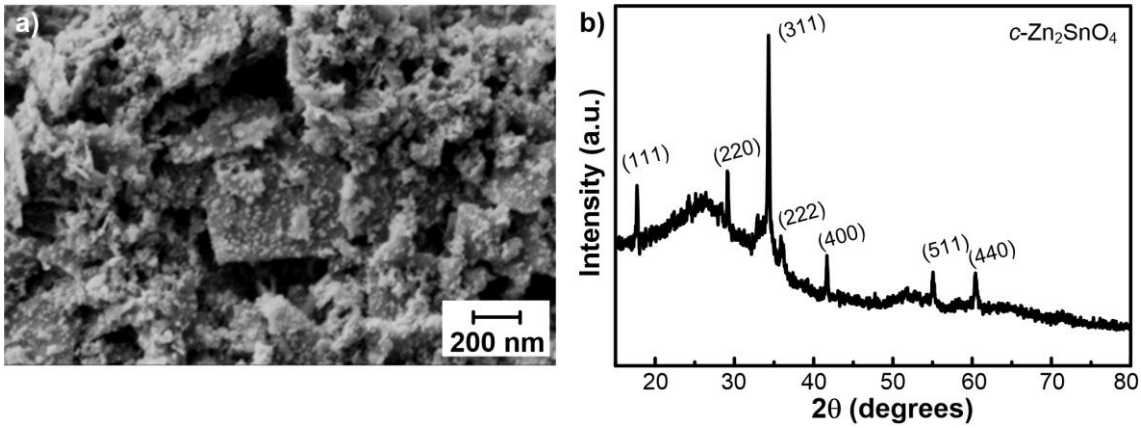

Figure 2.11. a) SEM image and b) XRD diffractogram of the hydrothermal synthesized ZTO nanopowder.

2.8. References

[1] K. Yamanaka, H. Oakamoto, H. Kidou, and T. Kudo, “Peroxotungstic Acid Coated Films for Electrochromic Display Devices,” *Jpn. J. Appl. Phys.*, vol. 25, pp. 1420–1426, 1986.

[2] B. Pecquenard, S. Castro-Garcia, J. Livage, P. Y. Zavalij, M. S. Whittingham, and R. Thouvenot, “Structure of Hydrated Tungsten Peroxides $[WO_2(O_2)H_2O]\cdot nH_2O$,” *Chem. Mater.*, vol. 10, no. 7, pp. 1882–1888, Jul. 1998.

[3] P. J. Wojcik, L. L. Santos, L. Pereira, R. Martins, and E. Fortunato, “Tailoring Nanoscale Properties of Tungsten Oxide for Inkjet Printed Electrochromic Devices,” *Nanoscale*, p. DOI: 10.1039/C4NR05765A, Nov. 2014.

[4] J. Wang, E. Khoo, P. S. Lee, and J. Ma, “Synthesis, Assembly, and Electrochromic Properties of Uniform Crystalline WO_3 Nanorods,” *J. Phys. Chem. C*, vol. 112, no. 37, pp. 14306–14312, Sep. 2008.

[5] A. C. Marques, L. Santos, M. N. Costa, J. M. Dantas, P. Duarte, A. Gonçalves, R. Martins, C. A. Salgueiro, and E. Fortunato, “Office Paper Platform for Bioelectrochromic Detection of Electrochemically Active Bacteria using Tungsten Trioxide Nanoprobes,” *Sci. Rep.*, vol. Accepted, 2015.

[6] a) W. Avansi Jr., C. Ribeiro, E. R. Leite, and V. R. Mastelaro, “Vanadium Pentoxide Nanostructures : An Effective Control of Morphology and Crystal Structure in Hydrothermal Conditions,” *Cryst. Growth Des.*, vol. 9, no. 8, pp. 3626–3631, 2009; b) B. Alonso, J. Livage, “Synthesis of Vanadium Oxide Gels from Peroxovanadic Acid Solutions: A 51V NMR Study”, *Journal of Solid State Chemistry*, vol. 148, no. 1, pp. 16-19, 1999

[7] a) I. Tsai, Y. Wang, and C. Wan, “Effect of synthesis method on the properties of $Ni(OH)_2$ for Ni/MH batteries,” vol. 106, pp. 99–106, 2001; b) K.K. Purushothaman, S. Joseph Antony, G. Muralidharan, “Optical, structural and electrochromic properties of nickel oxide films produced by sol–gel technique”, vol. 85, no. 5, pp. 978-984, 2011.

[8] A. Ramadoss, K. Krishnamoorthy, and S. J. Kim, “Facile synthesis of hafnium oxide nanoparticles via precipitation method,” *Mater. Lett.*, vol. 75, pp. 215–217, May 2012.

[9] H. Guan, Y. Wang, G. Chen, and J. Zhu, “Frequency and temperature effects on dielectric and electrical characteristics of α-MnO_2 nanorods,” *Powder Technol.*, vol. 224, pp. 356–359, Jul. 2012.

[10] P. K. Nayak, T. Busani, E. Elamurugu, P. Barquinha, R. Martins, Y. Hong, and E. Fortunato, “Zinc concentration dependence study of solution processed amorphous indium gallium zinc oxide thin film transistors using high-k dielectric,” *Appl. Phys. Lett.*, vol. 97, no. 18, p. 183504, 2010.

[11] A. Annamalai, D. Carvalho, K. C. Wilson, and M. Lee, “Properties of hydrothermally synthesized Zn_2SnO_4 nanoparticles using Na_2CO_3 as a novel mineralizer,” *Mater. Charact.*, vol. 61, no. 9, pp. 873–881, 2010.

Chapter 3. WO_3 AS ELECTROCHROMIC MATERIAL

The contents of **Chapter 3** were adapted from the publication:

"L. Santos, P. Wojcik, J. V. Pinto, E. Elangovan, J. Viegas, L. Pereira, R. Martins, E. Fortunato, *Structure and morphologic influence of WO_3 nanoparticles on the electrochromic performance of dual-phase a-WO_3/WO_3 inkjet printed films*, **Advanced Electronic Materials** 1 (1-2), **2015**, DOI: 10.1002/aelm.201400002".

At the same time, this publication appears as the front cover of the journal, as shown in **Figure A 1** in the Appendix.

3.1. Abstract

This work reports the optimization of tungsten trioxide (WO_3) nanoparticles produced via hydrothermal synthesis for application in electrochromic (EC) devices. The structure and morphology of the nanoparticles are controlled by changing the acidity of the aqueous solvent added to the sol-gel precursor (peroxopolytungstic acid) during synthesis. Orthorhombic hydrated WO_3 nanorods or monoclinic WO_3 nanoslabs are obtained when HCl is added, while synthesis only in aqueous medium results in a mixture of both types of polymorphs. Dual-phase thin films are processed by inkjet printing deposition of the nanoparticles in flexible ITO PET substrate followed by the deposition of the precursor solution. When compared with purely amorphous tungsten oxide films, the dual phase ones present higher optical densities and improved capacity, and cyclability stability. The best results, obtained for orthorhombic hydrated nanoparticles (*ortho*-$WO_3 \cdot 0.33H_2O$) are due to its high surface area and improved conductivity. Additionally, the ex situ XRD lithiation studies show evidences of a higher distortion of the monoclinic when compared with the orthorhombic crystallographic structure, which contribute to the inferior EC performance. These results validates the use of inkjet printing deposition with low processing temperatures for EC dual-phase thin films containing optimized nanoparticles which are compatible with low-cost substrates.

3.2. Introduction

Tungsten oxide (WO_x) is one of the most studied electrochromic (EC) inorganic materials due to its multiple oxidation states, high coloration efficiency and good cyclability stability.[1–3] The most accepted general reaction that describes the EC mechanism of the WO_3 with the associated coloration change can be written as:

$$\mathbf{WO_x\ (transparent) + y}M^+ \mathbf{+ ye^-} \leftrightarrow M_y\mathbf{WO_x\ (blue)} \qquad (3.1)$$

Where M^+ represents a cation such as H^+, Li^+, K^+ and so forth.[4] When an electron is injected into the material, a cation from the electrolyte will compensate the charge insertion, generating in this way a tungsten bronze (M_yWO_x) which corresponds to the colored state. In the opposite way, when a reversible voltage is applied, the inverse process takes place and the film gets to the former state in the bleached condition. The fully mechanism is still under discussion and several theories have been presented for both amorphous and crystalline phases.[1] The most accepted theory is explained by small polaron transitions (formation of W^{5+} sites) for amorphous films and Drude-like free electron scattering for crystalline films. The major difference between these two mechanisms, for amorphous and crystalline WOx, is the electron localization or delocalization, respectively.[5–7]

Recent developments of EC films have been focused on nanostructured materials. The advantages compared with the bulk material are not only the spatial confinement but also the large fraction of surface atoms, high surface energy, strong surface adsorption and increased surface to volume (S:V) ratio.[8–10] Many methods, from physical to chemical processes, have been developed to deposit WO_x thin films while nanostructured WO_x thin films were mainly produced by temperature annealing,[11] hot wire chemical vapor deposition,[12] sol-gel,[13] sputter-

ing,[14] precipitation,[15] electrodeposition[16,17] or hydrothermal methods.[18–20] Hydrothermal synthesis was chosen in this study to produce the WO_x nanoparticles since it presents several advantages regarding the better control on the shape and size of the structures, low synthesis temperatures and good homogeneity of the nanoparticles, which are important characteristics for large scale applications. [19,21]

Electronic devices processed by printing techniques of solutions became a relevant topic in the last decade due the process simplicity and cost effectiveness. [22] So far, organic semiconductors have been a common and obvious choice but the toxicity of some solvents and the need of "green" technologies have demanded for alternatives. The authors consider that the usage of inorganic semiconductors in water or alcohol based inks can be one possible approach.

Dual-phase inkjet printed thin films of tungsten oxide (*a*-WO_3/WO_x) have been reported earlier by our group,[11] nevertheless remained the need to further understand the influence of the structure and morphology of the nanoparticles in the EC performance of this kind of films. In this study, we obtained different WO_x nanostructures by hydrothermal synthesis from a sol-gel precursor (peroxopolytungstic acid) in aqueous acidified solution. The deposition by inkjet printing of the dual-phase thin films directly on flexible ITO PET commercial substrates was processed accordingly in order to increase the proportion of nanoparticles and verify how this determines the EC performance of dual-phase films in comparison with the purely amorphous films.

3.3. Results and Discussion

3.3.1. Nanoparticles Characterization

The crystallographic structure of the synthesized WO_3 nanoparticles was analyzed by XRD. All the diffraction peaks observed in **Figure 3.1a** can be indexed to the reference patterns from the International Centre for Diffraction Data (ICDD), namely orthorhombic hydrated WO_3 (*ortho*-$WO_3 \cdot 0.33H_2O$) with ICDD No. 01-072-0199 and monoclinic WO_3 (*m*-WO_3) with ICDD No. 43-1035. The influence of the acidity of the solvent was confirmed with the conversion from orthorhombic to monoclinic structure with the increase of proton concentration, which disturbs the PTA ($WO_3 \cdot xH_2O_2 \cdot yH_2O$) equilibrium and alters the kinetics of nucleation and growing of the nanoparticles during hydrothermal synthesis. Even if not fully understood, it is believed that the structure of PTA and the amount of the chelating peroxo ligands in the precursor, influences the structure of the nanoparticles.[23,24] At the same time, according to the crystal nucleation and growth theory, the supersaturation is the driven force of crystals nucleation and at a lower pH (higher concentration of H^+), a great number of WO_3 nuclei are quickly generated; the supersaturation reaches a low level and subsequently the nanoparticles grow at a slow rate.[25] So, depending on the supersaturation level, the growth of the nanoparticles can also occur in different directions. Other possible explanation, is related with the chloride ion that can act as structure directing agent and that indirectly, by the increase of the HCl concentration, will cap some of the facets of the crystals thus resulting in a different growth direction of the nanoparticles.[26]

The crystallographic structures of both polymorphs are represented in **Figure 3.1b**. Monoclinic structure is composed of WO_6 octahedral connected by covalent bonds in every corner, forming a stacked layer structure. In the orthorhombic hydrated polymorph some of the octahedral are composed of two terminals, one W=O double bond and one W-H_2O long bond ($WO_5(OH_2)$) which, by one hand, weaken the stacking of the layers in the c (or z) direction and by other hand, results in a less compact structure that beneficiates the ion intercalation/ deintercalation during the EC reaction (**Equation 3.1**). [18,23]

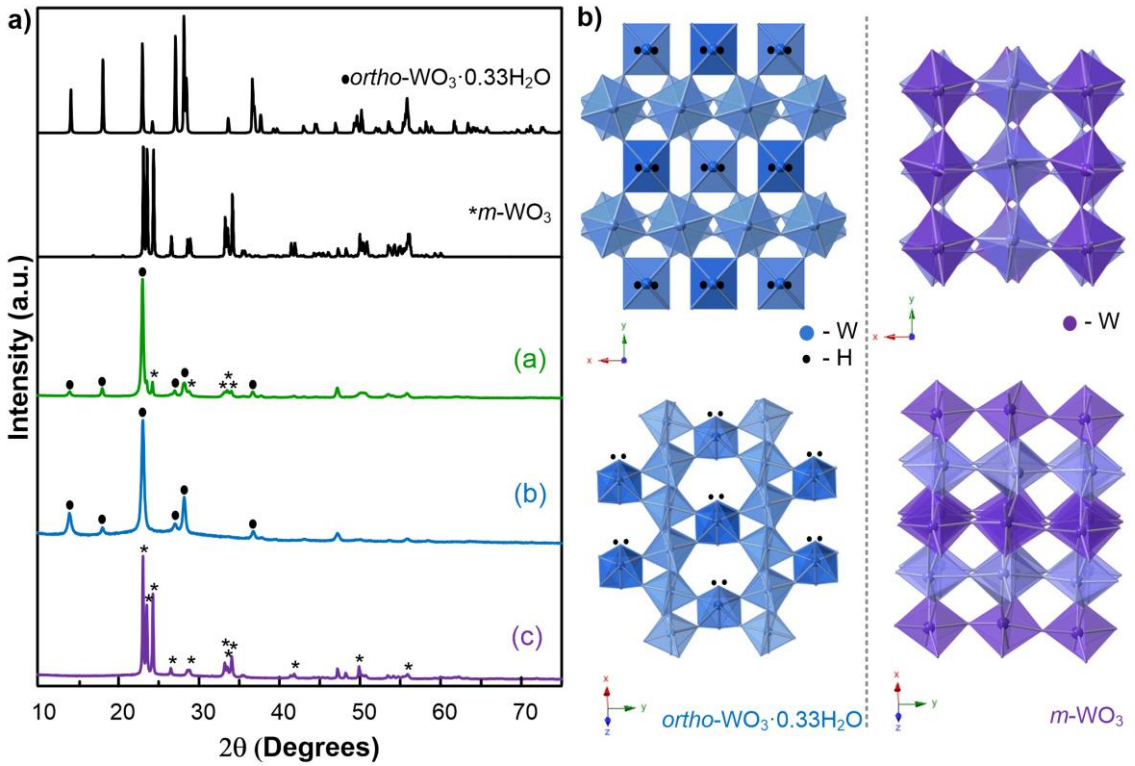

Figure 3.1. a) XRD diffractograms of the nanopowders synthesized n: (a) H_2O; (b) 0.3 M HCl and (c) 3 M HCl. Reference diffractograms for *ortho*-WO_3·0.33H_2O (ICDD: 01-072-0199) and *m*-WO_3 (ICDD: 43-1035) have been placed above; b) Graphic representation of the crystallographic structure of the synthesized polymorphs (*m*-WO_3 and *ortho*-WO_3.0.33H_2O) obtained using Crystal Maker® software.

The morphology of the nanoparticles was studied by SEM and TEM techniques. The distance between the center of 2 successive dots (lattice spacing), which was calculated as an average among 10 subsequent dots, is indicated on the corresponding TEM images. The mixture of nanorods and nanoslabs observed on the SEM images in **Figure 3.2a**, for the nanopowder synthesized in water, is in accordance with the presence of two polymorphs detected by XRD. The TEM images captured at low magnification (not shown here) show similar microstructures as observed in SEM. In this nanopowder the lattice was measured in both kind of nanoparticles and a spacing of 0.39 nm was determined for the nanorods, corresponding to the (002) plane of *ortho*-WO_3·0.33H_2O. The 0.30 nm lattice spacing determined for the nanoslabs correspond to the (112) plane of the *m*-WO_3.

In **Figure 3.2b** the lattice spacing of 0.38 nm of the nanorods can be attributed to the (002) plane of the *ortho*-$WO_3.0.33H_2O$, which is in accordance with the predominant peak observed in XRD. Finally, the regular shaped nanoslabs obtained in **Figure 3.2c** are only observed for the synthesis with high proton concentration (3 M HCl). The measured lattice spacing of 0.39 nm corresponds to the (002) plane of the *m*-WO_3.

Energy Dispersive X-ray Spectroscopy (EDS) of all nanoparticles detected, as expected, tungsten and oxygen elements (the mapping is also shown in the **Figure 3.2**) and both elements were evenly distributed in the full area of the nanoparticles.

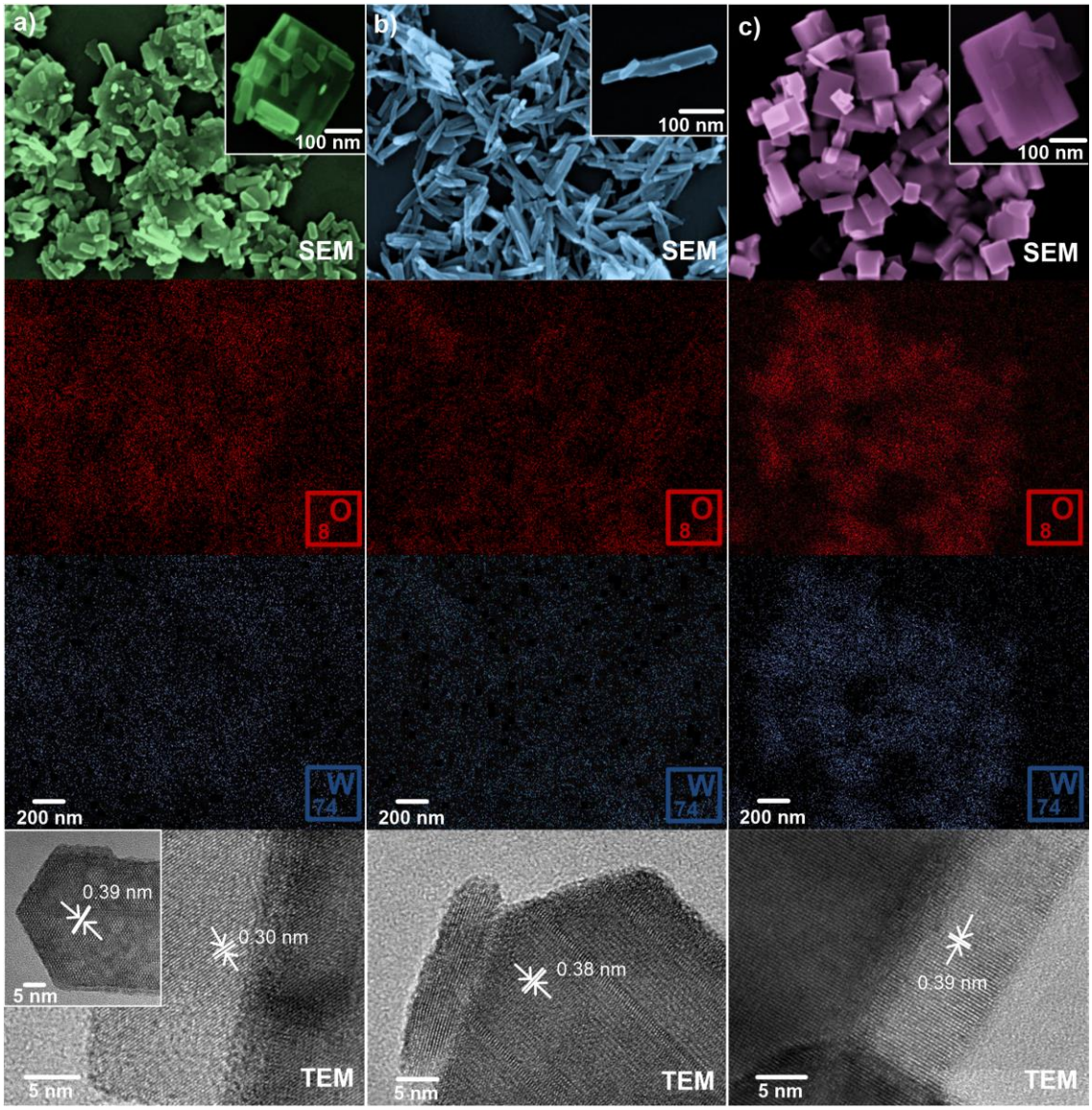

Figure 3.2. SEM images, EDS element distribution and TEM analysis of nanopowders obtained via hydrothermal synthesis performed in: a) H_2O; b) 0.3 M HCl and c) 3 M HCl. SEM images are false colored for a better visualization of the nanostructures.

Thermogravimetric (TG) studies were performed on synthesized powders in order to determine the coordinated water content and confirm the crystallographic structure. TG spectra presented in **Figure 3.3** shows distinct responses for each nanopowder. The total weight loss observed up to 600 °C for nanoparticles produced in non-acidified, 0.3 M HCl and 3 M HCl precursor was 2.2 wt% (*m*-WO_3 + *ortho*-$WO_3 \cdot 0.33H_2O$), 4.0 wt% (*ortho*-$WO_3 \cdot 0.33H_2O$) and 0.4 wt% (*m*-WO_3), respectively. The weight loss of *ortho*-$WO_3 \cdot 0.33H_2O$ is almost double than the theoretically calculated value of 2.58 % for structurally coordinated water. This discrepancy suggests the influence of physisorbed water on the total weight loss, which can be confirmed by weight loss observation even below 100 °C, while coordinated water continuously decrease up to 350 ºC. The weight loss of 2.2 % observed for the nanoparticles produced in non-acidified media, can be attributed to the existence of a mixture with 54 % of *ortho*-$WO_3 \cdot 0.33H_2O$ and 46 % of *m*-WO_3.

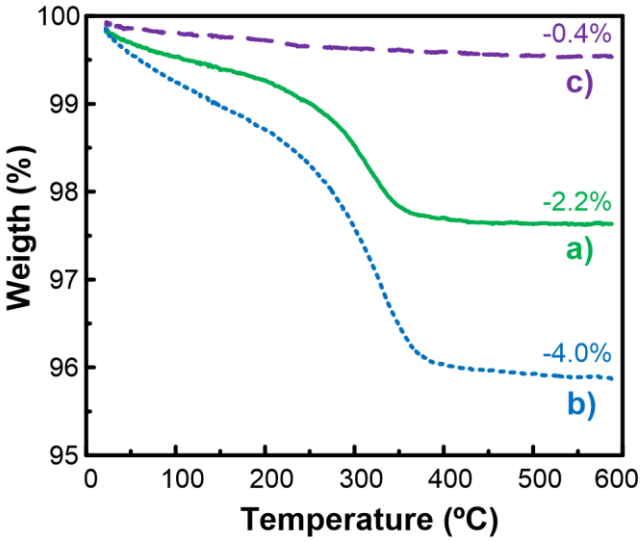

Figure 3.3. TG of nanopowders obtained via hydrothermal synthesis performed from in: a) H_2O; b) 0.3 M HCl and c) 3 M HCl

Brunauer–Emmett–Teller (BET) surface areas are consistent with the S:V ratio of the nanostructures verified in the SEM images presented in **Figure 3.2** and **Table 3.1**. This parameter is an important indicator since the increase of the S:V ratio means high active surface area and high number of reaction sites where redox reaction can occur. [27] The sample with single nanorods has the highest active surface area of 37.8 $m^2 g^{-1}$ being four times higher than the nanoslabs (8.7 $m^2 g^{-1}$). Worth mentioning that from the analysis of the isotherm plot for the three samples it was not detected any microporosity since the resulting isotherms were of type III, typical of solid materials with no porosity. Surface areas between 2 and 45 $m^2 g^{-1}$ have been reported for small *m*-WO_3 nanoparticles synthesized with different organic solvents [28] and of 33.8 $m^2 g^{-1}$ for *h*-WO_3 nanowires. [29]

Comparing the hydrodynamic diameters of the nanoparticles dispersed in water (calculated by DLS) with the nanoparticles length sizes (verified on the SEM images) one can assume that the nanoparticles are not physically agglomerated which also validates their usage for inkjet printing deposition. The nozzle of the Canon printer, used in this work, has a diameter of 9 µm and even if some authors refer to the need of using nanoparticles with a size ten times smaller than

the nozzle diameter, this relationship is not valid for every ink. The percentage of the solid content and the stability of the ink (agglomeration) also influences the way the nanoparticles behave during deposition. [30] Taking into account that in this work no nozzles were clogged, we can confirm that these inks are suitable for inkjet printing deposition.

Table 3.1. Comparison of nanoparticles sizes from SEM images and DLS hydrodynamic diameter, BET surface areas and fitted bulk conductivity calculated from Nyquist plots of WO_3 pellets.

Nanoparticles	BET surface area ($m^2 \cdot g^{-1}$)	SEM length sizes (nm)	DLS diameter (nm)	Conductivity (S/ cm)
***ortho*-$WO_3 \cdot 0.33H_2O$ + *m*-WO_3**	19.8 ± 0.05	116 ± 48; 223 ± 85	192.5 ± 75	6×10^{-8}
***ortho*-$WO_3 \cdot 0.33H_2O$**	37.8 ± 0.13	187 ± 46	138.0 ± 41	4×10^{-6}
***m*-WO_3**	8.7 ± 0.08	153 ± 68	140.1 ± 60	5×10^{-7}

Another important indicator is the conductivity of the nanopowders, since this affects its electron transfer ability during the redox reaction. Electrochemical impedance spectroscopy (EIS) was performed in cylindrical pellets, made with pressed nanopowders, between two stainless steel electrodes, in the range of 1 and 10^5 Hz. From the impedance modulus (Bode plot) in **Figure 3.4a**, it is clear that *ortho*-$WO_3 \cdot 0.33H_2O$ nanorods have lower impedance values as consequence of their hydrate form and high surface area. This effect was already demonstrated in previous studies and can be explained by the incorporated terminal bonds (W=O and W-H_2O) at the structure. [31] Nyquist plots, real versus imaginary impedance (**Figure 3.4b-d**) show a semicircle in the high frequency region and a straight line at low frequencies. The equivalent electric circuit represented inside **Figure 3.4b** considers the bulk impedance related to the intrinsic material properties, represented by the ZARC element (CPE and R in parallel) and the contact impedance due to the electrode-sample interface. This last contribution is represented by a constant phase element (CPE) in series with the first part of the circuit, similar to an empirical approach also used in the work of Orsini et al. [32,33] The good approximation to the experimental results, especially in the high frequencies region, makes us conclude that this model is valid for calculating the conductivity of these samples. Conductivity was calculated from the resistance (*R*) fitting obtained by EIS and using **Equation 3.2**:

$$\sigma = l/(R \times A) \qquad (3.2)$$

The thickness (*l*) and area (*A*) of the pellets were also considered for this calculation. In our work, the conductivity values (**Table 3.1**) are lower than the reported in the literature which can be due to the lack of an additional conductive layer between the pellet and the electrode or to a denser structure of the pellets. [33][34] Nevertheless, we are still able to compare the electron transfer ability between the three nanostructures. Due to the structure particularities of the *ortho*-$WO_3 \cdot 0.33H_2O$ nanorods (mentioned before) the conductivity is higher than the *m*-WO_3 nanoslabs by one order of magnitude and by two orders of magnitude when compared with the nanopowder consisting in a mixture of the two polymorphs. This last difference is a clear evidence that the conductivity is not only influenced by the structure of the nanoparticles but also by its morphology.

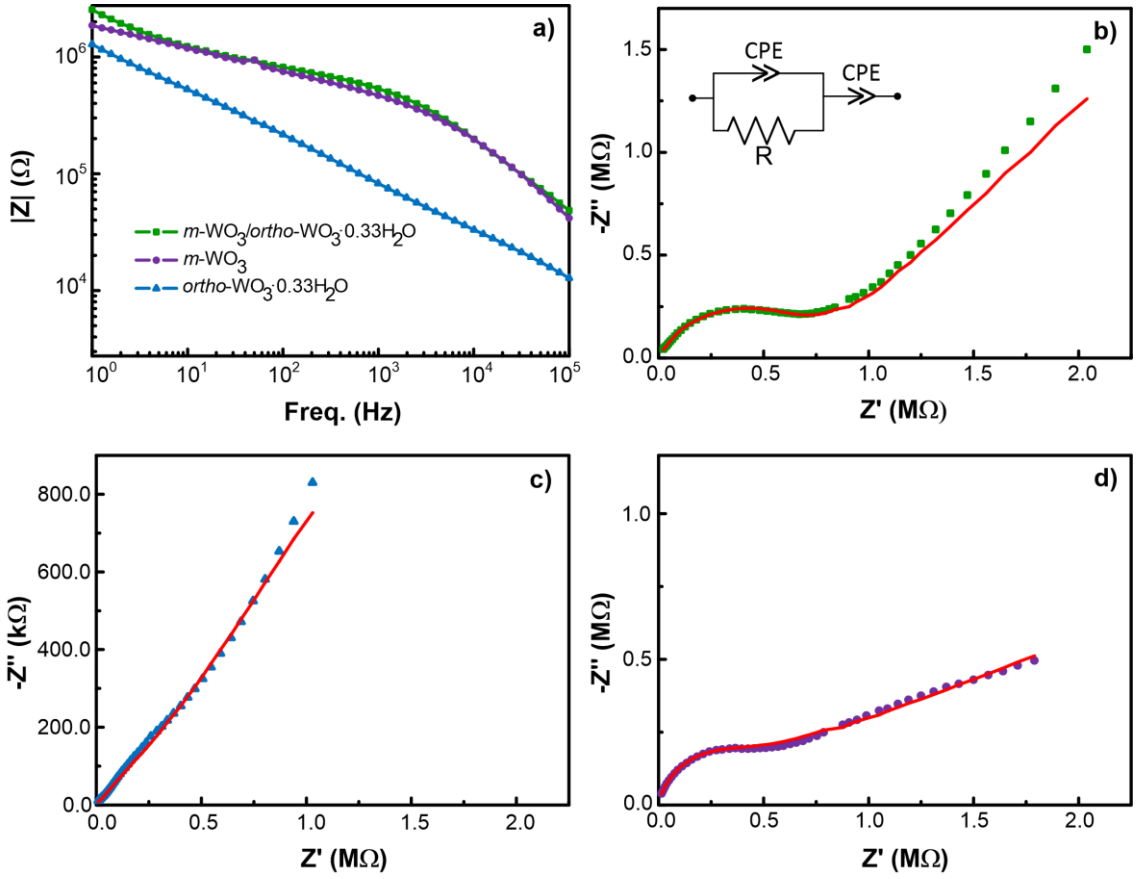

Figure 3.4. a) Impedance plot for the full frequency range. Nyquist plot of WO_x nanopowders performed at room temperature and their theoretical fit (red line) to a CPE circuit (inset) for: b) m-WO_3 + *ortho*-WO_3.0.33H_2O; c) *ortho*-WO_3.0.33H_2O; d) *m*-WO_3

The optical properties (**Figure 3.5**) of the nanopowders' dispersions in water can be directly related with the size and shape of the nanoparticles. The dispersions with *ortho*-WO_3·0.33H_2O nanorods show an absorption band in the wavelength range between 224 and 290 nm while the dispersion with *m*-WO_3 nanoslabs show a weak peak at 415 nm. The intensity of the absorption peaks are associated with the active surface area of the nanoparticles, scaling up for higher S:V ratios.[26]

The optical band gap energy (E_g) was calculated using the Tauc's plot (**Figure 3.5b** and **c**) and by applying the **Equation 3.3**:

$$\alpha h\upsilon = A(h\upsilon - E_g)^n \qquad (3.3)$$

Where *A* is a constant, $h\upsilon$ is the corresponding photon energy, α is the absorption coefficient and *n* depends on the type of the optical transition. For crystalline semiconductors *n* is ½ or 2 for direct or indirect allowed transitions, respectively. [4] Comparing both plots it was observed a better fitting and widest range of data points in **Figure 3.5c** therefore it was considered direct allowed transitions for the calculation of the optical band gap energy.

The red-shifted bands observed for the *m*-WO_3 dispersion corresponds to a band gap of 1.80 eV while *ortho*-WO_3.0.33H_2O dispersions show a band gap of 3.59 eV and 3.20 eV for the mixture

of both polymorphs. In the literature, it was also reported a similar band gap (1.73 eV) for monoclinic structures [35] but produced by high annealing temperatures. Nanoparticles produced by arc discharge method or nanostructured films show band gaps above 2.5 eV which are closer to the values obtained for *ortho*-$WO_3 \cdot 0.33H_2O$ dispersions. [36–38] The wider band gap results for *ortho*-$WO_3 \cdot 0.33H_2O$ are related with the structural distortion in the WO_6 octahedral that can lead to a displacement of the ions and bond lengths which results in a lowering of the valence band (oxygen 2p states) and raising of the conduction band (tungsten 5d state) thus increasing the band gap. [35] Nevertheless, the optical band gap energy is not directly related with the conductivity of the nanopowders since this last parameter depends not only on the electrons and holes but also on the movement of the ions. [39]

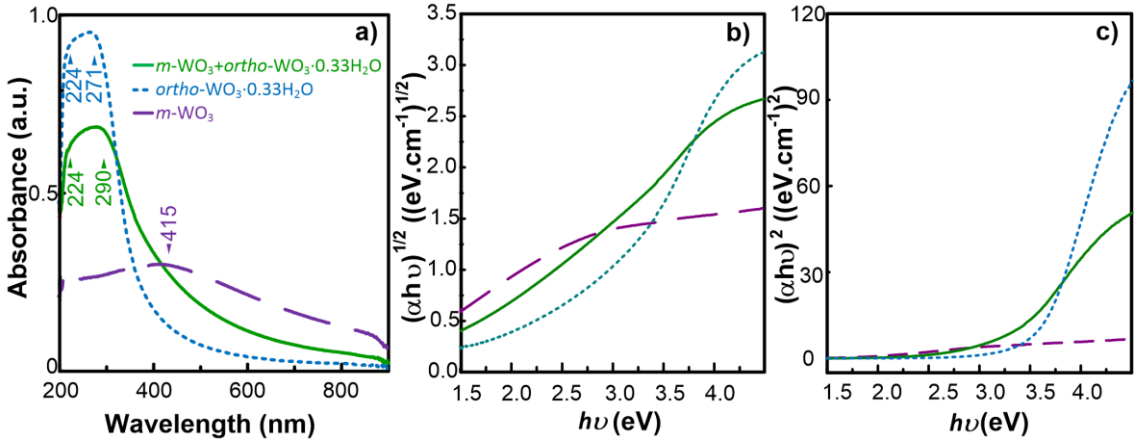

Figure 3.5. a) UV/Vis absorbance spectra and the correspondent Tauc's plots corresponding to: b) indirect and c) direct transitions of WO_3 nanoparticles dispersed in water.

3.3.2. Thin Film Production

Dual-phase thin films were produced by inkjet printing on flexible PET ITO commercial substrates. The inks were prepared by dispersing the nanostructures with constant stirring and sonication in an alcoholic solution with the appropriate viscosity and surface tension, 1.5 - 2 cP and 30 - 40 dyne cm^{-1}, respectively. Due to the discontinuous nature of the layer formed by the printed nanoparticles the optical modulation was adjusted by printing (also by inkjet) a PTA ink (without nanoparticles) on top of the nanostructures thus creating a dual-phase film of *a*-WO_3/WO_3. The proportion of the *a*-WO_3 layer was kept low so that the nanoparticles influence to the EC performance was not masked. The choice of this dual-phase structure compromised the optical density of the film since for full optimization more layers of *a*-WO_3 should be deposited. As demonstrated in the previous work, printed *a*-WO_3 film is not fully continuous [11] nevertheless, we obtained a coverage of more than 80 % of the nanostructures. The spatial configuration of the drops was verified by SEM for all dual-phase inkjet printed thin films (**Figure S 3.1a**). The optical band gap energy of the as-deposited thin films in ITO PET was determined as 3.90 eV showing an almost negligible influence of the nanoparticles to the transparency of the films (**Figure S 3.1b and c**). This result is in accordance with the literature for microwave sol-gel assisted synthesis of WO_3 films. [40] At the same time, the roughness of the films were also compared. The results varied from 120 nm

for the *a*-WO_3 to 70-100 nm for the dual-phase films, which in this work was not significant, as verified by the constant optical band gap energy determined for all printed films.

3.3.3. Electrochromic Characterization

In-situ transmittance measurements of the thin films described before, were performed in a typical three electrodes configuration with lithium based gel electrolyte, platinum wire as counter electrode, Ag/AgCl as reference electrode, and a sweep potential of ±2 V, for 30 s during five cycles and at 800 nm wavelength (**Figure 3.6**). This wavelength corresponds to the highest transmittance modulation registered (**Figure S 3.2**). The electrolyte was chosen in accordance with the previous work, due to its good EC performance and ion mobility. [11,41]

Coloration and bleaching times, calculated as the time taken to reach 90 % of full optical response, were below 5 seconds in all printed films.

Optical density (Δ*OD*) was calculated from the transmittance values using **Equation 3.4**: [4]

$$\Delta OD = \log(T_{bl}/T_{col}) \quad \textbf{(3.4)}$$

Where T_{bl} and T_{col} is the transmittance in the bleached and colored conditions, respectively.

Comparing with the purely amorphous film (**Table 3.2**), one observe a notorious improvement in Δ*OD* which is explained by the less compact film and increased active surface area that enhances the capability for intercalation (and deintercalation) of the lithium ions and electron injection (and removal) in dual-phase films. The variation of Δ*OD* is in accordance with the measured conductivities and surfaces areas of the nanopowders and confirms the influence of the structure and morphology of the WO_3 nanoparticles in the EC performance of inkjet printed WO_x dual-phase films.

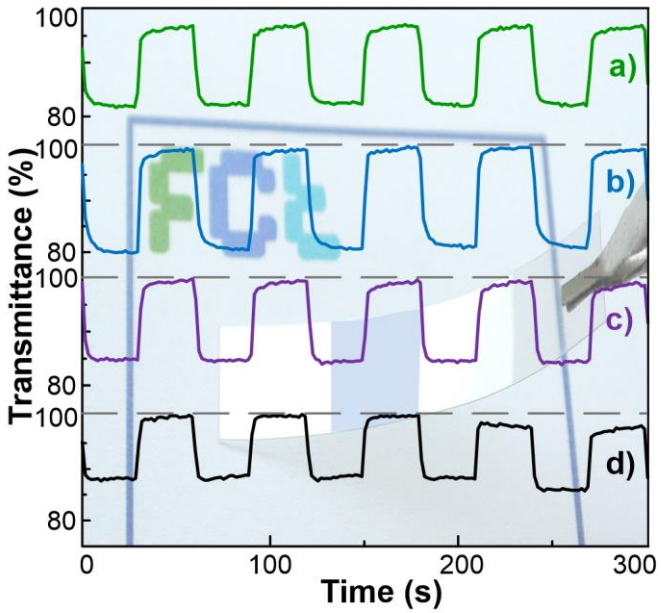

Figure 3.6. *In situ* transmittance measurements at 800 nm applying a potential of ± 2 V for 30 s of inkjet dual-phase thin films: a) *a*-WO_3/(*m*-WO_3+*ortho*-WO_3.0.33H_2O); b) *a*-WO_3/*ortho*-WO_3.0.33H_2O; c) *a*-WO_3/*m*-WO_3 and d) single *a*-WO_3 thin film.

The electrochemistry of the redox reaction of WO_3 was studied by cyclic voltammetry (CV) analysis (**Figure 3.7**) using the same potential range (2 to -2 V) and a scan rate of 50 mV/s, after 2 cycles of stabilization. The coloration occurs when the voltage and current decrease until a maximum negative value while the bleaching takes place when voltage and current reach to a peak maximum (i_{ox}) which then stabilizes in a positive value. The peak area is directly related with the charge capacity of the electrodes and when comparing different films it is visible that the *a*-WO_3 film show a much smaller capacity which is in accordance with the lower values of ΔOD, as explained before.

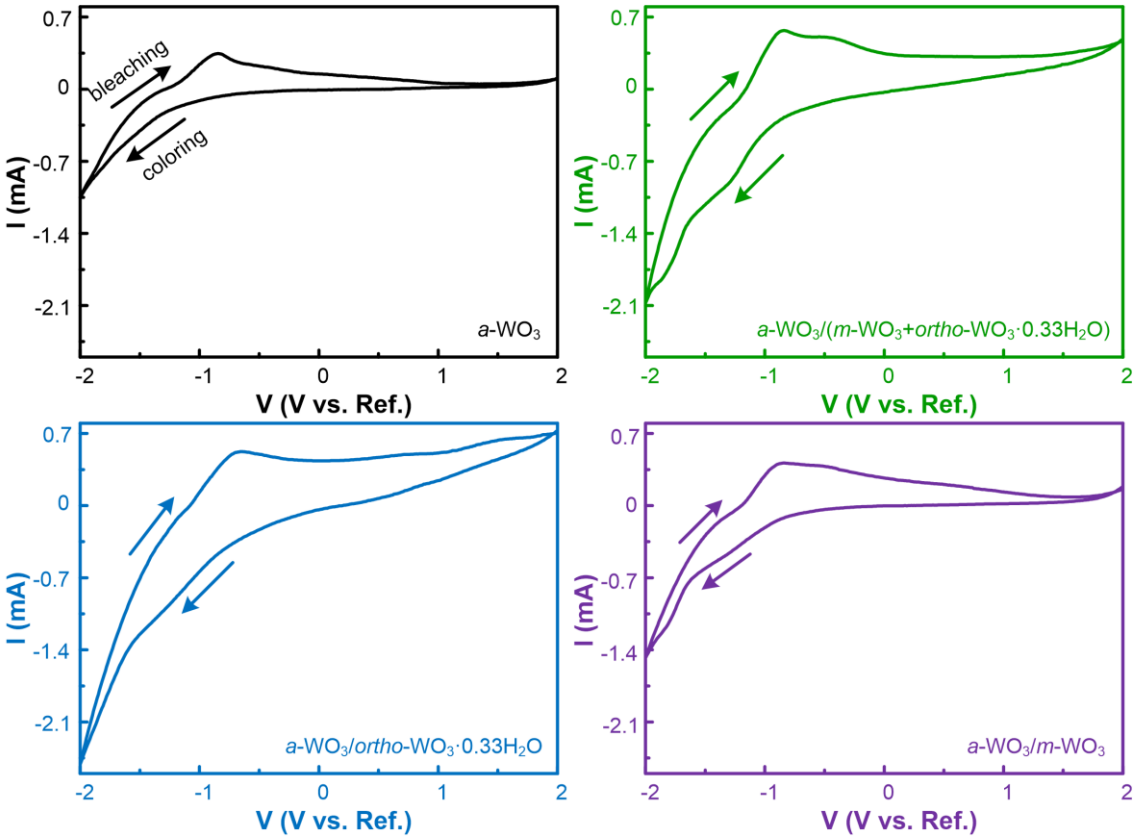

Figure 3.7. Cyclic voltammograms of inkjet printed dual-phase thin films performed in an electrochemical cell with platinum wire as counter electrode, Ag/AgCl as reference electrode in lithium based gel electrolyte at a scan rate of 50 mV/s.

Since the reduction peak in the cyclic voltammograms is not well defined, the reversibility of the reaction was studied by chronocoulometry. The charge inserted and extracted from the film was measured while a fixed potential of 2 and -2 V was applied during 30 seconds during three cycles. For this set of experiments the Q_{ratio} was calculated using the **Equation 3.5**: [40]

$$Q_{ratio} = Q_{di} / Q_i \qquad (3.5)$$

Where Q_{di} and Q_i correspond to the charge deintercalated and intercalated in the electrode while the voltage is applied. The results (**Table 3.2**) of 86/89 % in dual-phase films reflects a higher stability when compared with the charge ratio of 71 % for the amorphous film, even if not fully reversible.

Coloration efficiency (*CE*) is a typical parameter to compare EC performances of devices. In this work the inkjet printing deposition doesn't provide a fully continuous film and therefore the area of the electrode is overestimated. Nevertheless, the *CE* was calculated using **Equation 3.6**: [4]

$$CE = \Delta OD / Q_i \qquad (3.6)$$

Where ΔOD is the optical density at 800 nm wavelength and Q_i the charge density inserted with 2 V during 30 s. The results shown in **Table 3.2** summarize the differences between the inkjet printed thin films. The fact that the *CE* is not improved for the dual-phase films with *ortho*-$WO_3 \cdot 0.33H_2O$ nanoparticles is related with the fact that the active surface area of the nanoparticles are not considered in this calculation. The area used in charge density calculation is the physical area of the electrode. Further studies are at this moment being performed in order to evaluate the dependence of the electroactive area (that is increased by the presence of the nanoparticles) in the *CE* calculations. Despite that, we detected a superior optical modulation and reversibility on the EC performance of dual-phase films in comparison with amorphous thin films.

Table 3.2. Optical densities (ΔOD), charge ratio (Q_{ratio}) and coloration efficiency (*CE*) of inkjet printed thin films.

Type	ΔOD (10^{-2})	Q_{ratio} (%)	*CE* (cm^2/ C)
***a*-WO_3/ *ortho*-$WO_3 \cdot 0.33H_2O$ + *m*-WO_3**	6.9	89	1.92
***a*-WO_3/ *ortho*-$WO_3 \cdot 0.33H_2O$**	9.1	86	3.12
***a*-WO_3/ *m*-WO_3**	7.1	89	4.42
***a*-WO_3**	5.2	71	2.57

3.3.4. Stability Studies

Further studies were accomplished in order to evaluate the long term stability of the thin films. For that the CV measurements were performed during 1000 CV cycles, with a narrower potential range (between 0.5 to -1 V) and a reference electrolyte (0.5 M $LiClO_4$ in PC). The representation of the capacity loss in **Figure 3.8** drives from the charge difference between the first CV cycle and the following cycles. Charge was calculated as the integration of the full area of the cyclic voltammogram. The result demonstrates a much lower stability of the *a*-WO_3 thin film in comparison with dual-phase thin films and the differences between these are not significant, as concluded before. All the produced films show a similar behavior of deterioration with a higher rate during the first 50 cycles and lower rate, especially after 500 cycles.

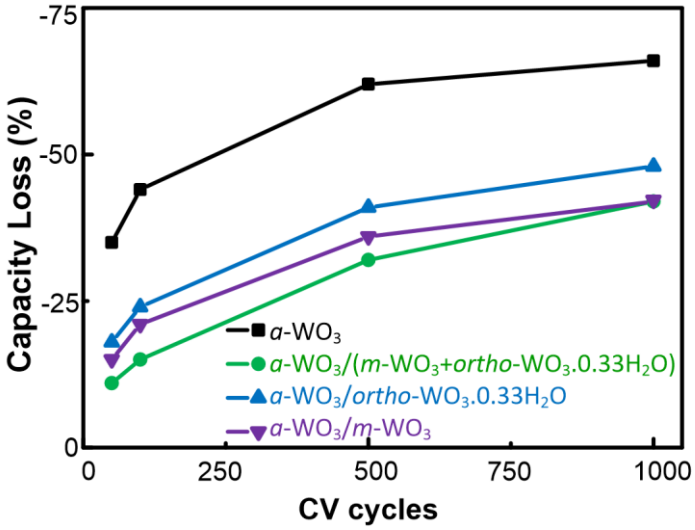

Figure 3.8. Stability of CV measurements of inkjet printed thin films for 1000 cycles for a potential range from 0.5 to -1V. Capacity loss represents the charge difference between first and following cycles obtained by the integration of the cyclic voltammogram.

To better understand the influence of both polymorphs in the EC performance, it was performed a more detailed observation of the structural modifications occurring in the nanoparticles during the redox reaction. Ex-situ XRD (**Figure 3.9**) of the two WO_3 polymorphs, in the coloring and bleach states were analyzed by applying an external potential of ±1 V during 1 min, in a reference electrolyte (0.5 M $LiClO_4$ in PC). The analysis was performed in the most intense peaks of both nanostructures corresponding to the (002) plane of *ortho*-$WO_3 \cdot 0.33H_2O$ and (002), (020), (200) planes of *m*-WO_3 nanoparticles. During the experiment it was not verified any deviation on the ITO (corresponding to the cubic In_2O_3 structure) peaks and the diffractograms were measured after drying of the electrolyte. In comparison to the as-deposit samples, the small shift of the (002) and (200) peaks (in the *ortho*-$WO_3 \cdot 0.33H_2O$ and *m*-WO_3 structures, respectively) towards a lower diffraction angle in the colored/ lithiated samples is a direct evidence of an expansion in the plane interlayer distance due to the introduction of Li^+ between the octahedral layers. [42] Furthermore, the *m*-WO_3 show a higher deviation of the (200) plane associated to a decrease of the intensity of the (020) peak that can be associated to a phase transformation [43] or to a higher structure distortion when compared with the orthorhombic one. Unfortunately, the authors were not able to confirm either the hypothesis or even to identify the formation of other tungsten bronzes reported in the ICDD database. Furthermore, this distortion is not fully recovered after bleaching which confirms the lower capability of these nanoparticles for EC applications. Worth mention that this effect was confirmed in different samples (results not shown). Nevertheless, the lower reversibility verified on *m*-WO_3 is not reflected in the long CV stability study presented before but this can be explained by the site saturation effects that occur in EC films and that affects both types of polymorphs. [1] Further studies are under development to better understand the mechanism of the EC reaction with WO_3 nanoparticles. Even so, this study contributes to the further development of printed electrochromic devices in flexible substrates and denotes the importance of the optimization of the structure and morphology of the nanoparticles to the electrochromic performance of the final device.

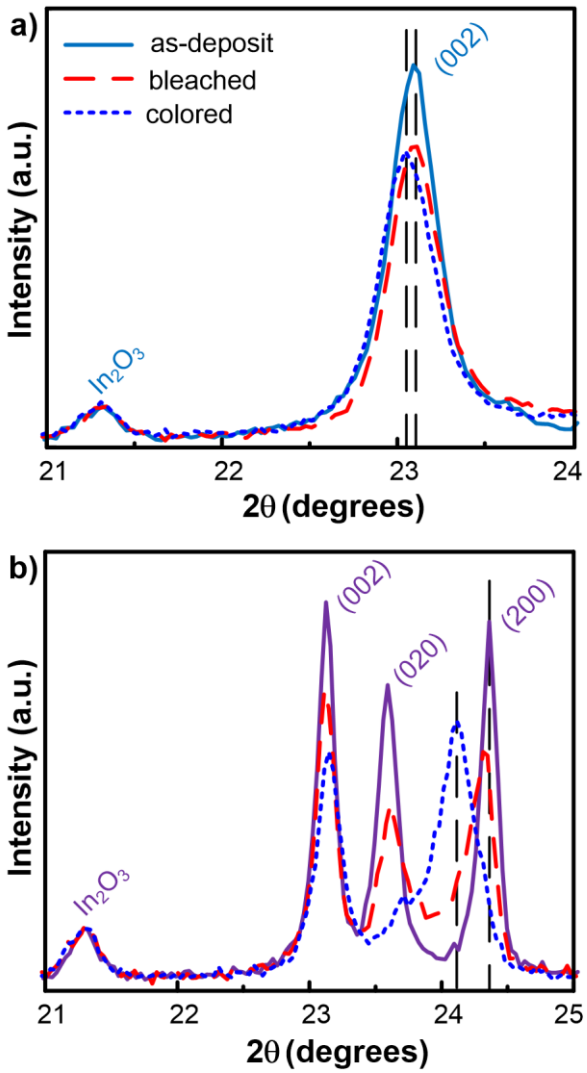

Figure 3.9. Ex-situ lithiation study of a) *ortho*-$WO_3.033H_2O$ and b) *m*-WO_3 nanoparticles deposited on ITO/glass substrates with 0.5 M $LiClO_4$ in PC electrolyte.

3.4. Conclusion

Tungsten oxide nanoparticles were produced by hydrothermal synthesis in aqueous solvent with different acidities. SEM and XRD confirmed different crystallographic structures and morphologies, such as *ortho*-$WO_3 \cdot 0.33H_2O$ nanorods and *m*-WO_3 nanoslabs or a mixture of both polymorphs. The absorption band between 224 and 271 nm was found in both samples with orthorhombic nanorods while monoclinic nanoslabs show a small absorption peak at 415 nm. The difference of intensities and red-shift on the absorption waves (and optical band gap energies) was attributed to the different active surface areas and sizes of the nanoparticles. Impedance spectroscopy made possible the determination of conductivity of the nanopowders in form of pellets and the higher value obtained for the *ortho*-$WO_3 \cdot 0.33H_2O$ was justified by the presence of adsorbed water in the structure and the terminal bonds of the WO_6 octahedral.

Inkjet printing was successfully adapted for the deposition of the synthesized WO_3 nanoparticles and its electrochromic characterization was compared with amorphous WO_3 films. The dual-phase films with *a*-WO_3/*ortho*-$WO_3 \cdot 0.33H_2O$ show a higher optical density while amorphous *a*-WO_3 films show the lower ability for lithium intercalation (and deintercalation) as it was already predicted due to its compact and denser structure and lower active surface area.

Electrochemical characterization confirms the improved performance for dual-phase films in terms of reversibility and stability of the reaction. Nevertheless, the coloration efficiency equation doesn't consider the different active surface areas of the nanoparticles thus making it difficult to compare between the dual-phase films. At the same time, the coloration efficiency was not a conclusive parameter in this study since it depends on the charge capacity results. Ex-situ XRD performed in the nanoparticles films shows a higher deformation of the monoclinic crystal structure during lithiation with a not fully reversible process.

To conclude, all the presented results prove the benefit of using dual-phase structures when building electrochromic devices and of using inkjet printing for low temperature processing devices, compatible with low cost and flexible substrates.

3.5. Experimental Section

Hydrothermal synthesis of nanostructured WO_X

For the hydrothermal synthesis of nanocrystalline WO_x powders, 0.4 g of peroxopolytungstic acid (PTA), synthesis procedure described elsewhere [11], was dissolved in an acidic aqueous solution. The HCl (37%, Merck) concentration was modified in each experiment (0, 0.3 and 3 M). The final solution was transferred to a 23 mL PTFE chamber, set inside a stainless steel autoclave (4745 general purpose vessel, Parr) and installed in the oven (L3/11/B170, Nabertherm) at 180 °C for 6 hours. The product of synthesis was collected by centrifugation at 3000 rpm for 2 min (F140, Focus instruments) and washed three times with water.

Thin film deposition

The deposition of dual-phase *a*-WO_3/WO_X films were performed in two separated printing steps. Firstly, nanostructured WO_X was dispersed in an alcoholic solvent (ethanol: water 1:1) with a weight fraction of 0.03 %, followed by ultrasonic treatment (UP400S, Hielscher) and filtering (Roth, 0.45 µm syringe filter). The inks composition result in viscosity and surface tension values of 1.5 – 2 cP and 30 – 40 dyne cm^{-1}, respectively, acceptable for conventional office printer. Several layers (1 cm^2 in area) were repeatedly printed (20-80 passes) using conventional desktop printer (Canon PIXMA IP4850) in regular intervals of around 1 minute while being exposed to a relative humidity of 50%, at 28 ºC on ITO PET substrates (Sigma-Aldrich, 1000 Å of ITO, 60 Ω/sq, T > 75% at 550nm). Variable numbers of layers, dependent on the solid content, were adjusted in order to obtain a uniform coverage. All films were dried at room temperature for several hours. Secondly, a PTA solution (8% w/w) was prepared in the same solvent. The solution was stirred for 15 minutes, 150 rpm at 60 °C and filtered (Roth, 0.4 µm syringe filter). An individual layer (1 cm^2 in area) was printed under equal environmental conditions on top of the previously

deposited nanoparticles. All films were dried at room temperature for 24 hours and annealed in air at 120 °C (EHRET, TK4067, Germany) for 1 hour.

Characterization

Morphological and structural characterization of WO_X was performed by Scanning Electron Microscopy (SEM) with X-ray microanalysis (Auriga SEM-FIB, Zeiss) and XRD (XPert PRO, PANalytical). Thermogravimetric (TG) experiments were accomplished directly with the powder in air with a heating ramp of 5 °C/min starting from RT up to 600 °C (STA 449 F3 Jupiter, Netzsch). The specific surface area was calculated using the Brunauer–Emmett–Teller (BET) method based on the nitrogen adsorption isotherm obtained at 77 K in a constant volume adsorption apparatus (ASAP 2010 V1.01B Micromeritics). Hydrodynamic diameter of the WO_x dispersions in alcoholic medium was confirmed by Dynamic Light Scattering (DLS) technique (W130i Avid Nano). UV-visible spectroscopy of WO_x dispersed in water was measured using the same nanoparticles content (T90+, PG Instruments) while thin films were measured in reference with PET ITO (UV/ VIS 3101 PC, Shimadzu). Electrochemical impedance spectroscopy (EIS) was performed in a potentiostat (600TM Gamry Instruments) with WO_x powders in a form of pellets made at a pressure of 8 tons, with a diameter of approximately 1 cm and a thickness of 1-3 mm. The electrochemical cell consisted in two stainless steel electrodes in each side of the pellet compacted in a homemade cell. Optical measurements of printed dual-phase films were performed in situ using a spectrometer set-up consist of HR4000 High-Resolution Spectrometer (Ocean Optics), Halogen Light Source HL-2000-FHSA (Mikropack) in range of 450-850 nm. The electrochemical cell consisting of working electrode (dual-phase EC film), platinum wire used as counter electrode and reference electrode of Ag/AgCl was filled with lithium based gel electrolyte prepared according to the recipe described elsewhere. [41] Resulting cell was driven by High Current Source Measure Unit (KEITHLEY 238) in order to induce electrochromic action in square wave ($\pm$2 V, 30 s per pulse). Spectra were recorded in reference to the uncoated substrate under equal conditions. The thickness and roughness of the inkjet printed films were measured with a Profilometer (AMBIOS XP-200, USA) in ITO glass substrates following the same experimental procedure as described for ITO PET. Electrochemical measurements (600TM Gamry Instruments) of printed films were performed in a typical three cell configuration with the same conditions previously described. In the ex-situ XRD studies the nanoparticles were deposited by doctor blade technique in order to improve the diffractograms intensities and increase the statistic results. The lithiation (and delithiation) of the films was performed in a 0.5 M $LiClO_4$ in PC electrolyte with a sweep potential of 1 V during 1 min.

3.6. Acknowledgements

This work was funded by the Portuguese Science Foundation (FCT-MEC) through project EXCL/CTM-NAN/0201/2012, Strategic Project PEst-C/CTM/LA0025/2013-14, project “APPLE” and “SMART-EC” that has received funding from the European Union Seventh Framework Programme (FP7/2007-2013) under grant agreements n° [FP7-NMP-2010-SME/262782-2] and [FP7-ICT-2009.3.9/258203] and the FCT-MEC doctoral grant SFRH/BD/73810/2010 given to L. Santos. Moreover, this work was also supported by E. Fortunato’s ERC 2008 Advanced Grant (INVISIBLE contract number 228144).

3.7. References

[1] C. G. Granqvist, Sol. Energy Mater. Sol. Cells 2012, 99, 1.

[2] R. J. Mortimer, Annu. Rev. Mater. Res. 2011, 41, 241.

[3] J. Zhang, X. L. Wang, X. H. Xia, C. D. Gu, J. P. Tu, Sol. Energy Mater. Sol. Cells 2011, 95, 2107.

[4] C. G. Granqvist, Handbook of Inorganic Electrochromic Materials, Elsevier, Amsterdam, Netherlands, 2002.

[5] S.-H. Lee, M. Je, H. M. Cheong, E. Ozkan, E. C. Tracy, S. K. Deb, Solid State Ionics 2003, 156, 447.

[6] C. M. Lampert, Sol. Energy Mater. 1984, 11, 1.

[7] S. Hotchandani, I. Bedja, R. Fessenden, P. Kamat, Langmuir 1994, 10, 17.

[8] H. Zheng, J. Z. Ou, M. S. Strano, R. B. Kaner, A. Mitchell, K. Kalantar-zadeh, Adv. Funct. Mater. 2011, 21, 2175.

[9] M. Deepa, T. K. Saxena, D. P. Singh, K. N. Sood, S. A. Agnihotry, Electrochim. Acta 2006, 51, 1974.

[10] J. Wang, E. Khoo, P. S. Lee, J. Ma, J. Phys. Chem. C 2008, 112, 14306.

[11] P. J. Wojcik, A. S. Cruz, L. Santos, L. Pereira, R. Martins, E. Fortunato, J. Mater. Chem. 2012, 22, 13268.

[12] C. M. White, D. T. Gillaspie, E. Whitney, S.-H. Lee, A. C. Dillon, Thin Solid Films 2009, 517, 3596.

[13] Z. Xie, L. Gao, B. Liang, X. Wang, G. Chen, Z. Liu, J. Chao, D. Chen, G. Shen, J. Mater. Chem. 2012, 22, 19904.

[14] C.-K. Wang, C.-K. Lin, C.-L. Wu, S. Brahma, S.-C. Wang, J.-L. Huang, Ceram. Int. 2013, 39, 4293.

[15] S. Songara, V. Gupta, M. Kumar Patra, J. Singh, L. Saini, G. Siddaramana Gowd, S. Raj Vadera, N. Kumar, J. Phys. Chem. Solids 2012, 73, 851.

[16] L. Liu, M. Layani, S. Yellinek, A. Kamyshny, H. Ling, P. S. Lee, S. Magdassi, D. Mandler, J. Mater. Chem. A 2014, 2, 16224.

[17] L. Santos, J. P. Neto, A. Crespo, D. Nunes, N. Costa, I. M. Fonseca, P. Barquinha, L. Pereira, J. Silva, R. Martins, E. Fortunato, ACS Appl. Mater. Interfaces 2014, 6, 12226.

[18] J. Yang, L. Jiao, Q. Zhao, Q. Wang, H. Gao, Q. Huan, W. Zheng, Y. Wang, H. Yuan, J. Mater. Chem. 2012, 22, 3699.

[19] D. Zhang, S. Wang, J. Zhu, H. Li, Y. Lu, Appl. Catal. B Environ. 2012, 123-124, 398.

[20] G. F. Cai, J. P. Tu, D. Zhou, X. L. Wang, C. D. Gu, Sol. Energy Mater. Sol. Cells 2014, 124, 103.

[21] J. Yang, W. Li, J. Li, D. Sun, Q. Chen, J. Mater. Chem. 2012, 22, 17744.

[22] R. R. Søndergaard, H. Markus, F. C. Krebs, J. Polym. Sci. Part B Polym. Phys. 2013, 51, 16.

[23] L. Zhou, J. Zou, M. Yu, P. Lu, J. Wei, Y. Qian, Y. Wang, C. Yu, Cryst. Growth Des. 2008, 8, 3993.

[24] L. Jiayin, H. Jianfeng, W. Jianpeng, C. Liyun, K. Yanagisawa, Ceram. Int. 2012, 38, 4495.

[25] J. Wang, E. Khoo, P. S. Lee, J. Ma, J. Phys. Chem. C 2009, 113, 9655.

[26] S. Rajagopal, D. Nataraj, D. Mangalaraj, Y. Djaoued, J. Robichaud, O. Y. Khyzhun, Nanoscale Res. Lett. 2009, 4, 1335.

[27] G.-C. Yi, Semiconductor Nanostructures for Optoelectronic Devices: Processing, Characterization and Applications, Springer, Berlin, Germany, 2012.

[28] Z. Lu, S. M. Kanan, C. P. Tripp, J. Mater. Chem. 2002, 12, 983.

[29] Z. Gu, H. Li, T. Zhai, W. Yang, Y. Xia, Y. Ma, J. Yao, J. Solid State Chem. 2007, 180, 98.

[30] A. Lee, K. Sudau, K. H. Ahn, S. J. Lee, N. Willenbacher, Ind. Eng. Chem. Res. 2012, 51, 13195.

[31] A. Al Mohammad, Acta Phys. Pol. A 2009, 116, 240.

[32] G. Orsini, V. Tricoli, J. Mater. Chem. 2012, 22, 23861.

[33] G. Orsini, V. Tricoli, J. Mater. Chem. 2010, 20, 6299.

[34] Y. M. Li, M. Hibino, M. Miyayania, T. Kudo, Solid State Ionics 2000, 134, 271.

[35] S. K. Deb, Sol. Energy Mater. Sol. Cells 2008, 92, 245.

[36] A. M. Cruz, D. S. Martínez, E. L. Cuéllar, Solid State Sci. 2010, 12, 88.

[37] A. A. Ashkarran, A. Irajizad, M. M. Ahadian, S. A. Mahdavi Ardakani, Nanotechnology 2008, 19, 195709.

[38] P. P. González-Borrero, F. Sato, a. N. Medina, M. L. Baesso, a. C. Bento, G. Baldissera, C. Persson, G. a. Niklasson, C. G. Granqvist, A. Ferreira da Silva, Appl. Phys. Lett. 2010, 96, 061909.

[39] A. Enesca, L. Andronic, A. Duta, S. Manolache, Rom. J. Inf. Sci. Technol. 2007, 10, 269.

[40] R. R. Kharade, S. S. Mali, S. P. Patil, K. R. Patil, M. G. Gang, P. S. Patil, J. H. Kim, P. N. Bhosale, Electrochim. Acta 2013, 102, 358.

[41] P. C. Barbosa, L. C. Rodrigues, M. M. Silva, M. J. Smith, P. B. Valente, A. Gonçalves, E. Fortunato, Polym. Adv. Technol. 2011, 22, 1753.

[42] L. Q. Mai, B. Hu, W. Chen, Y. Y. Qi, C. S. Lao, R. S. Yang, Y. Dai, Z. L. Wang, Adv. Mater. 2007, 19, 3712.

[43] S. Misra, N. Liu, J. Nelson, S. S. Hong, Y. Cui, M. F. Toney, ACS Nano 2012, DOI: 10.1021/nn301339g.

3.8. Supporting Information

Inkjet printed films characterization

The pattern of the inkjet printed films registered in **Figure S 3.1a** is due to the precursor layer (dark grey pattern) deposition. The same pattern was verified in all dual-phase films. The coverage of more than 80 % of the nanoparticles was assured with this method. The transmittance of the printed films was measured between 300 and 800 nm wavelength (**Figure S 3.1b**) which allowed the calculation of the optical band gap energy of the printed films (**Figure S 3.1c**). The constant and high values before and after deposition of the precursor layer reveals the full transparency of the films and the good homogeneity between the different dual-phase films.

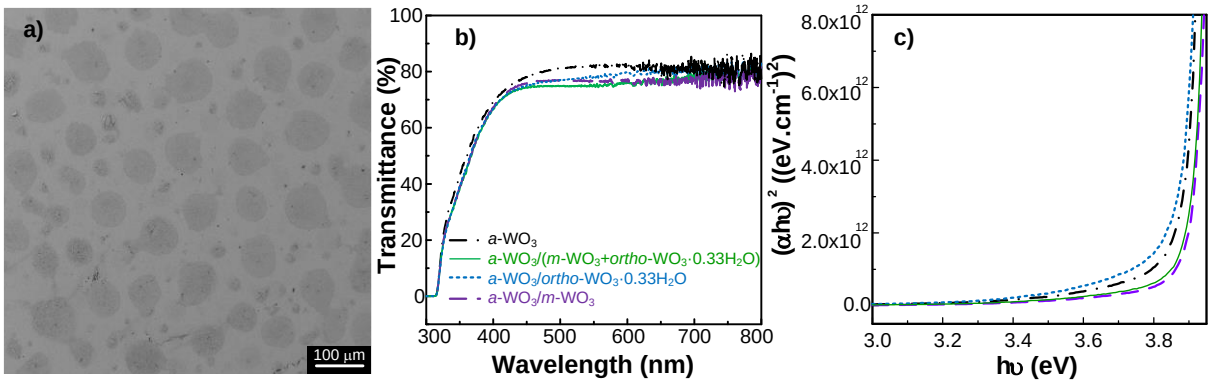

Figure S 3.1. a) SEM image of inkjet printed *a*-WO_3/*ortho*-WO_3.0.33H_2O (detail of the pattern formed by the *a*-WO_3 layer), b) Transmittance plots and c) Tauc's plots for all inkjet printed thin films.

UV-vis spectroscopy of inkjet printed films during EC performance

The transmittance plots (**Figure S 3.2**) in the visible region of the printed films were performed after applying a fixed potential (±2 V) during 60 s. The maximum optical modulation was verified at 800 nm wavelength. Worth mention that the optical modulation of the printed films was not optimized with the purpose of studying the influence of the nanoparticles in the dual-phase films and therefore maintaining a low amount of the amorphous part.

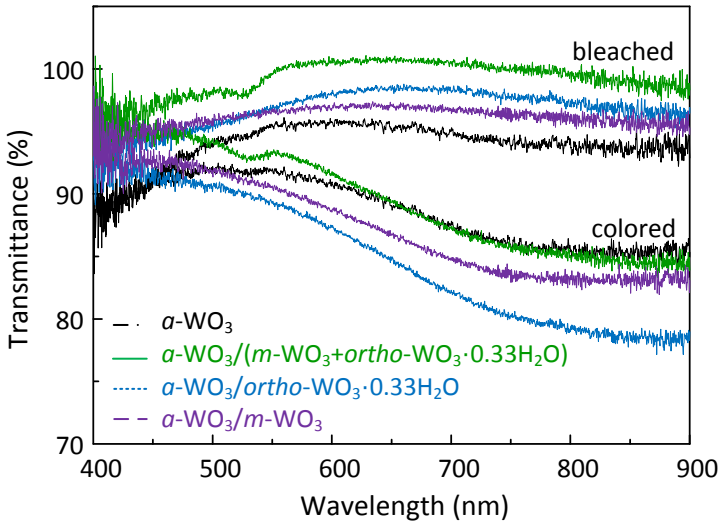

Figure S 3.2 Transmittance plots for all inkjet printed thin films in colored (2 V) and bleached (-2 V) states, after applying a fixed potential for 60 s.

Chapter 4. WO_3 AS pH SENSOR

The contents of **Chapter 4** were adapted from the publication:

"L. Santos, J. P. Neto, A. Crespo, D. Nunes, N. Costa, I. M. Fonseca, P. Barquinha, L. Pereira, J. Silva, R. Martins, E. Fortunato, *WO_3 nanoparticles-based conformable pH sensor*, **ACS Applied Materials & Interfaces** 6 (15), **2014**, 12226-12234, DOI: 10.1021/am501724h"

Moreover, the WO_3 electrodeposition was also the topic for a book chapter entitled:

"L. Santos, J. P. Neto, A. Crespo, P. Baião, P. Barquinha, L. Pereira, R. Martins, E. Fortunato, *Electrodeposition of WO_3 nanoparticles for sensing applications*, In **Electroplating of Nanostructures**, Aliofkhazraei, M., Ed.; InTech, 2015 - Accepted.*"*

4.1. Abstract

The pH is a vital physiological parameter that can be used on disease diagnosis and treatment as well as on monitoring other biological processes. Metal/ metal oxide based pH sensors have several advantages regarding their reliability, miniaturization and cost-effectiveness, which are critical characteristics for *in vivo* applications. In this work, WO_3 nanoparticles were electrodeposited on flexible substrates over metal electrodes with a sensing area of 1 mm^2. These sensors show a sensitivity of -56.7 ± 1.3 mV/pH, in a pH range of 9 to 5. A proof of concept is also demonstrated using a flexible reference electrode in solid electrolyte with a curved surface. A good balance between the performance parameters (sensitivity), the production costs and simplicity of the sensors was accomplished, as required for wearable biomedical devices.

4.2. Introduction

Cost-effective, flexible, lightweight, easy-to-fabricate and biocompatible wearable biomedical devices have recently attracted the focus of many research groups. The application of these devices is of extreme importance both in early diagnosis through continuous monitoring of complex health conditions and in patients under treatment.[1,2]

The pH value can be used as an indicator for disease diagnostics, medical treatments optimization and monitoring of biochemical and biological processes.[3] Nevertheless, the integration of pH sensing systems into the next generation of wearable devices requires a different architecture than currently used in typical glass-type electrodes and a minimal electrode size.[4] Flexible pH sensors have already been reported on paper substrates, silicon nitride membranes and polyimide substrates however, full conformation with non-planar surfaces, mechanical strain resistance and miniaturization are still challenges to overcome.[5–7]

Ion sensitive field-effect transistors (ISFET), optical fiber, hydrogel films and solid state pH sensors have been widely studied and reported for pH sensing.[8–13] Nevertheless, the power consumption, architecture and cost of the sensors are a drawback. Metal oxide based sensing electrodes present several advantages due to their low manufacture costs, compatibility with miniaturization processes, high sensitivity and abundancy.[14,15] Moreover, pH sensing can be achieved through a potentiometric method that is one of the most common, simple and portable electrochemical techniques.[16]

Amongst the oxide materials being studied (IrO_x, RuO_2, SnO_2, Ta_2O_5, TiO_2, ZnO), [6,7,12,17–19] tungsten oxide (WO_3) is a very promising material regarding its low cost and availability, improved stability, good morphological and structural control of the synthesized nanostructures, reversible change of conductivity, high sensitivity, selectivity and biocompatibility. [20] Furthermore, WO_3 is a well-studied wide band gap semiconductor (~ 2.75 eV.) used for several applications as chromogenic material, sensing material and catalyst.[21]

The first report of a WO_3 based pH sensor was published in 1987 by Wrighton et al.,[22] where a microelectrochemical transistor was operating either electrically or chemically by changing the gate voltage or the pH of the solution, respectively (**Figure 4.1**). Nevertheless, the use of

WO_3 with high surface area was mainly reported for gas sensor applications and has not been fully exploited as pH sensing layer.[23,24]

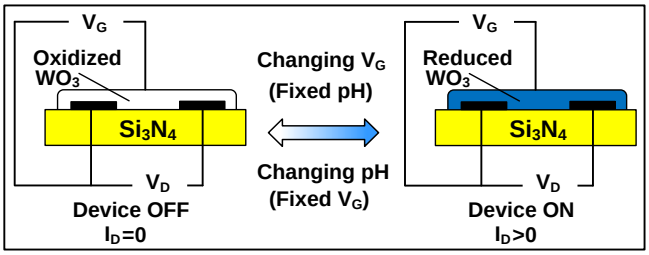

Figure 4.1. Simplified schematics of the first pH device using a WO_3 sensing layer. The device turns ON ($I_D > 0$) and OFF ($I_D = 0$) depending on the oxidized (insulating) or reduced (conductive) states of WO_3, respectively. Similar effect is observed by varying the pH (adapted from the work published by Wrighton et al.[22]).

In this work, WO_3 based pH sensors with a reduced sensing area of 1 mm^2 were produced by electrodeposition of the nanoparticles previously grown by hydrothermal synthesis. This method allowed the production of a thin WO_3 layer with improved surface area and showed good sensitivity and stable response in a pH range between 9 and 5, which is in accordance with most physiological fluids.

For the first time (to the authors' knowledge), wax printing was used to produce the insulator layer in the pH sensors. This material is compatible with solution techniques and therefore is a good alternative for the conventional materials (polymers, photoresist or oxides) that usually require an additional step of patterning and/or are deposited by physical and expensive routes.

The polyimide substrate allows a good conformation of the electrodes to curved surfaces thus making these suitable for applications in wearable biomedical devices.

4.3. Experimental Section

Hydrothermal synthesis of nanostructured WO_3

The chemicals used were of analytical grade without further purification. For the hydrothermal synthesis of WO_3 nanoparticles, 0.4 g of $Na_2WO_4.2H_2O$ (Fluka, 99 %) were first dissolved in 8 g of deionized water with 0.15 g of NaCl (Panreac, 99.5 %) as structure directing agent[25] and then acidified with 1 g of 6 M HCl solution (Fluka, 37 %). The final solution was transferred to a 23 ml PTFE chamber, set inside a stainless steel autoclave (4745 general purpose vessel, Parr) and installed in an oven (L3/11/B170, Nabertherm). The synthesis conditions were set at 180 °C for 1 hour followed by a cooling period to room temperature inside the oven. The synthesis product was collected by centrifugation at 3000 rpm for 2 min (F140, Focus instruments) and washed three times with water. The final powder was finally dried in the oven (TK4067, EHRET) at 60 ºC for at least 8 hours.

WO_3 characterization

Morphological and structural characterization of the powder was performed by Scanning Electron Microscopy (SEM, Auriga SEM-FIB, Zeiss), X-Ray Diffraction (XRD, XPert PRO, PANalytical) and Fourier Transform Infrared Spectroscopy (FTIR, Nicolet 6700, Thermo Electron Corporation). The nitrogen adsorption isotherm was obtained at 77 K in adsorption apparatus (ASAP 2010 Micromeritics) and the samples were degasified at 150 ºC overnight. Hydrodynamic diameter of the WO_3 nanoparticles in water was confirmed by Dynamic Light Scattering (DLS) technique (W130i Avid Nano).

Sensor fabrication

The fabrication of the sensor was executed in several steps as illustrated in **Figure 4.2a**. The polyimide film (50 µm thickness, DuPont) was cleaned by sonication (Bandelin Sonorex) in ethanol and isopropanol for 5 min and then dried under nitrogen flow before use. The mask used for patterning the electrode was made in acetate foil and defined with a laser cutter (Universal Laser System ULS3.50). A thin titanium layer (6 nm) was first deposited in order to improve adhesion of the 65 nm gold layer. The delimitation of the sensing area (1 mm^2) was achieved by a wax printed layer (Xerox ColorQube 8570DNPS) on top of the connection line, which also worked as an insulator layer. The electrodeposition of WO_3 (**Figure S 4.1** from supporting information) was performed using a Gamry Instruments Reference 600 potentiostat/galvanostat in a constant current mode (20 µA) for 900 s in a three electrode configuration. An Ag/AgCl reference electrode, a platinum wire counter electrode and a gold layer, acting as the working electrode, were used to define the sensing layer of the pH sensor. A stable WO_3 nanoparticle dispersion in water (1 mg/mL) was achieved after magnetically stirring for 45 min and sonication (HIELSHER M80) for 5 min, followed by filtration (Sartorius, 0.45 µm pore diameter). After WO_3 nanoparticles deposition, the electrodes were rinsed with deionized water and dried for one hour at 50 °C. The dimensions and macroscopic aspect of the final sensor are shown in **Figure 4.2b-c**. After deposition the homogeneity of the WO_3 sensing layer was confirmed by SEM analysis. For the Focused Ion Beam (FIB) experiments, the WO_3 nanoparticles were previously coated with a carbon sacrificial layer, Ga^+ ions were accelerated to 30 kV at 2 pA and the etching depth was kept around 200 nm. The adhesion of the nanoparticles was checked by dipping the electrode in phosphate buffer solution (PBS, 5 mM, pH 7) at 37 ºC for 8 days and measuring the amount of nanoparticles released into the solution by UV/Vis spectroscopy (Spectro-115U, Gamry Instruments). A previous calibration was performed with WO_3 dispersions in PBS with different concentrations. After this test the sensor was again analyzed by SEM.

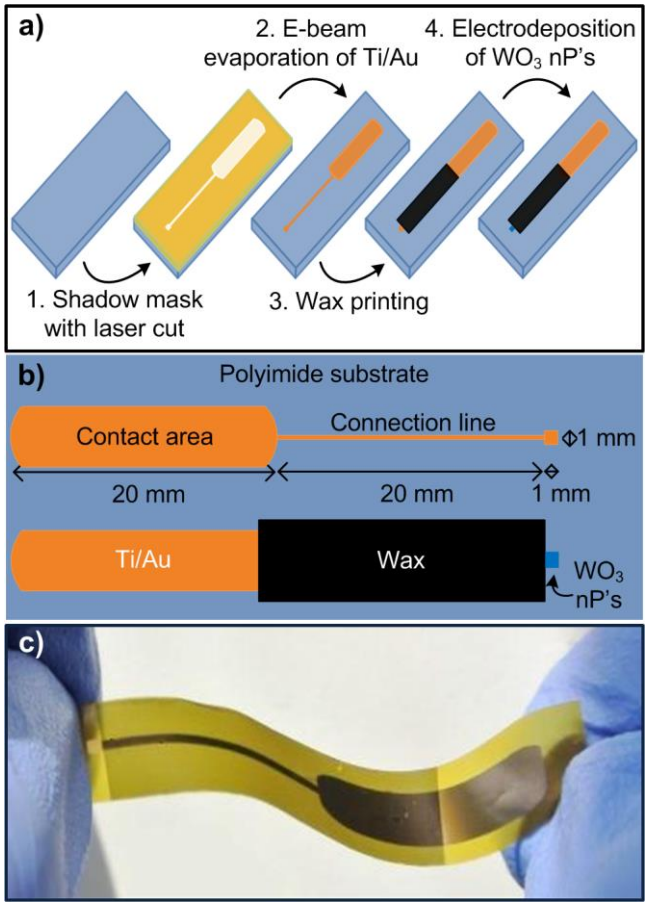

Figure 4.2. Scheme of the: a) sensor production procedure, b) sensor design and structure and c) photograph of the final fabricated sensor.

Sensor cytocompatibility

Cytocompatibility of the sensor was evaluated according to the International Standard (ISO 10993-5) using the extract method. Three combinations of the materials used in the sensor production were tested: 1) polyimide substrate with gold electrode; 2) polyimide, gold and wax layer; 3) the whole sensor (polyimide, gold, wax and WO_3). For each material combination, three specimens were cut in small pieces and put inside a centrifuge tube. Three milliliters of complete culture medium (DMEM supplemented with 10 % FBS and 1 % penicillin-streptomycin, all from Invitrogen) were added to each tube. The tubes were placed inside an incubator at 37 °C for 48 hours. All procedures involving the manipulation of cells or culture medium were performed under aseptic conditions inside a biological safety cabinet (ESCO Labculture II). Vero cells were seeded at a density of 5 k cells per well in a 96 well microplate (Sarstedt) and were incubated at 37 °C in a 5 % CO_2 humidified atmosphere incubator (Sanyo MCO19-AIC-UV). After 24 hours, the medium was removed and 100 µL of conditioned medium was added to each well. Four replicas were prepared for each material and time point. Adequate controls – a positive control where 10 µL of DMSO was added to each well and a negative control - were also prepared. After 24, 48 and 72 hours of incubation of the cells with the extracts, 10 µL of the cell viability indicator resazurin (0.25 mg/mL in PBS, Alfa Aesar) was added to each well and the cells were incubated two more hours

in the CO_2 incubator. Absorbance of the medium was measured at 570 nm with a reference wavelength of 600 nm (Biotex ELX 800UV microplate reader). The absorbance of no cell control wells, containing only complete medium and the resazurin solution was also measured. The relative cell viability was calculated from the ratio of absorbances measured for the experimental wells and the negative control wells.

pH sensor characterization

The electrochemical characterization was performed in a typical three electrodes cell configuration as described above. Electrochemical impedance spectroscopy (EIS) measurements were recorded in a frequency range of 1 to 10^6 Hz with an AC voltage of 10 mV. The pH sensitivity of the sensors was assessed by measuring the open circuit voltage variation when the sensors were immersed in commercial buffer solutions with a pH in the range of 5 to 9 (buffer solutions, Roth) for 120 s at room temperature.

Proof of concept

For the proof of concept a flexible Ag/AgCl reference electrode was built using the same dimensions already described for the pH sensor. Thin layers of chromium (7 nm), platinum (3 nm) and silver (30 nm) were sequentially deposited by electron-beam evaporation (procedure based on the work of Huang et al.[6]). The AgCl layer was formed by anodization of the silver film applying a constant current at 0.5 mA in 0.1 M HCl for 5 s. The electrode was rinsed with water and saturated in 3 M KCl solution before use. The characterization of the electrode was performed by EIS in PBS. See supporting information, **Figure S 4.2**. The solid electrolyte was prepared by dissolving gelatin (mass fraction of 8 %) in commercial pH buffer solutions from Roth (pH 8, 7 and 6) at 50 ºC. After complete dissolution, the solution was transferred to a recipient and cooled down in order to achieve the required curved conformation. The electrochemical measurements shown in the proof of concept section were obtained using the pH sensor as working electrode and the flexible Ag/AgCl reference electrode, both in contact with the solid electrolyte.

4.4. Results and Discussion

4.4.1. WO_3 Nanoparticles Characterization

Hydrothermal synthesis was the method chosen to prepare the nanoparticles due its low process temperature, easy control of the morphology and structure of the nanoparticles and good reproducibility. In this work, WO_3 nanoparticles were obtained from a commercial precursor (sodium tungstate) with a structure directing agent (sodium chloride) that promotes uniformity of the nanoparticles size and shape thus improving the reliability of the sensing layer.

The morphology of the synthesized WO_3 nanoparticles was observed by SEM (**Figure 4.3**). The size of the nanoparticles was estimated to be approximately 10 nm, resulting in nanoslab-type shape agglomerates. The mean hydrodynamic diameter of 75 nm determined by DLS for the nanoparticles dispersion in water is in accordance with the agglomerates sizes observed by SEM.

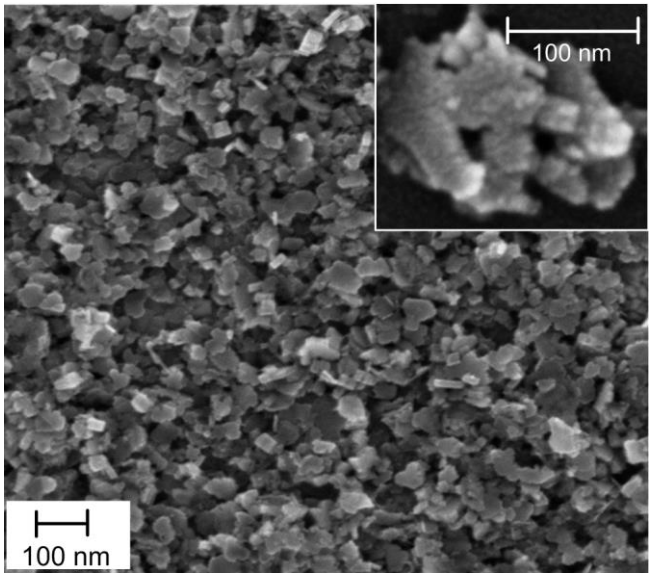

Figure 4.3. SEM image of WO_3 nanoparticles. The inset shows a higher magnification of the nanoparticles exhibiting nanoslabs-type shape agglomerates.

The WO_3 crystalline structure was verified by XRD (**Figure 4.4a**). The diffraction peaks are attributed to orthorhombic hydrated tungsten oxide (*ortho*-$WO_3 \cdot 0.33H_2O$), according to the reference pattern ICDD 01-072-0199, with a mixture of a secondary product (*) not yet identified. In the literature, [26] the particular peak at 10º was also found in WO_3 films deposited at low temperatures thus suggesting that the corresponding structure derives from the slow growing of the nanoparticles clusters. This is corroborated by the presence of broad peaks characteristic of small crystallite sizes and by energy dispersive spectroscopy (EDS) which indicated the presence of only W and O elements in the sample (result not shown here), confirming that the non-identified peaks do not arrise from any impurity.

Tungsten oxides follow a well-known[27] ReO_3-type structure built up of layers containing distorted corner-shared WO_6 octahedra. The obtained *ortho*-$WO_3 \cdot 0.33H_2O$ structure (represented in **Figure 4.4b**) includes two types of octahedra: one is formed by W-O covalent bonds and the other by two types of terminal bonds (W=O and W-OH). This structure will restrict the stacking along the *z* axis due to the weak interaction between adjacent layers thus preventing bulk type structures. The recorded FTIR spectra (**Figure 4.4c**) allowed the identification of both terminal groups and vibrations in WO_6 octahedron, which are in accordance to the state of the art. [28,29] The broad absorption band at 3485 cm^{-1} (-OH stretching) and sharp band at 1605 cm^{-1} (-OH in plane bending) indicates the presence of water molecules in the structure. The broad band between 570 cm^{-1} and 970 cm^{-1} has been ascribed to the O-W-O stretching and bending modes and stretching of the W=O double bond.

The surface area characterization was performed employing the Brunauer-Emmet-Teller (BET) method and the resulting nitrogen adsorption-desorption isotherm (**Figure 4.4d**) demonstrates a typical type IV behavior indicative of the presence of mesopores. The pore size distribution is mainly attributed to narrow mesopores in the range of 10 nm with some micropores <2 nm. The hysteresis shape (H1 type) also suggests the presence of rigid agglomerates of uniform size

with a narrow pore size distribution. This result confirms the previously described SEM images where the porosity is due to the agglomeration of small nanoparticles. The resulting active surface area (74 m^2/g) gives a good approximation of the real surface area of nanoparticles and is in accordance with previous studies. [30,31]

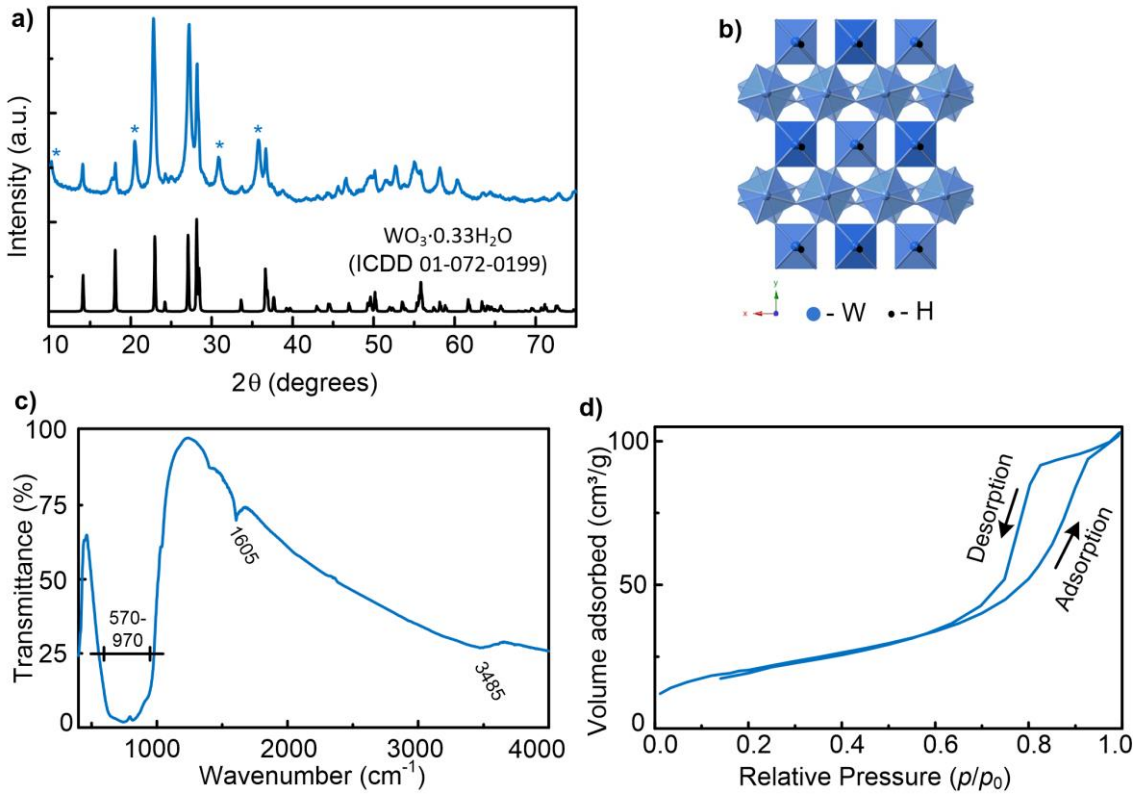

Figure 4.4. a) XRD diffractograms of WO_3 synthesized powder and orthorhombic $WO_3 \cdot 0.33H_2O$ reference pattern (the * peaks correspond to unidentified structure); b) Crystal structure simulation of orthorhombic $WO_3 \cdot 0.33H_2O$ (produced in crystal maker© software); c) FTIR spectrum and d) Nitrogen adsorption-desorption isotherms of WO_3 nanoparticles performed at standard temperature and pressure (STP).

From all the characterization results, we can conclude that the synthesized WO_3 powder is formed by agglomerates of small nanoparticles with a mesoporous structure. The reduced nanoparticle size is an important feature for the enhancement of the sensor performance since it increases the surface area.[32]

4.4.2. Sensor Assembly

The pH sensor was produced using the sequence previously shown in **Figure 4.2**. First, the gold layer was deposited by e-beam evaporation on a polyimide substrate. Then the sensing area was delimited by wax printing and finally, WO_3 nanoparticles were electrodeposited applying a fixed current method. All the materials used in the sensor production (polyimide, gold and WO_3) have already been proven to be biocompatible and adequate for biomedical devices. Nonetheless, the

wax and the whole sensor cytocompatibility were tested in a conventional procedure, as explained below.

4.4.3. Wax Cytocompatibility

Resazurin is a redox dye, blue and nonfluorescent, that is reduced to resorufin, pink and fluorescent, by viable metabolically active cells. The rate of dye reduction is directly proportional to the number of viable cells present. Resorufin has an absorption maximum at 570 nm while resazurin peak absorption is at 600 nm. The results summarized in **Table 4.1** show the relative cell viabilities obtained for the three material combinations, positive and negative controls. The relative cell viabilities are consistently above 90% for all experimental conditions and time points. We can conclude that none of the materials tested is cytotoxic, in particular the printed wax is not cytotoxic and can therefore be used as an insulator.

Table 4.1. Relative cell viabilities after 24, 48 and 72 hours of incubation of the cells with conditioned media.

Sample	24 h	48 h	72 h
Polyimide/Au	0.98 ± 0.04	1.00 ± 0.03	1.10 ± 0.05
Polyimide/Au/Wax	0.96 ± 0.03	1.00 ± 0.02	1.15 ± 0.08
Polyimide/Au/Wax/WO_3	1.01 ± 0.03	1.03 ± 0.02	1.20 ± 0.07
Negative control	1.00 ± 0.02	1.00 ± 0.02	1.00 ± 0.05
Positive control	0.03 ± 0.02	0.013 ± 0.002	0.012 ± 0.011

4.4.4. Sensing Layer

The electrodeposited WO_3 nanoparticles resulted in a uniform sensing layer with some small agglomerates, observed by SEM (**Figure 4.5a**). This image shows that even if the nanoparticles are agglomerated in nanoslabs in solution, after electrodeposition they can dissociate and produce a high quality thin layer with enhanced specific surface area. Milling with FIB (**Figure 4.5b**) allowed the determination of the sensing layer thickness in which is ~55 nm.

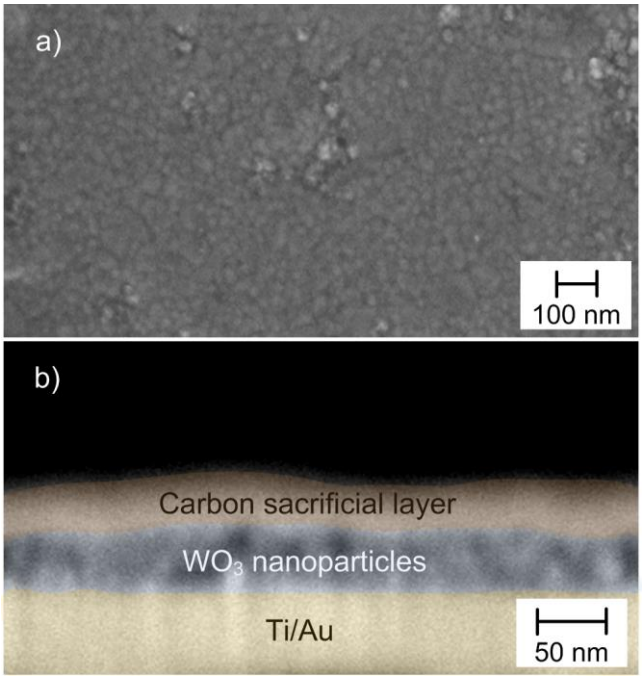

Figure 4.5. SEM images of: a) Sensing area after $WO_3 \cdot 0.33H_2O$ nanoparticles electrodeposition; b) Cross-section overview of Ti/Au, electrodeposited WO_3 nanoparticles and carbon sacrificial layers after FIB milling (The image was colored for better understanding of the layered structure).

The effective adhesion of the nanoparticles was tested by immersing the sensors in PBS solution at 37 ºC for 8 days and measuring the UV/Vis spectra of the solution during this period. The transmittance was compared with the calibration curve obtained for different dispersions of WO_3 nanoparticles in PBS at 280 nm (**Figure 4.6**). After eight days, the morphology of the sensing area was analyzed by SEM (image not shown) and no significant change was noticed. The slight decrease in transmittance after the sixth day corresponds to a WO_3 mass fraction of 0.002 % which represents a negligible deterioration of the sensing layer. Therefore we can confirm a good adhesion of the nanoparticles after immersion for one week in PBS at 37 ºC.

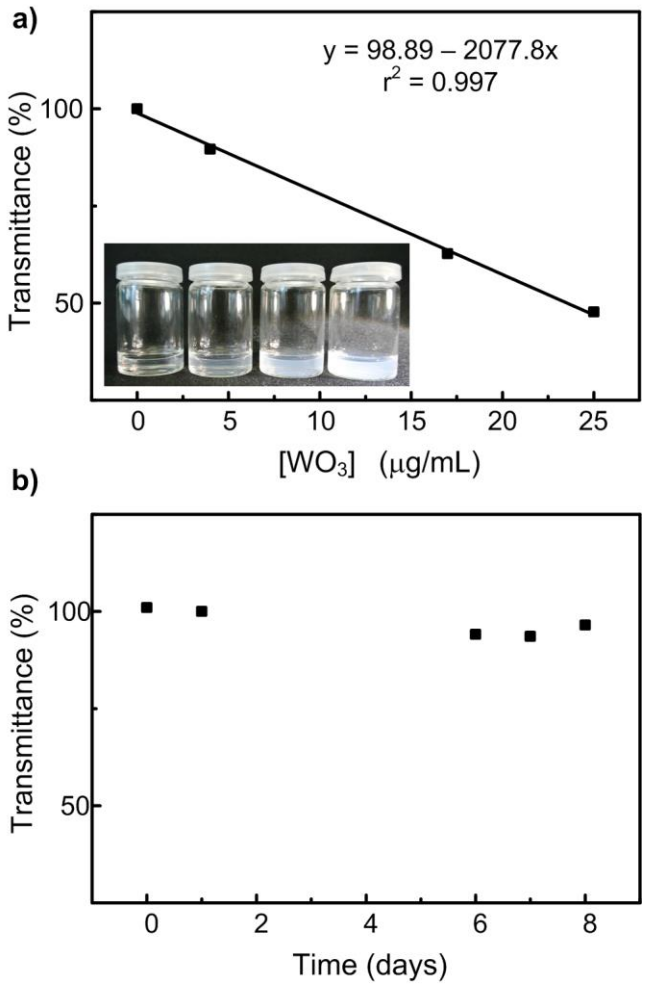

Figure 4.6. a) Calibration curve of transmittance values at 280 nm wavelength for WO_3 dispersions of different concentrations and b) Transmittance of the PBS solution after dipping the WO_3 sensor at 37 ºC for 8 days.

4.4.5. WO_3 Sensing Layer Electrochemical Characterization

The impedance modulus and phase angle of the electrode was analyzed before and after deposition of the WO_3 nanoparticles to evaluate the contribution of the coating to the overall charge transport characteristics at the electrode/solution interface (**Figure 4.7**). Both electrodes exhibit similar high-frequency impedance (10^4–10^6 Hz) and a near-resistive phase angle (approaching 0°) which is mainly determined by the contribution of the solution. [4] Nonetheless, the frequency range over which the phase value is near 0° increased by coating the electrode with WO_3 nanoparticles.

In the low-frequency range, the frequency dependent impedance and the phase angle near -90° indicates that the current flow is dominated by capacitive charging. The decrease of about one order of magnitude in the impedance after deposition of the nanoparticles is due to the increase of the electrochemical surface area and it clearly confirms that the deposited WO_3 layer will improve the sensitivity of the produced pH sensor.[4,33]

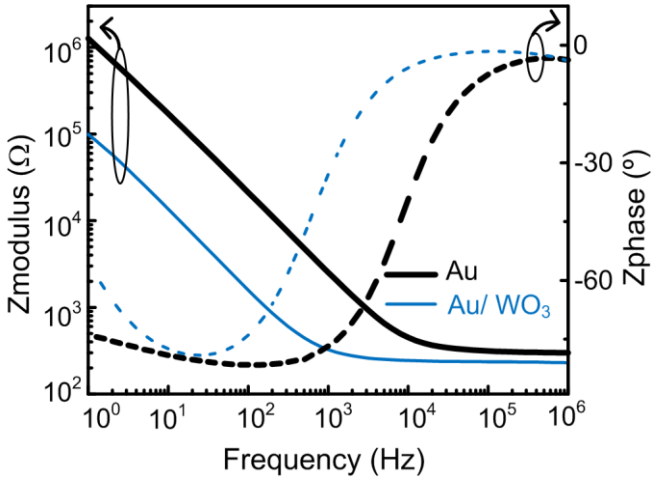

Figure 4.7. Impedance modulus (solid lines) and phase angle (dashed lines) plots of the electrode before and after $WO_3.0.33H_2O$ nanoparticles electrodeposition.

4.4.6. pH Sensitivity and Reproducibility

The pH sensitivity was confirmed by measuring the open circuit voltage when dipping the sensor in commercial buffer solutions for 120 s. The measurements were performed from pH 9 to pH 5 with three distinct sensors (**Figure 4.8a**).

The sensing mechanism for this material, even if not fully understood, is believed to be dependent on the redox reaction involving the double injection of cations and electrons to the structure, thus forming a tungsten oxide bronze with higher conductivity than tungsten oxide (**Equation 4.1**):

$$WO_3 + xe^- + xH^+ \leftrightarrow H_xWO_3 \qquad (4.1)$$

x corresponds to the number of protons (H^+) and electrons (e^-) involved in the reaction and H_xWO_3 represents the tungsten bronze. The reaction mechanism is explained by means of small polaron transitions (formation of W^{5+} sites) for amorphous films and Drude-like free electron scattering for crystalline films. The major difference between these two mechanisms for amorphous and crystalline tungsten oxide films is the electron localization or delocalization.[34-36]

The measured potential is therefore dependent on the pH and if there is a linear relation between these two parameters then it is described to have a Nernstian behavior. The sensitivity of the sensor can, in that case, be obtained by the slope of the linear regression according to the **Equation 4.2**:[3]

$$E = E^0 - (2.303\,RT/F)\cdot pH = E^0 - 0.05916\cdot pH \qquad (4.2)$$

Where E^0 corresponds to the standard electrode potential, R is the gas constant, T the temperature and F the Faraday's constant. The resulting theoretical maximum sensitivity is -59 mV/pH (T = 25 °C). In this situation all space charges are formed, owing to the redox reaction, indicating a good performance of the sensor. The pH sensors produced in this work (**Figure 4.8a**) demonstrated a mean sensitivity value of -56.7 ± 1.3 mV/pH, which is very close to the maximum theoretical value. This confirms the good sensitivity of the WO_3 nanoparticles to the variation of

proton's concentration in solution due to the redox reaction (**Equation 4.1**) involved in the process. The measured potential values of the three sensors in different pH solutions (**Table 4.2**) showed small standard deviation, between 2 and 11 mV, which indicates that the experimental method used to produce these pH sensors is stable and reproducible.

Two gold electrodes, without WO_3 nanoparticles, were also measured for comparison. The mean sensitivity decreased by 50% associated with a higher standard deviation in each point and a lower correlation coefficient of the linear fitting (**Figure 4.8b**). Therefore we confirmed that the pH sensitivity is enhanced due to the presence of the WO_3 nanoparticles layer.

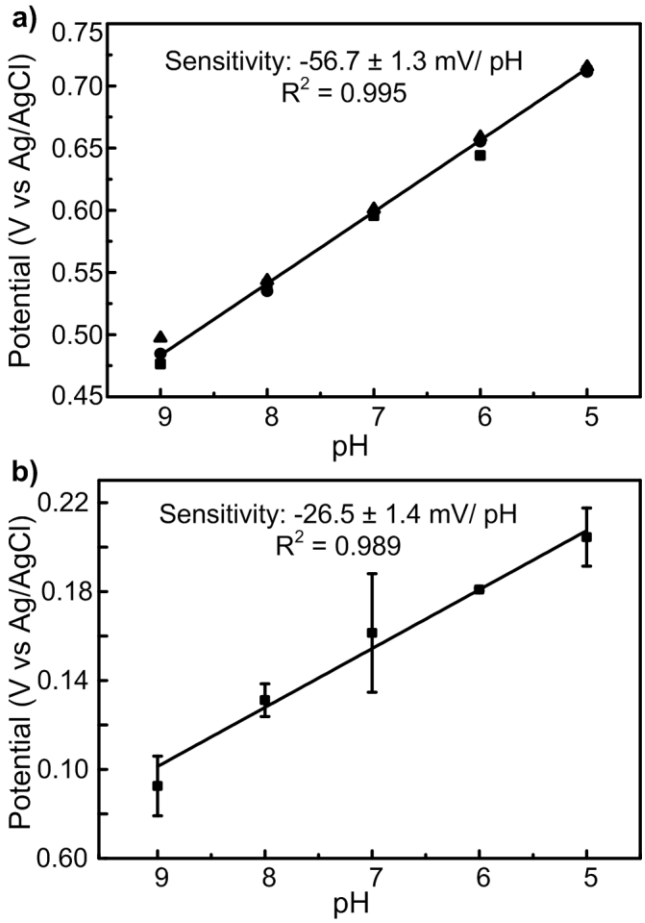

Figure 4.8. pH sensitivity measured from pH 9 to 5 of: a) Au/WO_3 nanoparticles electrodes; b) Au electrode. The sensitivity is indicated inside the graphic.

Table 4.2. Electrochemical potential values of three WO_3 sensors measured from pH 9 to 5 and corresponding sensitivity.

	Sensor 1	**Sensor 2**	**Sensor 3**	**Mean potential**
pH 9 (mV)	476	485	497	486 ± 11
pH 8 (mV)	541	535	544	540 ± 4
pH 7 (mV)	596	599	601	598 ± 3
pH 6 (mV)	644	655	659	653 ± 8
pH 5 (mV)	713	711	715	713 ± 2
pH sensitivity (mV/pH)	-57.6 ± 1.8	-57.4 ± 1.0	-55.2 ± 1.3	-56.7 ± 1.1
	(R^2 = 0.996)	(R^2 = 0.999)	(R^2 = 0.998)	(R^2 = 0.995)

4.4.7. Reversibility

The same sensor was continuously tested in cycles from pH 9 to pH 5 (**Figure 4.9**). This procedure aims to simulate the *in vivo* conditions where the pH sensor will be exposed for long periods to oscillating pH levels. It is clear that the electrochemical potential varies with the pH level but the sensitivity is slightly dependent on the scanning direction (**Table 4.3**). The sensitivity decreased by 11.6 % between the first and third cycle which we believe is related with reactions at the electrode surface and charge saturation sites that occurs during electrode aging.[3]

Further testing is being performed to evaluate the sensor sensitivity dependence on the WO_3 nanoparticles characteristics, such as active surface area and conductivity. Furthermore, the existence of two WO_3 crystallographic structures (**Figure 4.4a**) in the produced dispersion can also contribute to a faster degradation of the sensing layer. Nevertheless, the low hysteresis values, between 6 and 10 mV, obtained for all pH solutions are comparable with the literature[6,19] and confirms the sensor stability.

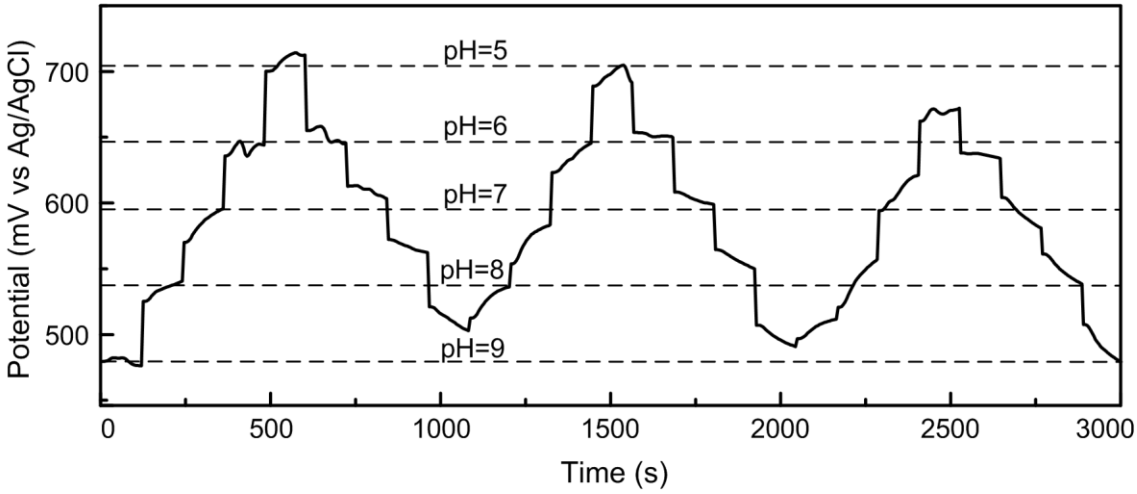

Figure 4.9. Electrochemical potential behavior of the pH sensor during three completes cycles for pH range of 9 to 5 and 5 to 9.

Table 4.3. Electrochemical potential values for the same WO_3 sensor measured from pH 9 to 5 and 5 to 9, during three complete cycles and the resulting sensitivity.

	Cycle 1	**Cycle 2**	**Cycle 3**	**Mean potential**
pH 9 (mV)	476	503	485 ± 4	488 ± 7
pH 8 (mV)	551 ± 7	543 ± 5	526 ± 9	540 ± 7
pH 7 (mV)	600 ± 3	591 ± 5	569 ± 8	587 ± 9
pH 6 (mV)	645 ± 1	648 ± 1	628 ± 4	640 ± 6
pH 5 (mV)	713	692	672	692 ± 10
pH sensitivity –	-57.6 ± 1.8	-48.7 ± 2.7	-47.2 ± 4.5	-50.9 ± 2.9
pH 9 to 5* (mV/pH)	(R^2 = 0.996)	(R^2 = 0.987)	(R^2 = 0.965)	
pH sensitivity –	-50.3 ± 2.6	-50.2 ± 1.7	-48.3 ± 2.0	-49.6 ± 0.7
pH 5 to 9* (mV/pH)	(R^2 = 0.990)	(R^2 = 0.996)	(R^2 = 0.993)	

*The uncertainty corresponds to the standard deviation of the linear regressions and R^2 is the correlation coefficient

4.4.8. Response Time

The sensor's response time was measured for three buffer solutions of different pH. The potential was measured before and after dipping the WO_3 electrode in the buffer solutions for approximately 20 s (**Figure 4.10**). The response time was calculated as the time necessary to reach 90 % of the maximum potential value, varying from 23 to 28 s in this pH range. These values are higher than those reported for other metal oxide electrodes,[37] which is attributed to differences in the structure of the sensor and in the experimental procedure. In our set up the electrode is kept in dry conditions before dipping in the solution therefore, the time to reach the equilibrium between the pH of solution and the electrode interface is higher than when the equilibrium is reached starting with the electrode already immersed in the electrolyte. The porosity of the sensing layer, when using WO_3 nanoparticles, is another factor that contributes to the increase of the time required to reach this equilibrium.[38] Nevertheless, the fact that this sensor can respond to pH variations in commercial buffer solutions, containing a complex mixture of different ions, allow us to conclude that this material has a good selectivity to protons.

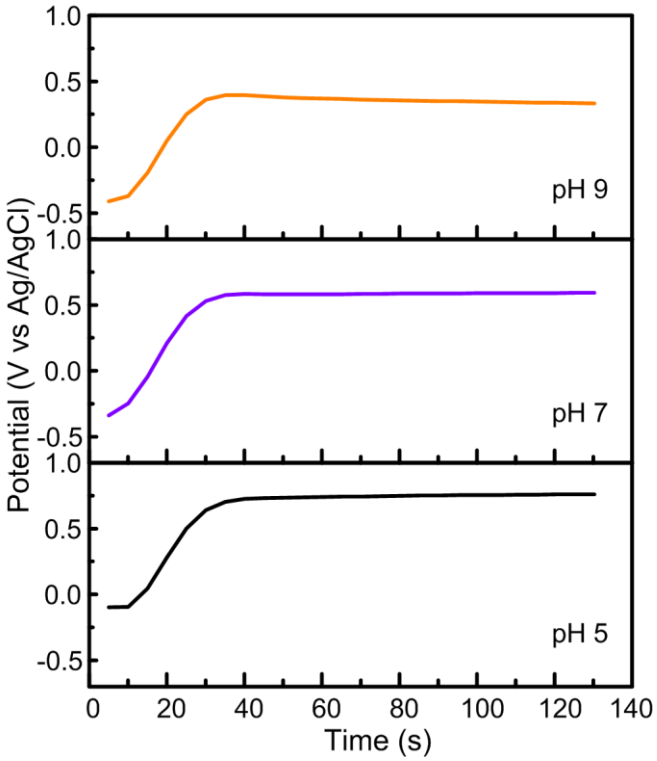

Figure 4.10. Electrochemical potential behavior of the electrode after dipping in buffer solution of pH 9, 7 and 5. The response time was calculated as the time necessary to reach 90% of the maximum potential value.

4.4.9. Proof of Concept: Flexible pH Sensor

In order to prove the potential application of the produced WO_3 sensor in wearable biomedical devices, we developed a flexible reference electrode with the same size and substrate as the pH sensor. The electrochemical potentials were recorded for 120 s in a gelatin-based electrolyte with a curved surface (**Figure 4.11**).

The lower sensitivity of this preliminary test is attributed to the solid electrolyte, namely the low ion mobility and the use of commercial buffer solutions that contains a mixture of different ions, which difficult the occurrence of the redox reaction in the electrode surface. Further studies are required in order to evaluate all the limitations of this concept and improve ion mobility of the solid electrolyte. Nevertheless, the flexibility and conformability of the sensors to curved surfaces were proved to be effective and therefore adaptable to applications as wearable biomedical devices.

As a conclusion, the sensitivity of the WO_3 nanoparticles based pH sensor in aqueous electrolyte is comparable to that of other metal oxides nanoparticles, such as RuO_2,[39] ZnO nanotubes[17] and IrO_x[6] with the advantage of solution processing, low temperature and facile manufacture, being adaptable to different sensor architectures.

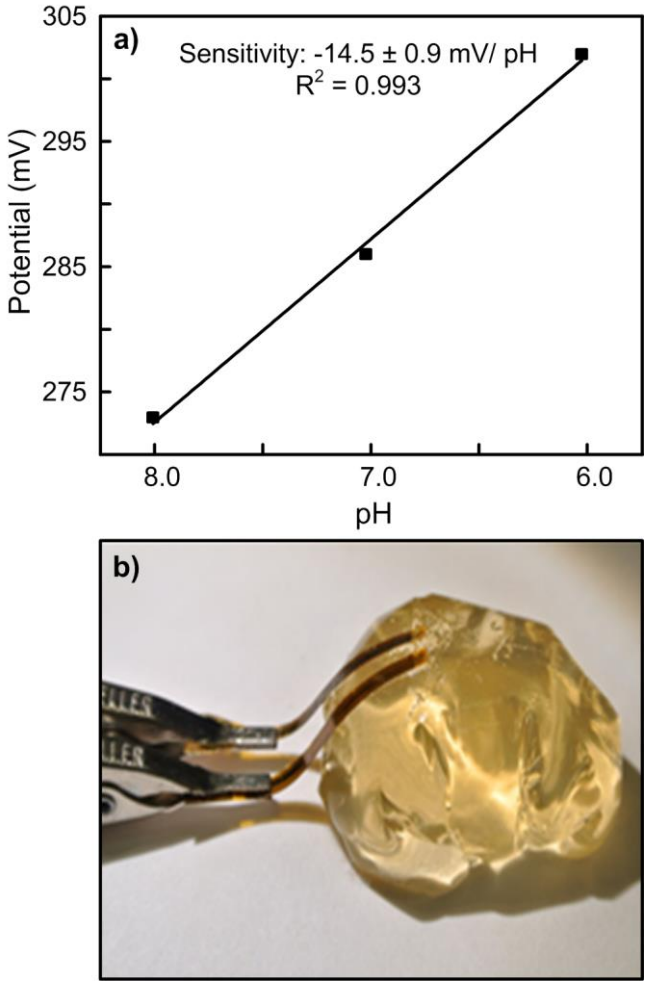

Figure 4.11. a) pH sensitivity of WO_3 sensor using a flexible Ag/AgCl reference electrode in a non-planar surface made of gelatin-based electrolyte; b) photograph of the prototype.

4.5. Conclusions

Flexible sensors based on WO_3 nanoparticles with a high surface area were produced by electrodeposition on gold electrodes with a sensing area of 1 mm^2. The wax printed layer, here used as an insulator, was proven to be cytocompatible and therefore, a good alternative for sensor assembly. The pH sensitivity of these electrodes shows a near-Nernstain response of -56.7 ± 1.3 mV/pH and reversibility was confirmed for three complete cycles in a pH range of 9 to 5.

The application of WO_3 flexible sensors to curved surfaces with a flexible Ag/AgCl reference electrode and solid electrolyte, shows a linear response in the pH range from 8 to 6, with a sensitivity of 14.5 mV/pH but with good possibilities of improvement, for instance, by optimizing the solid electrolyte and assembly processes.

As a conclusion, these results show that WO_3 nanoparticles are a promising material for the development of stable and flexible pH sensors with low cost fabrication processes, low power consumption and small size that can be integrated in biomedical flexible devices without the need for bulky glass reference electrodes. Furthermore, this type of sensor can also be adapted to

other applications in a variety of fields such as food packaging, soil monitoring in agriculture, erosion monitoring in construction or even lubricants.

4.6. Acknowledgments

This work was funded by the Portuguese Science Foundation (FCT-MEC) through project EXCL/CTM-NAN/0201/2012, Strategic Project PEst-C/CTM/LA0025/2013-14 and the FCT-MCTES doctoral grants SFRH/BD/73810/2010 given to L. Santos and SFRH/BD/76004/2011 given to J. Neto. Moreover, this work was also supported by E. Fortunato's ERC 2008 Advanced Grant (INVISIBLE contract number 228144).

4.7. References

(1) Pang, C.; Lee, C.; Suh, K.-Y. Recent Advances in Flexible Sensors for Wearable and Implantable Devices. *J. Appl. Polym. Sci.* **2013**, *130*, 1429–1441.

(2) Segev-Bar, M.; Haick, H. Flexible Sensors Based on Nanoparticles. *ACS Nano* **2013**, *7*, 8366–8378.

(3) Zhou, D. D. Microelectrodes for in-Vivo Determination of pH. In *Electrochemical sensors, biosensors and their biomedical applications*; Academic Press, Inc., 2008; pp. 261–305.

(4) Shanmugasundaram, B.; Gluckman, B. J. Micro-Reaction Chamber Electrodes for Neural Stimulation and Recording. *Conf. Proc. 33rd Annu. Int. Conf. IEEE Eng. Med. Biol. Soc.* **2011**, *2011*, 656–659.

(5) Bandodkar, A. J.; Hung, V. W. S.; Jia, W.; Valdés-Ramírez, G.; Windmiller, J. R.; Martinez, A. G.; Ramírez, J.; Chan, G.; Kerman, K.; Wang, J. Tattoo-Based Potentiometric Ion-Selective Sensors for Epidermal pH Monitoring. *Analyst* **2013**, *138*, 123–128.

(6) Huang, W.-D.; Cao, H.; Deb, S.; Chiao, M.; Chiao, J. C. A Flexible pH Sensor Based on the Iridium Oxide Sensing Film. *Sensors Actuators A Phys.* **2011**, *169*, 1–11.

(7) Kuo, L.-M.; Chen, K.-N.; Chuang, Y.-L.; Chao, S. A Flexible pH-Sensing Structure Using WO_3/IrO_2 Junction with Al_2O_3 Encapsulation Layer. *ECS Solid State Lett.* **2013**, *2*, P28–P30.

(8) Gerlach, G.; Guenther, M.; Sorber, J.; Suchaneck, G.; Arndt, K.-F.; Richter, A. Chemical and pH Sensors Based on the Swelling Behavior of Hydrogels. *Sensors Actuators B Chem.* **2005**, *111-112*, 555–561.

(9) Kinlen, P. J.; Heider, J. E.; Hubbard, D. E. A Solid-State pH Sensor Based on a Nafion-Coated Iridium Oxide Indicator Electrode and a Polymer-Based Silver Chloride Reference Electrode. *Sensors Actuators B Chem.* **1994**, *22*, 13–25.

(10) Pinto, J. V.; Branquinho, R.; Barquinha, P.; Alves, E.; Martins, R.; Fortunato, E. Extended-Gate ISFETs Based on Sputtered Amorphous Oxides. *J. Disp. Technol.* **2013**, *9*, 729–734.

(11) Safavi, A.; Bagheri, M. Novel Optical pH Sensor for High and Low pH Values. *Sensors Actuators B Chem.* **2003**, *90*, 143–150.

(12) Branquinho, R.; Pinto, J. V; Busani, T.; Barquinha, P.; Pereira, L.; Baptista, P. V.; Martins, R.; Fortunato, E. Plastic Compatible Sputtered Ta_2O_5 Sensitive Layer for Oxide Semiconductor TFT Sensors. *J. Disp. Technol.* **2013**, *9*, 723–728.

(13) Wang, X.-D.; Wolfbeis, O. S. Fiber-Optic Chemical Sensors and Biosensors (2008-2012). *Anal. Chem.* **2013**, *85*, 487–508.

(14) Zeng, J.; Hu, M.; Wang, W.; Chen, H.; Qin, Y. NO_2-Sensing Properties of Porous WO_3 Gas Sensor Based on Anodized Sputtered Tungsten Thin Film. *Sensors Actuators B Chem.* **2012**, *161*, 447–452.

(15) Barquinha, P.; Martins, R.; Pereira, L.; Fortunato, E. *Transparent Oxide Electronics*; John Wiley & Sons, Ltd, 2012.

(16) Bakker, E.; Pretsch, E. Modern Potentiometry. *Angew. Chemie* **2007**, *46*, 5660–5668.

(17) Fulati, A.; Ali, S. M. U.; Riaz, M.; Amin, G.; Nur, O.; Willander, M. Miniaturized pH Sensors Based on Zinc Oxide Nanotubes/Nanorods. *Sensors* **2009**, *9*, 8911–8923.

(18) Vieira, N. C. S.; Figueiredo, A.; Faceto, A. D.; de Queiroz, A. A. A.; Zucolotto, V.; Guimarães, F. E. G. Dendrimers/TiO_2 Nanoparticles Layer-by-Layer Films as Extended Gate FET for pH Detection. *Sensors Actuators B Chem.* **2012**, *169*, 397–400.

(19) Kurzweil, P. Metal Oxides and Ion-Exchanging Surfaces as pH Sensors in Liquids: State-of-the-Art and Outlook. *Sensors* **2009**, *9*, 4955–4985.

(20) Yuan, S.-J.; He, H.; Sheng, G.-P.; Chen, J.-J.; Tong, Z.-H.; Cheng, Y.-Y.; Li, W.-W.; Lin, Z.-Q.; Zhang, F.; Yu, H.-Q. A Photometric High-Throughput Method for Identification of Electrochemically Active Bacteria Using a WO_3 Nanocluster Probe. *Sci. Rep.* **2013**, *3*, 1315.

(21) Vernardou, D.; Drosos, H.; Spanakis, E.; Koudoumas, E.; Savvakis, C.; Katsarakis, N. Electrochemical and Photocatalytic Properties of WO_3 Coatings Grown at Low Temperatures. *J. Mater. Chem.* **2011**, *21*, 513.

(22) Natan, M. J.; Mallouk, T. E.; Wrighton, M. S. pH-Sensitive WO_3-Based Microelectrochemical Transistors. *J. Phys. Chem.* **1987**, *91*, 648–654.

(23) Choi, Y.-G.; Sakai, G.; Shimanoe, K.; Yamazoe, N. Wet Process-Based Fabrication of WO_3 Thin Film for NO_2 Detection. *Sensors Actuators B Chem.* **2004**, *101*, 107–111.

(24) Heidari, E. K.; Zamani, C.; Marzbanrad, E.; Raissi, B.; Nazarpour, S. WO_3-Based NO_2 Sensors Fabricated through Low Frequency AC Electrophoretic Deposition. *Sensors Actuators B Chem.* **2010**, *146*, 165–170.

(25) Wang, J.; Khoo, E.; Lee, P. S.; Ma, J. Synthesis, Assembly, and Electrochromic Properties of Uniform Crystalline WO_3 Nanorods. *J. Phys. Chem. C* **2008**, *112*, 14306–14312.

(26) Deepa, M.; Kar, M.; Agnihotry, S. A. Electrodeposited Tungsten Oxide Films: Annealing Effects on Structure and Electrochromic Performance. *Thin Solid Films* **2004**, *468*, 32–42.

(27) Yang, J.; Jiao, L.; Zhao, Q.; Wang, Q.; Gao, H.; Huan, Q.; Zheng, W.; Wang, Y.; Yuan, H. Facile Preparation and Electrochemical Properties of Hierarchical Chrysanthemum-like $WO_3 \cdot 0.33H_2O$. *J. Mater. Chem.* **2012**, *22*, 3699.

(28) Yayapao, O.; Thongtem, T.; Phuruangrat, A.; Thongtem, S. CTAB-Assisted Hydrothermal Synthesis of Tungsten Oxide Microflowers. *J. Alloys Compd.* **2011**, *509*, 2294–2299.

(29) Deepa, M.; Sharma, N.; Varshney, P.; Varma, S. P.; Agnihotry, S. A. FTIR Investigations of Solid Precursor Materials for Sol-Gel Deposition of WO_3 Based Electrochromic Films. *J. Mater. Sci.* **2000**, *35*, 5313 – 5318.

(30) Lu, Z.; Kanan, S. M.; Tripp, C. P. Synthesis of High Surface Area Monoclinic WO_3 Particles Using Organic Ligands and Emulsion Based Methods. *J. Mater. Chem.* **2002**, *12*, 983–989.

(31) Gu, Z.; Li, H.; Zhai, T.; Yang, W.; Xia, Y.; Ma, Y.; Yao, J. Large-Scale Synthesis of Single-Crystal Hexagonal Tungsten Trioxide Nanowires and Electrochemical Lithium Intercalation into the Nanocrystals. *J. Solid State Chem.* **2007**, *180*, 98–105.

(32) Vemuri, R. S.; Bharathi, K. K.; Gullapalli, S. K.; Ramana, C. V. Effect of Structure and Size on the Electrical Properties of Nanocrystalline WO_3 Films. *ACS Appl. Mater. Interfaces* **2010**, *2*, 2623–2628.

(33) Weiland, J. D.; Anderson, D. J.; Humayun, M. S. In Vitro Electrical Properties for Iridium Oxide versus Titanium Nitride Stimulating Electrodes. *IEEE Trans. Biomed. Eng.* **2002**, *49*, 1574–1579.

(34) Lee, S.-H.; Je, M.; Cheong, H. M.; Ozkan, E.; Tracy, E. C.; Deb, S. K. Effect of Crystallinity on Electrochromic Mechanism of Li_xWO_3 Thin Films. *Solid State Ionics* **2003**, *156*, 447–452.

(35) Lampert, C. M. Electrochromic Materials and Devices for Energy Efficient Windows. *Sol. Energy Mater.* **1984**, *11*, 1–27.

(36) Hotchandani, S.; Bedja, I.; Fessenden, R.; Kamat, P. Electrochromic and Photoelectrochromic Behavior of Thin WO_3 Films Prepared from Quantum Size Colloidal Particles. *Langmuir* **1994**, *10*, 17–22.

(37) Da Silva, G. M.; Lemos, S. G.; Pocrifka, L. A.; Marreto, P. D.; Rosario, A. V; Pereira, E. C. Development of Low-Cost Metal Oxide pH Electrodes Based on the Polymeric Precursor Method. *Anal. Chim. Acta* **2008**, *616*, 36–41.

(38) Olthuis, W.; Robben, M. A. M.; Bergveld, P.; Bos, M.; Van der Linden, W. E. pH Sensor Properties of Electrochemically Grown Iridium Oxide. *Sensors Actuators B Chem.* **1990**, *2*, 247–256.

(39) Maurya, D. K.; Sardarinejad, A.; Alameh, K. High-Sensitivity pH Sensor Employing a Sub-Micron Ruthenium Oxide Thin-Film in Conjunction with a Thick Reference Electrode. *Sensors Actuators A Phys.* **2013**, *203*, 300–303.

4.8. Supporting Information

Electrodepositon set-up

The sensing layer was produced by electrodeposition of a WO_3 nanoparticles dispersion with constant current appliance of 20 µA during 900 s in a three electrode configuration.

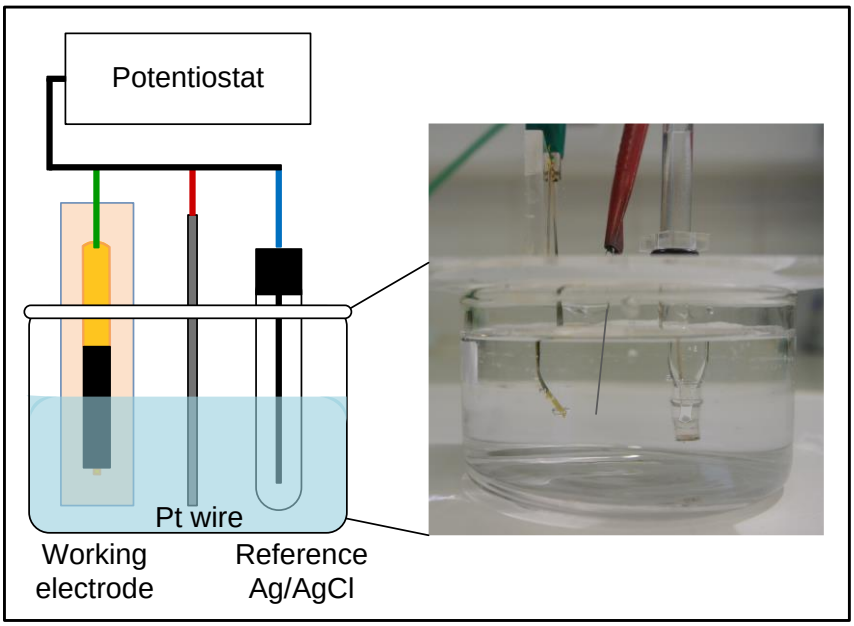

Figure S 4.1. Schematic and real image of the electrodeposition set-up composed by WO_3 nanoparticles dispersion in water, flexible gold working electrode, platinum wire as counter electrode and Ag/AgCl as reference electrode.

Electrochemical impedance spectroscopy of Ag/AgCl flexible reference electrode

Electrochemical impedance spectroscopy (EIS) was performed during the production of the reference electrode, before (after anodization of the Ag layer) and after saturation in 3 M KCl solution. This process enabled the stabilization of the reference electrode.

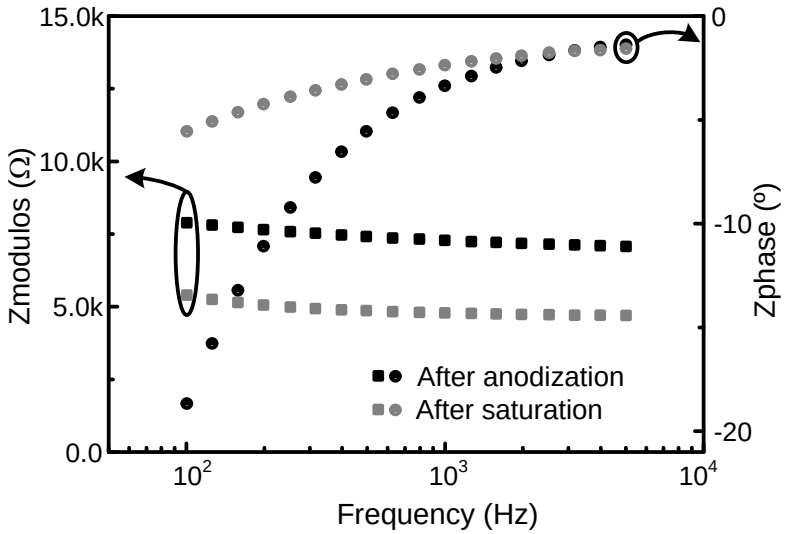

Figure S 4.2. Impedance modulus and phase angle of the flexible reference electrode after anodization of the Ag layer and saturation in KCl solution.

Chapter 5. WO_3 FOR BIOSENSOR APPLICATIONS

The contents of **Chapter 5** were adapted from the publication:

"L. Santos, C. Silveira, E. Elangovan, J. P. Neto, D. Nunes, L. Pereira, R. Martins, J. Viegas, J. J. G. Moura, S. Todorovic, M. G. Almeida, E. Fortunato, *Synthesis of WO_3 nanoparticles for biosensing applications*, **Sensors and Actuators B**, **2015** – Under revision"

5.1. Abstract

Direct electron transfer with redox proteins, in third generation biosensors, is already proved to be favored on electrodes modified with nanoparticles. In this work, different crystallographic and morphologic structures of tungsten oxide (WO_3) nanoparticles are modified by hydrothermal synthesis at 180 ºC. The electrochemical properties of WO_3 nanoparticles deposit on ITO electrodes are investigated and the analytical performance of the nitrite biosensor is presented as proof of concept. Despite the inherent features of each nanostructure, the heterogeneous electron transfer with the WO_3 nanoparticles modified electrodes is thoroughly improved and, very importantly, the cytochrome *c* nitrite reductase (cc*NiR*) enzyme is able to keep their biological function. When compared with bare commercial ITO electrodes, the exchange rate constant of WO_3/ITO electrodes with cytochrome *c* increased one order of magnitude, while the analytical parameters of the WO_3/ITO electrodes response to nitrite (the Michaelis-Menten constant is 47 µM and sensitivity of 2143 mA M^{-1} cm^{-2}) are comparable to those reported for carbon based electrodes. Therefore, these metal oxide nanoparticles are good alternative materials for electrochemical applications, such as non-mediated biosensors.

5.2. Introduction

Nanostructured metal oxides have attracted considerable attention due to their advantages over their bulk counterparts. Spatial confinement with large fraction of surface atoms, high surface energy, strong surface adsorption and increased surface to volume ratio are some of the important characteristics that make these materials ideal candidates for many applications in the fields of chemistry, materials and engineering, as well as in the frontiers of medicine [1,2].

In electrochemistry, nanoparticles based electrodes enable faster electron transfer kinetics, reduced overpotentials, increased electroactive surface areas, sometimes triggering electrochemical reactions that are not feasible with bulk electrodes [3,4]. Furthermore, the direct electron transfer with redox proteins can be favored not only due to the high surface area but also to the biocompatibility and improved interactions. Despite the huge variety of nanoparticles with different chemical natures, extensive studies are still being made to find new electrode materials, and surface functionalizations. Nanostructured metal oxides like TiO_2 and ZnO are well-recognized promoters of electron transfer with heme proteins, due to their electrical and optical properties [5–10]. However, to the best of authors' knowledge, only few studies employed nanostructured WO_3 as electron transfer facilitators: Feng et al. [11] reported that electrodeposited mesoporous WO_3 films enhanced the hemoglobin protein loadings, accelerated interfacial electron transfer and improved thermal stability of the adsorbed protein; Deng et al. [12] produced a WO_3 nanostructures based electrode that facilitated the electron transfer of cytochrome *c* (cyt *c*) protein; and Liu et al.[13] synthesized WO_3 nanowires with a high length-diameter ratio and then use them to immobilize hemoglobin and fabricate a nitrite biosensor. Actually, the unique properties of WO_3 such as reversible change of conductivity, high sensitivity, selectivity and biocompatibility

make this material a very promising candidate for the construction of novel (bio)sensing electrodes [14].

Tungsten oxide (WO_3) is a well-known n-type wide band gap semiconductor, inexpensive, environmentally friendly and chemically stable [15]. It is suitable for different applications, such as electrochromic devices [16–18], photocatalysts [19,20], and gas sensors [21–23]. Several techniques, both by physical and chemical routes, have been reported for the production of WO_3 nanoparticles [16,24–26]. Hydrothermal synthesis has several advantages like being simple and requiring low processing temperatures, offers a good homogeneity and control over the shape and size of the structures, and it is cost effectiveness, which are critical characteristics for large scale production as demanded by industries [25,26].

In this work, indium tin oxide (ITO) glass electrodes were modified with three types of WO_3 nanoparticles and applied in the fabrication of the nitrite biosensor by immobilization of the cytochrome c nitrite reductase (cc*NiR*) enzyme.

Previously characterized from the bioelectrochemical viewpoint, the multi-heme enzyme, cc*NiR* (**Figure 5.1**) can be regarded as a suitable biological model to study electrode materials. In general, it shows facile direct electron transfer in carbon electrodes such as, pyrolytic graphite and carbon nanotubes, while preserving the catalytic activity towards nitrite reduction [27–29]. In fact, cc*NiR* plays an important role in the nitrogen cycle where it catalyzes the nitrite reduction to ammonia is a six-electron transfer reaction (**Equation 5.1**) [30]:

$$\mathbf{NO_2^- + 6e^- + 8H^+ \rightarrow NH_4^+ + 2H_2O} \qquad \mathbf{(5.1)}$$

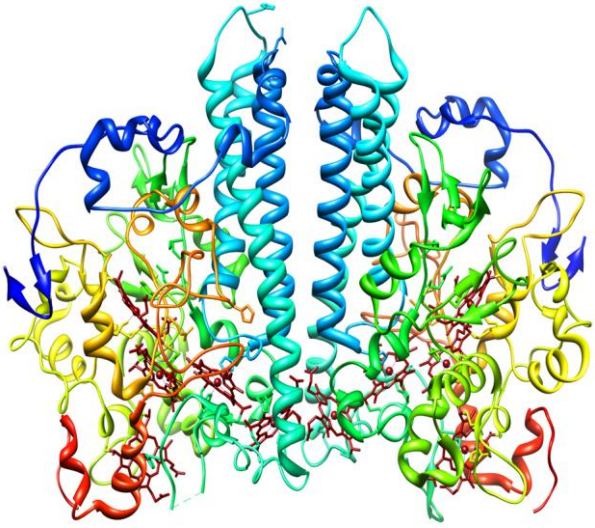

Figure 5.1. Representation of the 3D structure of cytochrome c nitrite reductase, with the heme groups coordinating a central iron atom (deep red spheres).

Herein, we show the potentialities of WO_3 nanoparticles in the low cost production of direct electron transfer based biosensors. The bioelectrodes composed of cc*NiR* in direct contact with WO_3 nanoparticles revealed a good electrocatalytic response in the presence of nitrite, paving the way for the development of non-mediated amperometric biosensors.

5.3. Experimental Section

Hydrothermal synthesis of nanostructured WO_3

All chemicals were of analytical grade and used without further purification. For the hydrothermal synthesis of WO_3 nanoparticles, $Na_2WO_4.2H_2O$ (0.4 g, Fluka, 99 %) was first dissolved in deionized water with NaCl (0.15 g, Panreac, 99.5 %) as structure directing agent [31] and then acidified with a variable amount of 3 M HCl solution (Fluka, 37 %) so that the final concentration of 2.7 (W1), 1.5 (W2) and 0.3 M (W3) was reached. The solution was transferred to a 23 mL PTFE chamber, set inside a stainless steel autoclave (4745 general purpose vessel, Parr) and installed in the oven (L3/11/B170, Nabertherm). The synthesis conditions were set for 180 °C during 2 hour and let cooling down to room temperature (RT) inside the oven. The synthesized product was collected by centrifugation at 3000 rpm for 2 min (F140, Focus instruments) and washed thrice with water. The resultant powder was finally dried in the oven (TK4067, EHRET) at 60 ºC for at least 8 hours.

Crystallographic and morphologic characterization of WO_3 nanoparticles were performed by SEM (Auriga SEM-FIB, Zeiss), TEM (Tecnai-G2, FEI) and XRD (XPert PRO, PANalytical). The specific surface area was calculated using the Brunauer–Emmett–Teller (BET) method based on the nitrogen adsorption isotherm obtained at 77 K in a constant volume adsorption apparatus (ASAP 2010 V1.01B Micromeritics). Hydrodynamic diameter of the WO_3 dispersions was confirmed by Dynamic Light Scattering (DLS) technique (W130i Avid Nano). Electrochemical impedance spectroscopy (EIS) was performed in potentiostat (600TM Gamry Instruments) for WO_3 powders in pellets formed at a pressure of 8 tons in a nanopowder hydraulic press, with a diameter of approximately 1 cm and a thickness of 1-3 mm. The electrochemical cell consisted of two gold electrodes in each side of the pellet compacted in a homemade cell and the experimental conditions were set as 10 mV of alternative voltage in a frequency range of 1-10^6 Hz.

Electrode preparation and characterization

Nanoparticles were first dispersed in water (weight fraction 0.1 %), sonicated for 5 min and filtered (0.45 µm syringe filter, Roth) prior to deposition. Commercial ITO glass (10 Ω/sq, Xinyan Technology) was used as working electrode. After cleaning and activation for 30 min in UV/ ozone (PSD-UV, Novascan), 10 µL of WO_3 dispersion was drop casted on the electrode surface followed by 1 hour annealing at 120 ºC. Electrochemical characterization of WO_3/ITO electrodes was performed in a three-electrode electrochemical cell (10 mL) composed of the working electrode, a Ag/AgCl reference electrode and a platinum wire as counter electrode (both from Radiometer). The measurements were performed with a potentiostat Autolab PGSTAT12 (Eco-Chemie) monitored by GPES 4.9 software (Eco-Chemie). The experiments were carried out at RT (20 ± 2 °C) in argon purged solutions (10 min); an argon atmosphere was also maintained inside the cell during measurements (**Figure S 5.1**). The WO_3/ITO electrodes were characterized by EIS and cyclic voltammetry (CV) at a 50 mV/s scan rate in 0.05 M tris-HCl pH 7.6 buffer with 0.1 M KCl, as supporting electrolyte. The Nyquist plots were obtained with an alternative voltage of 10 mV in a frequency range of 1-10^6 Hz. The redox probe $K_3Fe(CN)_6$ was prepared as 1 mM solution in 1 M KCl, while the cyt *c* (from horse heart, Sigma) was used as a 200 µM solution in 0.05 M phosphate buffer pH 7.6 and 0.1 M KNO_3. For *cc*NiR immobilization and good electrical contact

with the ITO glass, 5 µL of enzyme (1 mg/mL, 7 µM)[32] and 5 µL of WO_3 nanoparticles dispersion were deposited at the same time on the electrode and dried at 50 ºC for 1 hour. To test the activity to nitrite, small volumes of sodium nitrite standard solutions were added to the electrochemical cell containing 0.05 M tris-HCl pH 7.6 buffer with 0.1 M KCl as supporting electrolyte. The cell was argon purged after each addition while stirring and the CV (50 mV/s) was recorded. Catalytic currents were determined at the inversion potential (-0.8 V). All potentials are quoted versus the Ag/AgCl reference. Each experiment was performed in a new electrode. Raman and resonance Raman (RR) experiments were performed with a confocal microscope coupled to a Raman spectrometer (Jobin Yvon U1000) equipped with 1200 l/mm grating and liquid-nitrogen-cooled back-illuminated CCD detector. The samples were excited with the 413 nm line from a krypton ion laser (Coherent Innova 302). Raman spectra of WO_3 materials were measured with variable laser power (5-13 mW) and accumulation time (30 – 60 s), at RT, at different spots of the film deposited on a microscopic glass. RR spectra of c*c*NiR deposited on WO_3 films were typically measured with 1.2 mW laser power and 5 s accumulation time, at RT. The same samples were used to measure Raman spectra of WO_3 (in the presence of c*c*NiR) by focusing the laser onto the WO_3 film plane and increasing the laser power and accumulation time as described above.

5.4. Results and Discussion

5.4.1. WO_3 Nanoparticles Characterization

Tungsten oxide (WO_3) nanoparticles were hydrothermally synthesized from sodium tungstate (Na_2WO_4) precursor following the procedure described by Wang et al. [31] In this work, three different acidities (2.7, 1.5 and 0.3 M of HCl) were used with a constant amount of precursor and structure-direct agent (NaCl). The syntheses were achieved at 180 ºC for 2 hours in a conventional oven and the crystallographic and morphologic characterization was performed in the resulting powders.

The XRD patterns (**Figure 5.2a**), confirms that the powder synthesized at 2.7 M HCl (sample W1) is monoclinic WO_3 (*m*-WO_3), while the powders synthesized at 1.5 M HCl (sample W2) and 0.3 M HCl (sample W3) are orthorhombic hydrated WO_3 (*ortho*-$WO_3 \cdot 0.33H_2O$). In pure samples (W1 and W3), the diffraction peak from (002) plane is observed at a diffraction angle of ~23°. The pattern from W2 evidences the presence of a secondary product that cannot not be identified since the identified peaks (*) do not match with any of the reported ICDD data for crystalline WO_3, sub-stoichiometric WO_x or its hydrates, thus suggesting that the corresponding structure derives from the slow growing of the nanoparticles clusters under employed experimental conditions. The influence of HCl concentration to the WO_3 crystal growth is still not fully understood but it is believed that there is the interference of both ions (H^+ and Cl^-) in the reaction. The formation of the clusters only occurs at pH below 2, therefore the speed of the reaction is affected with protons' concentration and the chloride ions act as capping agent, thus promoting the growth of the crystals in a specific direction.[32]

In the literature, the particular peak at 10º was found in solution processed WO_3 films deposited at low temperatures which presented some degree of nanocrystallinity also with no clear

evidence of the structure associated.[33] The wider diffraction peaks from the sample W2 are an indicator of the small crystallite sizes obtained (according to the Scherrer equation).[34] This conclusion was further evidenced by Energy Dispersive Spectroscopy (EDS) that detected only tungsten and oxygen elements with no evidence of any contaminant (data not shown).

Tungsten oxides follow a well-known ReO_3-type structure which are built up of layers containing distorted corner-shared WO_6 octahedra stacked along (002) plane, as represented in **Figure 5.2b-c**.[35,36] The stable *m*-WO_3 can have an infinite array of corner-sharing WO_6 octahedra stacked in an arrangement held together by van der Waals forces. The stacking of such planes along the z axis leads to the formation of tunnels between these octahedra. The *ortho*-$WO_3 \cdot 0.33H_2O$ structure includes two types of octahedra, one is formed of W-O covalent bonds and the other includes two types of terminal bonds (W=O and W-OH). This structure may restrict stacking along the z axis due to the weak interaction between adjacent layers.[37]

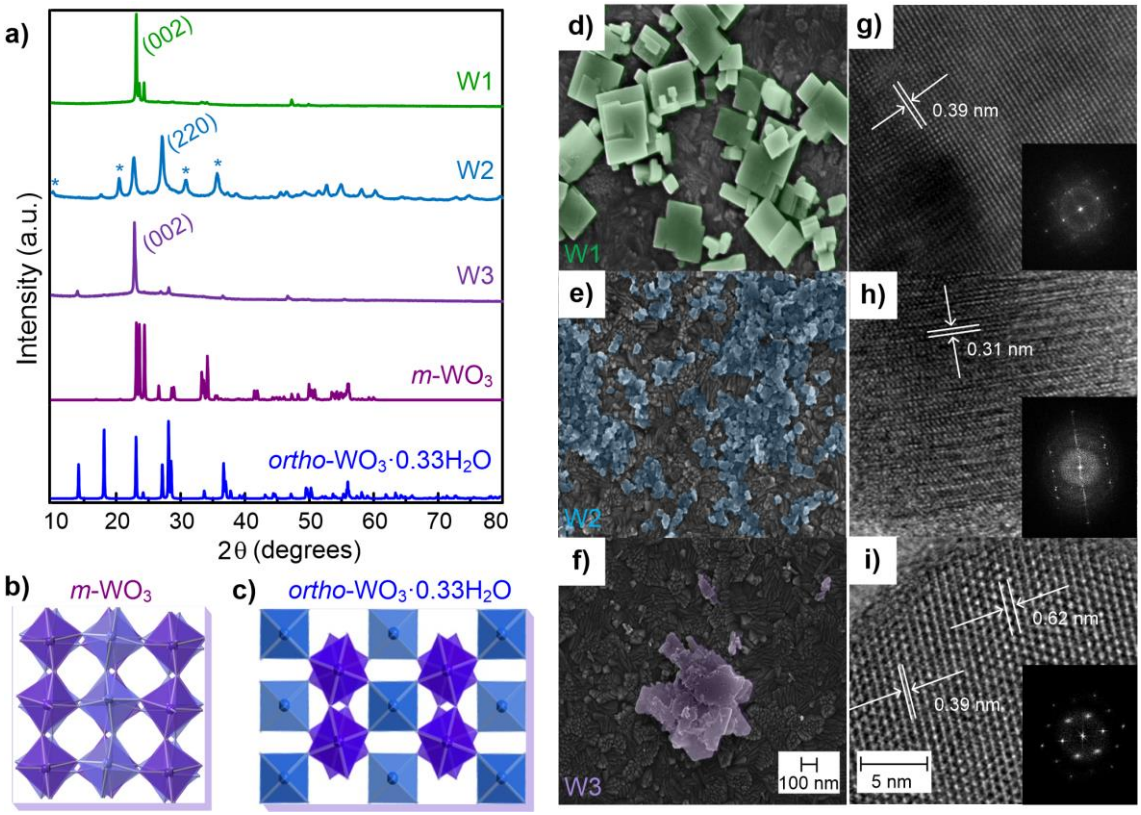

Figure 5.2. *Left side:* a) XRD patterns of hydrothermally synthesized WO_3 powders; W1) 2.7 M, W2) 1.5 M and W3) 0.3 M of HCl (reference diffractograms for *m*-WO_3, ICDD: 43-1035 and *ortho*-$WO_3 \cdot 0.33H_2O$, ICDD: 01-072-0199 has been placed at bottom), b) Representation of (002) crystallographic plane projection (performed in crystal maker© software) for *m*-WO3 and c) *ortho*-$WO_3 \cdot 0.33H_2O$. *Right side:* SEM microstructures and TEM lattice-images of hydrothermal synthesized WO_3 nanoparticles: d), g) W1; e), h) W2; and f), i) W3. SEM images were false colored for better visualization of the nanoparticles structure while the darker background corresponds to the ITO electrode. The inset on TEM lattice-images shows the corresponding FFT images. The size scales of SEM and TEM images are the same in the three samples.

Raman spectroscopy (RS) was utilized to further characterize structural features of the W1, W2 and W3 samples. The spectra (**Figure S 5.2**) reveal vibrational modes characteristic for WO_3, indicating hydrated W2 and W3 and more ordered W1 sample.[21,38,39] To confirm the detailed crystallographic and morphologic characteristics of the obtained nanostructures further investigations were performed by SEM (**Figure 5.2d-f**), TEM and Fast Fourier Transform (FFT) images (**Figure 5.2g-i**). The TEM images captured at low magnification (not shown here) show similar microstructures as observed in SEM, revealing the nanoslab-shape of the nanoparticles. The distance between the centers of 2 successive dots (lattice spacing), which was calculated as an average value between 10 such subsequent dots, is indicated on corresponding TEM images. The FFT image shows the view of different lattice planes through a particular zone axis. In W1, the observed lattice spacing of 0.39 nm corresponds to the (020) lattice plane of the *m*-WO_3. The lattice spacing measured in W3, 0.62 nm (brighter spots) and 0.39 nm (closest spots) correspond to (020) and (002) planes of *ortho*-$WO_3 \cdot 0.33H_2O$, respectively. The FFT images can be indexed to the [100] zone axis of *m*-WO_3 (in the sample W1) and to [001] zone axis of *ortho*-$WO_3 \cdot 0.33H_2O$ (in sample W3) [40]. Sample W2 shows a more irregular lattice and FFT images which cannot be clearly identified. Nevertheless, the area shown in the image with a spacing of 0.31 nm can be attributed to the (220) plane of *ortho*-$WO_3 \cdot 0.33H_2O$, which corroborates with the predominant peak observed in XRD (**Figure 5.2a**).

The size of the WO_3 nanoparticles was established by DLS technique and compared with SEM analysis (**Table 5.1**). The DLS results show slightly larger nanoparticles than SEM analysis that can be attributed to the hydrodynamic diameter that includes the solvent layer surrounding the nanoparticles, measured by DLS. Nevertheless, the proximity of the results is a good evidence of the stability and dispersion of the solution. Another feature of the nanoparticles relevant for their electrochemical performance is the active surface area, which was measured by nitrogen adsorption technique and by applying the Brunauer–Emmett–Teller (BET) equation (**Table 5.1**). Both nanoparticles characterized as *ortho*-$WO_3 \cdot 0.33H_2O$ presented higher surface areas, possibly, the crystallographic structure directly influences this result due to the presence of terminal groups (W=O and W-OH) in the hydrated structure [41].

Table 5.1. Comparison of nanoparticle sizes measured by SEM and DLS techniques along with BET surface areas and fitted bulk conductivity calculated from Nyquist plots of the 3 samples.

	Size measured in SEM (nm)	**DLS diameters (nm)**	**BET surface area ($m^2\ g^{-1}$)**	**Conductivity ($S\ cm^{-1}$)**
W1	190 ± 90	240 ± 50	12.05	3.0×10^{-6}
W2	46 ± 16	50 ± 13	73.74	4.2×10^{-6}
W3	234 ± 148	310 ± 83	40.84	7.4×10^{-6}

The electrochemical impedance spectroscopy (EIS) of WO_3 nanopowder was performed in a two electrode set-up with gold electrodes on both sides of the WO_3 pellet. Nyquist plots which

represent real versus imaginary impedance (**Figure S 5.3**), show a semicircle in the high frequency and a sloped straight line in the low frequency region. Conductivity (**Table 5.1**) was calculated from the resistance (*R*) fitting obtained by EIS and using the **Equation 5.2**:

$$\sigma = l/ (R \times A) \quad (5.2)$$

The thickness (*l*) and area (*A*) of the pellets were also considered for this calculation. Due to the structural particularities of the hydrated *ortho*-$WO_3 \cdot 0.33H_2O$ polymorph the conductivity is higher than the *m*-WO_3 structure.

5.4.2. Electrochemical Properties of WO_3 Films

Modified WO_3/ITO electrodes were produced by drop casting a water dispersion of WO_3 nanoparticles (weight fraction 0.1 %) on a commercial ITO glass substrate (**Figure S 5.4**). The distribution of the nanoparticles can be verified by SEM, as shown in **Figure 5.2d-f**. After each electrochemical experiment the surface of the electrode was rinsed with water and further analyzed by SEM; no visible difference was observed when comparing with the as-prepared electrode, thereby confirming the good adherence of the WO_3 nanoparticles to the ITO substrate.

The EIS data were compared between bare ITO and WO_3/ITO electrodes (**Figure 5.3a** and **Figure S 5.3b**). The W2/ITO electrode showed an atypical behavior described by a larger semicircle that characterizes the charge transfer resistance. This result suggests that the electron transfer is less efficient in the W2/ITO films, which could possibly reduce the sensitivity of the sensor [4]. In fact, the cyclic voltammogram (CV) of this electrode (**Figure 5.3b**) shows higher capacitive currents; the smaller particle size of the W2 nanopowder probably produces a more compact thin film that may somewhat obstruct the ITO surface, resulting in a less conductive electrode. The cathodic and anodic peaks observed in the range of -0.4 to -0.8 V are related to the electrochemical reduction/oxidation of tungsten coupled to proton intercalation/deintercalation, respectively (**Equation 5.3**). This results in the reversible formation of tungsten bronze (H_xWO_3) [42]:

$$\mathbf{WO_3 + \mathit{x}H^+ + xe^- \leftrightarrow H_xWO_3} \quad (5.3)$$

This reaction is much more evident with the W2/ITO electrode, which, as mentioned before, might be due to a higher number of nanoparticles and, consequently, to a higher number of available redox sites, thereby increasing the current peaks.

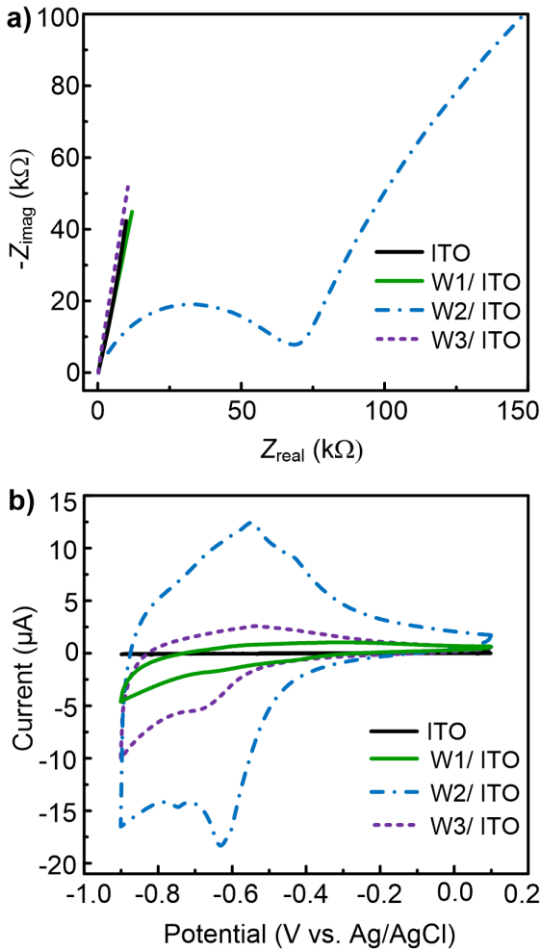

Figure 5.3. Electrochemical characterization of ITO and WO_3/ITO electrodes. a) Nyquist plots measured with an alternative voltage of 10 mV and frequency range 1-10^6 Hz; b) cyclic voltammograms performed at a scan rate 50 mV/s. The supporting electrolyte was 0.1 M KCl in 0.05 M tris-HCl pH 7.6 buffer.

The WO_3/ITO modified electrodes were then tested with the redox probe ferrocyanide ($Fe(CN)_6^{4-}$/ $Fe(CN)_6^{3-}$). Since the WO_3 nanoparticles typically have a pKa around 2.5 [43], it was expected that at neutral pH a repulsion between WO_3 and the ferrocyanide anions would occur. However, a well-defined pair of oxidation and reduction peaks was observed by CV (**Figure S 5.5**). The peak currents varied linearly with the square root of the scan rate, demonstrating a typical diffusion controlled electrochemical process. The redox process showed a good reversibility, with a current peak ratio (Ic/Ia) of 1.03 ± 0.02, independent of the scan rate, and peak separations (ΔEp) around 65 ± 10 mV. These results are in good agreement with a reversible one-electron transfer *(*Ic/ Ia = 1 and ΔEp = 59 mV) [44,45]. Moreover, the formal potential (E^0 = (Ec + Ea)/2 = 272 mV) is in accordance with the reported values [46]. The response obtained on the control electrode (bare ITO), with ΔEp and Ic/Ia values of 193 mV and 0.89, respectively, clearly indicates that the ferrocyanide electrochemistry is improved in the presence of the nanoparticles.

The electroactive area of the different electrodes was determined using the Randles-Sevick equation **(5.1)**.[44–46] Assuming a Nernstian behavior and diffusion controlled process, the peak current is related to the potential scan rate by **equation 5.4**:

$$\boldsymbol{I}\mathbf{p} = \mathbf{2.69} \times \mathbf{10^5}\, \boldsymbol{n^{3/2}\, A C D^{1/2}\, v^{1/2}} \qquad \textbf{(5.4)}$$

Where *I*p is the current peak (A), *n* the number of electrons, *A* the area (cm^2), *C* the concentration (mol cm^{-3}), *D* the diffusion coefficient (7.18×10^{-6} cm^2 s^{-1}) [46] and *v* the scan rate (V s^{-1}).

The electrochemical assays were performed in the buffer solution 0.05 M tris-HCl, pH 7.6. The electroactive area values (0.35 cm^2) were similar for the three measured electrodes and about 2-3 times larger than the electroactive area of the ITO electrode (0.17 cm^2) and the geometrical area (0.13 cm^2), respectively. Therefore, the roughness of the deposited WO_3 films, combined with the high surface area of the nanoparticles enlarges the electroactive area of the electrodes.

The kinetics of the heterogeneous electron transfer of cyt *c* (in solution) with the three different WO_3 nanoparticles was compared. A pair of redox peaks is seen in all CVs, in the scan rate range 35 - 750 mV/s, as a result of the direct electron transfer of the heme Fe^{III}/Fe^{II} redox couple. The process is diffusion controlled as indicated by the linear dependence of the peak current with the square root of scan rate (**Figure** 5.**4**). The parameters *I*c/*I*a, Δ*E*p and E^0 of the redox reaction were further compared to evaluate the reversibility of this redox system (**Table 5.2**). The results for all WO_3/ITO electrodes are consistent with a quasi-reversible one-electron transfer reaction.

But, as in the case of ferrocyanide, the electrochemistry of cyt *c* is favored in the presence of WO_3 nanoparticles when compared with bare ITO. This result indicates that the nanostructured WO_3 interface facilitates not only the electron exchange with small inorganic redox species but also with a much bigger and structurally delicate biological molecule such as cyt. *c*. Nevertheless, the formal potential of this hemoprotein showed a large upshift (ca. 200 mV) in comparison with the values reported in the literature [47]. Changes in the redox behavior of cyt *c* are usually associated with conformational rearrangements induced by the interaction with the electrode surface [48], such as the electrostatic attraction between the positively charged lysine residues in the vicinity of the cyt *c*'s heme group and the negatively functional groups from the electrode surface [49,50]. This effect was observed on both ITO and WO_3/ITO electrodes, but it was less pronounced in the presence of the nanoparticles since, at neutral pH, they provide more negatively charged surfaces.

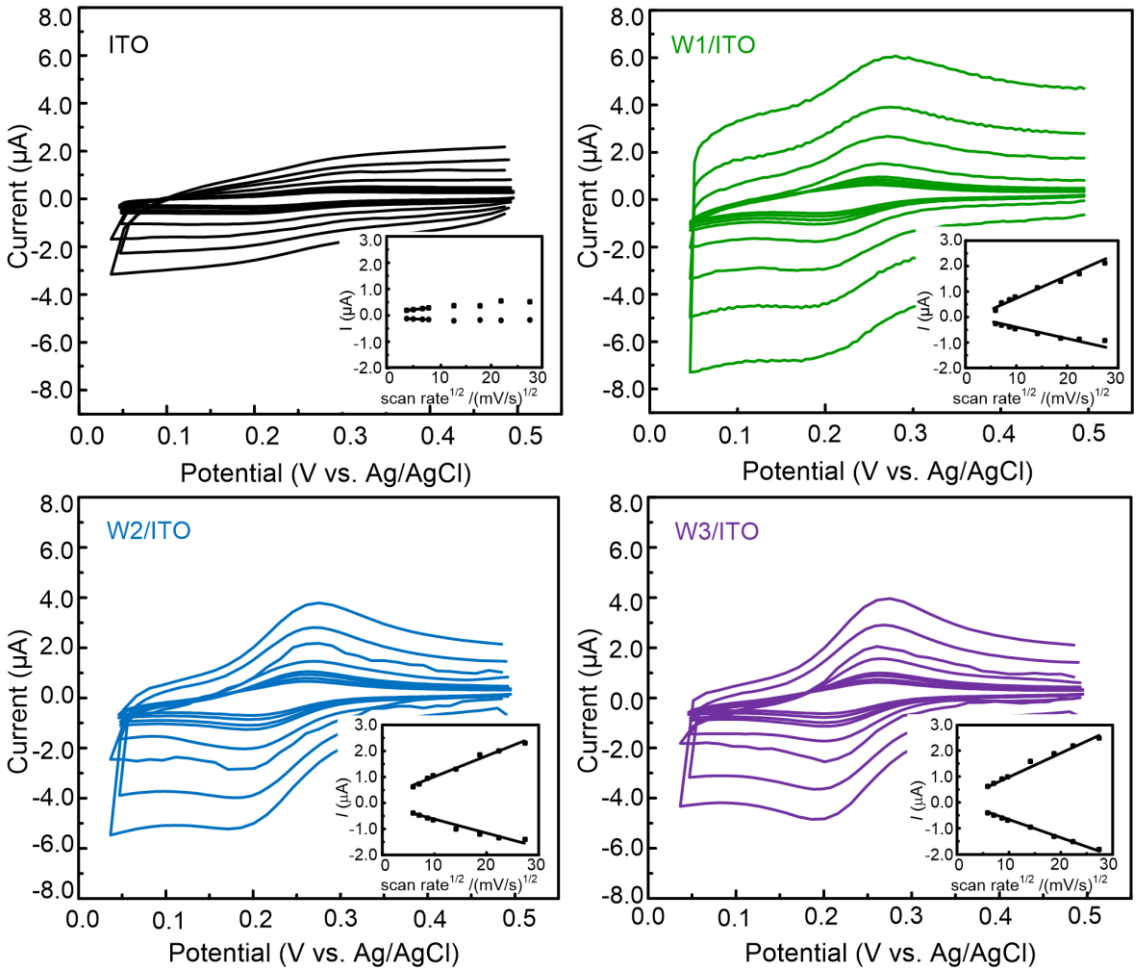

Figure 5.4. Cyclic voltammograms of cyt *c* at ITO and WO_3/ITO electrodes measured at variable scan rates, from 35 to 750 mV s^{-1}. Protein concentration was 0.2 mM in 0.1 M KNO_3, 0.05 M phosphate buffer pH 7.6., Inset: Variation of anodic and cathodic peak current as a function of the square root of the scan rate.

Table 5.2 Electrochemical parameters of cytochrome *c* on different WO_3/ITO electrodes (anodic and cathodic peak current ratio (*Ic*/*Ia*), peak separation (ΔEp), formal redox potential (E^0), diffusion coefficient (D_0) and heterogeneous exchange rate constant (k^0)), as obtained by cyclic voltammetry, in 0.05 M phosphate buffer, pH 7.6, 0.1 M KNO_3, at variable scan rates (from 35 to 750 mV s^{-1}).

	Ic*/*Ia	**ΔEp (V)**	**E^0 (V vs Ag/AgCl)**	**D_0 ($cm^2\ s^{-1}$)**	**k^0 ($cm\ s^{-1}$)**
ITO*	0.37	0.084	0.248	9.13×10^{-9}	6.19×10^{-4}
W1/ITO	0.41	0.060	0.233	4.07×10^{-8}	1.34×10^{-3}
W2/ITO	0.64	0.056	0.232	8.98×10^{-8}	2.62×10^{-3}
W3/ITO	0.74	0.052	0.235	9.90×10^{-8}	1.49×10^{-3}

* The electrochemical data concerns only the lowest scan rates due to the poor peak definition obtained at high scan rates.

The diffusion coefficient (D_0) values calculated using the Randles-Sevick equation (5.3) are lower than those reported in the literature [51]. Curiously, however, the D_0 values increase in the presence of the WO_3 nanoparticles when compared with bare ITO electrodes.

The exchange rate constants (k^0) were determined using the Kochi method [52,53] that derives from the Nicholson equation (5.5) [54]:

$$\boldsymbol{k^0 = 2.18 \left(\frac{\alpha \nu n F D_0}{RT}\right)^{0.5} exp\left(-\frac{\alpha 2nF\Delta Ep}{RT}\right)} \qquad \textbf{(5.5}$$

where α is the charge transfer coefficient (0.5) and ν is the scan rate (F, R and T are constants, with their usual meaning). The rate constants were consistent with data in the literature [51]. Overall, the electrodes modified with W2 and W3 exhibited slightly improved reversibility and kinetics. Both materials are orthorhombic and hydrated, in contrast with the monoclinic W1 nanoparticles. This suggests an influence of the structural and/or wettability properties of the materials on the electrochemical response of cyt *c*.

5.4.3. Proof of concept: nitrite biosensor

The immobilization of cc*NiR on ITO glass electrode is a critical parameter for a good analytical performance of the biosensor, and the best response was achieved by drop casting the enzyme solution together with the WO_3 nanoparticles dispersion. The structural integrity of cc*NiR, after immobilization, on the level of the active site and other heme groups, was verified by resonance Raman (RR) spectroscopy (**Figure S 5.6**) since the band frequencies, bandwidths and their relative intensities are similar of the RR spectrum of the native enzyme in solution [55].

In this work, cc*NiR was chosen as model enzyme due to its high catalytic activity towards nitrite reduction, which could have an important impact in the development of biosensors for pollution control and clinical diagnosis. This study aims at setting the basis for its application in nitrite biosensors using novel nanostructured materials as electrode supports.

The experimental evaluation of the response of the cc*NiR/WO_3/ITO electrodes to nitrite was performed by CV in buffered solution containing increasing concentrations of the analyte. The CVs show increased cathodic currents (onset at ca. ~350 mV) corresponding to the electrocatalytic reduction of nitrite by the immobilized enzyme (**Figure 5.5a**) [29], thereby attesting the biocompatibility of WO_3 nanoparticles. The cyclic voltammograms of control electrodes prepared without cc*NiR coats showed no response to nitrite additions (not shown). The catalytic current was determined at –800 mV as the difference between the cathodic currents measured in the presence and absence of nitrite.

The plot of catalytic current versus nitrite concentration could be fitted (**Figure 5.5b**) to the electrochemical version of Michaelis-Menten equation (**5.6**) [28]:

$$I_{cat} = \frac{I_{\max} C}{C + K_M} \quad \textbf{(5.6)}$$

where I_{max} is the catalytic current observed at the maximum turnover rate, C the substrate concentration (nitrite) and K_M the Michaelis-Menten constant.

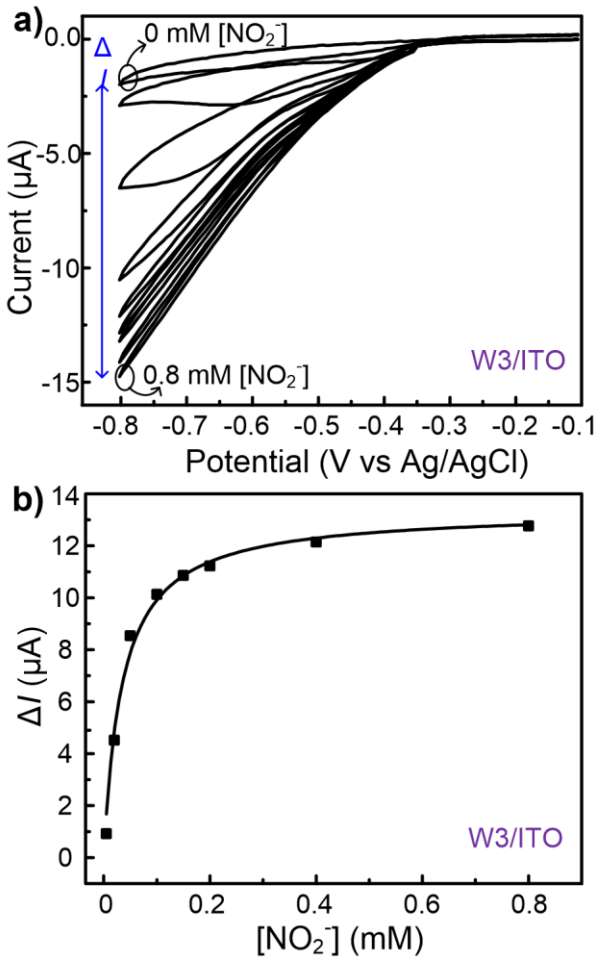

Figure 5.5. Typical electrochemical response of *cc*NiR/WO_3/ITO electrodes in response to variable nitrite concentration (0-0.8 mM). a) Cyclic voltammograms performed at a scan rate of 50 mV s^{-1} in 0.05 M tris-HCl pH 7.6 buffer with 0.1 M KCl; b) Catalytic current (measured at -0.8 V) as a function of nitrite concentration and fitting (solid line) of the experimental data to the Michaelis-Menten equation.

The W1 and W3 based electrodes provided very similar results in respect to Michaelis-Menten constant, linear range and sensitivity. The results with the W2 nanoparticles were inferior in terms of sensitivity. This can be mainly attributed to the higher electroactivity of the latter electrode in the potential window of the *cc*NiR's catalytic response (Figure 5.3), therefore making the electrode less sensitive to small current variations. Nevertheless, we cannot rule out other considerations related with the different size of the nanoparticles, their crystallographic structure and hydration level, which can influence protein orientation and/or activity.

Comparing with previous reported biosensors based on cc*NiR from *D. desulfuricans* (**Table 5.3**) the Michaelis-Menten constants values are similar to those obtained with less obstructing immobilizing matrices like the sol-gel silica film or the simple protein adsorption on pyrolytic graphite electrodes and carbon paste [27,55,56,58].

Table 5.3. Comparison of the kinetic and analytical parameters of the bioelectrode configurations tested in this work with previously reported amperometric or voltammetric biosensors also based on cc*NiR from *D. desulfuricans*. Michaelis-Menten constant (K_M); limit of detection (LOD); linear range and sensitivity. PG: pyrolytic graphite; SWCNT: single-walled carbon nanotubes; MWCNT: multi-walled carbon nanotubes; CPSPE: carbon paste screen-printed electrode; ND: not determined; R^2: correlation coefficient.

	K_M (μM)	LOD (μM)	Linear range (μM)	Sensitivity (mA M^{-1} cm^{-2})	Ref.
PG/SWCNT	715 ± 51	2.1	2.1 – 150	2400 ± 100	[27]
PG/modified MWCNT	1170 ± 70	1.4	1 – 100	1081 ± 120	[56,57]
PG/sol-gel silica	27 ± 1	0.12	0.25 – 50	430 ± 23	[55]
PG	43	0.6	0.6 - 150	520	[56]
CPSPE	ND	1.2	0.7 - 370	550	[58]
ITO	35 ± 4 (R^2 = 0.99)	5	5 - 50	1302 ± 208 (R^2 = 0.95)	This work
W1/ITO	43 ± 8 (R^2 = 0.97)	5	5 - 50	2143 ± 33 (R^2 = 0.999)	This work
W2/ITO	37 ± 3 (R^2 = 0.992)	5	5 - 50	1421 ± 179 (R^2 = 0.97)	This work
W3/ITO	47 ± 7 (R^2 = 0.98)	5	5 - 50	2143 ± 38 (R^2 = 0.999)	This work

In addition, a preliminary analytical characterization of the cc*NiR/WO_3/ITO electrodes is provided in **Table 5.3**. Despite only including few data points, the trends are clear: the limit of detection (LOD) determined as the lowest concentration of nitrite that could be measured [59] are relatively high while the linear range is comparatively narrow; though, they are prone to optimization, once the electrode modification is further developed. Actually, the main drawback of the cc*NiR/WO_3/ITO electrodes is the reproducibility of preparation, which might be due to the non-controlled manufacturing process. The high sensitivity values (slope of the linear fitting at low nitrite concentrations) are comparable with those reported for high surface area nanostructured materials such as the single and multi-walled carbon nanotubes [27, 56, 57]. This demonstrates, for the first time, the use of a metal oxide nanoparticle film as a good catalytic interface for cc*NiR, instead of the common carbon based electrodes (pyrolytic graphite, glassy carbon and carbon nanotubes) [27,29]. With the exception of the W2 type electrodes, the correlation coefficients (R^2) are very good.

5.5. Conclusions

Tungsten oxide nanoparticles were hydrothermally synthesized and fully characterized employing diverse microscopic, spectroscopic and electrochemical methods. The resulting nanoparticles were identified as three different crystallographic and morphologic structures; pure *m*-WO_3 (W1) and *ortho*-$WO_3 \cdot 0.33H_2O$ (W3) nanoslabs and a mixture of two polymorphs (W2). Their interfacial electron transfer properties were distinguished using different iron based electron transfer probes. The small iron complex ferrocyanide displayed efficient electron transfer on the nanoparticle based electrodes. The electroactive areas were significantively improved due to the increased surface area of the nanostructured films. The response of the small electron transfer protein cyt *c* on the electrodes modified with WO_3 nanoparticles revealed that particular features of the nanoparticles influence several parameters of the redox processes, e.g. the reversibility, D_0 and the k^0. The higher conductivity of the $WO_3 \cdot 0.33H_2O$ nanostructures (W2 and W3) contributed for faster and reversible redox reactions.

The structural and catalytic properties of large heme containing enzyme cc*c*NiR were preserved after interaction with all three WO_3 nanostructures; the cc*c*NiR modified electrodes showed good electrocatalytic activity towards the reduction of nitrite. The lowest response was attained with the W2 electrodes as a result of the high capacitive current and impedance of this material. Nevertheless, the comparison with bare ITO electrodes clearly demonstrated that cc*c*NiR/WO_3/ITO constructs represent a promising alternative for cc*c*NiR/carbon based biosensors. In fact, the sensitivities of 2143 mA M^{-1} cm^{-2} are similar to those obtained for carbon nanotubes. Taken together, our data indicate that the WO_3/ITO electrodes represent novel, biocompatible and efficient platforms for the study of protein electron transfer reactions. Further optimization of the electrode fabrication process is currently under development, aiming at the improvement of the electroanalytical performance of the electrodes and their suitability for the construction of miniaturized, fully integrated and cost-effective biosensing devices. For instance, the stability of response, the shelf-life and the selectivity of detection will be optimized; in addition, a careful reassessment of all kinetic and conventional analytical parameters will be carried out.

5.6. Acknowledgements

This work was funded by the Portuguese Science Foundation (FCT-MEC) through project EXCL/CTM-NAN/ 0201/2012, Strategic Project PEst-C/CTM/LA0025/2013-14 and doctoral grant SFRH/BD/73810/2010 (given to L. Santos). This work was also supported by E. Fortunato's ERC 2008 Advanced Grant (INVISIBLE contract number 228144). The authors thank Nuno Costa and Professor Isabel Fonseca from REQUIMTE at Universidade Nova de Lisboa for the nitrogen adsorption experiments. The author E. Elangovan thanks Mike Tiner and Mustapha Jouiad from Microscopic Suite of Masdar Institute for their facilities (TEM tool) and their knowledge transfer.

5.7. References

[1] G.-C. Yi, Semiconductor nanostructures for optoelectronic devices: Processing, characterization and applications, Springer, Berlin, Germany, 2012.

[2] C.C. Koch, I.A. Ovid'ko, S. Seal, S. Veprek, Structural nanocrystalline materials: Fundamentals and applications, Cambridge University Press, Cambridge, UK, 2007.

[3] Y. Wu, S. Hu, Biosensors based on direct electron transfer in redox proteins, Microchim. Acta. 159 (2007) 1–17.

[4] L. Rassaei, F. Marken, M. Sillanpää, M. Amiri, C.M. Cirtiu, M. Sillanpää, Nanoparticles in electrochemical sensors for environmental monitoring, Anal. Chem. 30 (2011) 1704–1715.

[5] Y. Zhang, P. He, N. Hu, Horseradish peroxidase immobilized in TiO_2 nanoparticle films on pyrolytic graphite electrodes: direct electrochemistry and bioelectrocatalysis, Electrochim. Acta. 49 (2004) 1981–1988.

[6] W. Zheng, Y.F. Zheng, K.W. Jin, N. Wang, Direct electrochemistry and electrocatalysis of hemoglobin immobilized in TiO_2 nanotube films., Talanta. 74 (2008) 1414–1419.

[7] L. Zhang, Q. Zhang, J. Li, Layered titanate nanosheets intercalated with myoglobin for direct electrochemistry, Adv. Funct. Mater. 17 (2007) 1958–1965.

[8] Q. Li, G. Luo, J. Feng, Direct electron transfer for heme proteins assembled on nanocrystalline TiO_2 film, Electroanalysis. 13 (2001) 359–363.

[9] Z. Deng, Q. Rui, X. Yin, H. Liu, Y. Tian, In vivo detection of superoxide anion in bean sprout based on ZnO nanodisks with facilitated activity for direct electron transfer of superoxide dismutase., Anal. Chem. 80 (2008) 5839–5846.

[10] G. Zhao, J.-J. Xu, H.-Y. Chen, Interfacing myoglobin to graphite electrode with an electrodeposited nanoporous ZnO film., Anal. Biochem. 350 (2006) 145–50.

[11] J.-J. Feng, J.-J. Xu, H.-Y. Chen, Direct electron transfer and electrocatalysis of hemoglobin adsorbed onto electrodeposited mesoporous tungsten oxide, Electrochem. Commun. 8 (2006) 77–82.

[12] Z. Deng, Y. Gong, Y. Luo, Y. Tian, WO_3 nanostructures facilitate electron transfer of enzyme: application to detection of H_2O_2 with high selectivity., Biosens. Bioelectron. 24 (2009) 2465–2469.

[13] H. Liu, C. Duan, C. Yang, X. Chen, W. Shen, Z. Zhu, A novel nitrite biosensor based on the direct electron transfer hemoglobin immobilized in the WO_3 nanowires with high length–diameter ratio, Mater. Sci. Eng. C. 53 (2015) 43–49.

[14] S.-J. Yuan, H. He, G.-P. Sheng, J.-J. Chen, Z.-H. Tong, Y.-Y. Cheng, et al., A photometric high-throughput method for identification of electrochemically active bacteria using a WO_3 nanocluster probe, Sci. Rep. 3 (2013) 1315.

[15] J.C. Hill, K. Choi, Effect of electrolytes on the selectivity and stability of n-type WO_3 photoelectrodes for use in solar water oxidation, J. Phys. Chem. C. 116 (2012) 7612–7620.

[16] P.J. Wojcik, A.S. Cruz, L. Santos, L. Pereira, R. Martins, E. Fortunato, Microstructure control of dual-phase inkjet printed *a*-WO_3/TiO_2/WO_X films for high performance electrochromic applications, J. Mater. Chem. 22 (2012) 13268–13278.

[17] C. Yan, W. Kang, J. Wang, M. Cui, X. Wang, C.Y. Foo, et al., Stretchable and wearable electrochromic devices., ACS Nano. 8 (2014) 316–22.

[18] C. Granqvist, A. Azens, P. Heszler, L. Kish, L. Osterlund, Nanomaterials for benign indoor environments: Electrochromics for “smart windows”, sensors for air quality, and photo-catalysts for air cleaning, Sol. Energy Mater. Sol. Cells. 91 (2007) 355–365.

[19] A. Enesca, L. Andronic, A. Duta, S. Manolache, Optical properties and chemical stability of WO_3 and TiO_2 thin films photocatalysts, Rom. J. Inf. Sci. Technol. 10 (2007) 269–277.

[20] I.M. Szilágyi, B. Fórizs, O. Rosseler, Á. Szegedi, P. Németh, P. Király, et al., WO_3 photocatalysts: Influence of structure and composition, J. Catal. 294 (2012) 119–127.

[21] R.F. Garcia-Sanchez, T. Ahmido, D. Casimir, S. Baliga, P. Misra, Thermal effects associated with the raman spectroscopy of WO_3 gas-sensor materials, J. Phys. Chem. A. 117 (2013) 13825–13831.

[22] J. Ma, J. Zhang, S. Wang, T. Wang, J. Lian, X. Duan, et al., Topochemical preparation of WO_3 nanoplates through precursor H_2WO_4 and their gas-sensing performances, J. Phys. Chem. C. 115 (2011) 18157–18163.

[23] J. Zeng, M. Hu, W. Wang, H. Chen, Y. Qin, NO_2-sensing properties of porous WO_3 gas sensor based on anodized sputtered tungsten thin film, Sensors Actuators B Chem. 161 (2012) 447–452.

[24] Z. Jiao, J. Wang, L. Ke, X. Liu, H.V. Demir, M.F. Yang, et al., Electrochromic properties of nanostructured tungsten trioxide (hydrate) films and their applications in a complementary electrochromic device, Electrochim. Acta. 63 (2012) 153–160.

[25] A. Sonia, Y. Djaoued, B. Subramanian, R. Jacques, M. Eric, B. Ralf, et al., Synthesis and characterization of novel nanorod superstructures and twin octahedral morphologies of WO_3 by hydrothermal treatment, Mater. Chem. Phys. 136 (2012) 80–89.

[26] D.-K. Ma, J.-L. Jiang, J.-R. Huang, D.-P. Yang, P. Cai, L.-J. Zhang, et al., An unusual zinc substrate-induced self-construction route to various hierarchical architectures of hydrated tungsten oxide., Chem. Commun. 46 (2010) 4556–4558.

[27] C.M. Silveira, J. Baur, M. Holzinger, J.J.G. Moura, S. Cosnier, M.G. Almeida, Enhanced direct electron transfer of a multihemic nitrite reductase on single-walled carbon nanotube modified electrodes, Electroanalysis. 22 (2010) 2973–2978.

[28] H.C. Angove, J.A. Cole, D.J. Richardson, J.N. Butt, Protein film voltammetry reveals distinctive fingerprints of nitrite and hydroxylamine reduction by a cytochrome *c* nitrite reductase., J. Biol. Chem. 277 (2002) 23374–23381.

[29] M.G. Almeida, C.M. Silveira, B. Guigliarelli, P. Bertrand, J.J.G. Moura, I. Moura, et al., A needle in a haystack: the active site of the membrane-bound complex cytochrome *c* nitrite reductase., FEBS Lett. 581 (2007) 284–288.

[30] M.G. Almeida, S. Macieira, L.L. Gonçalves, R. Huber, C.A. Cunha, M.J. Romão, et al., The isolation and characterization of cytochrome *c* nitrite reductase subunits (NrfA and NrfH) from *Desulfovibrio desulfuricans* ATCC 27774, Eur. J. Biochem. 270 (2003) 3904–3915.

[31] J. Wang, E. Khoo, P.S. Lee, J. Ma, Synthesis, assembly, and electrochromic properties of uniform crystalline WO_3 nanorods, J. Phys. Chem. C. 112 (2008) 14306–14312.

[32] S. Rajagopal, D. Nataraj, D. Mangalaraj, Y. Djaoued, J. Robichaud, O.Y. Khyzhun, Controlled growth of WO_3 nanostructures with three different morphologies and their structural, optical, and photodecomposition studies., Nanoscale Res. Lett. 4 (2009) 1335–1342.

[33] M. Deepa, M. Kar, S.A. Agnihotry, Electrodeposited tungsten oxide films: annealing effects on structure and electrochromic performance, Thin Solid Films. 468 (2004) 32–42.

[34] A.L. Patterson, The Scherrer formula for X-ray particle size determination, Phys. Rev. 56 (1939) 978–982.

[35] K. Reis, A. Ramanan, M.S. Whittingham, Hydrothermal synthesis of sodium tungstates, Chem. Mater. 2 (1990) 219–221.

[36] C.G. Granqvist, Oxide electrochromics: An introduction to devices and materials, Sol. Energy Mater. Sol. Cells. 99 (2012) 1–13.

[37] J. Yang, L. Jiao, Q. Zhao, Q. Wang, H. Gao, Q. Huan, et al., Facile preparation and electrochemical properties of hierarchical chrysanthemum-like $WO_3 \cdot 0.33H_2O$, J. Mater. Chem. 22 (2012) 3699-3701.

[38] O. Pyper, A. Kaschner, C. Thomsen, In situ Raman spectroscopy of the electrochemical reduction of WO_3 thin films in various electrolytes, Sol. Energy Mater. Sol. Cells. 71 (2002) 511–522.

[39] D. Vernardou, H. Drosos, E. Spanakis, E. Koudoumas, C. Savvakis, N. Katsarakis, Electrochemical and photocatalytic properties of WO_3 coatings grown at low temperatures, J. Mater. Chem. 21 (2011) 513-517.

[40] L. Zhou, J. Zou, M. Yu, P. Lu, J. Wei, Y. Qian, et al., Green synthesis of hexagonal-shaped $WO_3 \cdot 0.33H_2O$ nanodiscs composed of nanosheets, Cryst. Growth Des. 8 (2008) 3993–3998.

[41] N. Perret, F. Cárdenas-Lizana, D. Lamey, V. Laporte, L. Kiwi-Minsker, M. A. Keane, Effect of crystallographic phase (β vs. γ) and surface area on gas phase nitroarene hydrogenation over Mo_2N and Au/Mo_2N, Top. Catal. 55 (2012) 955–968.

[42] G.F. Cai, J.P. Tu, D. Zhou, X.L. Wang, C.D. Gu, Growth of vertically aligned hierarchical WO_3 nano-architecture arrays on transparent conducting substrates with outstanding electrochromic performance, Sol. Energy Mater. Sol. Cells. 124 (2014) 103–110.

[43] M. Anik, T. Cansizoglu, Dissolution kinetics of WO_3 in acidic solutions, J. Appl. Electrochem. 36 (2006) 603–608.

[44] A.A. Tanaka, T.A.F. Lassali, J.R. dos Santos Jr, C. Otani, M.C. Rezende, H.A. Polidoro, Electrochemical activities of glassy carbons produced by thermal degradation of polyfurfuryl alcohol resin, J. Braz. Chem. Soc. 2 (1991) 37–41.

[45] R.S. Nicholson, I. Shain, Theory of stationary electrode polarography, Anal. Chem. 36 (1964) 706-723.

[46] S.J. Konopka, B. McDuffie, Diffusion coefficients of ferri- and ferrocyanide ions in aqueous media, using twin-electrode thin-layer electrochemistry, Anal. Chem. 42 (1970) 1741–1746.

[47] A. El Kasmi, M.C. Leopold, R. Galligan, R.T. Robertson, S.S. Saavedra, K. El Kacemi, et al., Adsorptive immobilization of cytochrome *c* on indium/ tin oxide (ITO): electrochemical evidence for electron transfer-induced conformational changes, Electrochem. Commun. 4 (2002) 177–181.

[48] D.H. Murgida, P. Hildebrandt, Heterogeneous electron transfer of cytochrome *c* on coated silver electrodes. Electric field effects on structure and redox potential, J. Phys. Chem. B. 105 (2001) 1578–1586.

[49] R.A. Clark, E.F. Bowden, Voltammetric peak broadening for cytochrome *c*/ alkanethiolate monolayer structures: Dispersion of formal potentials, Langmuir. 13 (1997) 559–565.

[50] T. Daido, T. Akaike, Electrochemistry of cytochrome *c*: Influence of coulombic attraction with indium tin oxide electrode, J. Electroanal. Chem. 344 (1993) 91–106.

[51] S.A. Mozaffari, T. Chang, S. Park, Diffusional electrochemistry of cytochrome *c* on mixed captopril/ 3-mercapto-1-propanol self-assembled monolayer modified gold electrodes, J. Phys. Chem. C. 113 (2009) 12434–12442.

[52] R.J. Kllngler, J.K. Kochl, Electron-transfer kinetics from cyclic voltammetry. Quantitative description of electrochemical reversibility, J. Phys. Chem. 85 (1981) 1731–1741.

[53] N.K. Bhatti, M.S. Subhani, A.Y. Khan, R. Qureshi, A. Rahman, Heterogeneous electron transfer rate constants of viologen at a platinum disk electrode, Turk. J. Chem. 29 (2005) 659–668.

[54] R.S. Nicholson, Some examples of the numerical solution of nonlinear integral equations, Anal. Chem. 37 (1965) 667–671.

[55] C.M. Silveira, S.P. Gomes, A.N. Araújo, M.C.B.S.M. Montenegro, S. Todorovic, A.S. Viana, et al., An efficient non-mediated amperometric biosensor for nitrite determination., Biosens. Bioelectron. 25 (2010) 2026–32.

[56] C.M. Silveira, M.G. Almeida, J.J.G. Moura, Nitrite biosensing: Electrochemical biosensors based on cytochrome *c* nitrite reductase from *Desulfovibrio desulfuricans* ATCC 27774, Lambert Academic Publishing, Saarbrücken, Germany, 2014.

[57] C.M. Silveira, M. Pimpão, H.A. Pedroso, P.R.S. Rodrigues, J.J.G. Moura, M.F.R. Pereira, M.G. Almeida, Probing the surface chemistry of different oxidized MWCNT for

the improved electrical wiring of cytochrome *c* nitrite reductase, Electrochem. Commun. 35 (2013) 17-21.

[58] T. Monteiro, P.R. Rodrigues, A.L. Gonçalves, J.J.G. Moura, E. Jubete, L. Añorga, B. Piknova, A.N. Schechter, C.M. Silveira, M.G. Almeida, Construction of effective disposable biosensors for point of care testing of nitrite, Talanta 142 (2015) 246-251.

[59] S. Mitra, R. Brukh, Sample preparation: An analytical perspective, John Wiley & Sons, Inc, Hoboken, USA, 2003

5.8. Supporting Information

Representation of the electrochemical cell used in characterization processes

The electrochemical characterization of WO_3/ITO electrodes was performed in a three-electrode electrochemical cell composed by the working electrode, Ag/AgCl as the reference and platinum wire as the counter electrode. The experiments were carried out in argon purged buffer solutions and the argon atmosphere was maintained during electrochemical characterization of the 3 different iron-based probes (ferrocyanide, cytochrome *c* and cytochrome *c* nitrite reductase).

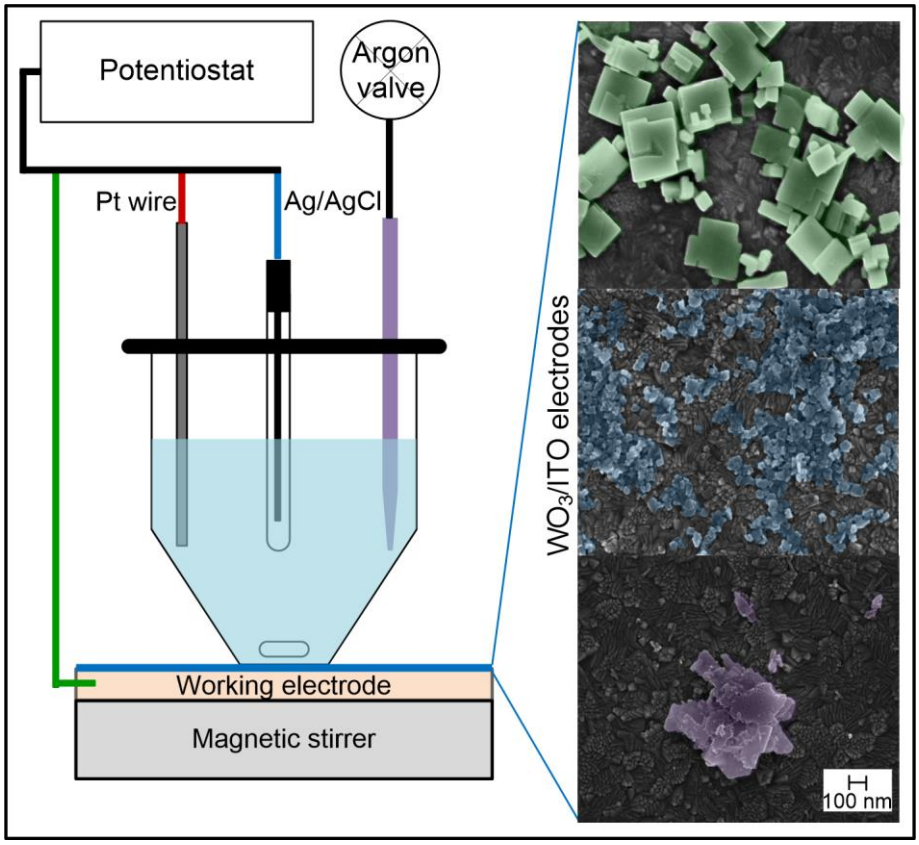

Figure S 5.1. Schematic representation of the set-up used in electrochemical characterization; composed by a WO_3/ITO working electrode, buffer electrolyte, platinum wire as counter electrode and Ag/AgCl as reference electrode.

Resonance Raman spectroscopy of WO_3 nanoparticles

Raman spectroscopy (RS) is widely used for investigation of the structural order of materials, which governs their physical properties and also for in situ characterizations of diverse tungsten oxide films and devices.[1] Therefore, Raman spectra of different tungsten oxides have already been well described in the literature.[1–4] The spectra obtained from all 3 samples (**Figure S 5.2**) show the presence of vibrational modes characteristic for WO_3 materials: the modes at ~800 cm^{-1} and ~700 cm^{-1} can be readily assigned to O-W-O stretching, while the weak band at 328 cm^{-1} can be associated with δ(O–W–O) bending vibrations.[1,2,4] In particular, the Raman spectrum of sample W1 reveals the fingerprint of well-defined monoclinic phase,[2] with narrow bands that suggest well-ordered structure. The modes at ~940 cm^{-1}, 675 cm^{-1} and 627 cm^{-1} are not present in the spectrum of W1. The former, assigned to terminal W=O bond vibration, indicates a presence of water in W2 and W3. It was actually demonstrated that this mode disappears from WO_3 films when annealed above 400 ºC,[4] together with the out-of-plane wagging γ(O−W−O) mode found in W2 and W3 at ~670 cm^{-1}. We further observe that the Raman spectrum of W2 exhibit strong similarities to those of W1 and W3, indicating that the secondary product detected in XRD of W2 is likely to be similar to these two polymorphs.

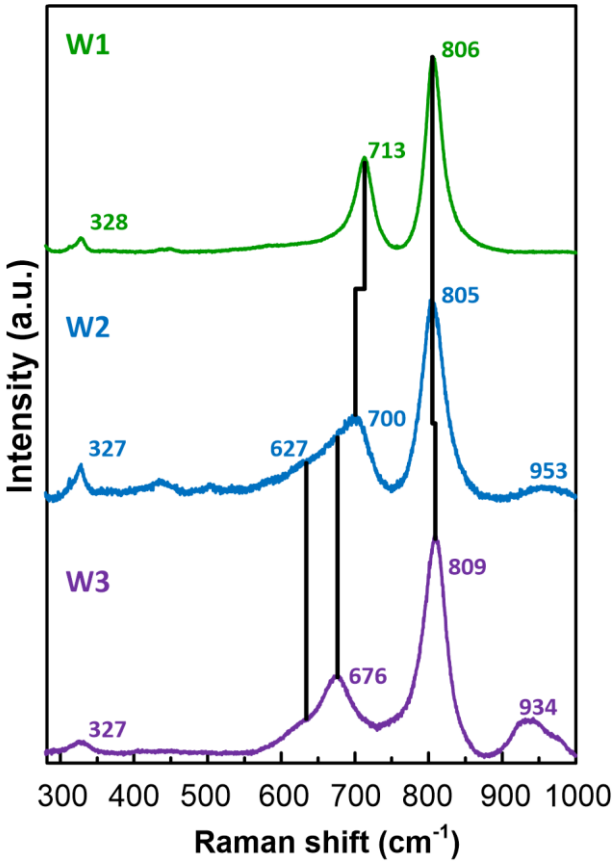

Figure S 5.2. Raman spectra obtained from the samples W1, W2 and W3 at RT with 413 nm laser excitation, 6.5 mW laser power and 30 s accumulation.

Electrochemical impedance spectroscopy of WO_3 and WO_3/ITO electrodes

The electrochemical impedance spectroscopy (EIS) of WO_3 nanopowder was performed in a two electrode set-up with gold electrodes on both sides of the WO_3 pellet. Nyquist plots which represent real versus imaginary impedance (**Figure S 5.3a**), show a semicircle in the high frequency and a sloped straight line in the low frequency region. The difference between the powders is clear since the semicircle diameter equals the resistance in the bulk WO_3. The results are in accordance with the literature since *ortho*-$WO_3 \cdot 0.33H_2O$ is typically a more conductive material due to the presence of double bonds and hydroxyl terminal groups.[5] Nevertheless, W2 shows a more resistive behavior than W3, which is probably due to the presence of the secondary product not yet identified.

The Nyquist plots of the WO_3/ITO electrodes are also represented (**Figure S 5.3b**), it is evident the distinct behavior of the W2/ITO which was assumed to be due to the higher nanoparticles coverage of the electrode, which decreases the electron transfer capability of the electrode.

All the fitting experiments were performed with the equivalent electric circuit that considers the bulk impedance related to the intrinsic material properties, represented by the ZARC element (CPE and R in parallel) and the contact impedance due to the electrode-sample interface. This last contribution is represented by a constant phase element (CPE) in series with the first part of the circuit [6].

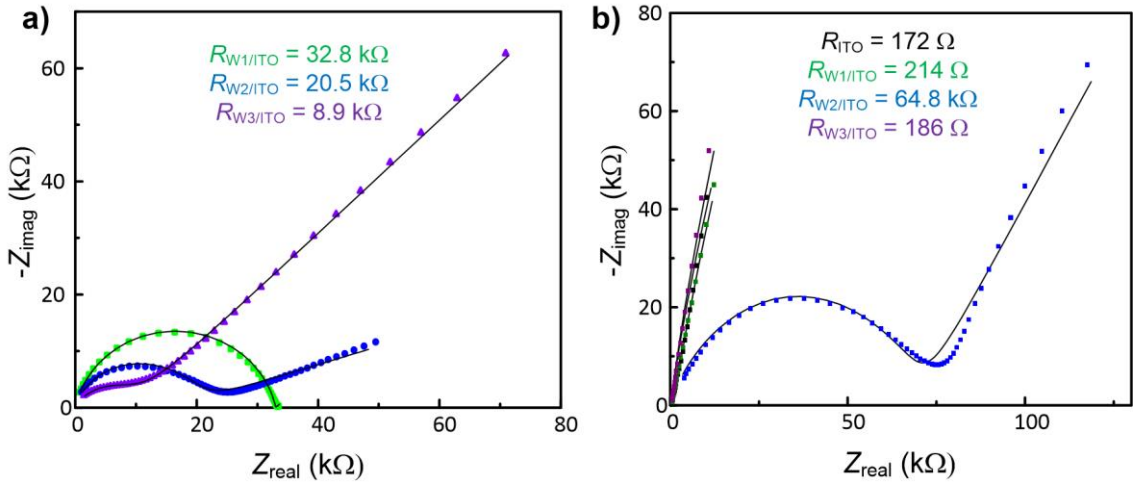

Figure S 5.3. Nyquist plots of: a) WO_3 pellets performed at RT between two gold flat electrodes and b) WO_3/ITO electrodes performed in 0.05 M tris-HCl pH 7.6 buffer with 0.1 M KCl as electrolyte. The alternative voltage was of 10 mV and the frequency range between 1-10^6 Hz. The theoretical fitting is represented by the solid lines.

Schematic representation of the WO_3/ITO electrodes preparation

The modified WO_3/ITO electrodes were produced by drop casting a water dispersion of WO_3 nanoparticles (weight fraction 0.1 %) on a commercial ITO glass substrate and dried at 120 °C for 1 hour.

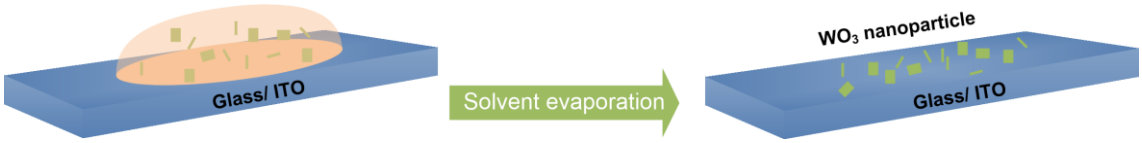

Figure S 5.4. Representation of the drop casting method for the preparation of the WO_3/ITO electrodes.

Electrochemical response of ITO and WO_3/ITO electrodes to $K_3Fe(CN)_6$ probe

The WO_3/ITO electrodes were tested with the electron transfer probe ferrocyanide and compared with bare ITO (control electrode). The cyclic voltammograms were performed with a variable scan rate from 10 to 250 mV s^{-1} and the linear dependence of the current peaks with the square root of the scan rate was demonstrated, as shown in **Figure S 5.4**. W1/ITO electrode is represented as an example since all three WO_3/ITO electrodes showed similar response.

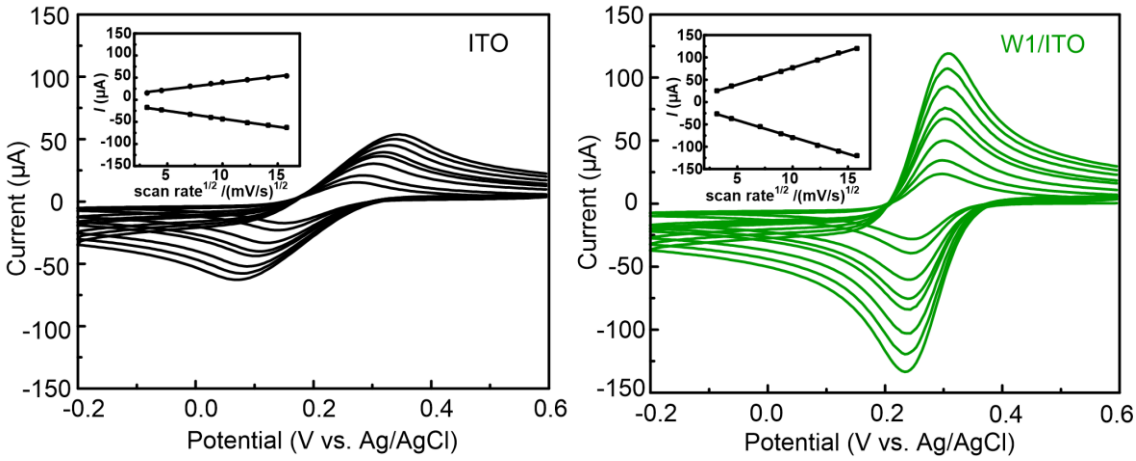

Figure S 5.5. Cyclic voltammograms of ITO and WO_3/ITO electrodes in 1 mM $[Fe(CN)_6]^{4-/3-}$ solution at variable scan rate, from 10 to 250 mV/s (insets correspond to the plots of peak current vs. square root of scan rate).

Resonance Raman spectra of cytochrome *c* after immobilization on WO_3/ITO electrodes

The immobilization of *cc*NiR on ITO glass electrode was achieved by drop casting the enzyme solution onto the WO_3 nanoparticles modified electrodes. Resonance Raman (RR) spectroscopy was used to evaluate the structural integrity of *cc*NiR after immobilization, on the level of

the active site and other heme groups, by comparison with the RR spectrum of the native enzyme in solution. Upon excitation into Soret band of electronic absorption spectra, RR spectra of heme proteins display, in the high frequency region, redox, spin and coordination state marker bands [7]. A careful inspection of *cc*NiR deposited on W1, W2 and W3 demonstrates that the enzyme is in ferric, low-spin state, as the υ_4 , υ_3, υ_2 and υ_{10} are present at 1373 cm^{-1}, 1504 cm^{-1} 1587 cm^{-1} and 1635 cm^{-1}, respectively. The band frequencies, bandwidths and their relative intensities are similar of the RR spectrum of the native enzyme in solution [8], which is dominated by the large number of 6-coordinated low spin heme moieties in the complex. Note that poor S/N is due to extremely short accumulation times and low laser power employed to minimize the enzyme photo-reduction. It, nevertheless, could not be fully avoided, as demonstrated by the presence of narrow band at 1360 cm^{-1}, indicative of ferrous *cc*NiR. The intensity of this band is in direct correlation with the exposure of the sample to the laser beam, being present in the spectra even for the shortest accumulation times and laser power, due to the static nature of the experimental set-up. Furthermore, confocal Raman measurements allowed probing the WO_3 film layer below the casted *cc*NiR. The spectra were identical to those shown in **Figure S 5.2**, confirming that none of the three films was affected by the presence of the enzyme (data not shown).

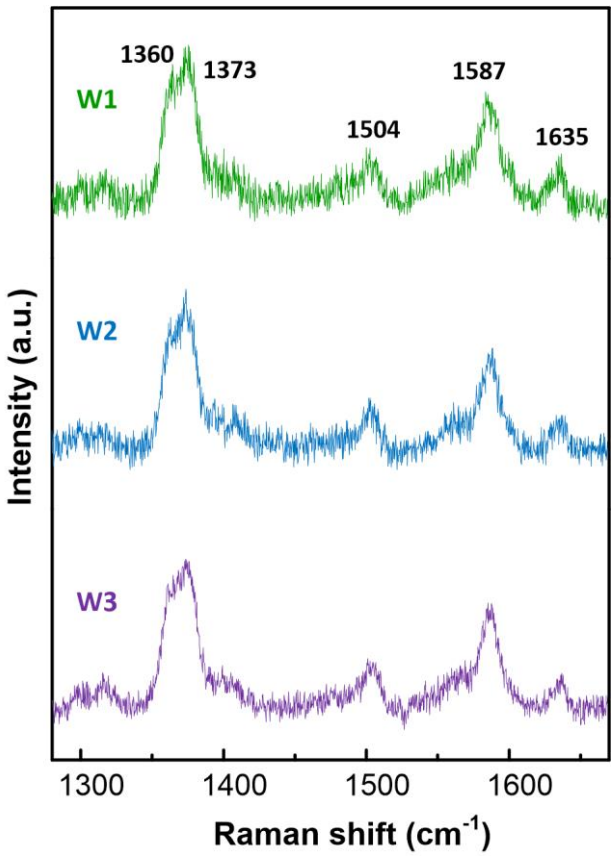

Figure S 5.6. Resonance Raman spectra of *cc*NiR immobilized in WO_3/ITO electrodes, measured with 413 nm excitation, 1.2 mW laser power and 5 s accumulation time, at RT. Each spectrum represents a sum of 5 individual spectra.

[1] O. Pyper, A. Kaschner, C. Thomsen, In situ Raman spectroscopy of the electrochemical reduction of WO_3 thin films in various electrolytes, Sol. Energy Mater. Sol. Cells. 71 (2002) 511–522.

[2] K. Kalantar-zadeh, A. Vijayaraghavan, M.-H. Ham, H. Zheng, M. Breedon, M.S. Strano, Synthesis of atomically thin WO_3 sheets from hydrated tungsten trioxide, Chem. Mater. 22 (2010) 5660–5666.

[3] D. Vernardou, H. Drosos, E. Spanakis, E. Koudoumas, C. Savvakis, N. Katsarakis, Electrochemical and photocatalytic properties of WO_3 coatings grown at low temperatures, J. Mater. Chem. 21 (2011) 513–517.

[4] R.F. Garcia-Sanchez, T. Ahmido, D. Casimir, S. Baliga, P. Misra, Thermal effects associated with the raman spectroscopy of WO_3 gas-sensor materials, J. Phys. Chem. A. 117 (2013) 13825–13831.

[5] A. Al Mohammad, Synthesis , Separation and electrical properties of WO_{3-x} nanopowders via partial pressure high energy ball-milling, Acta Phys. Pol. A. 116 (2009) 240–244.

[6] G. Orsini, V. Tricoli, Fractal mesoporosity and proton transport in WO_3 xerogels, J. Mater. Chem. 22 (2012) 23861.

[7] F. Siebert, P. Hildebrand, Vibrational spectroscopy in life science, WILEY-VCH, Weinheim, Germany, 2008.

[8] C.M. Silveira, S.P. Gomes, A.N. Araújo, M.C.B.S.M. Montenegro, S. Todorovic, A.S. Viana, et al., An efficient non-mediated amperometric biosensor for nitrite determination, Biosens. Bioelectron. 25 (2010) 2026–32.

Chapter 6. GIZO AS ACTIVE LAYER IN ELECTROLYTE-GATED TRANSISTORS (EGTs)

The contents of **Chapter 6** were adapted from the publication:

"L. Santos, D. Nunes, T. Calmeiro, R. Branquinho, D. Salgueiro, P. Barquinha, L. Pereira, R. Martins, E. Fortunato, *Solvothermal Synthesis of Gallium-Indium-Zinc-Oxide Nanoparticles for Electrolyte-Gated Transistors*, **ACS Applied Materials & Interfaces** 7, **2015**, 638-646, DOI: 10.1021/am506814t"

6.1. Abstract

Solution-processed field-effect transistors are strategic building blocks when considering low-cost sustainable flexible electronics. Nevertheless, some challenges still need to be overcome in order to achieve high-performance transistors. Processing temperature reduction, reliability, reproducibility in large areas and cost effectiveness are presently the main concerns both for the semiconductor and dielectric layers. This work reports electrolyte-gated transistors using as channel layer Gallium-Indium-Zinc-Oxide nanoparticles produced by solvothermal synthesis combined with a solid-state electrolyte based on aqueous dispersions of vinyl acetate stabilized with cellulose derivatives, acrylic acid ester in styrene and lithium perchlorate. The devices fabricated using this approach present a I_{ON}/I_{OFF} up to 10^6, threshold voltage (V_{Th}) of 0.3-1.9 V and mobility up to 1 $cm^2/V{\cdot}s$, function of Gallium-Indium-Zinc-Oxide ink formulation and annealing temperature. Electrolyte-gated transistors are a viable and promising alternative for nanoparticle based semiconductor devices as the electrolyte promotes a better interface and more efficient step coverage of the channel layer, reducing the operating voltage when compared with conventional dielectrics gating. Moreover we notice that by controlling the applied gate potential it is possible to change the operation mechanism of the electrolyte-gated transistors from electric double layer to electrochemical doping.

6.2. Introduction

The aim of low cost and sustainable devices, for a broad range of fully disposable commodities, has resulted in an increased interest in solution based deposition technologies and nanomaterials that are able to produce devices with enhanced performance and low power consumption.[1]

The first work of electrolytes used in transistors was reported in 1954 by Brattain and collaborators at Bell Labs.[2] At that time, the main goal was to reduce the surface defects of point contact in germanium transistors by adjusting the surface potential. Only 30 years later the use of electrolyte-gated transistors (EGTs) became popular, especially for organic transistors with the pioneer work of Wrighton et al.,[3] taking profit of the reversible electrochemical oxidation of the semiconducting polymers.

Recently, EGTs are once again attracting significant attention mainly due to the low operating voltage compared to conventional thin-film transistors (TFTs). This arises from the high capacitance of the electrolytes, usually in the order of 1-10 $\mu F\ cm^{-2}$, which exceeds the capacitance of high-κ dielectrics like Ta_2O_5 by at least one order of magnitude and even the one of ultrathin dielectrics based on self-assembled monolayers by a factor of ~5.[4] Furthermore, the static capacitance of the electrolyte is nearly thickness independent, resulting in large process margins, hence in increased yield when scaling the device fabrication to industrial applications. In particular, making this type of transistors attractive for roll-to-roll printing on flexible substrates.[5] **Figure 6.1** schematically illustrates and compares a conventional dielectric and an electrolyte-gate insulator, showing the voltage profile and the electric field distribution when a positive voltage is applied to the gate electrode.

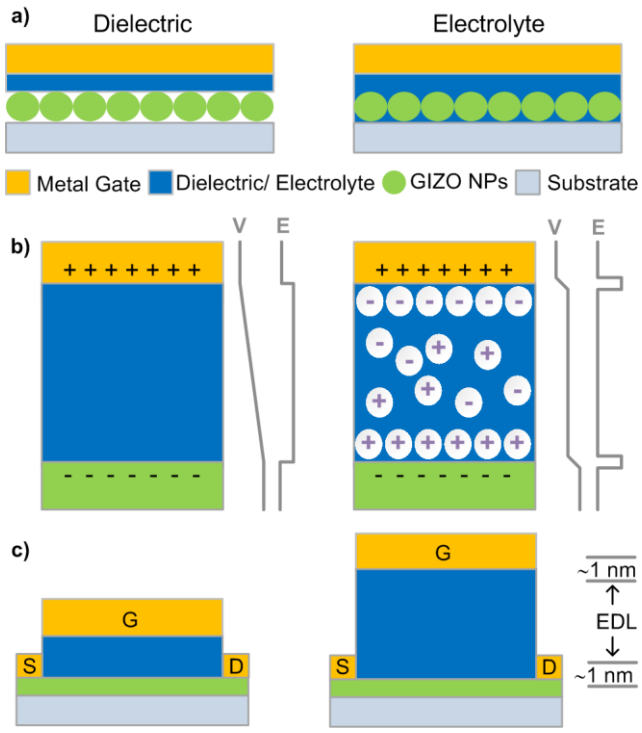

Figure 6.1. a) Comparison of the cross section of an inorganic GIZO based nanoparticles transistor using a conventional dielectric film and an electrolyte; b) Schematics of the voltage (V) and electric field (E) distributions in a conventional dielectric and in electrolyte gate insulator when a positive gate voltage is applied; c) Schematics of the transistors architecture for a conventional structure incorporating thick gate dielectric (~100 nm) and for an EGT in which the gate dielectric is replaced by a polymer electrolyte, with indication of both EDLs at the gate/electrolyte and semiconductor/electrolyte interfaces.

So far, the drawbacks of the EGTs are related to large leakage currents and high switching times, as well as large parasitic capacitances, especially when integrated in an electric circuit.[4] Recent studies have been reported describing several attempts to overcome such issues nevertheless, the operation behavior of these transistors is still not fully understood. In the present study, the operation mechanism of the EGTs have been distinguished in two different types, depending on the semiconductor material permeability to ions existing in the electrolyte and on the applied gate voltage.[4] When a positive gate voltage is applied, negative and positive ions accumulate at the gate/electrolyte and semiconductor/electrolyte interfaces, respectively, originating two electrical double layers (EDL).[6] The charging mechanism on this type of transistors with impermeable semiconductors is similar to that of field-effect transistors, since the EDL promotes a charge carrier accumulation (or depletion) in the transistor channel (**Figure S 6.1a**). These are designed as electric double layer transistors (EDLTs), and the active electrical thickness that enables channel modulation is in general much smaller than the geometric thickness of the electrolyte, thus resulting in a high electric field.[7]

When reversible electrochemical doping of the semiconductor (oxidation and/or reduction) occurs due to a high gate voltage or/and to the permeability of the semiconductor to ions, the electric double layer is only formed exclusively on the gate/electrolyte interface, as the ions are

expected to diffuse into the semiconductor layer (**Figure S 6.1b**). This type of transistors are designed as electrochemical transistors (ECTs).[4,6] It is already known from organic ECTs,[8,9] that the ions present in the electrolyte will influence the conductivity of the channel layer. Nevertheless, the understanding of the mechanism behind this process is still under investigation, especially regarding inorganic semiconductors. From a practical point of view, EDLTs can be more interesting than ECTs as the electrochemical doping of the semiconductor can be inhibited or controlled avoiding the high leakage current normally associated to ECTs.

Oxide semiconductors are already recognized as an important class of materials for electronic applications [10] either in crystalline or amorphous structures.[11,12] One advantage of these materials is the possibility to modulate their optical and electrical properties by changing the composition and/or deposition conditions. Moreover, these materials are already being used in stable and reliable electronic devices with outstanding performances.[11] For this propose, the multicomponent oxides are interesting due to the role of the different metal cations in the conduction mechanism.[12,13] The use of sputtered gallium-indium-zinc oxide (GIZO) with different atomic ratios as semiconductor in TFTs with superior electric performance was already widely demonstrated.[12,14–16] GIZO TFTs can also be solution-processed, which has been considered as an option for low-cost fabrication. The research activities in this particular deposition method have been focused in two main routes: molecular precursor[17,18] or nanoparticles deposition.[19] For this last route, EGTs are particularly interesting as the electrolyte promotes a more efficient step coverage of the channel layer.[20]

So far, not many studies were reported regarding EGTs based in inorganic nanoparticles as semiconductors (**Table 6.1**) but mimicking the results observed with organic semiconductors, implementation of these materials in EGTs offers opportunities to improve carrier mobilities and greatly reduce operating voltages and subthreshold slope, while increasing processing tolerances and potentiating lower fabrication costs.[4]

Table 6.1. Key factors of the reported work for EGTs with metal oxide nanoparticles: deposition technique, post-treatment, electrolyte, channel width to length ratio (W/L), on-off current ratio (I_{ON}/I_{OFF}), threshold voltage (V_{Th}), drain voltage (V_D), mobility (μ) and sub-threshold swing (SS).

	Deposition technique	**Post-treatment**	**Electrolyte**	***W/L***	I_{ON}/I_{OFF}	V_{Th} [V]	V_D [V]	μ [$cm^2 (V s)^{-1}$]	***SS*** [$V dec^{-1}$]
ZnO [21]	Spin coating	100 ºC	PVP	--	10^6	11.6	20	23.8	0.67
ZnO NR [20]	Drying	150 °C	Ionic liquid	50	4×10^4	-1	1	5.5	--
ZnO NW [22]	Harvesting	--	CSPE [a)]	--	10^7	0.93	0.5	62	0.12
ITO [23]	Inkjet printing	400 °C	CSPE [a)]	8	2×10^4	-0.22	0.8	5	--
In_2O_3 [24]	Inkjet printing	--	PVA + KF	12	2×10^3	0.54	0.4	0.8-0.26	--

[a)] (Composite solid polymer electrolyte)

In the present work, it has been developed GIZO nanoparticles by solvothermal synthesis with an initial atomic ratio of 2:7:1 in Ga:In:Zn, which was based on previously reported studies.

[11,12] This approach is expected to result in EGTs with an acceptable compromise between low threshold voltage (V_{Th} close to 0 V) and high mobility, aiming the enhancement of the devices performance with low power consumption. To the authors' knowledge, the study of the operation mechanism of inorganic EGTs by changing the ink composition, annealing temperature and applied gate voltage range has never been reported.

6.3. Experimental Section

Solvothermal synthesis and characterization of GIZO nanoparticles

All reagents were used without further purification. Gallium nitrate hydrate ($Ga(NO_3)_3 \cdot xH_2O$, Sigma-Aldrich, 99.9 %), indium acetate ($In(CH_3COO)_3$, Sigma-Aldrich, 99.99%) and zinc acetate ($Zn(CH_3COO)_2 \cdot 2H_2O$, Sigma-Aldrich, 99.5 %) were dissolved in 2-methoxythanol (6 mL, Fluka, 99 %) with a molar ratio of 3:6:2, respectively, and left stirring at 50 ºC for one hour with ethanolamine (0.2 mL, Fluka, 98 %). The final solution was transferred to a 23 mL PTFE (polytetrafluoroethylene) chamber, set inside a stainless steel autoclave (4745 general purpose vessel, Parr) and installed in an oven (L3/11/B170, Nabertherm) at 180 °C for 24 hours. The product of synthesis was collected by centrifugation at 4000 rpm for 5 min (F140, Focus instruments) and dispersed in ethanol (20 mL).

Morphological and structural characterization of GIZO nanoparticles was performed by Scanning Electron Microscopy (SEM) combined with Focused Ion Beam (FIB) using a Carl Zeiss AURIGA CrossBeam workstation coupled with energy dispersive X-Ray spectroscopy (EDS), and by transmission electron microscopy (TEM) using a Hitachi H8100 instrument operated at 200 kV, also equipped with EDS. For the FIB experiments the GIZO particles were previously coated with a carbon sacrificial layer, Ga^+ ions were accelerated to 30 kV at 50 pA and the etching depth was around 2 µm. The EDS was employed in 10 different samples to determine the composition of GIZO. For TEM experiments a drop of the sonicated dispersion was deposited onto 200-mesh copper grids covered with formvar and allowed to dry before observation. X-ray diffraction measurements have been performed using a PANalytical's X'Pert PRO MRD diffractometer with Cu$K\alpha$ radiation. The XRD data have been acquired in the 10–70 º 2θ range, with a step size of 0.016 º.

GIZO thin film deposition and characterization

The GIZO dispersion was mixed with ethylene glycol (Pronalab, 99.5 %) in two different weight proportions (1.4:0.6 and 1.6:0.4) in order to study the ink stability and its effect of on the properties of the devices. From now on, the ink with a weight fraction of EG 30 % is named as GIZO30 and the ink with 20 % of EG as GIZO20. Different weight fractions were also tested but the produced EGTs did not present any significant electric results (not shown). The solutions were left stirring for 24 hours, and prior to deposition were sonicated for two minutes and filtered with a 0.45 µm porous diameter filter.

Glass substrates (1737, Corning) were cleaned by sonication in acetone and isopropanol and activated by UV-ozone during 30 minutes. Deposition of the final GIZO ink was performed by spin coating 4 layers at 2000 rpm during 35 s and rapidly drying at 100 ºC for 1 min between each layer. After deposition, the substrates were annealed at 350 and 250 ºC for 1 h. GIZO inks were

characterized by differential scanning calorimetry and thermogravimetry (DSC-TG), accomplished directly with the solution in air with a heating ramp of 5 °C/min starting from RT up to 600 °C (STA 449 F3 Jupiter, Netzsch) while the hydrodynamic diameter was measured by Dynamic Light Scattering (DLS) technique (W130i Avid Nano). The optical band gap was calculated from the UV-visible spectra of the deposited thin films in glass (UV/VIS/NIR Lambda 950, PerkinElmer) and the surface roughness of the films was analyzed by atomic force microscopy (AFM) in a commercial microscope (Asylum research MFP-3D). The raw data was processed using planefit order 1 and flatten order 0 available in AFM software (IgorPro software). The nanoparticles size distribution was measured using Gwyddion software and scaled according to the magnification quoted by the microscope software.

Solid-electrolyte layer deposition and characterization

Composite solid polymer electrolyte (CSPE) was achieved by mixing an aqueous dispersion of acrylic acid esther in styrene stabilized with emulsifiers (pH 8, batch DM9764, Resiquímica), aqueous dispersions of poly vinyl acetate (PVAc) stabilized with cellulose derivatives (pH 4, batch 2045, Resiquímica) and lithium perchlorate ($LiClO_4$, Sigma-Aldrich, 98 %). The mixture was stirred at room temperature for 1 h and deposited by spin coating at 2500 rpm during 2 min. The films were left to dry at room temperature for 8 hours. Electrochemical characterization of the electrolyte was performed in a typical capacitor structure by depositing the electrolyte between two ITO-covered glass substrates (10 Ω/sq, Xinyan Technology) with an active area of 1 cm^2. Electrochemical impedance spectroscopy (EIS) was performed in a frequency range of 1 to 10^6 Hz with 10 mV AC voltage while cyclic voltammetry was achieved in a potential range between 2 and -2 V with a scan rate of 50 mV/s in a potentiostat (600TM Gamry Instruments).

Electrolyte-gated transistor assembly and characterization

Top-gated structure was achieved in several successive steps (**Figure S 6.2**). GIZO ink was firstly deposited by spin coating on glass substrates. Source and drain contacts of titanium (6 nm) and gold (65 nm) metals were then e-beam evaporated (home-made apparatus) and defined with a shadow mask. The electrolyte layer (14 µm) was deposited on top by spin coating and patterned manually. The top gate of IZO (indium zinc oxide, 200 nm) was deposited by radio frequency (13.56 MHz) magnetron sputtering, using a ceramic oxide target of In_2O_3:ZnO (89.3:10.7 weight fraction, Super Conductor Materials, Inc., 99.99 %). The film was deposited at room temperature in the presence of a mixture of argon (20 sccm) and oxygen (0.4 sccm) at a deposition pressure of 2×10^{-3} Pa with a r.f. power of 75 W and a target–substrate distance of 15 cm. [31] The patterning was achieved by mechanical shadow mask that was aligned in order to get the top-gated structure with gate-to-source and gate-to-drain overlaps of 100 µm. In this work we used conventional electrodes made by vacuum processed techniques but fully solution-processed transistors can be achieved by replacing the contacts with conductive inks deposited by printing techniques. For FIB experiments, Ga^+ ions were accelerated to 30 kV at 2 nA and the etching depth was around 15 µm.

The electrical characterization of the transistors was performed using a semiconductor parameter analyzer (Agilent 4155C) and a microprobe station (Cascade Microtech M150) inside a dark box.

6.4. Results and Discussion

6.4.1. Nanoparticles Characterization

The X-ray diffraction (XRD) measurements of the as-synthesized GIZO nanopowder is presented in **Figure 6.2a**, which is consistent with the presence of reduced-size nanoparticles due to the broad peak at 31.88 °. Nevertheless, the phase determination turned to be inconclusive since this peak may be attributed to the presence of a nanocrystalline phase of *c*-In_2O [26] (ICDD file number 006-0416) or *h*-$InGaZn_2O_5$ (ICDD file number 040-0252). The crystallite size was calculated from Scherrer equation,[27] with a value of about 2.5 nm. The XRD diffractogram obtained before annealing present similarities with the characterization performed for *a*-GIZO thin films produced by pulsed-laser deposition by Nomura et al.[15] So, further analysis conducted by transmission electron microscopy (TEM) was crucial to confirm the presence of a nanocrystalline phase in our sample. The TEM image (**Figure 6.2b**) confirms the nanometric individual particles with ~ 3 nm and the electron diffraction pattern (inset of **Figure 6.2b**), showing light rings together with evident diffuse halos, suggests a mixture of amorphous and nanocrystalline phases. Further annealing at 900 ºC was required to distinguish the ternary mixture of oxides.

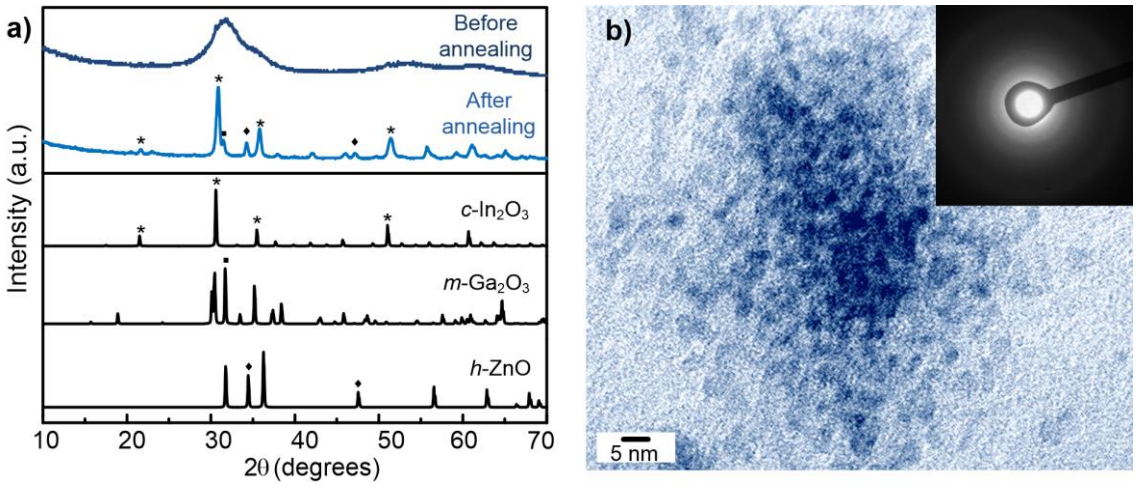

Figure 6.2. a) XRD diffractograms before and after annealing at 900 ºC and reference ICDD diffractograms of *c*-In_2O_3, *m*-Ga_2O_3 and *h*-ZnO (file numbers 06-0416, 41-1103 and 05-0664, respectively); b) TEM image of GIZO nanoparticles before annealing (inset shows the diffraction pattern of the nanoparticles).

SEM observations (**Figure 6.3a-b**) illustrates the as-synthesized powder with microstructures composed of agglomerates of reduced-size nanoparticles. Only after continuous stirring and sonication these agglomerates can dissociate in smaller nanoparticles groups. The Energy-dispersive X-ray spectroscopy (EDS) results **(Figure 6.3g-h)** revealed an atomic ratio of 1.4:4.7:1 in Ga:In:Zn, while the initial fraction of the precursors before solvothermal synthesis was of 2:7:1. Even if slightly deviated, especially for indium oxide, this is in accordance with the proposed composition able to result in transistors with optimal performances.[11,12] The element mapping (**Figure 6.3c-f**) shows an even distribution of the 3 metal cations, while the oxygen seems to indicate

a higher concentration on the surface, however this effect can be attributed to the 3D shape of the microstructure.

The optical band gap energy calculated for the GIZO nanoparticles dispersed in ethanol resulted in 3.67 eV (**Figure S 6.3**), which is in accordance with previous results of GIZO thin films produced by physical routes.[28]

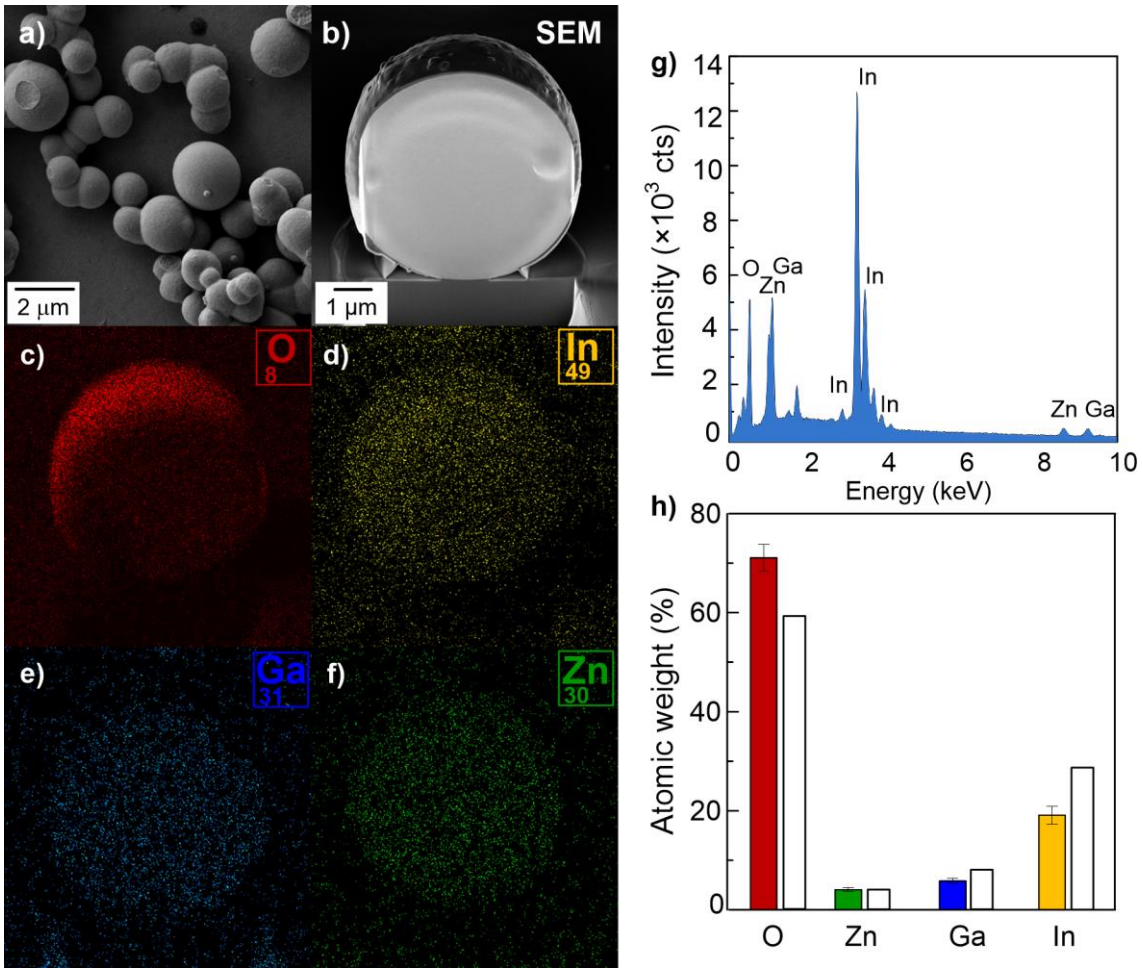

Figure 6.3. SEM images: a) before and b) after FIB milling; c) –f) EDS mapping of the elements; g) EDS spectrum and h) average of the atomic weights performed in 10 samples of GIZO (colored) and their percentages before synthesis (blank).

6.4.2. GIZO Inks and Film Characterization

The two produced inks were characterized by thermogravimetry (TG) and dynamic light scattering (DLS), so that it could be estimated the size and percentage of nanoparticles after sonication and filtration processes (**Figure S 6.4**). From the TG measurements it was observed that the GIZO nanoparticles weight fraction varied from approximately 1 to 3 % for inks GIZO30 and GIZO20, respectively. The influence of the EG as dispersant can be directly related with the DLS results since the mean hydrodynamic diameter of the agglomerates decreases from 100 to 70 nm with

the increase of EG proportion in the ink, thus confirming the stabilization effect of this reagent. Differential scanning calorimetry (DSC) characterization (**Figure S 6.4b**) substantiate the full degradation of the solvent and EG at 180 ºC. No further peaks were verified up to 600 ºC, which confirms the stable conformation of this structure.

Atomic force microscopy (AFM) measurements were performed in the substrates annealed at different temperatures (see the GIZO20 results in **Figure 6.4**). The average roughness of the films, annealed in the same conditions, varied from 9.3 to 11.7 nm for inks GIZO30 and GIZO20, respectively and this difference is related with the ink stability and hydrodynamic diameters determined by DLS. The effect of the annealing temperature was analyzed in the phase angle images. Phase imaging provided by AFM was already demonstrated as a useful technique to distinguish features as viscoelasticity, adhesion and also contact area, since it measures the energy dissipation involved in the contact between the tip and the material analyzed. [29] In this work, the material annealed at 350 ºC shows a more uniform phase angle distribution when compared to the material annealed at 250 ºC, which can be due to the presence of some impurities, like EG, that was not fully decomposed at lower temperature. Even if the DSC-TG characterization confirmed the full decomposition of EG at a lower temperature (180 °C), this difference can be related with heat dissipation between the hot plate and the film surface. The presence of small amounts of dispersant in the material will influence negatively on the electric and electrochemical response of the samples since it reduces the electric paths between source and drain through the GIZO nanoparticles.

AFM results also allowed the determination of the nanoparticles sizes distribution. A mean diameter of 18 nm was obtained in all measured materials, which is lower than the hydrodynamic diameters (70-100 nm) measured by DLS. This can be expected since the hydrodynamic diameter of the nanoparticles is measured in the dispersions and gives information of the inorganic core along with the solvent layer attached to the particle as it moves under the influence of Brownian motion. Thus, the AFM values are more representative of the real size of the nanoparticles. Moreover, no significant size deviations were detected between the substrates with different ink compositions and annealing temperatures.

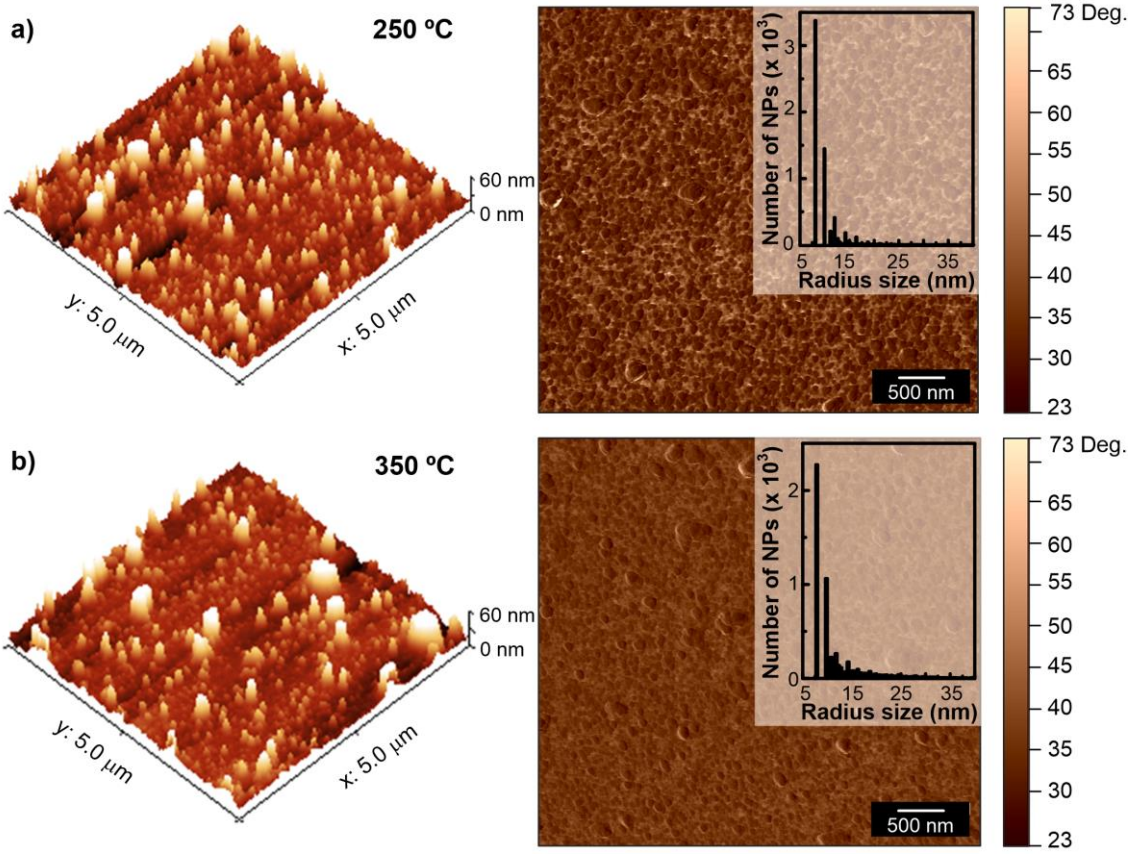

Figure 6.4. AFM topographic and phase images of GIZO20 films annealed at: a) 250 ºC and b) 350 ºC. The inset corresponds to the nanoparticles radius size distribution measured with the Gwyddion software.

6.4.3. Electrolyte Characterization

The solid electrolyte used in this work consists in a mixture of two thermoplastic polymers with $LiClO_4$, which can be easily deposited by spin coating and dried at room temperature, thus called composite solid polymer electrolyte (CSPE). Solid electrolytes are a good approach for EGTs since they can minimize and solve some of the problems associated to liquid electrolytes such as poor mechanical properties, problems in fabrication and also safety issues (leaking and hazardous environmental effects).[30–33]

The electrochemical characterization of the electrolyte was performed in a capacitor structure (ITO/electrolyte/ITO) and the impedance magnitude and phase angle were measured in the frequency range of 1 to 10^6 Hz (**Figure 6.5a**). Below 1 kHz the phase angle between current and voltage levels at around -90 °, while at high frequencies it gets close to zero indicating a transition from a capacitive to a purely resistive response.[4] The transition between the two regions, at a phase angle of -45 °, can be associated with the ionic relaxation and the EDL formation.[34] In the EDL formation regions, as the frequency becomes higher, the measured capacitance decreases. Accordingly, the specific capacitance obtained directly from the acquisition software also drops at higher frequencies. The frequency at which the capacitance starts to increase, is strongly dependent on the device configuration, such as size and dielectric thickness. For fast responses,

this frequency value must be as high as possible.[35] When the frequency decreases to 1 Hz, the capacitance gradually increases up to 2.6 µF cm^{-2}. Even if some authors consider this value as the double-layer capacitance (C_{DL}), in the present work the value was corrected according to studies previously reported[36,37] and using **Equation 6.1**:

$$C_{DL} = \left[Y_0 R_s^{-(\alpha-1)}\right]^{1/\alpha} \quad \textbf{(6.1)}$$

where Y_0 is the bulk capacitance, R_s the solution resistance and α is a constant (between 0 and 1). These parameters were obtained from the fitting results of the equivalent circuit (represented in **Figure 6.5a**) with a constant phase element (CPE) instead of a perfect capacitor. The resulting double layer capacitance of 0.85 µF cm^{-2} for this electrolyte is in the frontier of the usually reported values (> 1 µF cm^{-2}) for electrolyte-gated transistors. Nevertheless, this CSPE was considered, since it is compatible with solution deposition techniques allowing a good control of the layer thickness.

The conductivity was calculated according to **Equation 6.2**:

$$\sigma = l/(R_e \cdot A) \quad \textbf{(6.2)}$$

where l is the thickness of the electrolyte, A is the surface area of the sample and R_e is the bulk electrical resistance (1.3 × 10^3 Ω), resulting in a conductivity of 1.8 × 10^{-6} S cm^{-1}.

Cyclic voltammetry (CV) was performed in the potential range of 2 to -2 V and the measured current is mainly capacitive with no major faradaic contribution (**Figure 6.5b**).

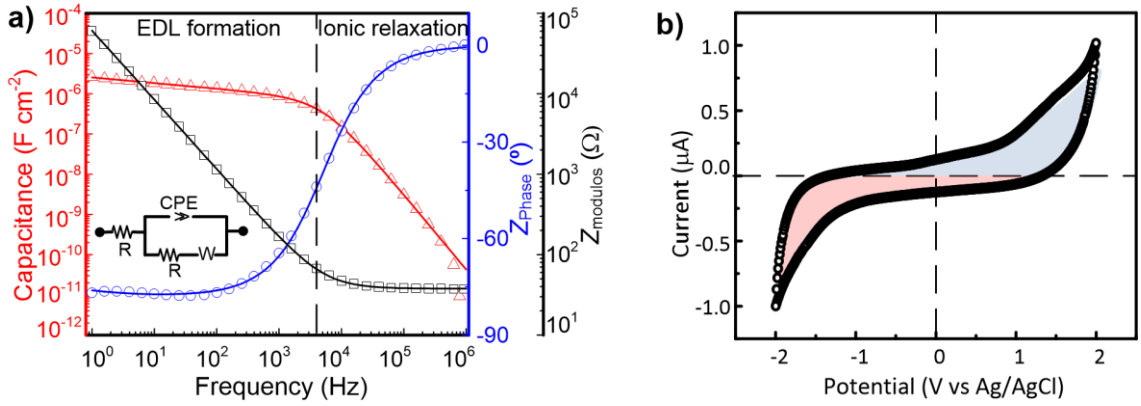

Figure 6.5. a) Impedance modulus (□), phase angle (○) and capacitance (Δ) plot from EIS measurement (the inset represents the equivalent electric circuit, where *R* is the resistance, *W* the Warburg and CPE the constant phase elements) and b) Cyclic voltammogram of ITO/electrolyte/ITO capacitor structure at a scan rate of 50 mV/s. EIS conditions: alternative voltage 10 mV and frequency range 1-10^6 Hz.

6.4.4. EGTs Characterization

Focused ion beam (FIB) experiments allowed the determination of the EGTs layers thicknesses. The analysis shows that the GIZO nanoparticles film is 30-40 nm thick and the electrolyte layer

measures approximately 12 µm. Even if already demonstrated by AFM, it is visible that the GIZO nanoparticles form a continuous layer where the relatively rough surface of the nanoparticles is totally covered by the electrolyte in the channel region. The difference in the GIZO layer thickness, when using different deposition conditions, was negligible in this sizes range.

Electrical characterization of the EGTs was performed at room temperature and in air. The resume of the results can be found in **Table 6.2** for the two ink compositions, two annealing temperatures and different gate voltage range.

Saturation (μ_{SAT}) and linear mobilities (μ_{LIN}) were calculated accordingly with the **Equations 6.3** and **6.4** for FETs:[11]

$$\mu SAT = \frac{\left(\frac{d\sqrt{I_D}}{dV_G}\right)^2}{\frac{1}{2}C\frac{W}{L}} \quad \textbf{(6.3)}$$

and,

$$\mu LIN = \frac{\left(\frac{dI_D}{dV_G}\right)}{C\frac{W}{L}V_D} \quad \textbf{(6.4)}$$

where, *W/L* corresponds to the width and length ratio of the channel, I_D is the drain current, V_G the gate potential, V_D drain potential and *C* to the capacitance.

Subthreshold swing (*SS*) was given by **Equation 6.5**:[11]

$$SS = \left(\frac{d\log(I_D)}{dV_G}\Big|_{max}\right)^{-1} \quad \textbf{(6.5)}$$

Table 6.2. Resume of the electric characterization of the produced EGTs: channel weight and length ratio (*W/L*), drain voltage (V_D), gate current range (V_G), on-off current ratio (I_{ON}/I_{OFF}), threshold voltage (V_{Th}), mobility (μ) and subthreshold swing (*SS*).

	Post-treatment	*W/L*	V_D [V]	V_G range [V]	I_{ON}/I_{OFF}	V_{Th} [V]	μ* [cm^2 (V s)$^{-1}$]	*SS** [V dec^{-1}]
GIZO30	250 ºC	35	1	-10 to 10	1×10^4	1.6	0.1 (μ_{SAT})	0.22
GIZO20					1×10^5	1.9	1 (μ_{SAT})	0.24
GIZO30	350 ºC	15	0.5	-2 to 2	8×10^3	0.7	2×10^{-2} (μ_{LIN})	0.09
GIZO20					1×10^6	1.4	1 (μ_{LIN})	0.11
GIZO30	350 ºC	15	0.5	-2 to 1	1×10^3	0.6	6×10^{-3} (μ_{LIN})	0.09
GIZO20					5×10^3	0.3	2×10^{-2} (μ_{LIN})	0.09

* Both µ and SS were calculated in the forward sweep direction, from negative to positive gate voltage.

EGTs produced at 250 ºC, when compared with the 350 ºC, required higher V_D and V_G in order to obtain I_{ON}/I_{OFF} values in the 10^4-10^5 range. This fact can be related with the dispersant presence (EG), as demonstrated in the AFM phase images. The EGTs annealed at 350 ºC show

lower V_{Th} and subthreshold swing (*SS*) at a considerable smaller V_G sweep (-2 to 2 V), indicative of a higher-quality channel layer. This improved performance is attributed to an enhancement of the degree of nanoparticles compactness (fully dispersant degradation and higher number of conductive paths between the nanoparticles), leading to a more homogenous and uniform film. Moreover, the reduction of the GIZO defect density results in a lower subgap density of states and hence in an easier movement of the Fermi level towards the conduction band as V_G increases. Similar behavior was reported for GIZO TFTs prepared by physical deposition routes.[38]

For the EGTs annealed at 350 ºC, the I_{ON}/I_{OFF} decreases substantially when V_G is swept between -2 and 1 V. Furthermore, the hump observed in the transfer characteristics at $V_G \approx 1$ V suggests that a different operation mechanism starts to be dominant above this V_G value. This leads to the conclusion that the operation mechanism is different and depends on this parameter. To corroborate this conclusion, the I_G was also compared in the two operation modes. The transfer characteristics, gate current and output characteristics are shown in **Figure 6.6**. For the case of a wider V_G range, the I_G is not totally flat which can indicate the occurrence of redox reactions and consequently doping of the semiconductor (ECT). This is more evident for the sample GIZO20, which can be related to the ink properties that generates a thicker film with more electric conduction pathways between source and drain due to the lower amount of dispersant. Nevertheless, since the gate leakage doesn't increase significantly, evidence of a breakdown, it suggests that this type of operation mechanism is also possible in inorganic semiconductors. [4] I_G is mainly due to the parasitic capacitance of the electrolyte, commonly observed in EGTs, and can be further minimized by changing the configuration of the transistor and by reducing the sizes of the components, like the gate-to-source and gate-to-drain overlaps.

For a narrow V_G range, from -2 to 1 V, I_G is mainly capacitive thus revealing the occurrence of electric double layer in the semiconductor/electrolyte interface (EDLTs). Nevertheless, *SS* is not expected to benefit from this operation mechanism, as it is more affected by the properties of the semiconductor film than by the occurrence of doping (redox reactions) in the interface. Thus, in the transistors annealed at 250 ºC, *SS* increases due to the presence of dispersant in the films. This also suggests that the electrochemical doping of the semiconductor occurs only into few nanometers in depth and not in the bulk semiconductor.[6] Being In_2O_3 the main component of the semiconductor with a theoretical isoelectric point of 8.7,[39] the surface of the semiconductor is positively charged at the working pH from the electrolyte (below 8). This effect would also contribute for a low level of Li^+ doping (repulsive effect) into the semiconductor surface.

All produced EGTs show hysteresis of the drain current due to the slow ion motion in the solid electrolyte or to some charge trapping effects.[40] Nevertheless, the clockwise direction of the hysteresis is consistent with trapping effects that are clearly reduced in the transistors operating in EDL mode,[14] given that for the lower V_G sweep charges are only induced (not injected) in the semiconductor layer by a capacitive effect, resulting in a lower density of charges that have to be drawn during the reverse direction of the V_G sweep.

The negative differential resistance, occurring in both operation modes, suggests an adsorption process at the nanoparticle surface.[24] In addition, I_D increases with increasing V_G, confirming the n-type behavior of the GIZO nanoparticles.

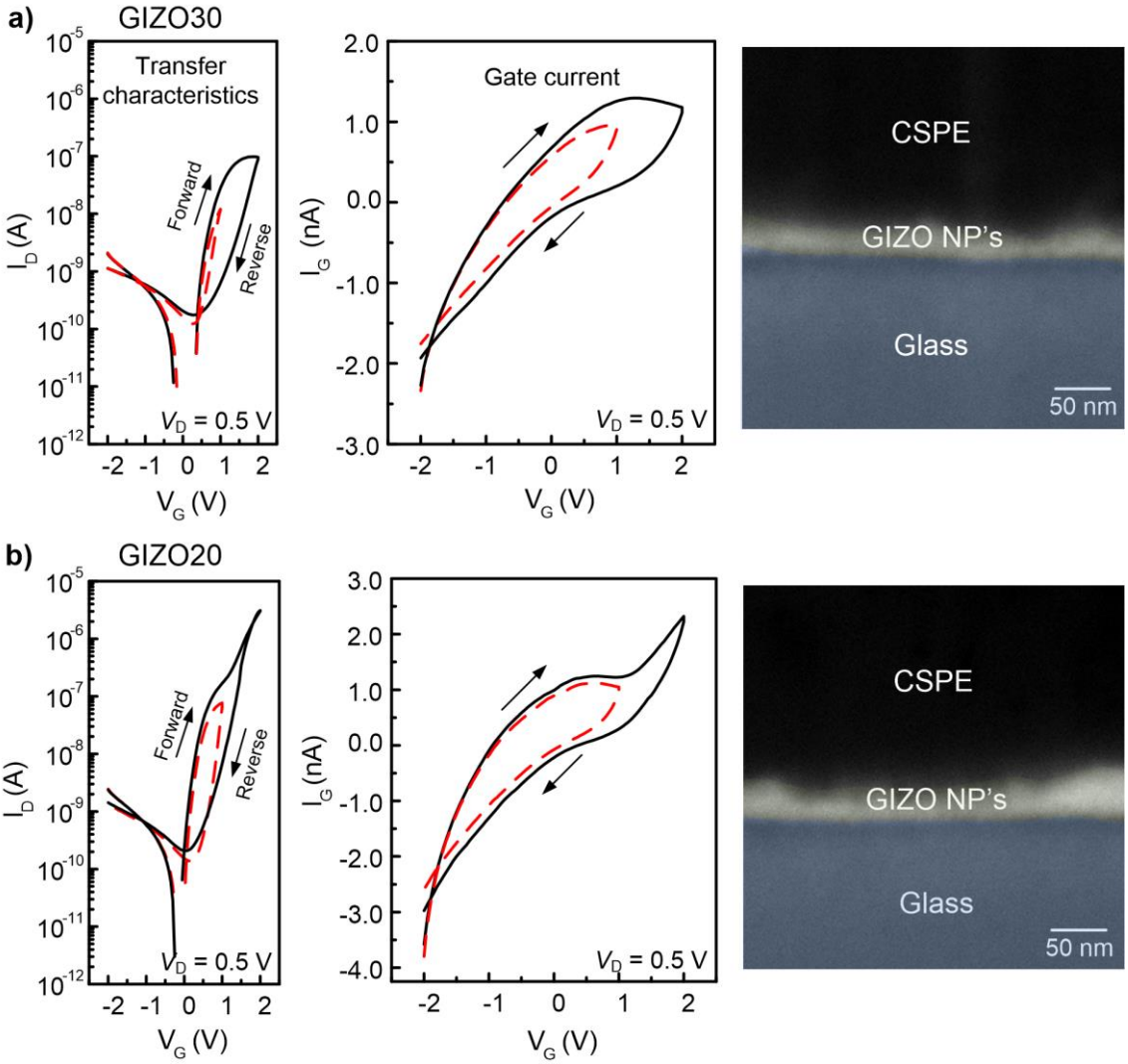

Figure 6.6. Transfer characteristics, gate current with different gate voltage ranges (the red dashed line corresponds to V_G from -2 to 1 V and the solid black line from -2 to 2 V) and high resolution SEM image, after FIB milling, of the cross-section of EGT built with: a) GIZO30 and b) GIZO20 after 1 h annealing at 350 °C. Transfer characteristics and gate current were measured with 0.5 s delay time and the arrows represent the sweep direction.

Comparing with the previously reported results for EGTs based on metal oxide nanoparticles (**Table 6.1**), this results are in the same order of magnitude, but using for the first time a ternary oxide nanoparticles, which should bring advantages in terms of further device optimization, as the semiconductor properties, which are heavily dependent on the relative cationic concentration. The evaluation of the influence of the ink composition, annealing temperature and applied gate voltage allowed the discussion of the operation mechanisms that can occur in such type of transistors.

6.5. Conclusion

In the present work, metal oxide GIZO nanoparticles were synthesized and employed as semiconductor layer, which used a composite solid polymer electrolyte as gate insulator in EGTs. The effect of the ethylene glycol as dispersant reveals the importance of achieving the right proportion in the ink formulation in order to get a stable solution, however without reducing the electric conduction paths between source and drain contacts, after ink deposition. The annealing temperature was crucial to reduce the defect density of GIZO film that allowed V_{Th} closer to 0 V with full degradation of the dispersant (ethylene glycol) and therefore, lower operating voltages. The dependence of the gate voltage in the electrical performance of the EGT was also investigated. The operation mechanism of the transistors was evaluated and it was shown evidences that the mechanism can vary from electric double layer to electrochemical doping, when increasing the gate voltage range, which allowed an improved I_{ON}/I_{OFF} and mobility values without the occurrence of voltage breakdown.

Further characterization and development of solid electrolytes and better understanding of the structure of the transistor are essential in order to improve EGTs performances. Nevertheless, this study proves that GIZO nanoparticles can easily be incorporated in EGTs compatible with solution-processed technologies, low process temperature and flexible devices, demanded for several applications, as flexible electronics and sensors.

6.6. Acknowledgment

This work was funded by the Portuguese Science Foundation (FCT-MEC) through project EXCL/CTM-NAN/0201/2012, Strategic Project PEst-C/CTM/LA0025/2013-14, “POINTS” FP7-NMP-263042, “i-FLEXIS” FP7-ICT-611070 and the FCT-MEC doctoral grant SFRH/BD/73810/2010 given to L. Santos. Moreover, this work was also supported by E. Fortunato’s ERC 2008 Advanced Grant (INVISIBLE contract number 228144). The author’s would like to acknowledge Dr. Pawel Wojcik from CENIMAT/I3N for the design of the mechanical masks used in this work, Prof. P. Carvalho from Instituto Superior Técnico of Universidade de Lisboa for the TEM analysis and Resiquímica for the polymers supply.

6.7. References

(1) Martins, R.; Pereira, L.; Fortunato, E. The Future Is Paper Based, Inf. Disp. (1975)., 2014, 30, 20.

(2) Brattain, W. H.; Garrett, C. G. B. Electrical Properties Of The Interface Between A Germanium Single Crystal And An Electrolyte, Phys. Rev., 1954, 94, 750.

(3) White, H. S.; Kittlesen, G. P.; Wrighton, M. S. Chemical Derivatization Of An Array Of Three Gold Microelectrodes With Polypyrrole: Fabrication Of A Molecule-Based Transistor, J. Am. Chem. Soc., 1984, 106, 5375–5377.

(4) Kim, S. H.; Hong, K.; Xie, W.; Lee, K. H.; Zhang, S.; Lodge, T. P.; Frisbie, C. D. Electrolyte-gated Transistors For Organic And Printed Electronics., Adv. Mater., 2013, 25, 1822–1846.

(5) Hong, K.; Kim, S. H.; Lee, K. H.; Frisbie, C. D. Printed, Sub-2V ZnO Electrolyte Gated Transistors And Inverters On Plastic., Adv. Mater., 2013, 25, 3413–3418.

(6) Fujimoto, T.; Awaga, K. Electric-double-layer Field-effect Transistors With Ionic Liquids., Phys. Chem. Chem. Phys., 2013, 15, 8983–9006.

(7) Pereira, L.; Gaspar, D.; Guerin, D.; Delattre, a; Fortunato, E.; Martins, R. The Influence Of Fibril Composition And Dimension On The Performance Of Paper Gated Oxide Transistors., Nanotechnology, 2014, 25, 094007.

(8) Yuen, J. D.; Dhoot, A. S.; Namdas, E. B.; Coates, N. E.; Heeney, M.; McCulloch, I.; Moses, D.; Heeger, A. J. Electrochemical Doping In Electrolyte-gated Polymer Transistors., J. Am. Chem. Soc., 2007, 129, 14367–14371.

(9) Kergoat, L.; Piro, B.; Berggren, M.; Horowitz, G.; Pham, M.-C. Advances In Organic Transistor-based Biosensors: From Organic Electrochemical Transistors To Electrolyte-gated Organic Field-effect Transistors., Anal. Bioanal. Chem., 2012, 402, 1813–1826.

(10) Lin, W.-N.; Ding, J.-F.; Wu, S.-X.; Li, Y.-F.; Lourembam, J.; Shannigrahi, S.; Wang, S.-J.; Wu, T. Electrostatic Modulation Of $LaAlO_3/SrTiO_3$ Interface Transport In An Electric Double-Layer Transistor, Adv. Mater. Interfaces, 2014, 1, 1300001.

(11) Fortunato, E.; Barquinha, P.; Martins, R. Oxide Semiconductor Thin-film Transistors: A Review Of Recent Advances., Adv. Mater., 2012, 24, 2945–2986.

(12) Olziersky, A.; Barquinha, P.; Vilà, A.; Magaña, C.; Fortunato, E.; Morante, J. R.; Martins, R. Role Of Ga_2O_3–In_2O_3–ZnO Channel Composition On The Electrical Performance Of Thin-film Transistors, Mater. Chem. Phys., 2011, 131, 512–518.

(13) Martins, R.; Barquinha, P.; Ferreira, I.; Pereira, L.; Gonçalves, G.; Fortunato, E. Role Of Order And Disorder On The Electronic Performances Of Oxide Semiconductor Thin Film Transistors, J. Appl. Phys., 2007, 101, 044505.

(14) Barquinha, P.; Pereira, L.; Gonçalves, G.; Martins, R.; Fortunato, E. Toward High-Performance Amorphous GIZO TFTs, J. Electrochem. Soc., 2009, 156, H161.

(15) Nomura, K.; Ohta, H.; Takagi, A.; Kamiya, T.; Hirano, M.; Hosono, H. Room-temperature Fabrication Of Transparent Flexible Thin-film Transistors Using Amorphous Oxide Semiconductors., Nature, 2004, 432, 488–492.

(16) Suresh, A.; Wellenius, P.; Dhawan, A.; Muth, J. Room Temperature Pulsed Laser Deposited Indium Gallium Zinc Oxide Channel Based Transparent Thin Film Transistors, Appl. Phys. Lett., 2007, 90, 123512.

(17) Nayak, P. K.; Busani, T.; Elamurugu, E.; Barquinha, P.; Martins, R.; Hong, Y.; Fortunato, E. Zinc Concentration Dependence Study Of Solution Processed Amorphous Indium Gallium Zinc Oxide Thin Film Transistors Using High-k Dielectric, Appl. Phys. Lett., 2010, 97, 183504.

(18) Banger, K. K.; Yamashita, Y.; Mori, K.; Peterson, R. L.; Leedham, T.; Rickard, J.; Sirringhaus, H. Low-temperature, High-performance Solution-processed Metal Oxide Thin-film Transistors Formed By A “Sol-gel On Chip” Process., Nat. Mater., 2011, 10, 45–50.

(19) Yang, Y.-H.; Yang, S. S.; Kao, C.; Chou, K.-S. Chemical And Electrical Properties Of Low-Temperature Solution-Processed In – Ga – Zn-O Thin-Film Transistors, IEEE Electron Device Lett., 2010, 31, 329–331.

(20) Thiemann, S.; Gruber, M.; Lokteva, I.; Hirschmann, J.; Halik, M.; Zaumseil, J. High-mobility ZnO Nanorod Field-effect Transistors By Self-alignment And Electrolyte-gating., ACS Appl. Mater. Interfaces, 2013, 5, 1656–1662.

(21) Faber, H.; Hirschmann, J.; Klaumünzer, M.; Braunschweig, B.; Peukert, W.; Halik, M. Impact Of Oxygen Plasma Treatment On The Device Performance Of Zinc Oxide Nanoparticle-based Thin-film Transistors., ACS Appl. Mater. Interfaces, 2012, 4, 1693–1696.

(22) Nasr, B.; Wang, D.; Kruk, R.; Rösner, H.; Hahn, H.; Dasgupta, S. High-Speed, Low-Voltage, And Environmentally Stable Operation Of Electrochemically-Gated Zinc Oxide Nanowire Field-Effect Transistors, Adv. Funct. Mater., 2012, 23, 1750–1758.

(23) Dasgupta, S.; Stoesser, G.; Schweikert, N.; Hahn, R.; Dehm, S.; Kruk, R.; Hahn, H. Printed And Electrochemically Gated, High-Mobility, Inorganic Oxide Nanoparticle FETs And Their Suitability For High-Frequency Applications, Adv. Funct. Mater., 2012, 22, 4909–4919.

(24) Dasgupta, S.; Kruk, R.; Mechau, N.; Hahn, H. Inkjet Printed , High Mobility Inorganic-Oxide Field Effect Transistors Processed At Room Temperature, ACS Nano, 2011, 5, 9628–9638.

(25) Gonçalves, G.; Barquinha, P.; Raniero, L.; Martins, R.; Fortunato, E. Crystallization Of Amorphous Indium Zinc Oxide Thin Films Produced By Radio-frequency Magnetron Sputtering, Thin Solid Films, 2008, 516, 1374–1376.

(26) Kim, Y.-H.; Han, M.-K.; Han, J.-I.; Park, S. K. Effect Of Metallic Composition On Electrical Properties Of Solution-Processed Indium-Gallium-Zinc-Oxide Thin-Film Transistors, IEEE Trans. Electron Devices, 2010, 57, 1009–1014.

(27) Koch, C. C.; Ovid'ko, I. A.; Seal, S.; Veprek, S. Structural Nanocrystalline Materials: Fundamentals And Applications; Cambridge University Press: Cambridge, UK, 2007.

(28) Barquinha, P. Ph.D Thesis, Universidade Nova de Lisboa, Portugal, 2010.

(29) Eaton, P.; West, P. Atomic Force Microscopy; Oxford University Press: Oxford, UK, 2010.

(30) Christie, A. M.; Lilley, S. J.; Staunton, E.; Andreev, Y. G. Increasing The Conductivity Of Crystalline Polymer Electrolytes, Nature, 2005, 433, 50–53.

(31) Fan, L.-Z.; Hu, Y.-S.; Bhattacharyya, a. J.; Maier, J. Succinonitrile As A Versatile Additive For Polymer Electrolytes, Adv. Funct. Mater., 2007, 17, 2800–2807.

(32) Fergus, J. W. Ceramic And Polymeric Solid Electrolytes For Lithium-ion Batteries, J. Power Sources, 2010, 195, 4554–4569.

(33) Long, S. Ionic Conduction In Doped Succinonitrile, Solid State Ionics, 2004, 175, 733–738.

(34) Guo, L.-Q.; Yang, Y.-Y.; Zhu, L.-Q.; Wu, G.-D.; Zhou, J.-M.; Zhang, H.-L. Effects Of Humidity On Performance Of Electric-double-layer Oxide-based Thin-film Transistors Gated By Nanogranular SiO_2 Solid Electrolyte, AIP Adv., 2013, 3, 072110.

(35) Yuan, H.; Shimotani, H.; Ye, J.; Yoon, S.; Aliah, H.; Tsukazaki, A.; Kawasaki, M.; Iwasa, Y. Electrostatic And Electrochemical Nature Of Liquid-gated Electric-double-layer Transistors Based On Oxide Semiconductors., J. Am. Chem. Soc., 2010, 132, 18402–18407.

(36) Jovic, V.; Jovic, B. M. EIS And Differential Capacitance Measurements Onto Single Crystal Faces In Different Solutions Part I : Ag (111) In 0 . 01 M NaCl, J. Electroanal. Chem., 2003, 541, 1–11.

(37) Brug, G. J.; Van den Eeden, A. L. G.; Sluyters-Rehbach, M.; Sluyters, J. H. The Analysis Of Eletrode Impedances Complicated By Thepresence Of A Constant Phase Element, J. Electroanal. Chem., 1984, 176, 275–295.

(38) Kamiya, T.; Nomura, K.; Hosono, H. Present Status Of Amorphous In–Ga–Zn–O Thin-film Transistors, Sci. Technol. Adv. Mater., 2010, 11, 044305.
(39) Zhou, Y.-M.; Shan, Y.; Sun, Y.-Q.; Ju, H.-X. Adsorption Of Collagen To Indium Oxide Nanoparticles And Infrared Emissivity Study Thereon, Mater. Res. Bull., 2008, 43, 2105–2112.
(40) Kang, M. S.; Lee, J.; Norris, D. J.; Frisbie, C. D. High Carrier Densities Achieved At Low Voltages In Ambipolar PbSe Nanocrystal Thin-film Transistors., Nano Lett., 2009, 9, 3848–3852.

6.8. Supporting Information

Semiconductor/electrolyte interface of an electric double layer and electrochemical transistors

The EDL (**Figure S 6.1a**) is formed by three distinct regions: inner Helmholtz plane (IHP), outer Helmholtz plane (OHP) and diffusion layer (DL). The first region consists in the adsorbed ions on the surface, the second the solvated ions in contact with the surface and the diffusion layer is dependent of the ions concentration in the bulk of the electrolyte. For high ion concentration, the contribution of the diffusion layer and adsorbed ions to the EDL can be neglected. In this case, it is determined by the solvated ions, which are usually considered as being confined in a region with a thickness of 1 nm.[1]

The charging mechanism of electric double layer transistors (EDLTs) transistors is similar to that of field-effect transistors since the EDL promotes a charge carrier accumulation (or depletion) in the channel of the transistor (**Figure S 6.1a**), while for electrochemical transistors (ECTs) the EDL is only formed in the gate/electrolyte interface since the ions will diffuse into the semiconductor layer (**Figure S 6.1b**).

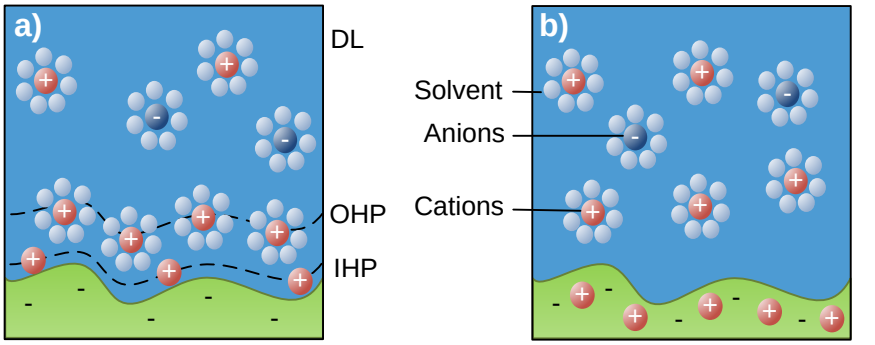

Figure S 6.1. Schematic representation of the semiconductor (green)/electrolyte (blue) interface when a positive gate voltage is applied, considering: a) electric double layer and b) electrochemical operation modes.

[1] a) Ueno, K.; Shimotani, H.; Iwasa, Y.; Kawasaki, M. Electrostatic Charge Accumulation Versus Electrochemical Doping In SrTiO3 Electric Double Layer Transistors, *Appl. Phys. Lett.*, 2010, *96*, 252107; b) Shimotani, H.; Asanuma, H.; Tsukazaki, A.; Ohtomo, A.; Kawasaki, M.; Iwasa, Y. Insulator-to-metal Transition In ZnO By Electric Double Layer Gating, *Appl. Phys. Lett.*, 2007, *91*, 082106.

Scheme of the final transistor structure

A common layer of GIZO layer was deposited by spin coating as semiconductor on glass. Source and drain contacts were produced by e-beam using a shadow mask and the electrolyte deposited on top by spin coating. The access to the contacts was defined manually by scratching the electrolyte. Finally, the IZO top gate was produced by sputtering with a shadow mask where gate-to-drain and gate-to-source overlaps were both set to 100 µm (as demonstrated in **Figure S 6.2**). No photolithography processes were used.

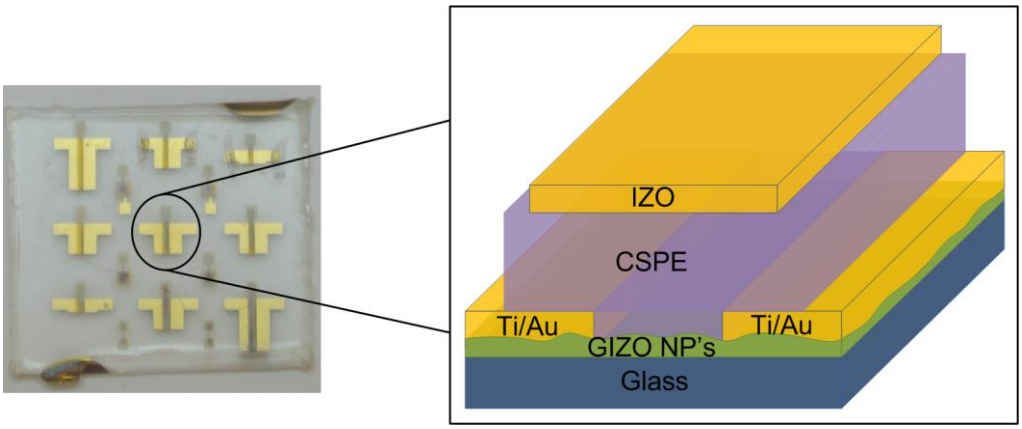

Figure S 6.2. Final transistor structure with top gate, electrolyte and GIZO nanoparticles as semiconductor

Absorption spectra of GIZO nanoparticles dispersion

The optical band gap energy of the GIZO nanoparticles dispersed in ethanol was calculated using the Tauc's plot (**Figure S 6.3**) and by applying the equation:

$$\alpha h\upsilon = A(h\upsilon - Eg)^n$$

where A is a constant, $h\upsilon$ is the corresponding photon energy, α is the absorption coefficient and n depends on the type of the optical transition. For crystalline semiconductors n is ½ or 2 for direct or indirect allowed transitions, respectively.[1] A better fitting of the experimental data was obtained when considering direct allowed transitions, which resulted in an optical band gap of 3.67 eV. The calculated value is in-between the reported values for the single crystalline oxides[2] with direct band gap transitions at 3.37 eV for ZnO, 3.6 eV for In_2O_3 and 4.9 eV for Ga_2O_3. Furthermore, the result is in accordance with previous results of GIZO thin films produced by physical routes.[3]

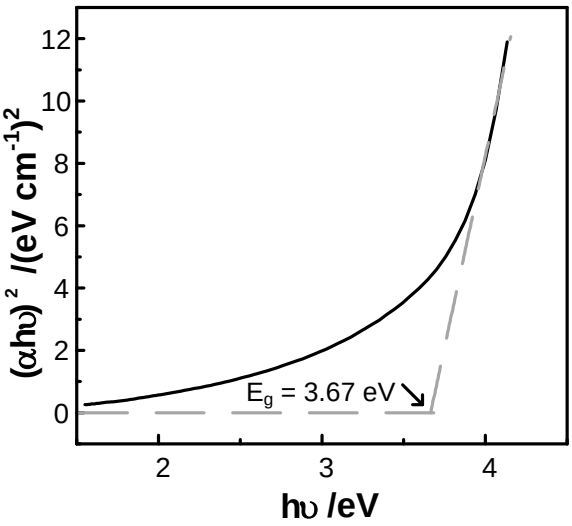

Figure S 6.3. Tauc's plot for GIZO nanoparticles dispersion.

DLS and DSC-TG characterization of the GIZO inks in ethylene glycol

The size distribution of GIZO agglomerates after filtration confirm the effect of the dispersant agent; lower amount of ethylene glycol (EG) produces larger agglomerates (GIZO20). The size of the agglomerates in solution is below 100 nm but this number is increased by the solvation layer (**Figure S 6.4a**). After deposition both inks produced a continuous layer of nanoparticles.

Thermal stability of the prepared inks was evaluated by DSC-TG experiment performed at room temperature in air. The nanoparticles weight fraction was calculated as the remaining weight fraction after solvent and dispersant degradation. The dispersant is fully degraded at 180 ºC and no further peak was observed up to 600 ºC, which revealed a good stability of the oxide phase produced by solvothermal synthesis (**Figure S 6.4b**).

[1] Granqvist, C. G., *Handbook of Inorganic Electrochromic Materials*, Elsevier, Amsterdam, Netherlands, 2002.

[2] a) Tahir, D.; Lee, E. K.; Kwon, H. L.; Kun Oh, S.; Kang, H. J.; Heo, S.; Lee, E. H.; Chung, J. G.; Lee, J. C.; Tougaard, S. Electronic and optical properties of GIZO thin film grown on SiO2/Si substrates, *Surf. Interface Anal.* 2010, *42*, 906; b) Kang, D.; Song, I.; Kim, C.; Park, Y.; Kang, T. D.; Lee, H. S.; Park, J.-W.; Baek, S. H.; Choi, S.-H.; Lee, H. Effect of Ga/In ratio on the optical and electrical properties of GaInZnO thin films grown on SiO2/Si substrates, *Appl. Phys. Lett.* 2007, *91*, 091910.

[3] Barquinha, P., Ph.D Thesis, Universidade Nova de Lisboa, Portugal, 2010.

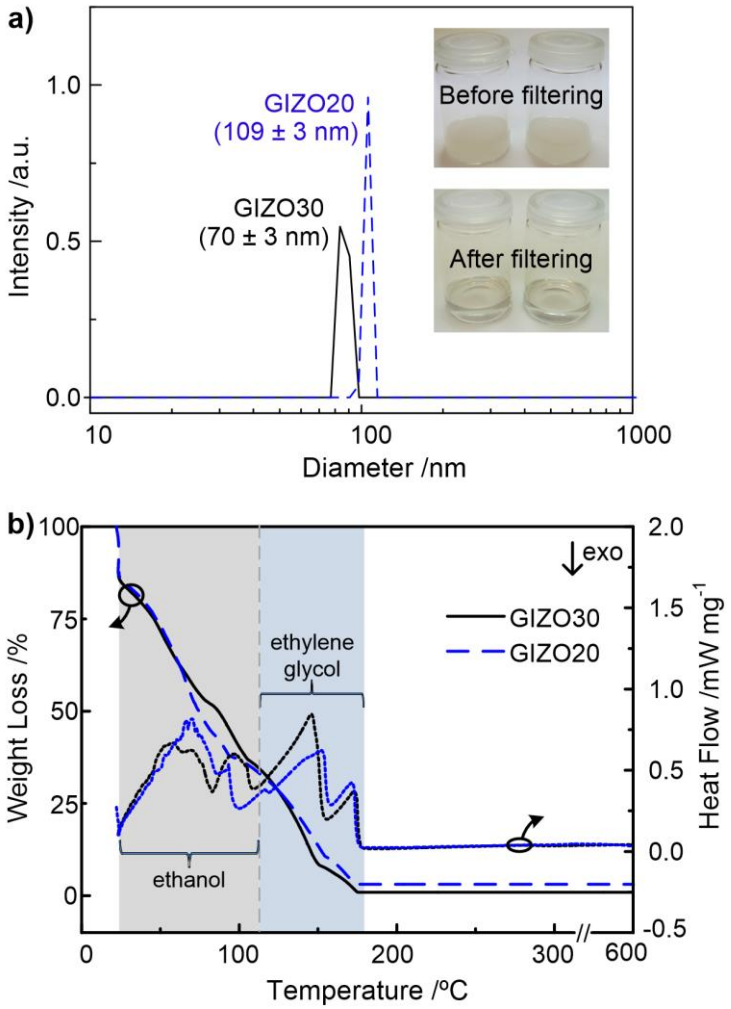

Figure S 6.4. a) DLS size distributions and b) DSC-TG curves performed in air up to 600 ºC, for the two GIZO inks after filtration.

Chapter 7. CONCLUSIONS AND FUTURE WORK

In this work, metal oxides nanoparticles with different morphologies and structures were successfully produced and characterized. Owing to the broad variety of electrochemical devices and applications, it was selected 4 types of devices.

1) Electrochromic device: Tungsten oxide nanoparticles with different crystallographic structures and morphologies were deposited by inkjet printing to form dual-phase films. The *a*-WO_3/*ortho*-$WO_3 \cdot 0.33H_2O$ electrode show the higher optical density due the increased active surface area of the nanorods combined with the type of structure with improved ionic conductivity. Furthermore, ex-situ XRD performed in the nanoparticles shows a higher deformation of the monoclinic crystal structure (*m*-WO_3) during lithiation with a not fully reversible process. Nevertheless, all the presented results proves the benefit of using dual-phase structures when building electrochromic devices.

2) pH sensor: Nanostructured WO_3 probes were produced by electrodeposition on gold electrodes with a sensing area of 1 mm^2. The wax printed layer, here used as an insulator, was proven to be cytocompatible and therefore, a good alternative for sensor assembly. The pH sensitivity of these electrodes shows a near-Nernstain response of -56.7 ± 1.3 mV/pH and reversibility was confirmed for three complete cycles in a pH range of 9 to 5. The application of WO_3 flexible sensors to curved surfaces with a flexible Ag/AgCl reference electrode and solid electrolyte, shows a linear response in the pH range from 8 to 6, with a sensitivity of 14.5 mV/pH but with good possibilities of improvement.

3) Biosensor: The electron transfer properties of the WO_3 nanoparticles were distinguished using three different iron based electron transfer probes, where it was demonstrated that the higher conductivity of the *ortho*-$WO_3 \cdot 0.33H_2O$ nanostructures contributed for faster and reversible redox reactions of cytochrome *c*. Importantly, upon the fabrication of the biosensor, the structural and catalytic properties of c*c*NiR were preserved upon interaction with all three nanostructures; the c*c*NiR modified electrodes showed good electroactivity towards the reduction of nitrite. The comparison with bare ITO electrodes clearly demonstrated that c*c*NiR/WO_3/ITO constructs represent a promising alternative for c*c*NiR based 3rd generation biosensor. In fact, the sensitivities of 2143 mA M^{-1} cm^{-2} are similar to those obtained for single-walled carbon nanotubes.

4) Electrolyte-gated transistor: GIZO nanoparticles were deposited by spin coating and used in electrolyte-gated transistors, which promotes a good interface between the semiconductor and the dielectric. The produced transistors work at low potential and with improved ON-OFF current ratio, up to 6 orders of magnitude. The annealing temperature was crucial to reduce the defect density of GIZO film that allowed V_{Th} closer to 0 V with full degradation of the dispersant (ethylene glycol) and therefore, lower operating voltages. The dependence of the gate voltage in the electrical performance of the EGT was also investigated. The operation mechanism of the transistors was evaluated and it was shown evidences that the mechanism can vary from electric double layer to electrochemical doping, when increasing the gate voltage range, which allowed an improved I_{ON}/I_{OFF} and mobility values without the occurrence of voltage breakdown.

The variety of fields addressed in this dissertation demonstrates the need to use a multidisciplinary approach when dealing with nanoscience and provides a broad view of the potentialities presented by these materials and devices developed during this work. Summarizing, the solvothermal synthesis is a very versatile method to control the growth and morphology of the nanoparticles and can be adapted to different types of metal oxide nanostructures. The low temperatures and reduced-cost techniques used in the production of the devices are compatible with flexible substrates and can, potentially, be adapted for disposable devices. Simultaneously, the use of nanomaterials in the devices contributes for the miniaturization and versatility demands in nanotechnology.

7.1. Future Perspectives

Since research work is a continuous process, many questions and different paths remain to be answered and explored. In this section, some recommendations and future perspectives are addressed regarding the different fields presented in this thesis.

Electrochromic devices

The development of stable dispersions and new deposition techniques opened the possibility to produce nanostructured electrodes with improved stability, life time and low power consumption, which are promising characteristics to replace the dual-phase electrodes. The *ortho*-$WO_3 \cdot 0.33H_2O$ nanorods show to be promising candidates to develop electrochromic devices with a good optical modulation and reduced working times, due to its hydrated structure and high surface area.

Also the high capacitance of V_2O_5 and $Ni(OH)_2$ nanostructures makes this materials very promising for counter-electrodes of the electrochromic devices, which combined with the WO_3 electrodes can be a good solution to develop fully nanostructured devices.

The main concern in the development of these devices is the electrolyte. So far, solid electrolytes presents poor performances in terms of ionic conductivity and longtime stability which are crucial parameter for a good electrochromic performance of the electrodes. Thus, further optimization of the solid electrolytes should be evaluated.

Sensing devices

The optimization of the sensing performances of WO_3 are at the present moment being analyzed with a complete study of the deposition conditions and its reproducibility. Nevertheless, nanostructured metal oxides, in general, can be suitable as sensing probes due to the high surface area and capacitance, and should be tested accordingly.

For the fabrication of flexible devices, the conductive layer can be modified with the use of a conductive ink, making it fully solution processed. Also, the test in curve surfaces should be conducted in liquid electrolytes before developing a better interface suitable for solid analytes.

Furthermore, the fabrication of a stable solid reference electrode is still a challenge within the scientific community.

Electrolyte-gated transistors

The application of electrolyte-gated transistors with organic semiconductors are already developed for sensing applications, and it should also be further explored with the use of oxide semiconductors. The adaption of the transistor structure to liquid analytes can be a good alternative to improve the limit detection of different types on ions in solution.

For electronic purposes and for further miniaturization of the transistors, the double layer of the electrolyte should also be improved as well as the deposition techniques should be adapted for scaling compatible techniques.

In general, I believe that the future is nano!

Nanotechnology and nanoparticles are already present in our daily life. The metal oxide nanoparticles are just a small part of all the nanoparticles developed in the world and even so, the application possibilities are already huge. The use of flexible substrates opened the window for wearable applications and the consumers are already available for this opportunity. The possibility to monitor body signals continuously is already available in the market (**Figure 7.1**) and, in the near future will be worn by most people. To get there, the development of cheaper and stable components is still required, not only the sensing devices but also batteries, displays, firmware and memories. Considering this application, I think that this work brings some insights to the development of new and promising devices that can be integrated in wearable platforms.

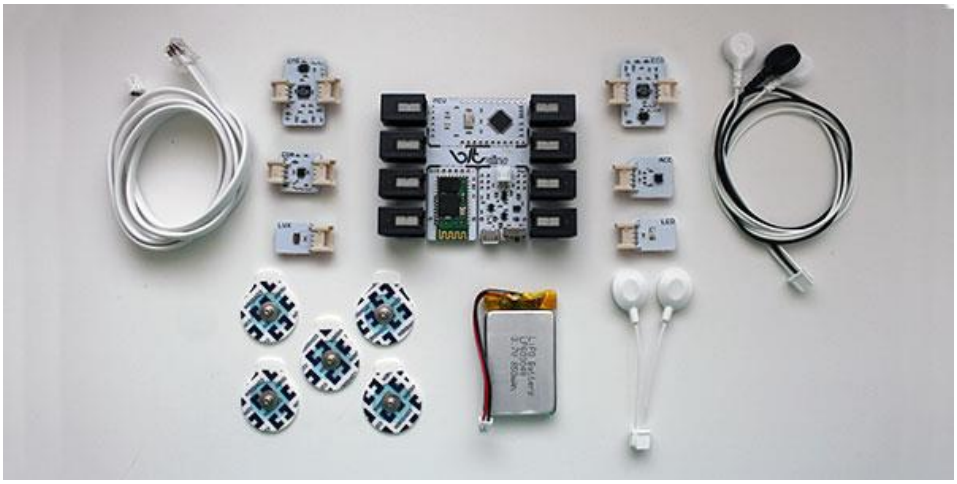

Figure 7.1. Bitalino plugged kit, available at www.bitalino.com, as an example of a commercial wearable sensor.

Chapter 8. APPENDIX 1

The work presented in Chapter 3, was also publicized as the front cover of Advanced Electronic Materials journal, as shown in **Figure A 1**.

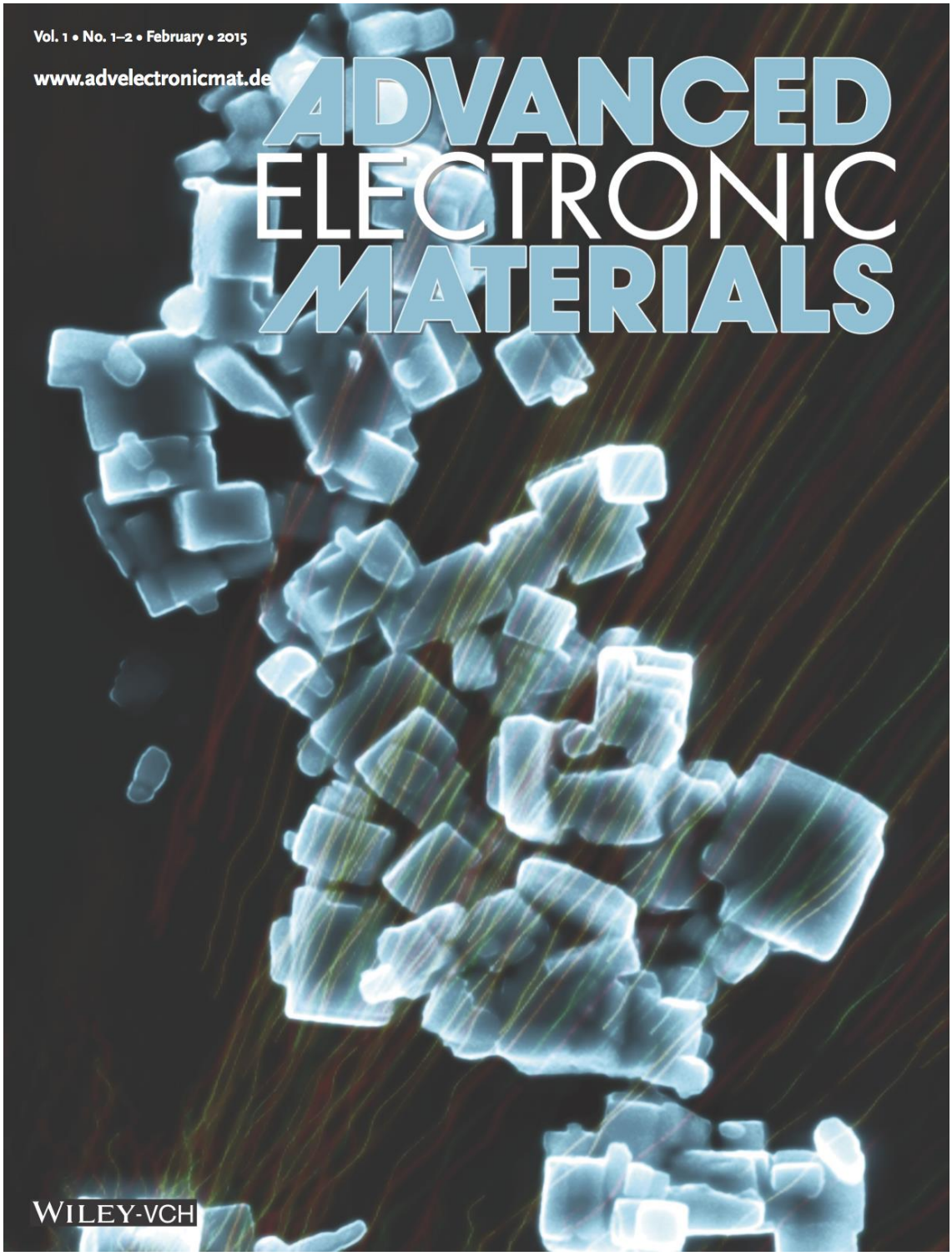

Figure A 1. Front cover of the first issue of Advanced Electronic Materials.